

Transition Dynamics between the Multiple Steady States in Natural Ventilation Systems: From Theories to Applications in Optimal Controls

by

JINCHAO YUAN

B.E. Thermal Engineering
Tsinghua University, 2001

M.S. Architectural Engineering
Pennsylvania State University, 2003

Submitted to the Department of Architecture
in partial fulfillment of the requirements for the degree of
Doctor of Philosophy in Building Technology
at the

MASSACHUSETTS INSTITUTE OF TECHNOLOGY

September 2007

© 2007 Massachusetts Institute of Technology.
All rights reserved.

Signature of Author_____

Department of Architecture
August 10, 2007

Certified by_____

Leon R. Glicksman

Professor of Mechanical Engineering and Building Technology

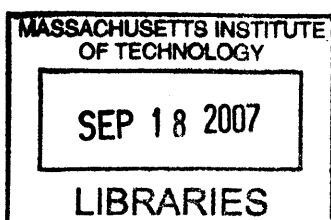
/ \ Thesis Supervisor

Accepted by_____

Julian Beinart

Professor of Architecture

Chair of the Department Committee on Graduate Students



Thesis Committee Members

Leon R. Glicksman, Professor of Mechanical Engineering and Building Technology

Leslie K. Norford, Professor of Building Technology

Ain Sonin, Professor of Mechanical Engineering

Transition Dynamics between the Multiple Steady States in Natural Ventilation Systems: From Theories to Applications in Optimal Controls

by

JINCHAO YUAN

Submitted to the Department of Architecture
on August 10, 2007, in partial fulfillment of the
requirements for the degree of
Doctor of Philosophy in Building Technology

Abstract

In this study, we investigated the multiple steady state behavior, an important observation in numerical and experimental studies in natural ventilation systems. Theoretical models are developed and their applications in numerical simulations and ventilation controls are presented.

In a system with multiple steady states, how the system reaches different steady states is determined by the initial values of the systems and the dynamical system characteristics of the system. Mathematical models are developed to model the dynamical system behavior of a series of ventilation systems, ranging from simple single-zone systems to complex systems with thermal mass. More importantly, we found that the system can transform from one steady state to another under sufficient perturbations (disturbances) when multiple steady states exist. A successful transition is determined by both the magnitudes and durations of the perturbations.

The transition dynamics are found to be important in theoretical, computational, and control applications. For example, the actual stability of a mathematically (or locally) stable steady state is highly correlated to the minimum perturbation requirements for a state transition. If two indicative parameters—the minimum perturbation time and the minimum perturbation magnitude—are small for the system to transit from one steady state to another, a mathematically stable steady state can be unstable in actual conditions, where stochastic disturbances exist as “strong perturbations”. Further, building thermal mass is also found to have significant impacts on the state transitions between the multiple steady states. With thermal mass, the state transition becomes more difficult to occur.

The state transition dynamics can also be applied to numerical simulations. We have developed a convenient dynamical simulation method to identify the possible steady states in buildings with complex geometries and test the stabilities of the obtained steady states. The method can determine nearly all the possible steady state the system may reach in a feasible range using different search methods; whether the steady states obtained are stable in an actual environment can also be determined by a disturbance test based on the transition dynamics between the multiple steady states.

Further, the state transition dynamics can be strategically applied in hybrid ventilation controls. In the past, designers and engineers have viewed the multiple steady states as negative aspect of ventilation design and have been trying to avoid the multiple steady states as much as possible. In this study, we have developed positive applications of multiple steady states based on a dynamic state transition in real-time to enhance the ventilation efficiency of a hybrid ventilation system and to reduce the energy usage in buildings.

A coupled multi-zone airflow and thermal program for transient entire building simulations is also developed in parallel with the study. With the understanding on the multiple steady state issues, the developed program has overcome a few non-trivial numerical problems reported in other similar simulation programs and has shown good numerical performance in coupled airflow and thermal analysis. The program is also used as a tool for identifying the multiple steady states in buildings with complex geometries and for testing the actual stabilities of the obtained steady states in real conditions.

Thesis Supervisor: Leon R. Glicksman
Title: Professor of Mechanical Engineering and Building Technology

Acknowledgments

I would like to express my sincere thanks to my advisor, Prof. Leon Glicksman for offering me the opportunity to work on this project. He has always given me valuable ideas and encouragement in completion of this thesis. My thanks are extended for his tireless support, great advice and directions throughout the work. His high standards and deep knowledge in research have provided me the most valuable help in my research work.

I would also express my great gratitude to Dr. Leslie Norford at the Building Technology program for his valuable consulting on various topics related to my research. His advice on experimental data and the control systems is very helpful for me to accomplish the thesis. I would also thank Professor Ain Sonin in the Department of Mechanical Engineering for his valuable comments on fluid mechanics and heat transfers.

I would like to thank my colleagues in Building Technology for their precious help and generous support throughout my research and study. I owe my special thanks to Gang Tan and Matthew Lehar for discussions and help in coding; Henry Spindler and Christine Walker for their help in locating the experimental validation data; Peter Armstrong and Bryan Urban for their help in my teaching assistant courses. I would also like to extend my thanks to the secretaries Kathleen Ross, Nancy Dalrymple, and Rachel McPherson in the Building Technology program office, and Renee Caso in the Department of Architecture headquarters for their help in the numerous administrative issues. To the all my colleagues in the Building Technology Program, thank you for their collaboration and friendship.

My sincere love and thanks to my parents, Mingfang Yang and Chaogang Yuan for their non-reserved love and support. My thanks also extend to the other family members, Dee Fang, and Yan Wang, for their support in my study. for their help in administrative issues. To the all my colleagues in the Building Technology Program, thank you for their collaboration and friendship.

My sincere love and thanks to my parents, Mingfang Yang and Chaogang Yuan for their non-reserved love and support. My thanks also extend to the other family members, Dee Fang, and Yan Wang, for their support and understanding.

Dedication

To my mother Mingfang Yang

Contents

Abstract	3
Acknowledgements	5
Dedication	7
1 Introduction to building airflow / thermal simulations and multiple steady states phenomenon	25
1.1 General background	25
1.2 Existing building airflow and thermal models	26
1.2.1 Multi-zone model	27
1.2.2 CFD model	27
1.2.3 Zonal Model	28
1.3 Need for efficient airflow simulation tools	29
1.3.1 Temperature solution	29
1.3.2 Transient dynamics solution	30
1.3.3 Thermal mass modeling	30
1.4 Multiple steady state phenomena—challenges to coupled airflow and thermal simulations	31
1.5 Objectives of present work	32
1.5.1 Coupled airflow and thermal simulation models	32
1.5.2 Transition dynamics between multiple steady states	33
1.5.3 Applications of multiple steady states	33
1.6 Outline of thesis	34
I Coupled airflow and thermal simulation program	37
2 Integrated transient multi-zone airflow and thermal model with thermal mass solution	39
2.1 Essential elements of multi-zone models	39
2.1.1 Mass balance equation	40
2.1.2 Energy conservation	40
2.1.3 Flow path equations	41
2.2 Integrate energy equations into multi-zone models	42

2.2.1	Existing airflow-thermal coupling studies	42
2.2.2	Framework for energy equation solution	43
2.3	Thermal mass solution	44
2.4	Coupled multi-zone airflow, thermal, and mass models	45
2.4.1	Transient airflow and thermal dynamics solving	45
2.4.2	Thermal mass temperature solution	47
2.4.3	Numerical coupling strategies	48
2.4.4	Other features of the program	50
2.5	Numerical procedures enhancement	51
2.5.1	Air temperatures solution	51
2.5.2	Thermal mass solution	53
2.5.3	Airflow flow solution	54
2.6	Program interfaces	54
2.7	Summary	55
3	Validations of the simulation program	57
3.1	Validation procedures	57
3.2	Prototype test building descriptions	58
3.3	Comparison with CONTAMW	59
3.4	Comparison with steady state CFD	59
3.4.1	Case 1—A Luton (central atrium) type building	61
3.4.2	Case 2—A chimney type building	64
3.4.3	Summaries	67
3.5	Compare with transient field measurement data	69
3.5.1	New models in the research version	69
3.5.2	Building monitoring data	71
3.5.3	Simulation results	74
3.5.4	Possible uncertainties	76
3.5.5	Summaries	77
3.6	Conclusions	77
II	Dynamical system analysis of multiple steady states	79
4	Multiple steady states in a single zone natural ventilation system—A dynamical system analysis	81
4.1	Introduction	81
4.2	System equations	83
4.3	System characteristics and solution behaviors	85
4.4	Conditions for the system to have multiple steady states	88
4.4.1	General cases of $UA \geq 0$	89
4.4.2	Special case of $UA=0$	89
4.4.3	Graphical representation	91
4.5	Critical point of the initial temperature	92
4.5.1	Theoretical critical point	92

4.5.2	Practical point of view on the initial conditions	93
4.6	Discussions and potential applications	94
4.7	Conclusions	95
5	Multiple steady states in a single-zone natural ventilation system with thermal mass—Dynamical system analysis	97
5.1	Introduction	97
5.2	Mathematical Models	99
5.2.1	Governing equations	99
5.2.2	Solution behaviors	102
5.2.3	Two extreme cases	104
5.3	Conditions for multiple steady states to exist	106
5.3.1	A similar system view	106
5.3.2	A parameter-dependency view	106
5.4	Initial values and dynamical system characteristics	107
5.4.1	Mechanisms for the system to reach different steady states . .	109
5.4.2	Systems that have only one steady state	110
5.5	Local stability analysis of the three steady states	112
5.5.1	Generalize the dynamical system characteristics	112
5.5.2	Demonstrate the eigen characteristics	113
5.5.3	Steady States 1 and 3	114
5.5.4	Steady State 2	115
5.5.5	Summary on eigenvalues	116
5.6	Discussion	117
5.7	Conclusions	117
6	Multiple steady states in a single-zone natural ventilation system with thermal mass—Transient behaviors and impact of mass	121
6.1	Introduction	121
6.2	Transient behaviors	123
6.3	Trajectory characteristics near Steady States 1 and 3	125
6.3.1	Trajectories near SS1 and SS3	126
6.3.2	Applications of linear approximations	127
6.3.3	Nonlinear effect—Bottleneck effect revisit	128
6.4	Trajectory characteristics near Steady State 2	129
6.4.1	Eigen characteristics	130
6.4.2	Compute the separatrices	130
6.5	Impact of thermal mass parameters on separatrices shapes	132
6.5.1	Impact of hA_m values	132
6.5.2	Impact of $M_m c_m$ on the separatrices	134
6.6	Factors that affect the shape of the separatrices	136
6.6.1	Special point O	136
6.6.2	Vector directions on phase plane	139
6.6.3	Eigenvector direction at SS2	139
6.7	Impact of thermal mass parameters on other dynamical behaviors .	139

6.8	Impact of hA_m on dynamical behaviors	140
6.8.1	Impact of M_mc_m on dynamical behaviors	141
6.9	Conclusions	143

III Transition dynamics between multiple steady states 147

7	Transitions between the multiple steady states in a natural ventilation system with combined buoyancy and wind driven flows	149
7.1	Introduction	149
7.1.1	Dynamical system analysis of the system	151
7.2	System responses under strong perturbations	156
7.2.1	Heat source perturbation	157
7.2.2	Wind velocity perturbation	158
7.3	Minimum perturbation magnitude	158
7.3.1	Heat source perturbation	159
7.3.2	Wind velocity perturbation	160
7.3.3	Explanation to a previous study	163
7.3.4	Summary on the minimum perturbation magnitude	165
7.4	Minimum perturbation time	165
7.5	Robustness of the stable steady states	169
7.5.1	Case introduction	169
7.5.2	Minimum perturbation magnitude explanation	170
7.5.3	Minimum perturbation time explanation	172
7.6	Applications of minimum perturbation time	174
7.6.1	Determination of the actual existence of a steady state in actual systems	175
7.6.2	Sensitivity studies on other parameters	178
7.6.3	Discussion on more general applications	180
7.7	Conclusions	180
8	Transitions between the multiple steady states in a single-zone natural ventilation system with thermal mass	183
8.1	Introduction	183
8.2	Mathematical models	185
8.3	System behavior under strong perturbations—minimum perturbation magnitude	186
8.4	System behavior under strong perturbations—minimum perturbation time	188
8.5	Impact of hA_m on state transitions	189
8.5.1	Heat source perturbations	189
8.5.2	Pressure perturbations	189
8.6	Effect of air to mass heat capacity ratio	193
8.7	Conclusions	194

IV Applications of multiple steady states in buildings 197

9 Using the dynamical system characteristics to guide chimney and wind scoop designs—how to deal with the multiple steady states	199
9.1 Introduction	199
9.2 Dynamical system models	201
9.2.1 Building configuration	201
9.2.2 Governing equations	202
9.3 Steady state behaviors	203
9.3.1 Buoyancy-dominated steady state	203
9.3.2 Wind-dominated state	205
9.4 Conditions for multiple steady states to exist	205
9.5 Dynamical system analysis	206
9.5.1 Impact of initial values	206
9.5.2 Eigen characteristics of the system at steady states	207
9.6 Ventilation applications	210
9.6.1 Chimney designs	210
9.6.2 Wind scoop designs	211
9.7 Conclusions	211
10 Identification of the multiple steady states in buildings with complex geometries by a computer model	215
10.1 Introduction	215
10.2 Dynamics model—a single-variable case	216
10.3 Dealing with thermal mass	219
10.4 Generalization to multiple-zone cases	220
10.5 Exhaustive search methods	221
10.6 An example multiple-zone building (Case 1)	222
10.7 Results	225
10.8 Another case with four steady states (Case 2)	227
10.9 Test the stabilities of the obtained steady states	229
10.9.1 Theoretical background	229
10.9.2 A practical test method	230
10.10 Test on the two cases	230
10.10.1 Test results	230
10.10.2 Stability of SS3 (in Case 2)	232
10.10.3 Further tests	234
10.11 Discussions	235
10.12 Conclusions	236
11 An innovative natural ventilation control strategy based on state transitions between multiple steady states	239
11.1 Introduction	239
11.2 Theories	240
11.3 Characteristics of the two stable steady states	243

11.4	State switch strategy using perturbations	244
11.5	Triggering criteria	245
11.6	Stop criteria	246
11.7	Switch time	246
11.8	Optimal perturbation magnitude for minimum energy cost	247
11.9	Compare with conventional ventilation strategy	247
11.10	Model identifications and parameters estimations	249
11.11	Sensitivity studies	251
11.12	Model implementation	256
11.13	Preliminary results	257
11.14	Learning and self-tuning	257
11.15	Conclusions	258
12	Conclusions and recommendations	261
12.1	Conclusions	261
12.1.1	Coupled airflow simulation	261
12.1.2	Dynamical system analysis of multiple steady state phenomena	262
12.1.3	Transition dynamics between the multiple steady states	263
12.1.4	Applications of multiple steady states	264
12.2	Recommendations	265
12.2.1	Coupled program	265
12.2.2	Multiple steady state phenomena	266
A	Interface of the CoolVent program	275
A.1	Major model assumptions	275
A.2	Major parameters used in the program	276
A.2.1	Airflow resistance	276
A.2.2	Load values and schedules	276
A.2.3	Wind pressure coefficients	277
A.3	Program interface	277
A.4	Stage 1—General information	278
A.4.1	Weather/Environment parameters	278
A.4.2	Terrain information	279
A.4.3	Parameters for temperature solution	280
A.4.4	Buttons	281
A.5	Stage 2—Detailed descriptions	281
A.5.1	Central atrium type	281
A.5.2	Chimney type	281
A.5.3	Cross ventilation type	282
A.5.4	Single-sided ventilation type	285
A.5.5	Thermal mass description	287
A.5.6	Windows control strategies	287
A.5.7	Buttons	288
A.6	Stage 3—Visualization and output	288
A.6.1	Animated visualization	288

A.6.2	Graphical report by charts	291
A.6.3	Text report by text files	291
B	Supplemental validation studies on the CoolVent program	293
B.1	Compare with analytical models	293
B.1.1	Transient air temperature dynamics by exponential decay tests	293
B.1.2	Transient heat transfer with thermal mass	295
B.1.3	Transient heat transfer through semi-infinite body	296
B.2	Comparing with Matlab ODE solver	298
B.3	Summary	300

List of Figures

2-1	Building representation of CONTAMW	39
2-2	An example of thermal mass modeling (Source: EnergyPlus documentation [26])	44
2-3	Structures of the developed multi-zone airflow and thermal program .	46
2-4	The thermal mass modeling network	47
2-5	“Ping-pong” coupling strategy vs. “Onion” coupling strategy	49
2-6	“Ping-pong” strategy for airflow, thermal, and thermal mass coupling .	50
2-7	Program interface for design users	56
3-1	A natural ventilated building in UK (Superimposed on the graph presented in Walker [61])	58
3-2	CoolVent vs. CONTAMW simulation results for a three-story building .	60
3-3	Zone divisions for CoolVent, especially in the atrium area	61
3-4	CoolVent and CFD results summaries (Luton Building, pure buoyancy flow)	62
3-5	CFD visualization of the pure buoyancy-driven flows in the Luton building	63
3-6	CoolVent and CFD simulation results summaries (Luton Building, hybrid buoyancy/wind flows)	65
3-7	CoolVent and CFD simulation results summary (Chimney type, pure buoyancy flows)	66
3-8	Internal and exiting temperatures of the two office zones in CFD simulation results (Chimney type, pure buoyancy flows)	67
3-9	CoolVent and CFD simulation results summary (Chimney type, hybrid buoyancy/wind flow)	68
3-10	Models for combined internal radiation and convection in a space . .	69
3-11	The shading fraction on the north office in the beginning and end of August (atrium side)	71
3-12	Monitored Electricity usage for a week during the validation period .	73
3-13	The floor-average temperatures in Luton building (Aug 2 to Aug 12)	75
3-14	Distribution of prediction errors for the three floors	76
4-1	Configuration of a single-zone combined buoyancy and wind driven natural ventilation system	82
4-2	Dynamics behavior of the system: $f(T^{**}) = dT^{**}/dt$ vs. T^{**} for $UA > 0$ (solid line) and $UA = 0$ (dashed line)	86

4-3	The flow rate q vs. dimensionless zone temperature T^{**} ($q > 0$ stands for upward buoyancy-dominated flow)	88
4-4	Three possible scenarios of the steady state solutions of the system	90
4-5	Multiple steady states regions for different UAs	91
4-6	Buoyancy dominate conditions for different UA values	94
5-1	Configurations of a single-zone natural ventilation system with thermal mass	100
5-2	The air and the thermal mass temperatures vs. time: initial stage and full range	103
5-3	Two steady states the system can reach starting from two different initial values	103
5-4	$f_0(T_a^*)$ and $f_\infty(T^*)$ for the two extreme cases	105
5-5	The change of the steady states of the system for different r values	108
5-6	Trajectories, fixed points, attraction regions, and separatrices on the phase plane (parameters in Table 5.1)	110
5-7	The trajectories for systems that have only one steady state: a). $r < P^{**}UA/Z$ (only has SS1); b). $r > 1$ (only has SS3)	111
5-8	Bottleneck the system encounter due to a “ghost” fixed point	112
6-1	The trajectory characteristics of a system with multiple steady states on the phase plane ($h = 5 \text{ W/m}^2\text{-K}$, and $M_m = 6250 \text{ kg}$)	124
6-2	The air and the thermal mass temperatures vs. time: initial stage and full range	125
6-3	Fast and slow eigendirections of the linearized system near SS1 and SS3	127
6-4	Trajectories and time characteristics for a system that has only one steady state (SS1)	129
6-5	Trajectories and time characteristics for another system that has only one steady state (SS3)	130
6-6	Stable and unstable manifolds of the saddle point (Steady State 2)	131
6-7	Trajectories and separatrices for two different hA_m values ($A_m = 100 \text{ m}^2$)	132
6-8	The separatrices for different hA_m values ($A_m = 100 \text{ m}^2$)	134
6-9	Separatrices and attractions regions on the phase plane when for two different M_m values	135
6-10	The separatrices for different thermal mass weights	136
6-11	Separatrices vs. Nullclines on phase plane	137
6-12	The change of the eigenvalues with hA_m values at SS1 and SS3 ($A_m = 100 \text{ m}^2$)	141
6-13	Variations of the two eigenvalues of the linearized system at SS2 with different hA_m values	142
6-14	Eigenvalues of the linearized system for different $M_m c_m$ values: a.) at SS1; b.) at SS3	143
6-15	Eigenvalues of the system linearized at SS2 for different $M_m c_m$ values	144

7-1	A single zone natural ventilation system with opposing wind and buoyancy forces	151
7-2	Solution characteristics of the system: dT^{**}/dt vs. T^{**}	153
7-3	Three possible scenarios of the steady state solutions of the system	155
7-4	A strong perturbation acting on the system	157
7-5	System under a heat source increase perturbation ($\Delta E/E = 55.7\%$)	157
7-6	System under a wind velocity decrease perturbation ($\Delta v_{ref}/v_{ref} = -10\%$)	158
7-7	Unsuccessful flow pattern switch under stronger wind perturbations ($\Delta v_{ref}/v_{ref} = -25\%$)	161
7-8	Transitions between steady states under a gradually reducing wind velocity decrease perturbation	162
7-9	System under wind velocity increase perturbation ($\Delta v_{ref}/v_{ref} = 5\%$)	163
7-10	The change of the system curve and the steady state solutions when velocity increases ($\Delta v_{ref}/v_{ref} = 15\%$)	164
7-11	The minimum perturbation time (s) vs. heat source perturbation $\Delta E/E$ for transition from wind dominated to buoyancy dominated flow	167
7-12	Minimum perturbation time (s) vs. wind velocity decrease perturbation $\Delta v_{ref}/v_{ref}$ for transition from steady state 1 to 3	168
7-13	Minimum perturbation time vs. wind velocity increase perturbation $\Delta v_{ref}/v_{ref}$ for transition from steady state 3 to 1	168
7-14	Observed behavior of the steady state of the system (Superimposed on the experimental results by Heiselberg et. al [35])	170
7-15	Minimum perturbation magnitude $\Delta E_{min}/E$ vs. ξ for transitions between two stable steady states	171
7-16	Minimum perturbation magnitude $ \Delta P^* /P^*$ vs. ξ for transitions between two stable steady states	172
7-17	Minimum perturbation time vs. ξ ($\Delta v_{ref}/v_{ref} = 10\%$) for transition from the buoyancy dominated steady state 3 to the wind dominated steady state 1	173
7-18	Minimum perturbation time vs. ξ under pressure (wind velocity) perturbations ($ \Delta P_{min}^* /P^* = 0.25$)	174
7-19	Minimum perturbation time vs. ξ ($\Delta E/E = 0.5$) for transition from wind dominated steady state 1 to buoyancy dominated steady state 3	175
7-20	Minimum perturbation time (s) vs. Wind velocity perturbations for different ξ values from 0. 3 to 0.9 (switch from buoyancy dominated state 3 to wind dominated state 1)	176
7-21	Minimum perturbation time (s) vs. heat source perturbations for different ξ values from 0. 1 to 0.9 (switch from wind dominated state 1 to buoyancy dominated state 3)	177
7-22	Minimum perturbation time for different ξ values under a 10% velocity increase perturbation (transition from buoyancy to wind dominated states) for water bath experiment in Heiselberg et. al [35])	177

7-23	Stable steady states for with from both stability and robustness of steady state solutions	178
7-24	Minimum perturbation time vs. ξ with different initial wind velocities for transition from buoyancy dominated to wind dominated states	179
8-1	A single-zone air-mass natural ventilation system with opposing wind and buoyancy forces	184
8-2	A “strong” perturbation	185
8-3	Responses of the system to heat source perturbations of two different durations ($\Delta E/E = 1.1137$, $hA_m = 840 \text{ W}/\text{°C}$)	190
8-4	Minimum perturbation time vs. hA_m value under heat source perturbation ($\Delta E/E = 1.1137$) for transition from SS1 to SS3	191
8-5	Minimum perturbation time vs. hA_m for transitions from SS3 to SS1 under pressure perturbation ($\Delta P/P = 0.2$)	192
8-6	Minimum perturbation time vs. hA_m for transitions from SS1 to SS3 under pressure perturbation ($\Delta P/P = -0.2$)	193
9-1	Configurations for a building with two zones in a typical atrium design	201
9-2	Two possible steady states of the system	204
9-3	Dynamical system characteristics of the system shown on the phase plane	207
9-4	Buoyancy-dominated natural ventilation design consideration	211
9-5	Wind-dominated ventilation design considerations	212
10-1	A single-zone natural ventilation system with opposing wind and buoyancy forces	217
10-2	Transient characteristics of the system	218
10-3	Two different (stable) steady states the system can reach, starting from two different initial temperatures	218
10-4	Grid search for single-variable systems	219
10-5	A single-zone natural ventilation system with thermal mass	220
10-6	A general grid search for a 2-D system	222
10-7	A coarsest grids ($m = 2$) grid search applied to a 2-D system	223
10-8	Random initialization for a 2-D system	223
10-9	The geometries of the simulated building	224
10-10	Three possible stable steady states obtained in a sample multi-zone building model	226
10-11	The modified building geometries	227
10-12	The four possible steady states in a new sample building with a higher roof chimney	228
10-13	Stability tests under wind velocity disturbances within $\pm 5\%$ (for Case 2)	231
10-14	Stability tests under wind velocity disturbances within $\pm 5\%$ (for Case 1)	232
10-15	System temperatures output under different levels of stochastic wind velocity perturbations (for SS3 in Case 2)	233

10-16	Stability tests under wind velocity disturbances within $\pm 30\%$ (for Case 2)	234
10-17	Stability tests under wind velocity disturbances within $\pm 30\%$ (for Case 1)	235
11-1	A natural ventilation system with flows driven by combined buoyancy and wind forces	241
11-2	The transient temperature characteristics of the system	242
11-3	The volume flow rate of the system as a function of the system temperature	242
11-4	The two theoretically stable ventilation patterns	243
11-5	A strong perturbation acts on the system	244
11-6	The Energy consumption for a state switch vs. the perturbation magnitudes	248
11-7	The comparison between energy consumption of a State Switch strategy and a conventional fan-on flow boosting strategy	249
11-8	The Equivalent Fan-on Time vs. $\Delta P/P$ for a sample case	250
11-9	The steady state points for different heat source strength and wind velocity combinations ($UA = 80 \text{ W}/^\circ\text{C}$, $h = 3 \text{ m}$, $A = 0.566 \text{ m}^2$)	251
11-10	The steady states that have a corresponding lower temperature solution and the steady states that do not have one ($UA = 80 \text{ W}/^\circ\text{C}$, $h = 3 \text{ m}$, $A = 0.566 \text{ m}^2$)	252
11-11	Identification results for four different opening areas ($UA = 80 \text{ W}/^\circ\text{C}$, $h = 3 \text{ m}$)	253
11-12	Identification results for four different UA values ($h = 3 \text{ m}$)	254
11-13	The model identification results for four different h values ($UA = 80 \text{ W}/^\circ\text{C}$)	255
11-14	A two-zone building for implementing and testing the control strategy	257
11-15	Test results on a two-zone building	258
11-16	Updated model and training results	259
A-1	Stage 1 of CoolVent program	278
A-2	Central Atrium prototype	282
A-3	Chimney type prototype	283
A-4	Cross ventilation prototype	284
A-5	Single-sided Ventilation prototype	285
A-6	Side window spacing specifications	286
A-7	Animation output	289
A-8	Temperature history output	291
A-9	Text report output	292
B-1	Exponential decay case without heat source	294
B-2	Exponential decay case with heat source	295
B-3	Analytical vs. CoolVent predicted thermal mass temperatures	297
B-4	Analytical vs. CoolVent: thermal mass temperatures at $t = 5560\text{s}$	298

B-5	Analytical vs. CoolVent predicted semi-infinite body temperatures . . .	299
B-6	Matlab vs. CoolVent under cyclic sine temperature input	300

List of Tables

3.1	Sample occupant schedule in August 2003	72
3.2	Summary of the temperature prediction errors for the three floors	74
5.1	Major parameters used in the example cases	101
8.1	Minimum perturbation times vs. hA_m value for the transitions from wind dominated SS1 to buoyancy dominated SS3 under heat source perturbation ($\Delta E/E = 1.1137$)	189
8.2	Minimum perturbation times vs. hA_m value for transition from SS3 to SS1 under pressure perturbation ($\Delta P/P = 0.2$)	191
8.3	Minimum perturbation times vs. hA_m values for transitions from SS1 to SS3 under pressure perturbation ($\Delta P/P = -0.2$)	192
8.4	Minimum perturbation times to switch from solution 1 to 3 vs. r value (under heat source perturbation, $\Delta E/E = 1.1137$, $hA_m = 840$) for fixed air mass	194
8.5	Minimum perturbation times to switch from solution 3 to 1 vs. r value (under pressure perturbation, $\Delta P/P = 0.2$, $hA_m = 840$) for fixed air mass	194
A.1	Input parameters for steady state simulations	279
A.2	Input parameters for transient simulations	279
A.3	TM2 weather files included in current CoolVent release	280
A.4	Terrain information	280
A.5	Temperature solution parameters	280
A.6	Central atrium type specifications	283
A.7	Chimney type building specifications	284
A.8	Cross ventilation type specifications	284
A.9	Single-sided ventilation parameters	285
A.10	Specifications for side window spacing	286
A.11	Thermal mass parameters	287
A.12	Window control strategies options	288
A.13	Snapshot input settings	290

Chapter 1

Introduction to building airflow / thermal simulations and multiple steady states phenomenon

1.1 General background

Energy efficiency, thermal comfort, and indoor health are the three major concerns for sustainable building designs. Energy efficiency issues are directly related to the operation cost of the building. In a macroscopic view of energy consumptions in the United States, it is estimated that 40% of total energy is consumed in buildings. Equally important, the comfort and health issues in buildings can affect the occupants' physical and mental conditions, as well as productivity in workplaces. For example, SBS (Sick Building Syndrome), which may be caused by toxic indoor pollutant sources and poor ventilations, can greatly reduce the productivities of the building occupants. To lost of productivity due to SBS is estimated to be 20 to 160 billion U.S. dollars per year (Fisk [31]).

To achieve the goal of sustainable designs, a widely used strategy for building ventilation is *natural ventilation*. Natural ventilation introduces the outdoor airflows inside building by wind or buoyancy forces, with minimal employment of the energy-consuming mechanical equipment. To properly guide natural ventilation designs, computer simulations have been intensively used in the design practice. Through computer simulations, designers are able to examine the performance of the building in energy efficiency, thermal comfort, and indoor health.

However, efficient modeling of natural ventilation flows is still a challenging problem. For natural ventilation, the temperature differences within a building can be important driven forces of the airflows, especially in buoyancy-driven systems. Therefore, the thermodynamics are strongly coupled with the fluid dynamics in natural ventilation systems. Due to the strong coupling, the coupled solution of temperature and airflow in natural ventilation systems becomes more difficult than that in mechanical ventilation systems. One of the challenges comes from the solution multiplicity of the natural ventilation systems (see Axley [10]), which is still an unfamiliar issue to

modelers and program developers.

A further need of computer simulation lies in the need of building operation and control strategies, such as ventilation and night cooling controls. In order to develop smart control strategies, the transient behavior of the building system needs to be well understood. For example, the transient interaction between the air and the thermal mass will have a huge impact on the system's flows and temperatures. To utilize this dynamics effect, night cooling preset strategies (e.g., Braun [13], Rabl and Norford [52], Braun et al. [14], Armstrong et. al [4, 5]) are widely used, which allow the thermal mass to store “cooling” during the night—usually using a chiller—and to release the “cooling” during the day. With natural ventilation, free cooling of the outdoor air may even be used in steady of the power-consuming chiller to precool the thermal mass. However, in order to adequately apply the night cooling strategies, transient simulations that couple the flow and temperature solutions are necessity.

In summary, computer simulations of natural ventilations are necessary for both designs and operations of buildings, especially naturally ventilated buildings, in order to achieve energy efficiency, thermal comfort, and indoor health.

1.2 Existing building airflow and thermal models

In order to simulate building airflows, mathematical models have been developed based on fundamental heat transfer and mass transport theories. In early days when computers were still not popular, most of the models were simple analytical or empirical models based on fundamental fluid dynamics and heat transfer laws. The complexity of the model was generally confined by the available computational power. However, well tested empirical and analytical models have still been widely used nowadays.

Modern computer technologies greatly enhance our computational power. In this context, computer models are built to solve the underlying physics problem in building flows by solving the linear and nonlinear algebra equations, or ordinary and partial differential equations. The improvement of computational powers allows much more complex models in solving airflow and thermal problems in buildings with complex geometries and more complicated boundary conditions.

Two types of most widely used models for building airflow and thermal simulations are the *multi-zone* models and the *Computational Fluid Dynamic* (CFD) models. A multi-zone model usually treats a single zone (usually a room or a space or) as a node that connects with the other nodes by flow paths. It is usually used to calculate the macro-scale bulk airflow and thermal distribution/transport within an entire building. A CFD model divides the domain of interest—usually a single room or space—into finer cells and calculates the micro-scale velocity and temperature distributions within the domain. The two types of models share similar principles of mass and energy conservation, but they are usually different in problem formulations and solution algorithms. More specifically, they have major differences in model complexities, space discretization (meshing) methods, boundary condition specifications, and solution procedures.

Another type of widely used models for building simulations is the *zonal* models. A zonal model is an intermediate model between a “micro-scale” CFD model and a “macro-scale” multi-zone model. The discretization method for a zonal model is similar to that for a CFD model (although usually coarser), but the equation set applied to each cell is similar to a multi-zone model (although differences exist).

1.2.1 Multi-zone model

A multi-zone model takes a room within a building as one zone connected by flow paths to the other zones and to the outside environment (Schaelin et al. [53]). Within one zone (room), perfect mixing, uniform density, and uniform temperature are assumed; and mass balance for the fluid (air) is applied. The energy conservation can also be applied to a multi-zone model, although most multi-zone models do not incorporate it, mainly due to the complexity of the heat transfer phenomena.

The simplified assumptions of a multi-zone model make it suitable for fast computation of the bulk flow in an entire building level. However, the detailed airflow and temperature distributions within a single zone in a multi-zone model can sometimes be important, especially for buoyancy dominated natural ventilation flows. The lack of a detailed model to consider the internal temperature distributions can even significantly affect the bulk flow rate predictions in a natural ventilation system.

Further, most of the micro-scale fluid mechanics details are neglected in a multi-zone model. For example, the fluid is generally assumed to be inviscid and incompressible, and obey the Bernoulli equation. More importantly, the airflows in a multi-zone model are assumed to be driven by the static pressure differences between the zones, with a power-law assumption on the pressure drop across the flow paths. The momentum effect of the fluid, especially near a jet, is completely neglected in a multi-zone model. Since the momentum effect will also be important to the airflow and temperature distributions in a single space, the neglecting of the momentum effect in a multi-zone model adds further uncertainties to the bulk flow predictions in a natural ventilation system.

1.2.2 CFD model

A CFD model divides a single space (or a room) into fine control volumes, which are usually order(s) of magnitude smaller than the space. For each control volume, mass, momentum, and energy conservation equations are applied. For example, the mass conservation principle is described by the continuity equations. Compared to multi-zone models, a CFD model solves an additional set of equations—the momentum equation, which significantly enhances the accuracy of air dynamics predictions. With a finer mesh and the momentum equation, CFD is more suitable for detailed microscopic applications where the detailed air velocities and temperatures distributions are important to the airflow predictions.

One of the major concerns for the applications of CFD in building simulations is the computational time. The solution of the momentum equation is very time consuming. A direct solution of the Navier-Stokes equation (which is usually referred

as *Direct Numerical Simulation* (DNS)) is almost impossible in a scale of even a single room. A general practice to approximate the Navier-Stokes equation is to use the *Reynolds-Averaged Navier Stokes* (RANS) equations. A typical RANS model uses *turbulence models* to describe the dynamics of the turbulences, among which $k-\epsilon$ models (see Chen [19], Chen and Zhao [20]) are mostly widely used for building airflow simulations. In general, $k-\epsilon$ models can meet requirement of simulations in a scale of a room, although they are still too time consuming for a larger room or building size (and finer grids). Faster turbulence models (e.g. Srebric [55]) have been being developed over years, trying to meet the requirement of building airflow simulations.

The computational speed of CFD is especially problematic for applications that need transient simulations, especially applications that require real-time speed. Although CFD models can be used for transient simulations, every single time step will typically cost a computational time in the order of an hour for typical room sizes. Therefore, it is difficult to carry out transient simulations for building airflows using CFD in applications that need a speed that is close to real-time speed, such as real-time controls.

Another concern about CFD is the complexity of the problem descriptions. CFD models require detailed boundary conditions such as the inlet (diffuser), window, and wall. For example, in the vicinity of a diffuser, the momentum can be much higher than in the domain regions outside of the diffuser jet(s). In the region near a wall, the air flow patterns and temperature gradients can be different from those in other regions due to the boundary layer effect. Further, complex boundaries exist in the vicinity of a window, where the heat flux by conduction, convection and radiation happen simultaneously. On one hand, these elaborate descriptions enable CFD to predict building airflows with a relative higher accuracy, especially in a single space where geometry and other boundary conditions can be clearly defined. On the other hand, they also complicate the problem description and prolong the input and computational time for building simulations.

1.2.3 Zonal Model

Zonal modeling is an intermediate approach between multi-zone modeling and CFD modeling. A zonal model is similar to a CFD model in the discretization method and similar to a multi-zone model in the equations solved. It discretizes a single zone into small sub-volumes that are similar to CFD models (usually coarser), while it does not incorporate momentum equations.

Compared to multi-zone models, a zonal model is capable of providing more detailed the micro-scale flow and temperature distributions within a building due to the finer grids. Furthermore, zonal models enable easier incorporation of the energy equation than the multi-zone models (Inard et al. [38]). Nevertheless, convergence problems exist in the current effort of incorporating energy equations into zonal models (e.g., Axley [11]).

Although the fast computational speed makes zone models attractive for entire building airflow and thermal simulations, there are also several concerns about zonal models. For example, similarly to CFD models, a zonal model also requires series of

special boundary conditions such as the inlets (diffusers), windows or walls. Another important concern about zonal models is that they usually do not deal with thermal mass. In most of the current available zonal models, thermal mass models have not been incorporated. In entire building level simulations, the interactions of the air with thermal mass can be important. Also, the use of Bernoulli-like equations in place of the Navier-Stokes equations may lead to large errors in flow predictions, compared to CFD.

1.3 Need for efficient airflow simulation tools

Despite the various existing models that can be applied to different applications, there are still shortcomings in the existing models, in that they lack at least one of the following features: temperature solution, transient dynamics solution, and thermal mass modeling. The need of efficient building airflow and thermal simulations for entire building level natural ventilation designs and operations requires a new building airflow and thermal program to have these three important features. Other than the three features, the computational speed and flexibility in modeling is also an important concern in a new building airflow and thermal simulation program.

1.3.1 Temperature solution

Since temperature differences between zones are one of the major driving forces for natural ventilation flows, temperature solving capability is very important to natural ventilation modeling. A previous study by Arens et al. [2] found that airflow and contaminant distributions in a space are very sensitive to zone temperatures in a displacement ventilation system. Yuan [69] demonstrated a case where a small temperature difference between two adjacent zones can reverse the buoyancy-driven flow in a simple multi-zone building. However, most stand-alone multi-zone models do not solve energy equations to predict temperatures. Although CFD is capable of predicting the temperatures in a natural ventilation building with acceptable accuracy, prohibitive computational time and complicated problem descriptions limit its applications in efficient entire-building level simulations.

The technique of incorporating the thermal (or energy) equation into multi-zone models arises when fast macro-scale simulations of natural ventilation flows are needed in ventilation design. Walton [63] incorporated the energy equation into a multi-zone model CONTAMR97. However, bugged by numerical problems (Axley [9]), the program has not yet been open to the public. Tan [58] developed a multi-zone program that is specially focused on steady state natural ventilation airflow simulation. However, non-trivial numerical problems still exist—due to the coupling between the flow and energy equations in buoyancy dominated flows—and limit its applications.

1.3.2 Transient dynamics solution

In building simulations, the boundary parameters and input parameters, such as outdoor air temperature, solar radiation strength, internal load profile, and facade operations, are usually all time dependent. Therefore, the transient behavior of the system is important, especially for the applications where time-dependent responses are of special interest, for example, a full day/month/year airflow or energy simulation of an entire building.

The transient dynamics of a system are usually described by *Ordinary Differential Equations* (ODEs), or *Partial Differential Equations* (PDEs) when the space variation is considered. In a time dependent system, the system's current state will affect its future behavior. This time-dependency is critical to some applications in building operation and control simulations. For example, the transient interactions between the air and the thermal mass in a building are the basis for more advanced night cooling strategies.

Another important factor of the transient behavior is the related multiple steady state phenomenon, which will be discussed in detail in a later part of the thesis. The transient behavior of the system is found to be intrinsically related to the system's long-term behavior (Yuan and Glicksman [70, 74]). For example, starting from different initial conditions, the system may reach different steady states when certain conditions are satisfied. As will be shown in a later part of the thesis, the transient behavior of the system will have further impact on the building airflow and thermal simulations when the state transition dynamics between the multiple steady states can occur. The outcome of the simulation can be different when the boundary conditions are applied to the system in different ways. Therefore, transient behavior of the system needs to be adequately considered in the airflow simulations.

1.3.3 Thermal mass modeling

Another important issue in building airflow simulations is the thermal mass. The thermal storage properties of the thermal mass—for example, a concrete floor or masonry wall—can be used in engineering practice to modulate the indoor air temperature change against harsh outdoor air conditions. Due to its large thermal capacity, thermal mass will usually lag behind and “hold back” the air temperature change.

Several previous studies exist on coupling the thermal mass into the airflow model. In the CONTAMR97 developed by Walton [63], the thermal mass effect was considered. However, no details are available for the modeling technique. Further, the program was reported to be numerically unstable due to the complex coupling effect and the existence of multiple steady states (Axley [9]). Other programs that considered thermal mass are mostly load/energy calculation programs such as EnergyPlus ([26]), which requires complicated input for geometric information and plant system input. Current available commercial CFD software such as Phoenics (CHAM [17]) does not provide a convenient feature for simultaneous coupling the airflow and thermal mass solving, either. To meet the need of convenient thermal mass simulation integrated with the airflow and thermal transport, in this thesis, the thermal mass

models will be incorporated into a coupled multi-zone airflow and thermal simulation program for efficient transient airflow simulations.

1.4 Multiple steady state phenomena—challenges to coupled airflow and thermal simulations

A major challenge to coupled airflow and thermal simulations—especially in natural ventilated systems—is the possible existence of multiple steady states. For example, Chen and Jiang [21] reported the difficulties in simulating the airflow patterns by CFD in several systems. The numerical simulation shows the CFD solution jumps back and forth between different values as the iteration steps proceed during a simulation. Further experiment and analytical studies were conducted in buildings with simple geometries (e.g., Linden [44]; Li et al. [42]; Gladstone and Woods [32]; Heiselberg et al. [35]; and Yuan and Glicksman [70]).

The multiple steady state behavior imposes several challenges to the computational modeling of natural ventilation systems. The first one is the modelers' choice on the multiple steady states. If, for example, an airflow simulation program shows two or more distinct steady states under the same boundary conditions, how can one distinguish the stable steady states from those unstable ones? Advice was provided in some previous studies to distinguish the locally stable and unstable steady states in buildings with simple geometries such as a building with one or two zones. However, for the locally stable steady states, are they equally stable or one of them is more stable than the other? Existing studies have not provided an insight on such an issue. In this thesis, we will develop methods to examine the relative stabilities of the locally stable steady states; and apply the methods to measure the actual stabilities (or robustness) of the steady states in a real environment.

The second challenge is the influence of multiple steady states on the coupled airflow and thermal simulations, for example, the numerical problems reported by Axley [9] on CONTAMR97 (Walton [63]). When multiple steady states exist in a ventilation system, traditional numerical simulation strategies may cause numerical stability issue and fail. In this paper, an understanding of those issues and possible solutions are provided to overcome those problems.

The third challenge of multiple steady states is in the ventilation controls. A typical ventilation controller monitors the building parameter change in real-time and takes actions to maintain the building environment in a comfort level. Most of the control strategies were implemented without consideration of the dynamics of multiples steady states. However, with the existence of multiple steady states, the control strategies in the previous models may not work properly due to lack of knowledge of the multiple steady states. In this thesis, such knowledge about multiple steady states will be provided and possible applications in control strategies are investigated.

The final challenge is how to positively use the multiple steady state behavior. Axley [10] reviewed the natural ventilation modeling and discussed in general the possible impact of the multiple steady state behavior. The conclusion seems to be

pessimistic at the time the work was published. However, we are not pessimistic about this issue. The positive applications of the multiple steady states in ventilation controls will be investigated in a later part of this thesis. In contrast to the general “phobia” on the multiple steady states in previous studies, we will show that positive applications of multiple steady states are quite realistic and the “phobia” on multiple steady states could be relieved when the underlying dynamics are understood.

1.5 Objectives of present work

There are three major objectives of this thesis, which are tightly related to each other:

- develop efficient coupled transient airflow and thermal models for use in an entire building simulation, especially for natural ventilation.
- address transient dynamics of multiple steady state behavior in natural ventilation systems;
- explore the multiple steady state behavior in airflow thermal simulation and its positive applications in natural ventilations.

1.5.1 Coupled airflow and thermal simulation models

Model development

A program featuring the solution of transient airflows and temperatures for an entire building with thermal mass will be developed. The program is also expected to have features for simple window and zonal control strategies that are also implemented in the program, which enables the simulation of natural ventilations control strategies for extreme weather conditions. The program is also expected to have certain levels of expandability. For example, a separate sub-model for internal radiation should be able to work with in the program to enhance thermal prediction accuracies.

Numerical performance

Adequate numerical techniques are expected to be applied in the program to achieve both efficiency and numerical stability. The numerical simulation techniques are expected to overcome possible problems in the thermal mass and air dynamics simulation as well as basic airflow simulations.

Validation

The coupled program is expected to be validated by various data sources. The validation test should cover the transient features of the program, such as the transient flow/thermal solution and thermal mass solution.

1.5.2 Transition dynamics between multiple steady states

Dynamical system analysis

For the multiple-steady-state phenomena, the present study is expected to develop new methods to explain and discover various building flow phenomena. The focus would be especially on the transient dynamics, rather than pure steady state properties of the system. For example, we would like to answer the question such as how the local stability of the different steady states obtained by steady state equation can be explained by the transient dynamical system characteristics of the system; and whether there are ways to determine which specific steady state the system will finally reach when multiple steady states exist in a system.

State transitions

A further objective of this study is to investigate the actual stabilities of the mathematically stable steady states. Some previous studies (e.g., [35, 41, 44]) have proved that two (or more) “mathematically” stable steady states can occur in a single natural ventilation system. However, are these two “mathematically” stable solutions equally stable in reality or one is more stable than the other? This is one of the questions that are expected to be answered in the present study.

Further, the multiple steady state behavior is expected to have significant impacts on to the numerical stability of airflow simulation models, for example, the numerical problems reported by Axley [9] on CONTAMR97 (Walton [63]). The studies in the present study also expect to address some of the numerical stability issues in general airflow and thermal analysis problems.

Thermal mass and its impact on the multiple steady states

In previous studies about multiple steady states, the objective of study is generally the fluid. However, a real building generally have thermal mass inside, especially in buildings that actively use thermal mass strategies. Therefore, a further question about the multiple steady state phenomena is whether the existence of thermal mass can affect the multiple steady state behavior of the system. For example, if a thermal mass is added to the system, how would the stability of the system change? Will a system with lighter thermal mass behave very differently from a system with heavy thermal mass, and how? These are also the questions that the present study expects to answer.

1.5.3 Applications of multiple steady states

Guide ventilation design

Although multiple steady state phenomena may cause potential problems in numerical simulation, there might be positive applications of the multiple steady state phenomena. One of the objectives of the thesis is to explore the possible positive applications of the multiple steady state phenomena. For example, how should the

designers consider the multiple steady states in their building design? Does the existence of multiple steady states pose new criteria to the design of natural ventilation systems? These are also the objectives of the present thesis study.

Identify multiple steady states in complex buildings

For simple buildings, analytical models may be developed to investigate the multiple steady state behaviors of the system. However, with complex building geometries, such analytical models may not be possible. How to systematically identify possible multiple steady states in these complex buildings is a challenge in building simulations. In this study, we would expect to resort to some adequate computational algorithms to fulfill this task of solution seeking. Further, for the solution obtained, a systematic and effective test method is expected to test the their actual stabilities in real environment.

Active applications in ventilation controls

The multiple steady state phenomena also pose challenges to the building control strategies. If a controller is not well trained to handle the existence of multiple steady states in a natural ventilation system, a control strategy may fail to work as expected. In this sense, multiple steady state behavior seems to be harmful to general ventilation control practice. However, is it possible to find a positive application of the multiple steady states phenomena if a controller is designed to handle it? This is one of the most important questions we expect to explore in the present study.

1.6 Outline of thesis

Chapter 2 introduces the transient multi-zone air-thermal-mass simulation models developed to couple airflow, temperature, and thermal mass solutions. The framework of coupling between the airflow model, air temperature solving, and thermal mass solving are also discussed in this section. Numerical techniques in solving the coupled system equations are also discussed in this chapter.

Chapter 3 validates the program from different aspects by different methods. For example, the airflow and temperature solutions are validated by steady state CFD simulation results. Different buoyancy driven cases and wind driven cases are conducted. Further, the transient and thermal mass solving capabilities of the program are validated by the field measurement data obtained in a natural ventilated building that actively uses thermal mass to modulate the indoor temperatures.

Chapter 4 discusses the important issues of dynamical system analysis of the multiple steady state phenomena in building simulation. The nonlinear dynamics features of the system will be discussed in detail. In Chapter 5, the conditions for multiple steady states to exist in a single-zone system with opposing wind and buoyancies are investigated. The mechanism of how the system reaches different steady states is explained using the dynamical system analysis.

Chapters 5 and 6 investigate the dynamical system behavior of a single-zone natural ventilation system with thermal mass. The impact of thermal mass on the ex-

istence of multiple steady states, the way the system reaches different steady states, and the local stabilities of the different steady states are discussed. A generalization of the system characteristics will be explained by the eigen characteristics of the linearized system equations near the steady state points.

Chapter 7 discusses the transition dynamics between different steady states based on the dynamical system analysis in Chapter 4. The transition dynamics can be used to explain several unsolved issues found in previous flow experiments and numerical simulation studies. We will especially show how to quantitatively use the transition requirement to describe the actual stability of a locally stable steady state.

Chapter 8 investigates the impact of thermal mass on the state transition dynamics between the multiple steady states. The changes in the magnitude and time requirements for such a transition when thermal mass is introduced will be investigated. The results are compared with a system without thermal mass and their differences are discussed.

Chapter 9 discusses the multiple steady state phenomena of a building with two zones. In this chapter, we will investigate the underlying dynamics features of the system and present a new eigen characteristic of the system that is different from the air-mass system investigated in Chapter 5. The results provide new knowledge to the design of several typical ventilation designs and possible applications will be discussed.

Chapter 10 discusses the multiple steady state behavior in complex geometries, including two-zone to multi-zone buildings. A general numerical framework is proposed to solve such a problem. A computational algorithm will be developed to explore the state space to find these steady states. Two examples are provided to demonstrate the existence of multiple steady states in a complex building with multiple zones. An effective method to test the actual stabilities of the obtained steady states are also developed and discussed.

Chapter 11 discusses the applications of the state transition dynamics in ventilation controls. A control strategy based on state transitions are proposed and quantitatively investigated for their efficiency in energy saving. Optimal operation strategies are provided to maximize ventilation effectiveness and energy efficiency. The test of the controller performance is conducted in a hypothetical two-zone building.

Chapter 12 summarizes the conclusions from all previous chapters. Future research recommendations on airflow simulations and multiple steady state applications are made.

Finally, the thesis also includes two appendixes. Appendix A provides a detailed description of the CoolVent program interfaces. Appendix B provides supplemental validation studies conducted on CoolVent that test the model implementation and performances.

Part I

Coupled airflow and thermal simulation program

Chapter 2

Integrated transient multi-zone airflow and thermal model with thermal mass solution

2.1 Essential elements of multi-zone models

Multi-zone models take an individual room or space within a building as one zone that is connected to other zones and/or outside environment by flow paths. The flow paths represent the connections between two adjacent zones with airflow movement in one or both directions. Typical flow path elements in buildings are windows, doors, fans, cracks and openings. HVAC and duct systems can also be simulated as special zones and flow paths. Figure 2-1 illustrates the building representation method by a widely used multi-zone program—CONTANW [64].

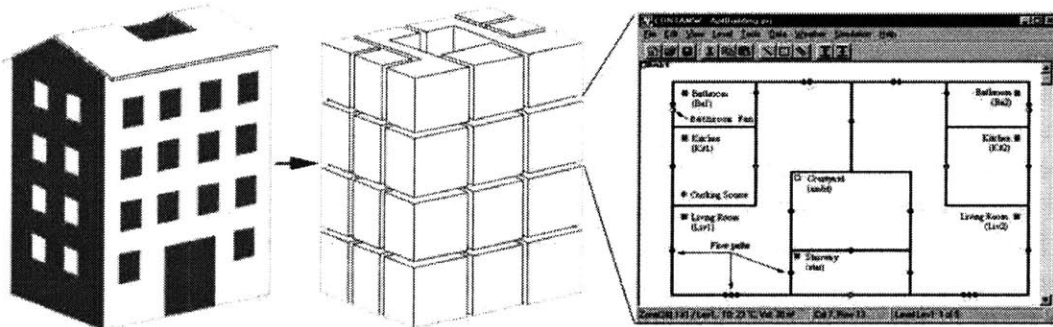


Figure 2-1: Building representation of CONTAMNW
(Source:www.bfrl.nist.gov/IAQanalysis/default.htm)

In multi-zone models, perfect mixing is assumed within a zone (usually a physical space, shown in Figure 2-1). Thus, within this zone, air density and temperature are assumed to be uniform. Two sets of governing equations—mass balance and energy conservation—can be applied to each zone to calculate airflow rates and heat transfer strengths. However, since an accurate heat transfer prediction within buildings

usually requires additional equations with complex boundary conditions or separate additional programs, most of the multi-zone models do not solve energy equations. Therefore, as essential parts of multi-zone models, the governing equations for airflow calculation will be discussed in this section.

2.1.1 Mass balance equation

Most of multi-zone models have common sets of equations to describe zones (nodes, cells, rooms) and flow paths. The common equation sets include node equation sets and flow path (pressure) equation sets.

Node equations are applied to each zone (or node, usually a space) in a typical multi-zone model. The principle of air mass balance applied to the zone for a transient problem is

$$\frac{dm_i}{dt} = \rho_i \frac{\partial V_i}{\partial t} + V_i \frac{\partial \rho}{\partial t} = \sum_j F_{ji} + F_i, \quad (2.1)$$

where

m_i = mass of air in zone i [kg];

$F_{j,i}$ = air flow rate [kg/s] between zone j and zone i ; positive value indicates flow from j to i and negative value indicates flow from i to j ;

F_i = non-flow processes that could add or remove significant quantities of air from the zone, usually sources and sinks [23].

The mass of air is connected to pressure and temperature of the zone by the ideal gas law. The air can be treated as an ideal gas within the temperature and pressure range for building airflow simulations. Therefore, the mass of air m_i in zone i is

$$m_i = \rho_i V_i = \frac{P_i V_i}{R T_i}, \quad (2.2)$$

where

P_i = zone pressure [Pa];

V_i = zone volume [m^3];

T_i = zone temperature [K]; and

R = specific gas constant for air, 287.055 [J/kg-K].

Some multi-zone models, such as models before CONTAMW 1.0 [24] (an older version of CONTAMW), assume quasi-steady-state conditions. The non-flow airflow processes in Equation (2.1) are not considered in CONTAMW1.0, either. Therefore, the differential term with time was neglected, which transforms Equation (2.1) into:

$$\sum_j F_{ji} = 0. \quad (2.3)$$

2.1.2 Energy conservation

The general law of energy conservation can be applied to the multi-zone model as well. Here we assume that there is no humidification / dehumidification process going on

in zones so that only sensible heat is considered. For any internal zone i , the energy conservation equation states

$$\rho_i c_{pa} V_i \frac{dT_i}{dt} = \sum_{j:F_{ji}>0} \rho_j c_{pa} T_j - \sum_{i:q_{ij}>0} F_{ij} c_{pa} T_i + S_i, \quad (2.4)$$

where

F_{ij} = mass flow rate from zone j to zone i ;

T_j = air temperature of zone j ;

T_i = air temperature of zone i ;

S_i = heat gain in zone i . The source term S_i in the above equation is a time dependent function. It is, in general, the sum of external and internal heat source gains which varies at different time of a day.

Since the temperature differences between zones can represent a major driving force in ventilation systems (e.g., natural ventilation systems), thermal problems are more complexly coupled with airflow calculation than contaminant transport. Therefore, most multi-zone models do not incorporate energy equations. Another reason to neglect the multi-zone thermal models is that incorporation of thermal equations usually needs additional tools to estimate the thermal loads, which is again coupled with airflow and thermal simulations.

2.1.3 Flow path equations

Flow paths are the connections between zones that allow airflow in one (usually small openings) or both directions (usually large openings). The flow path represents characteristics of elements such as doors, windows, and structural leakages that connect rooms and allow flow movements. The airflow through a path is usually driven by pressure and/or temperature difference between connected zones.

Flow path equations are applied to describe the air movement through the flow paths. These equations are usually based on one-dimensional fluid mechanics laws. For the pressure driven flow paths, the volumetric air flow rate from zone j to zone i , $Q_{j,i}$ [kg/s], is a function of the pressure difference along the flow path, $P_j - P_i$, the area of the opening [m^2], and the discharge coefficient,

$$F_{ji} = f(P_j - P_i), \quad (2.5)$$

where

F_{ji} = flow rate from zone j to zone i , [kg/s];

P_j, P_i = pressure at zone j and i separately, [Pa].

The power-law equation is widely used to present the function f in Equation (2.5), which states

$$Q_{j,i} = C \cdot (\Delta P)^n, \quad (2.6)$$

where

$Q_{j,i}$ = Volume flow rate through the flow path, [m^3/s];

F_{ji} = Mass flow rate through the flow path, [kg/s];

C = flow coefficient of the flow path opening;
 n = flow exponent of the flow path opening, usually 0.5 for large openings, 1.0 for narrow openings, and 0.6–0.7 for typical infiltration openings [23].

In order to consider the gravity force and close the equation system, the Bernoulli equation is applied to flow paths to describe the inter-zonal pressure difference, which states:

$$\Delta P = (P_1 + \frac{\rho v_1^2}{2}) - (P_2 + \frac{\rho v_2^2}{2}) + \rho g(z_1 - z_2), \quad (2.7)$$

where

ΔP = pressure difference between two zones, [Pa];

P_1, P_2 = static pressure at position 1, 2, [Pa];

ρ = fluid density, [kg/m^3];

v_1, v_2 = fluid velocity at positions 1 and 2, [m/s];

g = acceleration of gravity, [m/s^2];

z_1, z_2 = elevation of positions 1 and 2, [m].

In general, the kinetic pressure terms are not considered in building applications. This yields an equation as follows:

$$\Delta P = P_1 - P_2 + \rho g(z_1 - z_2). \quad (2.8)$$

As a complete description of the multi-zone model, another set of equations for solving species concentration, are also solved if contaminant transport is the target to be solved. For example, a general form of contaminant mass balance equation is described in CONTAMW documentation [23].

2.2 Integrate energy equations into multi-zone models

To solve the energy equation built in the multi-zone models, a general practice is to incorporate airflow models with energy/load calculation programs. However, this method has been mostly developed to enhance the accuracy of energy/load calculations, which is a general practice in several major energy/load programs such as ESP-r [27] and EnergyPlus [26]. For examples, ESP-r implemented the coupling of multi-zone models into the energy calculations and EnergyPlus incorporated a multi-zone model to predict the impact of infiltration on energy calculations. However, the heat transfer and thermal phenomena within buildings are also of importance to the airflow modeling, especially for such simple models such as multi-zone models.

2.2.1 Existing airflow-thermal coupling studies

Up to date, several efforts have been documented in the literature. Some important examples of such research efforts are described in this section.

Walton [63] developed an algorithm to solve energy equations in a test version of CONTAMR97. Heat transfers through walls, windows and internal sources, as well

as thermal storage effect of building materials were modeled for building thermal dynamics. Several natural ventilation cases were studied to test the program. However, the program does not always provide a stable solution due to numerical problems encountered in natural ventilation simulations due to various reasons (Axley [8–10]).

A few powerful energy programs have combined airflow models into energy / load calculations. Beausoleil-Morrison [12] integrated a heat transfer and an airflow model into ESP-r [27]. As in previous coupling work on CFD and multi-zone modules by Negrao [49], a thermal simulation module, multi-zone airflow simulation module, and CFD simulation module are integrated into ESP-r to calculate the surface temperatures, energy flows, and air flows throughout the building. Another energy program, EnergyPlus [26], has successfully incorporated the multi-zone airflow model into the energy calculation. The program couples COMIS [29] in energy calculations as an option. However, in both EnergyPlus and ESP-r, the airflow modules are usually considered as a part that takes into account the infiltration or inter-zonal air movement to make energy program calculation more accurate. The energy program is the main focus, and air flow models cannot be run without the energy options.

For the stand-alone multi-zone airflow and thermal program, Tan [58] built a simplified multi-zone model that was specially designed for natural ventilation system. The model calculates the steady state temperature and airflows by the input heat sources and other boundary conditions. However, the program is oriented toward steady state solutions and lacks several important features that qualify it as a fully functional coupling program for designers. For examples, the program lacks capabilities to handle transient simulations, thus time varying, time dependent boundary conditions such as weather conditions and windows operation strategies, and more importantly, thermal mass solutions. Furthermore, nontrivial numerical problems that bug the program impeded its further applications in fast and reliable design simulations.

2.2.2 Framework for energy equation solution

Although it is straightforward to incorporate an energy/load program calculation into a multi-zone model, the complexity of the external energy program generally prohibits the fast and efficient calculation of the program. Tailing a multi-zone program to an energy program is more of a general practice than tailing an energy program to a multi-zone model. Therefore, in order to design an efficient multi-zone program for natural ventilations modeling, the models for load calculation should be considered.

The multi-zone and energy program coupling studies has provided us a general frame work on the energy equation solving for multi-zone models. The heat gains from solar radiation, thermal mass storage, and internal heat gain are all parameters to be considered in a multi-zone model. Further, the internal radiance model, which has a strong effect on the indoor air temperature modeling, has to be addressed for an effective energy equation solving. These issues will be discussed in detail in Chapter 3.

2.3 Thermal mass solution

The existence of thermal mass will be greatly affected by the temperature distribution of the building. To solve the thermal mass temperature, additional differential equations needs to be added to the system. The existing differential equations for air temperature calculation also need to be modified. The heat transfer between the air and the thermal mass can be calculated either by natural convection correlations or simply by taking an effective heat transfer coefficient that accounts for both convection and radiation occurred on the surfaces.

The dynamics involved are the airflow/pressure network, convective/conductive heat transfer, and the coupling effects between the airflow and the heat transport. The thermal mass can be treated as a lumped sum for rough estimation or a series of separated layers for detailed analysis. The later is widely used in building thermal mass simulations since the Biot number¹ is usually large (> 0.2) and the spatial temperature difference inside the mass is significant. Figure 2-2 shows a simple example of modeling the thermal mass by dividing the mass into two layers (source: EnergyPlus documentation [26]).

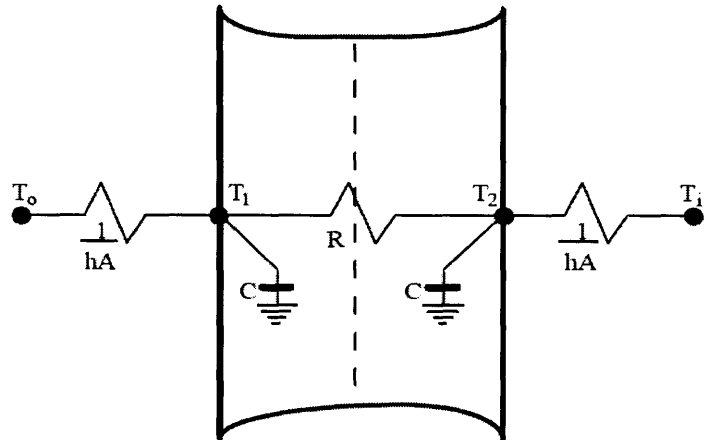


Figure 2-2: An example of thermal mass modeling (Source: EnergyPlus documentation [26])

The typical method for solving the thermal mass temperatures is called the *conduction transfer functions* (CTFs) method (see [16, 54]). The CTFs method approximates heat flux on the thermal mass surface by an infinite series of the historical temperatures of the air and the mass. An older method for such a thermal mass solution problem is called the *Laplace Transform* method, which is a classical way of solving a dynamical system. The CTFs method is the standard method used in EnergyPlus, while the Laplace method is used in one of the predecessors of EnergyPlus. The CTFs method is viewed as superior than the Laplace method since there is no need to solve the roots in the Laplace domain in computing the surface heat flux [26]. For the technical details for these two methods are provided can be found in the EnergyPlus documentation [26].

¹Biot number is defined by $Bi = \frac{hl}{k}$, where h is the surface heat transfer coefficient; l is the characteristics length; and k is the thermal conductivity of the mass materials.

The CTFs method is an efficient method to model the air-mass interactions for energy simulation programs. However, the CTFs method has a convergence problem when the time steps are small, especially when the thermal mass is massive (heavy) [26]. Unfortunately, in this study, the time steps we used for airflow simulations are typically much smaller than those for an energy simulation program such as EnergyPlus. Therefore CTFs method is not the best choice for our needs. In stead, we used a different thermal mass solution technique by directly solving the difference equations, which will be introduced in Section §2.4.2.

2.4 Coupled multi-zone airflow, thermal, and mass models

CoolVent, a new transient multi-zone model that incorporates the airflow, temperature, and thermal mass solutions, is developed to meet the requirement for transient entire building airflow/thermal simulations. The name “CoolVent” is after its thermal mass modeling features, which was originally targeted for night cooling studies. The main features of the program include:

- transient dynamics solution;
- thermal mass integration;
- enhanced numerical stabilities;
- simple control strategies.

In this section, the model details and the above features of the CoolVent program will be discussed.

2.4.1 Transient airflow and thermal dynamics solving

The transient airflow and temperature solutions involve the coupling of the airflow network and energy equations simultaneously. The program can be viewed as three major modules: air flow network model, air temperature dynamics, and thermal mass dynamics. Other features include wind pressure calculation, solar radiation estimation, and internal radiation models, which will be introduced in later sections. Figure 2-3 shows the general framework of the program.

The airflow network model is a standard multi-zone network model. The pressure of each zone is calculated based on the zonal air mass balance given in Equation (2.3) and the pressure resistance relationship presented in Equation (2.7).

The air temperature model is governed in principle by Equation (2.4). However, the detailed terms of the energy exchange on the right hand side needs further development. The first term is described by the energy transport brought in by the airflow movements between zones. Therefore, the flow rate calculation results from the airflow network will be used. However, this is a coupled procedure and the energy

Program Structures

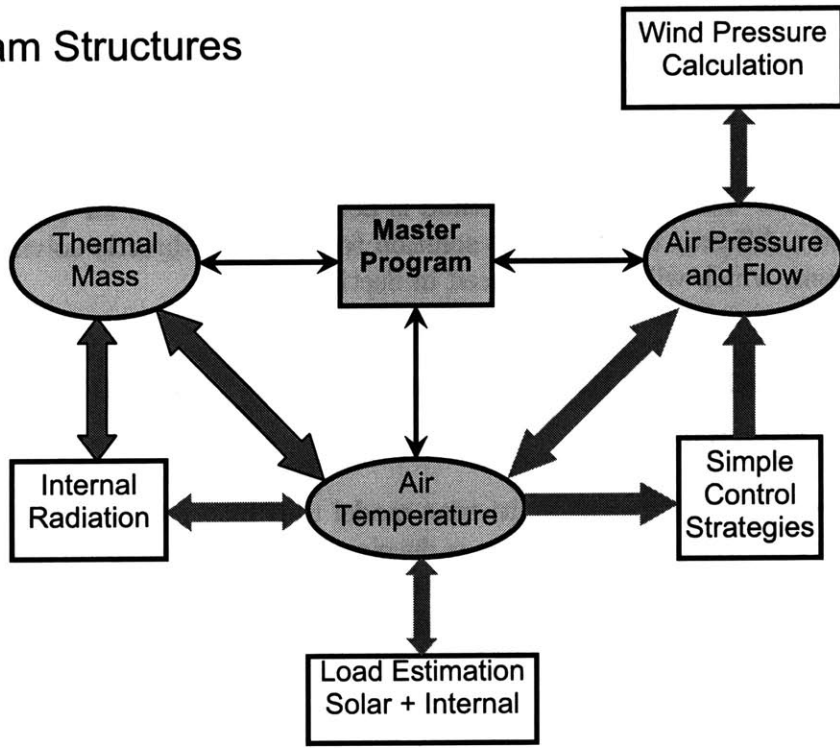


Figure 2-3: Structures of the developed multi-zone airflow and thermal program

calculation result will affect the pressure distributions (especially for buoyancy driven natural ventilation) in the airflow network as well.

The second term in the energy equation involves the heat transfer in terms of internal heat gain or loss. This part is largely contributed by the solar radiation and internal heat sources. Estimation of these terms generally requires another module or input from an energy program. In our study, the energy calculation model is estimated in several different ways in different versions of the software. However, the program preserves the expandability to incorporate additional energy estimation modules.

The third term in the energy equation involves the heat transfers associated with the interactions between the zonal air and the thermal mass. As a first estimation, the convective heat transfer between the air and the thermal mass will be estimated by a general form as follows:

$$Q_j = \sum_i h_i A_i (T_{mi} - T_j), \quad (2.9)$$

where

T_j is the zone temperature [$^{\circ}\text{C}$ or K];

T_{mi} is the corresponding thermal masses (layer) surface temperatures that are connected to the zone j . Each zone can have multiple thermal masses connected to it, for example, the ceiling, the floor, and the wall if applicable;

h_i is the convective heat transfer coefficient between the air and the thermal mass. It can have different values for natural convection or force convection; A_i is the contact areas of between a thermal mass and the zone.

The heat transfers between the airflow and the thermal mass will not only affect the airflow dynamics, but also the dynamics of the thermal mass. Another important part of the program, solution for the variation of the thermal mass temperature will be introduced in the following subsection.

2.4.2 Thermal mass temperature solution

Physically, the governing equation across the thermal mass is the heat diffusion equation without internal sources:

$$\frac{\partial T}{\partial t} = \lambda \nabla^2 T, \quad (2.10)$$

where λ is the thermal diffusion coefficient of the thermal mass materials.

In dealing with building thermal mass, only one-dimensional heat transfer across the thickness of the thermal mass is considered. Equation (2.10) can be simplified as a one-dimensional diffusion equation. Numerically, this makes it possible to represent the diffusion equation by a circuit network that is composed of resistors and capacitors using the idea of finite elements (or differences). The circuit flow network is shown in Figure 2-4.

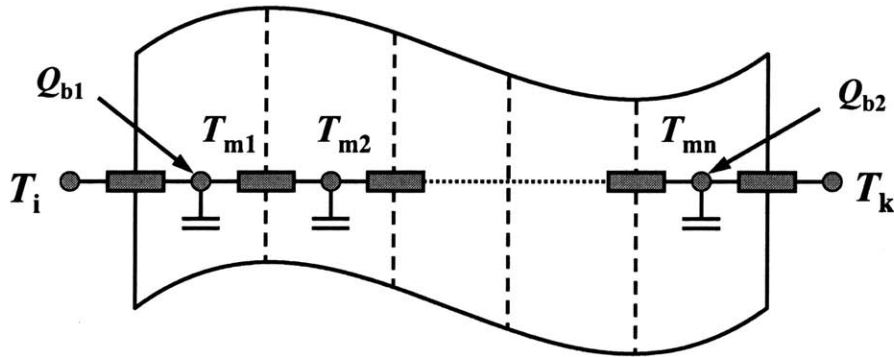


Figure 2-4: The thermal mass modeling network

The thermal mass model in Figure 2-4 can handle two types of boundary conditions. The first type is temperature boundary condition. In this scenario, the temperature of the zonal air that contacts with the thermal mass is given. The second type is the hybrid of a temperature boundary and a direct heat flow boundary condition. The heat flow boundary is used to consider the direct solar radiation onto the thermal mass in a research version of the program in Chapter 3.

For the thermal mass network shown in Figure 2-4, the energy balance for each slice of thermal mass is as follows:

$$\rho_m c_{pm} \Delta x_i \frac{\Delta T_i}{\Delta t} = \frac{T_{i-1} - T_i}{R_{i-1}/2 + R_i/2} + \frac{T_{i+1} - T_i}{R_i/2 + R_{i+1}/2}, \quad (2.11)$$

where

ρ_m = thermal mass density, [kg/m³];

c_{pm} = thermal mass specific heat, [W/kg-K];

Δx_i = thickness of the thermal mass layer i , [m];

T_i = the temperature (in °C or K) of thermal mass layer i at a particular time (step);

R_i , R_{i-1} , R_{i+1} = thermal resistance components that composes the left hand of the thermal mass layer (per unit area) and the right hand of the thermal mass layer. For the internal layers, R_i is the conduction resistance of the thermal mass layer i , which is

$$R_i = \frac{\Delta x_i}{kA_m}. \quad (2.12)$$

For the boundary cells, the convective heat transfer between the air and the thermal mass should be considered. Equation (2.11) is expressed as (let $i = 1$ for example)

$$\rho_m c_{pm} \Delta x_i \frac{\Delta T_i}{\Delta t} = \frac{T_a - T_i}{\frac{1}{hA_m} + R_i/2} + \frac{T_{i+1} - T_i}{R_i/2 + R_{i+1}/2}, \quad (2.13)$$

where R_i and R_{i+1} can be obtained by Equation (2.12).

2.4.3 Numerical coupling strategies

The history of coupling multi-zone airflow and thermal can be traced back to the study done by Hensen [36]. Hensen proposed two ways to couple the airflow and thermal modules in a transient airflow simulation program. The two strategies have “vivid” names that describe the characteristics of the way they exchange data between the airflow and thermal modules during each time step: one is called “Ping-pong” coupling strategy, which was also called a “Decoupled” solving strategy; the other is called “Onion” strategy, which was also called a “Coupled” solving strategy. The two strategies are shown in Figure 2-5. In the “Ping-pong” strategy, the airflow and the thermal modules will be run in a sequence without iterations within each step. In the “Onion” strategy, the airflow and thermal modules will run in a sequence as well, except internal iterations are taking place with each time steps till agreement has been reached between the airflow and the thermal module. Therefore in the “Onion” strategy, the sequence of coupling is usually run multiple times and the computational effort is slightly higher if the time step is the same.

The performances of the “Ping-pong” and “Onion” strategies were also compared in Hensen’s study. For relatively small time steps (6 minute), the “Ping-pong” strategy and the “Onion” strategy showed very close results in both air flow rates and temperatures. The “Onion” strategy is a little bit more advantageous in that it is not so sensitive to the time steps. For example, with a much larger time step (1 hour), the results predicted by the “Onion” strategy can still be very close to the results predicted by both “Onion” and “Ping-pong” using 6-minute time steps. However, the “Ping-pong” method has shown a much larger difference with the results predicted by either “Onion” or “Ping-pong” with 6-minute time steps. This difference is mainly due to the mismatch in the airflow and air temperature in long time step (1 hour)

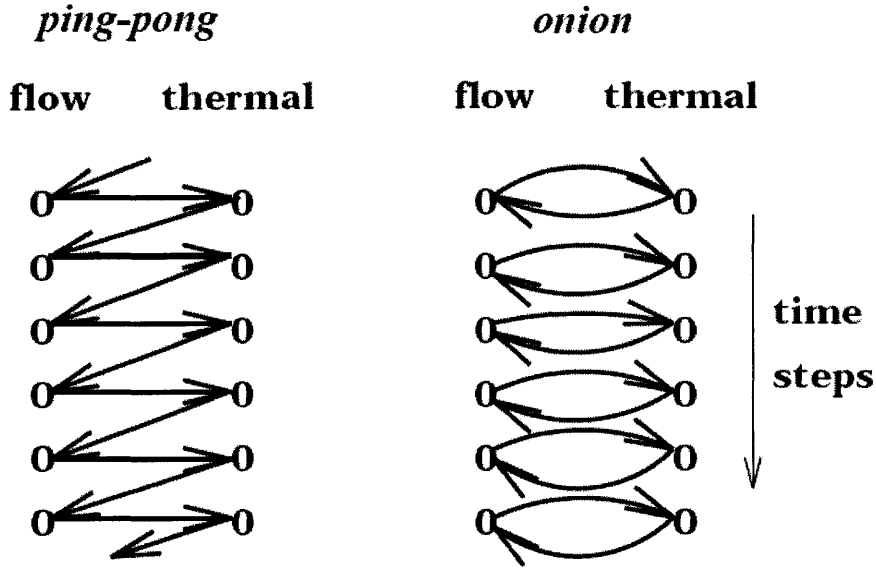


Figure 2-5: “Ping-pong” coupling strategy vs. “Onion” coupling strategy (Source: Hensen [36])

during applying the “Ping-pong” strategy. Therefore, the “Onion” strategy is less time step dependent in general practice. It provides opportunities for the program to run simulation in a relatively large time step.

In CoolVent, a “Ping-pong” strategy shown in Figure 2-6 is used when coupling the three different models for several reasons. First of all, the time step we use is about 0.5 to 1 minute, much smaller than 6 minutes. The rationale of using this small time step is actually in the nonlinear dynamics issue that are related to the multiple steady states, especially in natural ventilation modeling, which is the direct goal of our developed tool. The occurrences of multiple steady states in simulation are not uncommon in ventilation simulations, especially in natural ventilation simulations (see [11, 21]). In the theoretical studies conducted in the later chapters, we will demonstrate how a small time step and a large time step may yield totally different results (steady states), when the nonlinear behaviors related to multiple steady states are involved.

Secondly, the using of “Ping-pong” strategy is partially related to the thermal mass modeling in our program. Our program incorporates an additional module for the thermal mass. With the large thermal capacity of the thermal mass, the temperature change with the thermal mass is usually much less than that of the air. Therefore, it gives the program a natural privilege in modulating the temperature change in each time steps, especially with smaller time steps.

In general, several iterations can be sufficient for each time step in an “Onion” strategy. In general practice, for example, in EnergyPlus [26], the maximum number of internal iteration in a time step will not exceed 5. If the results do not converge in 5 iterations, the program will just proceed using the values obtained in the 5th iteration to assure that the program runs smoothly. Although an internal iteration

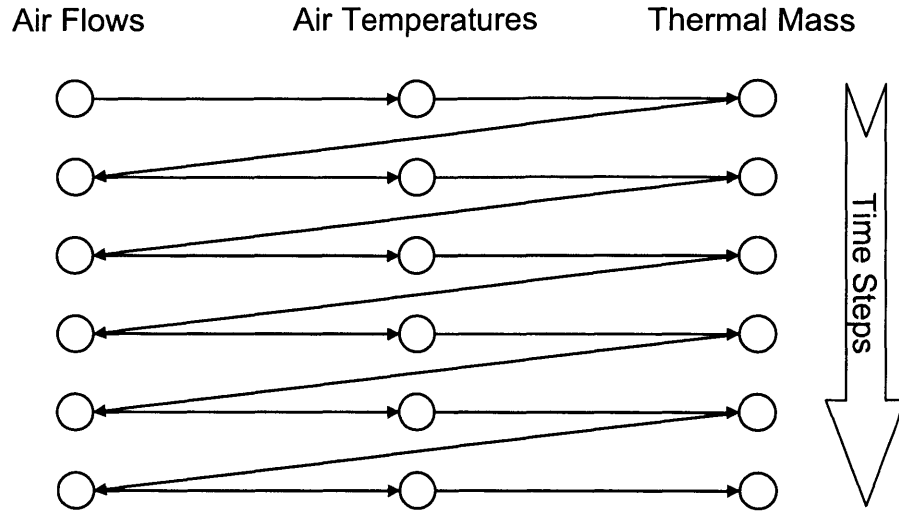


Figure 2-6: “Ping-pong” strategy for the three major modules in the air and thermal coupling program with thermal mass solution capabilities

procedure is currently not implemented in our program, our program does provide room for advance the “Ping-pong” strategy currently in there to an “Onion” strategy.

The three major parts of the program are coupled as an integrated program. The data exchange between modules occurs in the program memory level. This is different from other more complicated coupling programs such as TRANSYS [47], where the data exchange of different modules happens in the storage media (such as the hard disk) level.

2.4.4 Other features of the program

Several other features are also implemented in the program. These features include a simple windows control strategy, estimations of solar and internal load, and wind pressure calculations. Another “research” version of the program will be introduced in the Chapter 3. The “research” version incorporates an internal radiation model that interacts with the air and the thermal mass.

The simple control strategy allows the user to apply intuitive window open/close actions according to the outdoor temperature and the zonal temperatures. For example, if the outdoor air temperature drops to a very low temperature in the winter, the user can set a strategy to close the window automatically based on either the outdoor temperature or the sensed indoor temperature.

Since the heat load is important to the program calculation, a solar and internal load estimation module is also developed to calculate the solar load from the weather file based on the city name and the internal zonal load from building functionality inputs. The sum of the two loads is used as the heat source strength input for the program.

For wind driven natural ventilation, a Wind Pressure Coefficient (WPC) model is developed to calculate the wind pressure for the exterior openings such as windows or

roof louvers. The model used is based on a previous study by Grosso [34], where the experimental data from different sources were processed to generate a multi-factor model based on the local geographic and building geometry information.

2.5 Numerical procedures enhancement

2.5.1 Air temperatures solution

The implementation of the airflow and thermal involves solving of the air temperature based on the airflow, the thermal mass temperatures, and other time dependent input such as the heat load. The governing ODE of the air temperatures can be expressed in explicit or implicit forms.

The explicit method is very straightforward, which is shown as follows:

$$V_i \rho_i c_{pa} \frac{T_{i,t+1} - T_{i,t}}{\Delta t} = \sum_{j:F_{ji}>0} F_{ji} c_{pa} T_{j,t} - \sum_{j:F_{ij}>0} F_{ij} c_{pa} T_{i,t} + \sum_k h_{k,i} A_{k,i} (T_{mk} - T_{i,t}) + S_i. \quad (2.14)$$

On the right hand side of the equation, every term has been obtained at time t in the numerical computation. Therefore, the method just involves multiplication and addition operations, which makes the method efficient. In numerical simulations, the formula shown in Equation (2.14) is also called “forward Euler” formula. Despite its simplicity in numerical implementation, there is a stability issue with the “forward Euler” method. The time steps cannot be too large. Otherwise, the problem will show numerical vibrations or even divergence.

Another numerical scheme is called “implicit” scheme, or “backward Euler” formulation, which is shown as follows:

$$V_i \rho_i c_{pa} \frac{T_{i,t+1} - T_{i,t}}{\Delta t} = \sum_{j:F_{ji}>0} F_{ji} c_{pa} T_{j,t+1} - \sum_{j:F_{ij}>0} F_{ij} c_{pa} T_{i,t+1} + \sum_k h_{k,i} A_{k,i} (T_{mk,t} - T_{i,t+1}) + S_i. \quad (2.15)$$

On the right hand of the equation, “almost” every temperature term is the new temperature values at time step $t+1$. Here we used “almost” because the implicit method shown in Equation (2.15) is not a complete “implicit” method. Strictly speaking, a complete “implicit” method requires the flow rates F_{ij} and the thermal mass temperatures T_{mk} are at time $t+1$ as well. However, a complete “implicit” formula requires solving a set of nonlinear equations, which increases both computational time and the instability in numerical solving. In later sections, we will see the numerical impacts brought by the nonlinear behaviors of the systems.

Here we argue that a complete “implicit” method will not be necessary if the time steps are small enough. As was discussed in the previous sections, we do use a small time step in the program due to the nonlinear issues in the coupled airflow and thermal problems. The quasi “implicit” method shown in Equation (2.15) will provide enough stability in simulation and allow the quick linear equation evaluation which is more efficient and stable than nonlinear equation evaluation required by a

complete “implicit” method.

The explicit method and implicit method are both first order accuracy methods. Namely, the errors are in the order of Δt . An “average” of the explicit and implicit method, can reduce error to approximately the order of $(\Delta t)^2$, which is called second order accuracy. Strictly speaking, only the average of the implicit method and the complete explicit method (which is also called the “Crank-Nicholson” method) can achieve the exact second order accuracy. In our study, in order to achieve a set of linear equations to solve during the differential equation solving, we use the average of Equations (2.14) and (2.15) as follows:

$$V_i \rho_i c_{pa} \frac{T_{i,t+1} - T_{i,t}}{\Delta t} = \\ \frac{1}{2} \left(\sum_{j:F_{ji}>0} F_{ji} c_{pa} T_{j,t} - \sum_{j:F_{ij}>0} F_{ij} c_{pa} T_{i,t} + \sum_k h_{k,i} A_{k,i} (T_{mk} - T_{i,t}) + S_i \right) \\ + \frac{1}{2} \left(\sum_{j:F_{ji}>0} F_{ji} c_{pa} T_{j,t+1} - \sum_{j:F_{ij}>0} F_{ij} c_{pa} T_{i,t+1} + \sum_k h_{k,i} A_{k,i} (T_{mk} - T_{i,t+1}) + S_i \right). \quad (2.16)$$

When Equation (2.16) is applied to every zone i (from 1 to n), a set of n linear equations will be obtained. In general, these linear equations can be written as the following form:

$$\begin{bmatrix} a_{11} & \cdots & a_{1i} & \cdots & a_{1n} \\ \vdots & \vdots & \vdots & \vdots & \vdots \\ a_{i1} & \cdots & a_{ii} & \cdots & a_{in} \\ \vdots & \vdots & \vdots & \vdots & \vdots \\ a_{n1} & \cdots & a_{ni} & \cdots & a_{nn} \end{bmatrix} \begin{bmatrix} T_{1,t+1} \\ \vdots \\ T_{i,t+1} \\ \vdots \\ T_{n,t+1} \end{bmatrix} = \begin{bmatrix} b_1 \\ \vdots \\ b_i \\ \vdots \\ b_n \end{bmatrix}. \quad (2.17)$$

Denote

$$A = \begin{bmatrix} a_{11} & \cdots & a_{1i} & \cdots & a_{1n} \\ \vdots & \vdots & \vdots & \vdots & \vdots \\ a_{i1} & \cdots & a_{ii} & \cdots & a_{in} \\ \vdots & \vdots & \vdots & \vdots & \vdots \\ a_{n1} & \cdots & a_{ni} & \cdots & a_{nn} \end{bmatrix}. \quad (2.18)$$

The property of matrix A determines whether the Equation (2.17) is well behaved. From Equations (2.16) and (2.17), the matrix A is positively diagonally dominant, which means any diagonal element a_{ii} is positive and greater than the sum of the absolute values of the other elements in the same row. With a diagonally dominant matrix, the linear equations can almost always be solved by adequate methods without numerical problems.

The system equations derived by the implicit method, Equation (2.16) also have the diagonally dominant properties. This means the system can be easily solved without numerical problems for both the implicit method and “averaged” method.

2.5.2 Thermal mass solution

Similar to the equations for the air temperature, the discretized equations for the thermal mass temperature (Equation (2.11)) can also be solved either by an explicit scheme or an implicit scheme. The explicit scheme states

$$\rho_m c_{pm} \Delta x \frac{T_{i,t+1} - T_{i,t}}{\Delta t} = \frac{T_{i-1,t} - T_{i,t}}{R_{i-1}/2 + R_i/2} + \frac{T_{i+1,t} - T_{i,t}}{R_i/2 + R_{i+1}/2}, \quad (2.19)$$

where the R_{i-1} and R_i are the thermal resistances on the two side of the nodes of the nodes (per unit area). The internal cells and the boundary cells have some differences in the R_{i-1} and/or R_i values, which will be explained shortly.

The implicit scheme for the thermal mass equations is as follows:

$$\rho_m c_{pm} \Delta x \frac{T_{i,t+1} - T_{i,t}}{\Delta t} = \frac{T_{i-1,t+1} - T_{i,t+1}}{R_{i-1}/2 + R_i/2} + \frac{T_{i+1,t+1} - T_{i,t+1}}{R_i/2 + R_{i+1}/2}. \quad (2.20)$$

A “Crank-Nicholson” scheme, which averages the explicit and the implicit schemes, can be applied to achieve the second order accuracy:

$$\begin{aligned} \rho_m c_{pm} \Delta x \frac{T_{i,t+1} - T_{i,t}}{\Delta t} &= \frac{1}{2} \left(\frac{T_{i-1,t} - T_{i,t}}{R_{i-1}/2 + R_i/2} + \frac{T_{i+1,t} - T_{i,t}}{R_i/2 + R_{i+1}/2} \right) \\ &+ \frac{1}{2} \left(\frac{T_{i-1,t+1} - T_{i,t+1}}{R_{i-1}/2 + R_i/2} + \frac{T_{i+1,t+1} - T_{i,t+1}}{R_i/2 + R_{i+1}/2} \right). \end{aligned} \quad (2.21)$$

Equation (2.21) involves only terms that can be written in a band matrix form as:

$$\begin{bmatrix} b_1 & c_1 & & & \\ a_1 & b_2 & c_2 & & \\ \dots & \dots & \dots & & \\ & a_{n-1} & b_{n-1} & c_{n-1} & \\ & & a_n & b_n & \end{bmatrix} \begin{bmatrix} T_{1,t+1} \\ \vdots \\ T_{i,t+1} \\ \vdots \\ T_{n,t+1} \end{bmatrix} = \begin{bmatrix} d_1 \\ \vdots \\ d_i \\ \vdots \\ d_n \end{bmatrix}. \quad (2.22)$$

The tri-diagonal band matrix in Equation (2.22) is can be quickly solved by the “Thomas Algorithm” (Press [51]), which has complexity of only $O(n)$. This the algorithm is very fast, since solving a similar n -dimensional linear system shown in Equation (2.22) can have a complexity of $O(n^3)$ ². This means the program can handle large amount of thermal mass layers without significantly contributing to the total computational time.

²This is a general statement for dense matrix and Gaussian Elimination type method. For sparser matrix, or matrix with special structures, the complexity can be reduced depending on the specific algorithms and matrix properties.

2.5.3 Airflow flow solution

Solving the airflow network is a classical problem for multi-zone models. Mature algorithms have been developed to solve such network (e.g., CONTAMW 2.0 [64], COMIS [29]). During each time step, the airflow pressure will be solved in a pressure network. The flow network consists of a set of nonlinear equations. To solve the nonlinear (steady state) equations, a Newton algorithm is generally used. There are many forms of Newton methods. They can be different in terms of defining the differentials, the progress steps, and the region of values. Due to the specialty of our flow network, we can obtain the differentials by closed form formulas. A basic Newton-Raphson [51] method for multiple dimensional nonlinear equation systems was used in the predecessor of the present program [58]. However, the numerical performance of the method is not satisfactory in the airflow solving stage.

In this study we have modified the original Newton-Raphson method used by Tan [58] to achieve better numerical performance. The major advancement is the Newton step control. A careful analysis shows that the possible numerical instability of the original program mainly comes from the uncontrolled step movement. When the system proceeds to a new guess point from an old one, the original program did not control some “wild” movements that may potentially increase the residuals. Therefore, the modified algorithm tries to make the Newton step movement in the range that the total residual is decreasing each time. When a residual growth is identified in the Newton step progress, a bisectional step reduction is activated until it reaches the goal of residual decrease or hit the preset minimum step movement. By implementing this step control strategy, the modified program becomes much more stable in airflow solving than its predecessor that used an uncontrolled basic Newton-Raphson [51] method.

2.6 Program interfaces

A Windows based interface is developed to facilitate the user to handle the input and output of the models. In the interface, we offered four prototypes of typical natural ventilation designs. The user can input the general design parameters such as weather and geographical conditions, building functionalities, and building geometries. After the calculation using the models described in the previous sections, the program can visualize the zonal temperatures by different colors and generate text summaries from the results.

The interface program has two stages for the inputs and a final stage for results visualizations and summaries as is shown in Figure 2-7. The first stage is shown in Figure 2-7(a). This stage allows the users to select building types, cities, months for simulation, and other terrestrial information. It also allows the user to select simulation types - transient (by default) or steady state.

Figure 2-7(b) shows the second stage after a building type is selected in the first stage. This stage allows the user to input the detailed geometry information about the building, such as the dimensions, window size, roof height, and number of floors.

The thermal mass and the control strategies can also be configured in this stage. When the inputs are ready, the core calculation module can be called.

The final stage is for the results visualization and output, which is shown in Figure 2-7(c). The simulation results will be visualized. The zonal temperatures are represented by different colors. For steady states, the images for different times are animated in a sequence. The interval and the speed for each of the frame are adjustable in the animation.

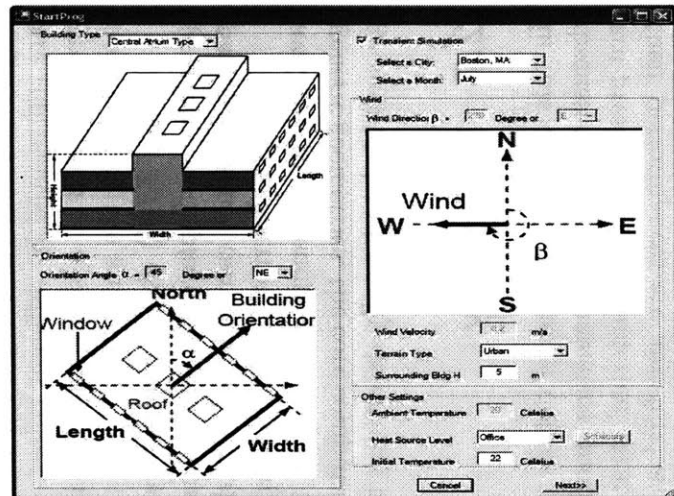
Figure 2-7(d) shows another type output and report method provided by the program — display the results through a chart. The temperature histories in a particular space can be selected and displayed against the outdoor air temperature.

Detailed descriptions of the input parameters, buttons, and other options are available in Appendix A. Although the interface program only supports four types of generic geometries, the core computational models can be applied to more complicated geometries by manually describing the airflow network.

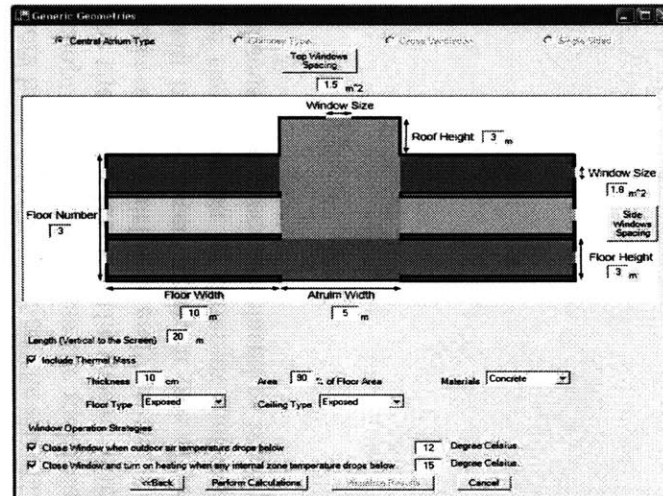
2.7 Summary

In this chapter, the model details of the coupled airflow and thermal program are discussed. First, mathematical models for the three major modules of the program are presented. The numerical strategies to solve each of the modules and improve their performances are also further discussed. Finally, other supporting features of the program and the interface for input and output are presented.

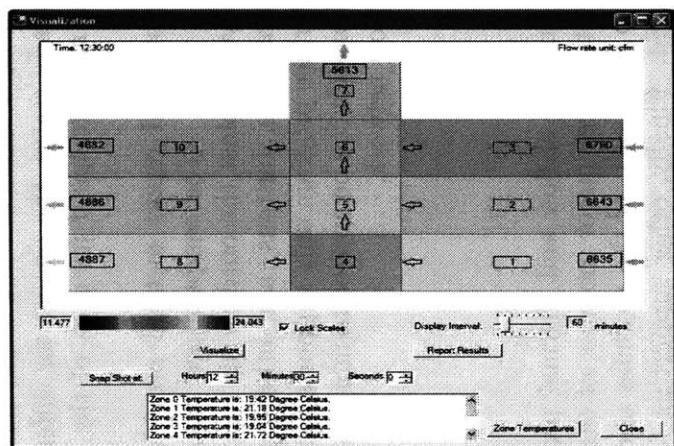
In the development the program, we found that the multiple-steady-state behaviors have great impact on the simulation results and numerical performances. In later chapters we will discuss the multiple steady states behaviors theoretically, which will be the major focus of the thesis. With the understanding of the theoretical fundamentals of the multiple steady states, the related numerical issues in airflow simulations will be discussed again in one of the later chapters. In Chapter 3, the validations of the program by different methods will be discussed. After that, we will start to discuss the theories related to multiple steady states in Chapter 4.



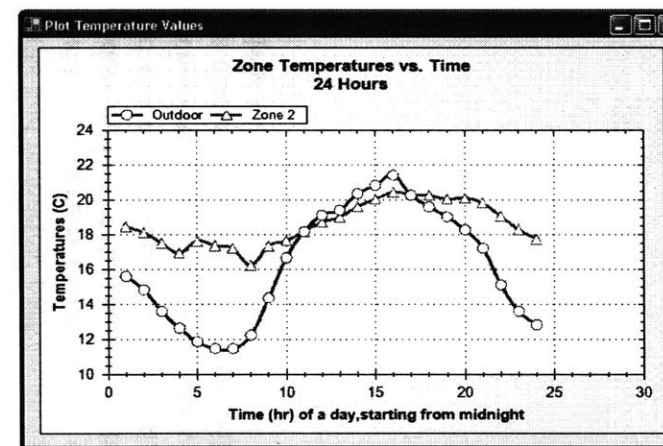
(a) Input Stage 1



(b) Input Stage 2



(c) Result visualization



(d) Result summary and report

Figure 2-7: Program interface for design users

Chapter 3

Validations of the simulation program

During and after the development of the coupled airflow and thermal analysis program CoolVent in Chapter 2, a series of tests and validations have been conducted on the program. The purpose of the validations is to test both the model implementation (e.g. air temperature and thermal mass dynamics) and the effective of the major assumptions (e.g. the multi-zone simplification). Through the validations, we expect to gain confidence about the correct implementation of the models and the reasonability of the results under current assumptions.

In Appendix B, we first provided a few comparisons of CoolVent with simple analytical models. Most of these simple cases were conducted during the development of the CoolVent program as sanity tests. In this chapter, we will conduct in depth validation studies of CoolVent program by comparision with more advanced data sources. The CoolVent program results will be compared with three types of data – CONTAMW, steady state CFD, and transient field monitoring results – step by step.

3.1 Validation procedures

In this chapter, we provide three more validation tests. We first compare CoolVent with a similar multi-zone program—CONTAMW [64]. We will test the multi-zone airflow prediction performance of CoolVent by comparing the steady state airflow simulation results with CONTAMW in a steady state case.¹ The test means to provide a basis for the multi-zone feature performance comparison.

Secondly, we compare CoolVent with Computation Fluid Dynamics (CFD) results. We will use steady state CFD [18] simulation results to test the effectiveness of the multi-zone airflow and full-mixing temperature assumptions. These assumptions are important to natural ventilation modeling in buildings with multiple zones, especially buildings with strong buoyancy-driven flows. the steady state CFD simulations intend to validate the steady state air flow and temperature solving capabilities of the program.

¹Transient airflow is not used since CONTAMW does not provide dynamic temperature solving. CONTAMW does, however, allow the zonal temperature to be manually scheduled.

Finally, and most importantly, we compare CoolVent with transient field measurement data. The transient validation is targeted on examining the accuracy of the transient thermal mass and airflow simulation capabilities of the program. We will compare the program prediction results with the field monitoring data obtained in an actual multi-floor, multi-space building. Complex boundary conditions, load estimation, and radiation models will be applied to model the operation conditions of the monitored building. Furthermore, the flexibilities and expandabilities for the program to incorporate more complex models in future versions are also examined.

3.2 Prototype test building descriptions

The three stages of validations uses building geometries that originate from the same prototype.² Figure 3-1 shows the configuration of the prototype building. It is a naturally ventilated building located in Luton, United Kingdom. (We call it “Luton” type hereafter.) It is a three-floor office building, with a dimension of $25\text{m} \times 17.2\text{m} \times 14.5\text{m}$. The actual orientation of the building (windows) is Northeast-Southwest. For simplicity in the present study, we simply denote the Northeast side as North side and the Southwest side as South side. The building consists of an atrium space in the middle and multiple open plan office spaces on the two sides.

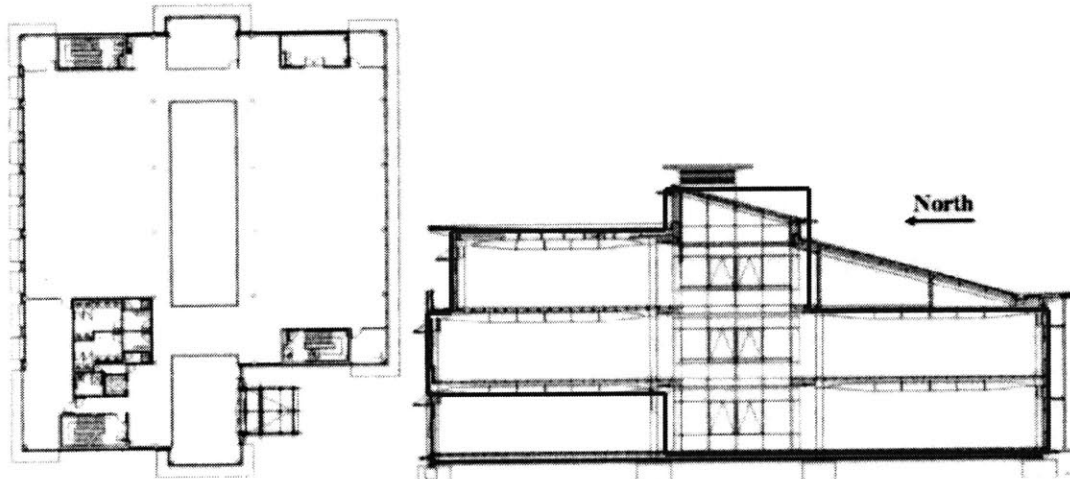


Figure 3-1: A natural ventilated building in UK (Superimposed on the graph presented in Walker [61])

The office spaces are 45% glazed on the south or north walls (depending on the orientation of an office). The other side is open to the central atrium area. Seven windows are aligned on the same side. Each window has an upper vent which is open all the time from May to October and a lower awning which is open during work hours

²One exception is in the second stage (CFD). Other than the Luton building, another building with a different geometry is also simulated.

in weekdays. The office spaces have carpeted and raised floors. The office ceilings are exposed concrete slabs of $\sim 10\text{cm}$ thick. Each half-floor, open-plan office space is occupied by 15–20 persons in general and each person has a computer.

3.3 Comparison with CONTAMW

As our first test case, a flow rate comparison between CoolVent and CFD is conducted in a prototype building in this building. We compared CoolVent and CONTAMW results for a three-floor building shown in Figure 3-2. The zone divisions are denoted by the dashed lines. Through this dividing method, we only consider one-way flows within these zones. This building will be investigated once again in later sections (Section §3.4.1) with a different zone division method so that two-way airflows can be further considered.

Since CONTAMW cannot solve the air temperature from heat source, we first start the simulation with CoolVent by prescribing the heat sources. After obtaining the steady state temperatures by CoolVent, the temperature values are manually input into CONTAMW to calculate the flow rates. To do this we insured that the two programs have the same zone temperatures for a steady state flow rate calculation.

Figure 3-2 shows the simulation results obtained by the two programs. For nearly all the airflow rates, the predictions by the two programs are very close. The major discrepancy is the upper-left zone, where a 13% disagreement occurs between the predictions by the two programs. This is mainly due to the different assumptions used in CONTAMW code and CoolVent in dealing with buoyancy forces. CONTAMW uses the ideal gas law to calculate the air status for buoyancy forces, while CoolVent uses the Boussinesq assumption [28] for buoyancy force calculation. Since the temperature difference between this upper-left zone and the other zones is very high, larger buoyancy force differences may occur using the two different assumptions.

3.4 Comparison with steady state CFD

CFD simulations are conducted in full scale to test the airflow and temperature prediction accuracy of the program. The natural ventilation flows and zone temperatures within the prototype test building are tested for two types of conditions – flows set up by pure buoyancy forces and flows due to combined (hybrid) buoyancy and wind forces.

Two cases are tested on the natural ventilated flows in this section: the pure buoyancy-driven natural ventilation and the combined buoyancy and wind-driven natural ventilation. For CoolVent, the airflow rate between zones and the zonal temperatures are reported. For CFD, the averaged zone temperatures and airflow rates across the openings are reported so that they can be compared to CoolVent on the same basis.

In this section, we will perform the both simulations (buoyancy and hybrid) on two buildings. The first one is the Luton building discussed in Section §3.2. The

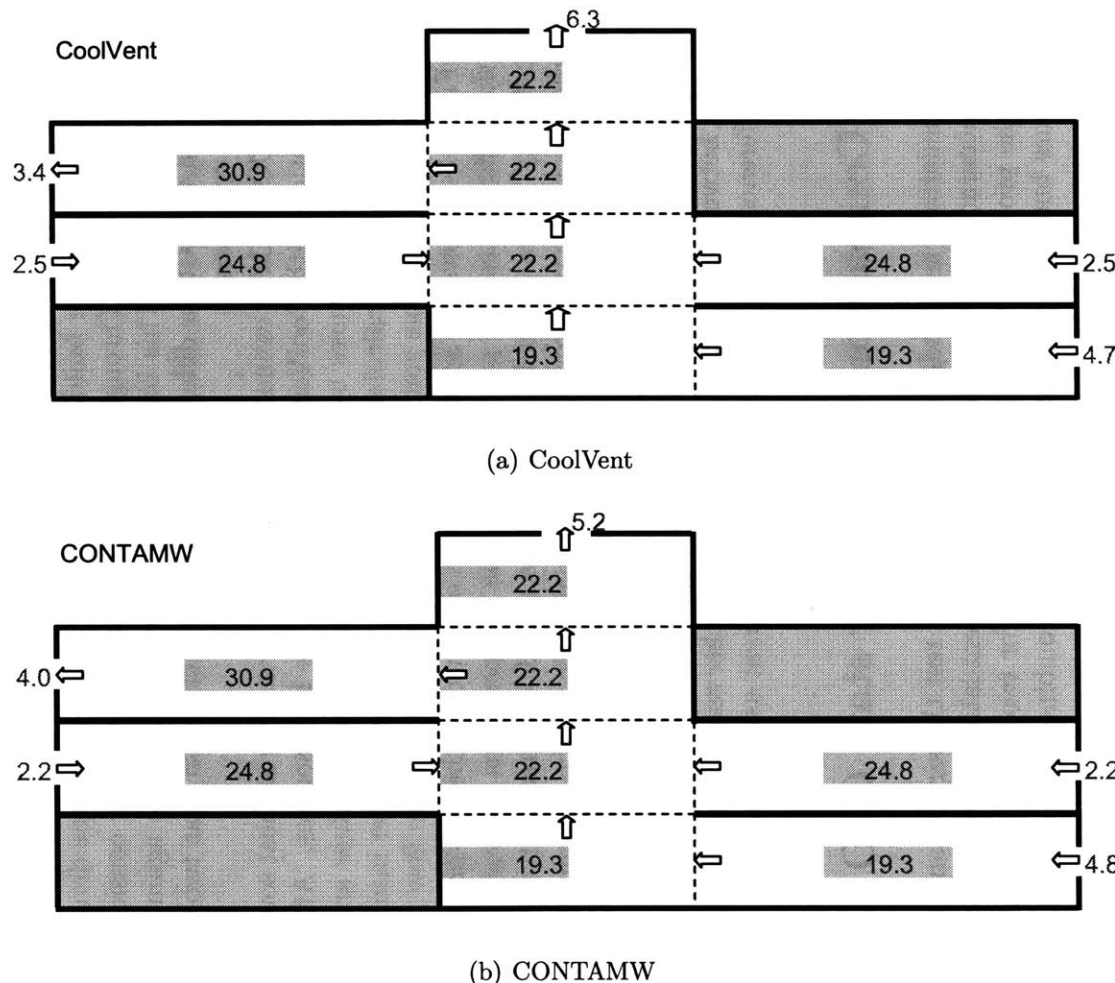


Figure 3-2: CoolVent vs. CONTAMW simulation results for a three-story building^a

^aThe shaded numbers stand for the zone temperatures in °C; other numbers are for air flow rate in kg/s; arrows indicate the major flow directions. The same notations are used in the rest of this chapter.

second building is similar to the Luton building, except that there is only one side that has office spaces, which is shown in Figure 3-7.

3.4.1 Case 1—A Luton (central atrium) type building

For CoolVent, the building is divided into different zones. Figure 3-3 shows the zone division: the dashed lines and dot-dashed lines divide the building into 11 zones. This zone division is slightly different from the division in the previous study of CONTAMW validation in Figure 3-2: the zones in the atrium are finer in order to capture the two-way flows between the atrium and the connected offices. For CFD, the temperature values are averaged in the eight zones divided by the thick dashed lines. The airflow values for the two-way flows between the atrium and the connected zones are also reported to compare with CoolVent results.

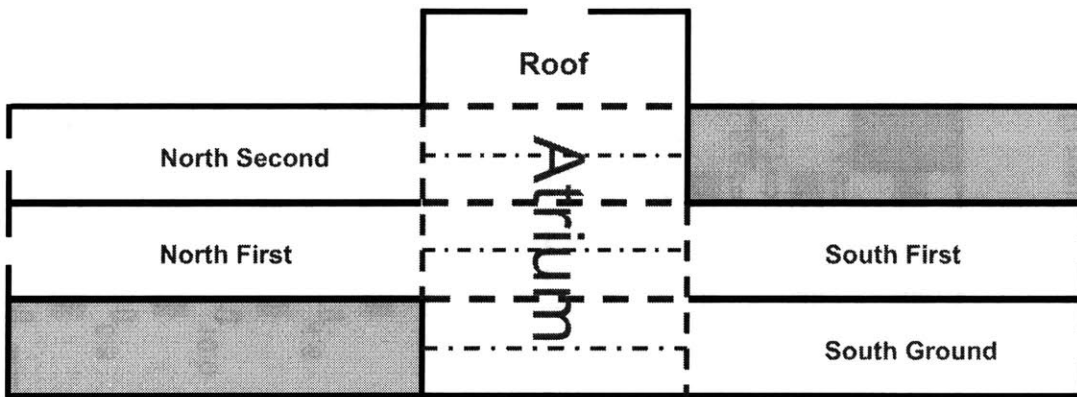


Figure 3-3: Zone divisions for CoolVent, especially in the atrium area

The simulations are conducted with the following night operation set up. The ambient temperature is set at 13 °C. The office zones are assumed to have a heat load of 15 W/m². The upper vents of the office windows are open and the lower windows are closed. In the first case, no wind is assumed. In the second case, an exterior wind velocity of 1.5 m/s blowing from the south is assumed.

3.4.1.1 Pure buoyancy-driven flows

The natural ventilation flows are simulated by multi-zone and CFD models respectively. The results are compared in Figure 3-4(a) (CoolVent) and Figure 3-4(b) (CFD).

The results show that the zone temperatures and inter-zonal flow rates predictions made by the two programs are close. For temperatures, the CoolVent program shows agreement with CFD within 0.5 °C. For airflow values, CoolVent shows an agreement with CFD within 15% for the vertical openings. However, for the horizontal openings (e.g. the airflows in the atrium), CoolVent has difficulties capturing the two-way flows between zones. The two-way flows are clearly shown in the CFD

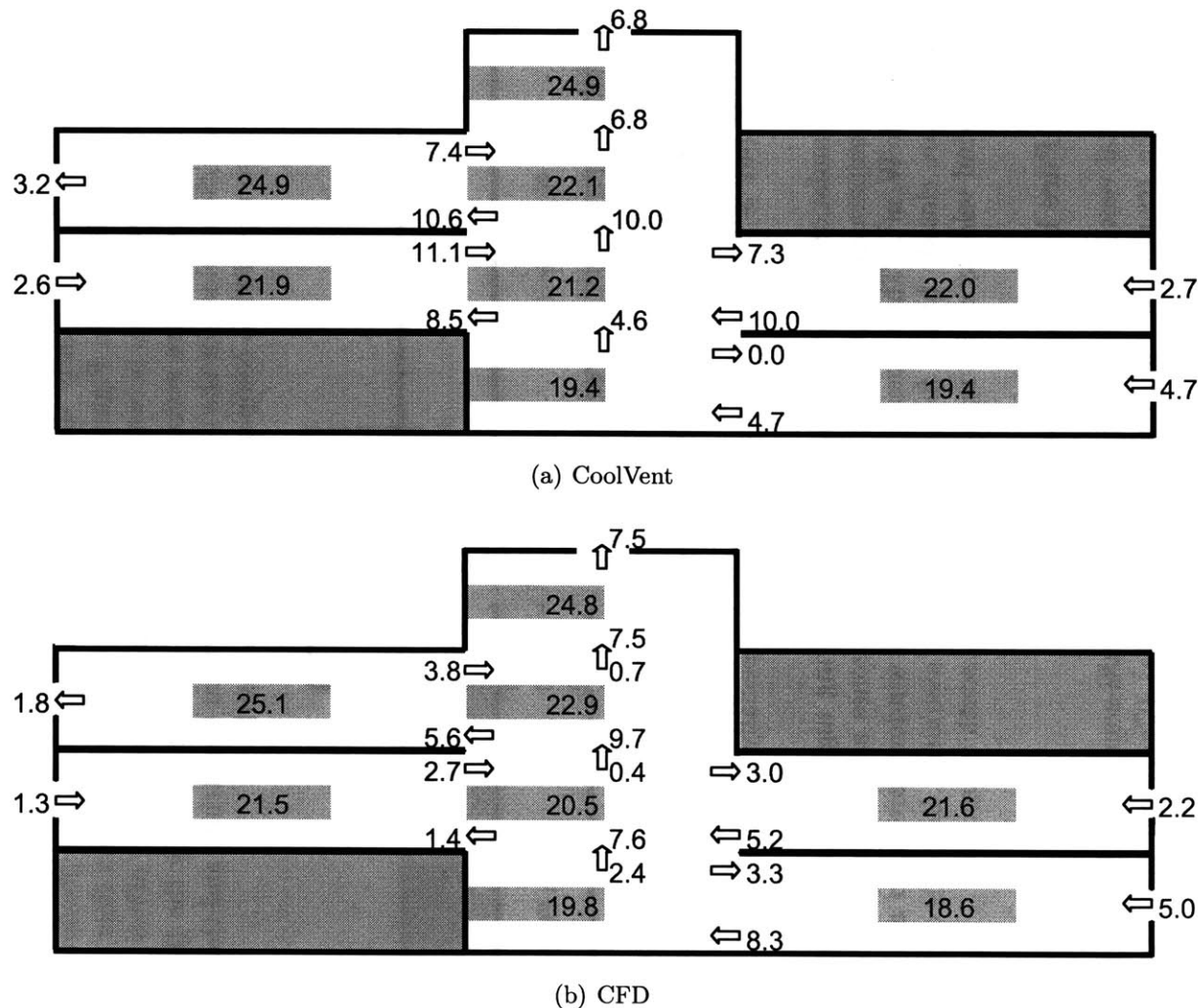


Figure 3-4: CoolVent and CFD results summaries (Luton Building, pure buoyancy flow)

flow visualization shown in Figure 3-5. There the vertical two-way flows through the horizontal opening between the ground and the first floor atriums are significant.

The largest discrepancy in flow rates between the CoolVent and CFD simulations occurs in the upper-left (Second floor, North office) zone (see Figure 3-4). Both CoolVent and CFD predicted an outward flow for this zone. However, the flow rate predicted by CoolVent is $\sim 39\%$ higher than the rate predicted by CFD. This large discrepancy is partly due to the strong stratification predicted by CFD inside this upper-left office zone, as is shown Figure 3-5. Since the stratification in this upper zone is very strong, the buoyancy forces inside the zone will be significantly reduced. Even though the CoolVent and CFD predicted almost the same zone-averaged temperatures in this upper-left zone ($24.9\text{ }^{\circ}\text{C}$ vs. $25.1\text{ }^{\circ}\text{C}$), CFD results will have an existing air temperature that is much hotter than the average zone temperature due to the strong stratification effect. Therefore for CFD, the buoyancy force inside the zone will be significantly reduced, compared to the uniformed temperature scenario in CoolVent (basically a multi-zone model assumption), which makes the CoolVent airflow prediction significantly higher than the CFD prediction in this zone.

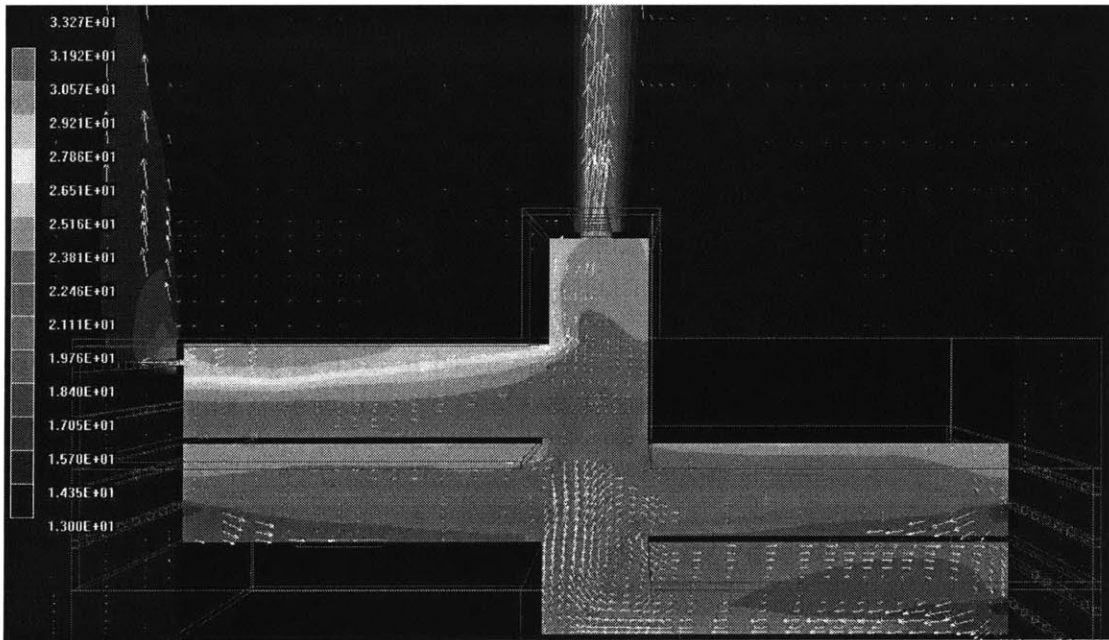


Figure 3-5: CFD visualization of the pure buoyancy-driven flows in the Luton building

This result discrepancy in the upper-left zone does show a common short-coming of the multi-zone model—over-simplified full-mixing model. For microscopic airflow inside a single space, the finer grids of CFD indeed present an advantage in predicting the internal stratification effect. However, if we view this discrepancy in an entire building simulation level, it also justifies why energy equations should be incorporated in multi-zone airflow models to consider the temperature differences between different zones (rooms) in order to better capture the stratification effect in an entire building level.

To overcome the shortcoming of oversimplified zonal temperatures, a possible solution is to divide a zone into an upper part and a lower part, or different layers, to partly capture the internal stratifications with a single space. Yuan and Srebric [78] used such a dividing method to predict the airflow and contaminant concentrations in an office space with displacement ventilation (where the stratification is strong), and the results agreed reasonable well with the CFD simulation results.

3.4.1.2 Hybrid buoyancy/wind-driven flows

In this case, a south wind of 1.5 m/s is incorporated. The natural ventilation flow is driven by the combination of the south wind and the internal buoyancy forces. Figure 3-6(a) shows the CoolVent simulation results. Figure 3-6(b) shows the CFD simulation results.

In this case, the maximum temperature difference between CoolVent predictions and CFD results is ~ 1 °C. The largest flow rate discrepancy is also in the upper-left (Second floor, North office) zone, where CFD shows a 38% lower flow rate than the CoolVent predictions. This large discrepancy is again partly due to the strong stratification inside this upper-left zone predicted by CFD (see the argument in Section §3.4.1.1). There are also discrepancies in the results predicted by the two programs in the two-way flows. Although the bulk flows between two zones are the almost same in most of the zones, the magnitudes of the two-way flows can be different.

3.4.2 Case 2—A chimney type building

In the second building, we used another type of common geometry shown in Figure 3-7, which we call it the “chimney” type, for a similar test. The zone division is similar to that of the Luton building case discussed in Section §3.4.1. Two cases are conducted – a pure buoyancy case and a combined buoyancy and wind case.

Again these simulations are conducted with the following night operation set up. The ambient temperature is still 13 °C. The two offices zones have a heat load of 15 W/m² each. The upper vents of the office windows are open and the lower windows are closed. An exterior wind velocity of 1.5 m/s blowing from the south is assumed for the combined wind and buoyancy-driven case.

3.4.2.1 Pure buoyancy-driven flows

Figure 3-7(a) shows the CoolVent results for the pure buoyancy-driven chimney case. Figure 3-7(b) shows the CFD results summaries for the same case.

In this case, relatively large discrepancies between the CoolVent predictions and the CFD results occur in the second floor south office. CFD shows a much lower averaged zone temperature in this zone than CoolVent. This is due to the detailed airflow and temperature distribution in this zone. In general, the exiting temperature is higher than the average temperature in CFD. However, the exiting temperature is almost the same as the zonal temperature in the multi-zone model. Figure 3-8 shows the exiting temperatures of the two office zones in this case. Since the net flows

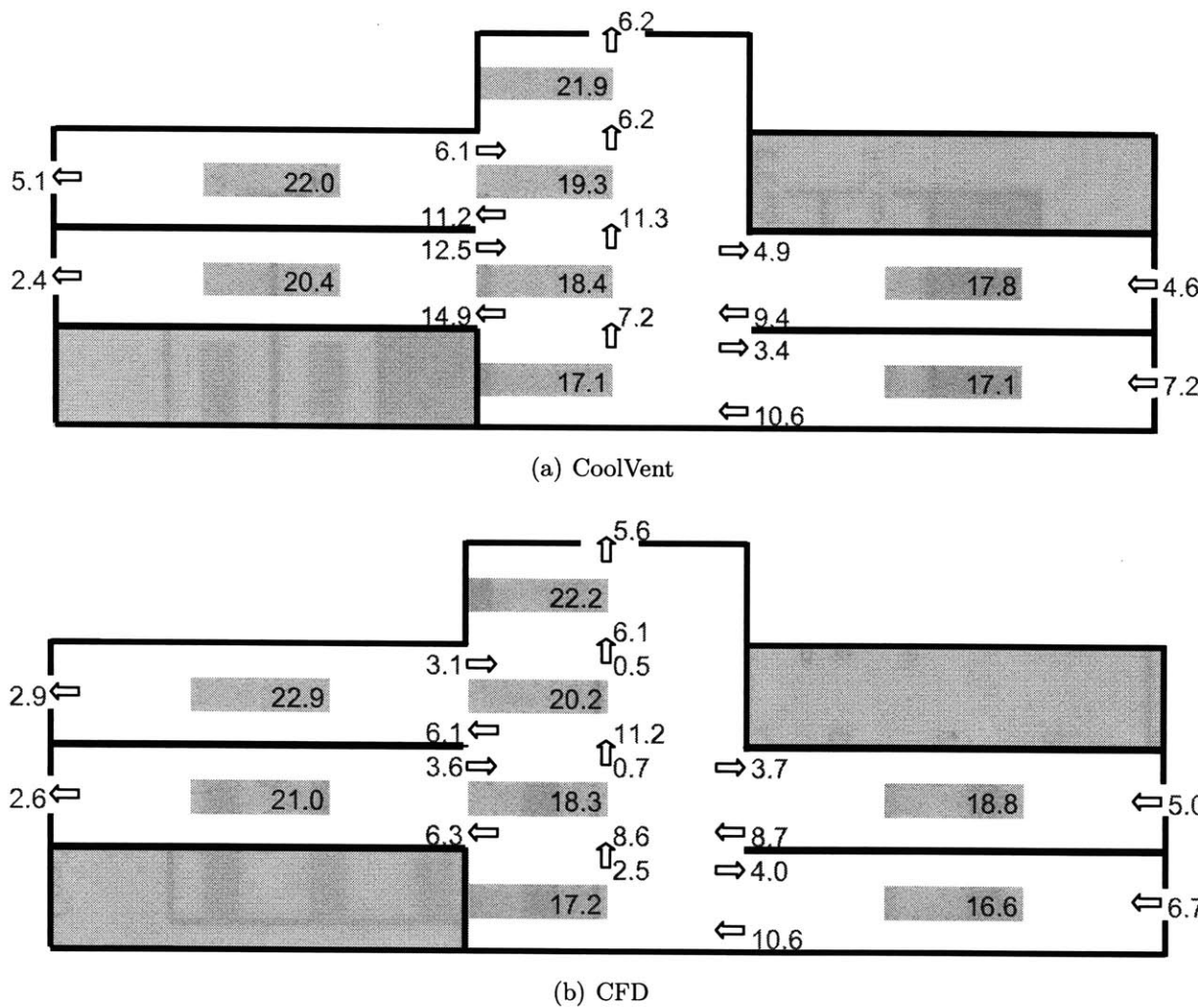
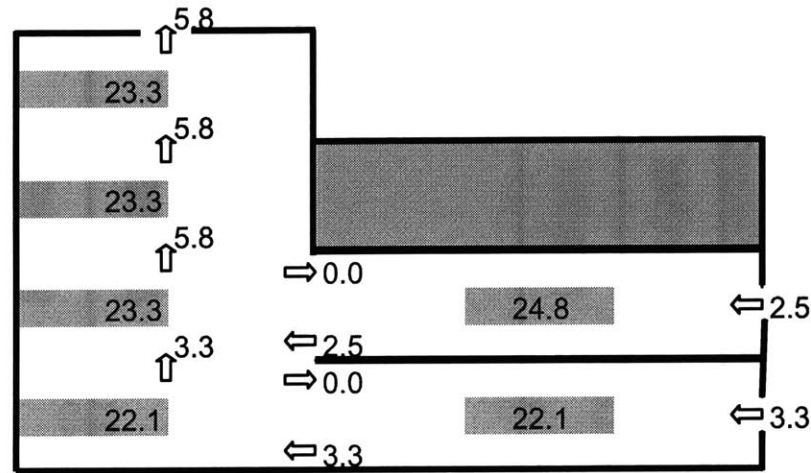
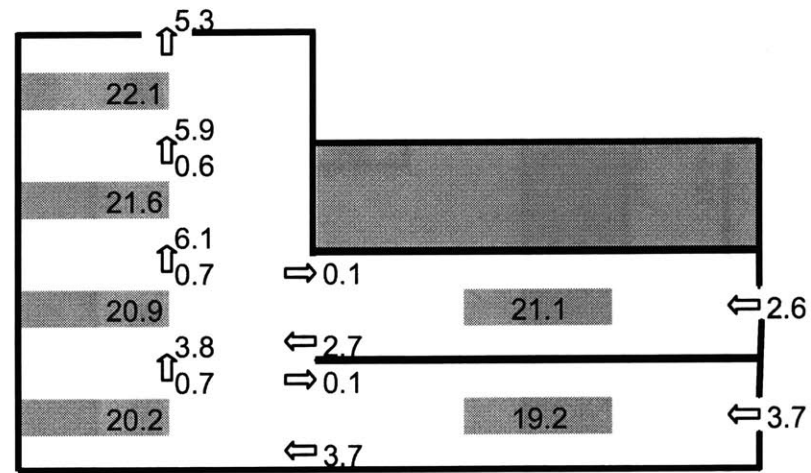


Figure 3-6: CoolVent and CFD simulation results summaries (Luton Building, hybrid buoyancy/wind flows)



(a) CoolVent



(b) CFD

Figure 3-7: CoolVent and CFD simulation results summary (Chimney type, pure buoyancy flows)

coming out of the zone are close for CoolVent and CFD, the exiting temperature predicted by the two programs are also close. Therefore it follows that CFD average zone temperature is lower than the multi-zone results.

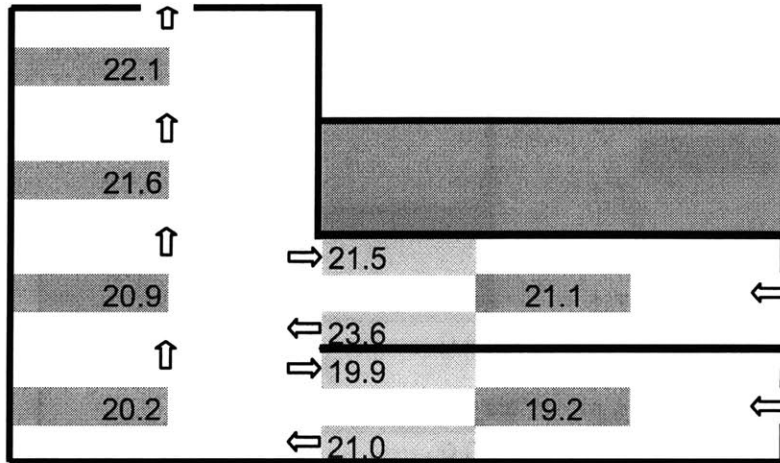


Figure 3-8: Internal and exiting temperatures of the two office zones in CFD simulation results (Chimney type, pure buoyancy flows)

3.4.2.2 Hybrid buoyancy/wind-driven flows

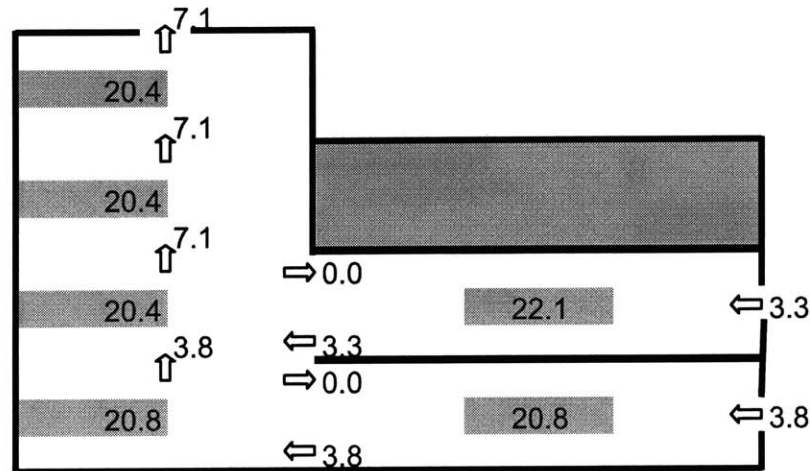
Figure 3-9(a) shows the CoolVent results and Figure 3-9(b) shows the CFD results summaries for the combined buoyancy and wind-driven chimney case.

In general, the two-way flows in the chimney case are much less than in the Luton building case due to the simple geometries. This is also shown in CFD results (see Figures 3-7(b) and 3-9(b)), where the vertical openings nearly have no reversal flows. In these two cases, the air flow results predicted by CoolVent and CFD agree reasonably well.

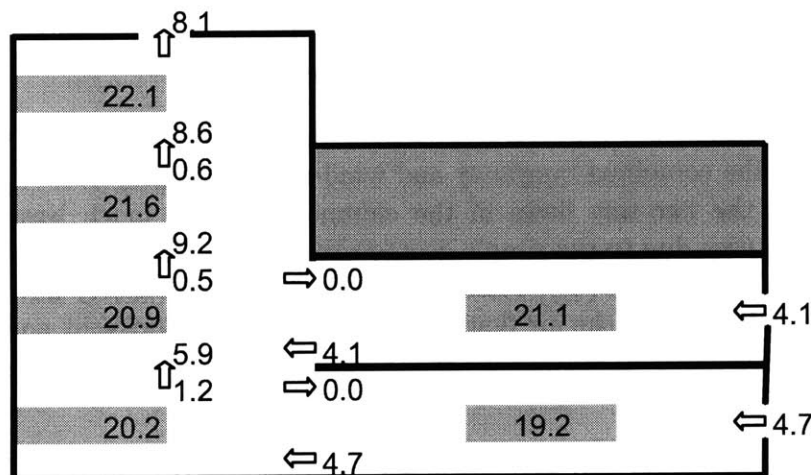
3.4.3 Summaries

The results show a general reasonable agreement between the CoolVent predictions and the CFD simulations. The differences between the predictions and measurements are within ± 1 °C in most of the validation cases. The bulk flows predicted by the CoolVent program also agrees with CFD results within in 20% in most cases. However, in some cases (e.g. Figure 3-4) they do not agree well on the exact two-way flow magnitudes on the south second floor.

There are some larger discrepancies between the CoolVent and the CFD results in the occupied zone in the pure chimney buoyancy case. These discrepancies are mainly due to the detailed airflow and temperature distribution within the zone, which can be the general weakness of multi-zone models.



(a) CoolVent



(b) CFD

Figure 3-9: CoolVent and CFD simulation results summary (Chimney type, hybrid buoyancy/wind flow)

3.5 Compare with transient field measurement data

In previous test cases, the transient simulations and airflow predictions are decoupled—either the airflow is given in a transient simulation or the temperature dynamics are not considered in airflow solution. In this section we will conduct a full case in which the transient temperature solution, the thermal mass solution, and airflow solving are fully coupled. We used the field monitoring data in an existing natural ventilated building that was monitored consecutively for a few months during summer 2003 by Walker et al [62]. CoolVent program is validated by field measurement data for its accuracies in all the aspects including program implementation, assumption reasonability, and boundary conditions handling.

3.5.1 New models in the research version

3.5.1.1 Internal radiation model

The naturally ventilated building to be investigated is the same Luton building (Figure 3-1) used in the steady state CFD validation in Section §3.4. Figure 3-10 shows the simple radiation model corresponding to the office space shown in Figure 3-1. Since the office has a carpeted raised floor, it has a large thermal resistance for vertical heat transfer beneath the raised floor surface. Therefore, the floor downside is assumed to be adiabatic in this simplified model. The shortwave solar radiation and long wave (infrared) radiation are considered. The solar radiation coming from the window is assumed to be absorbed by the floor and then transferred to the air above it as well as to the ceiling. All surfaces are assumed to be diffusive gray surfaces. The solar energy is assumed to be uniformly distributed over the floor area.

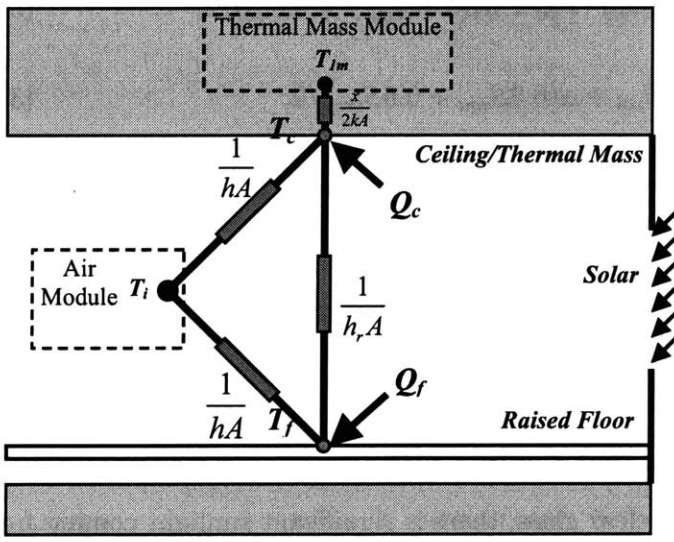


Figure 3-10: Models for combined internal radiation and convection in a space

Two surface heat balance equations are to be solved for the ceiling surface tem-

perature T_c and the floor surface temperature T_f by

$$(T_{1m} - T_c) \cdot 2kA/x + Q_c + (T_i - T_c) \cdot hA + (T_f - T_c) \cdot h_r A = 0 \quad (3.1)$$

and

$$Q_f + (T_i - T_f) \cdot hA + (T_c - T_f) \cdot h_r A = 0 \quad (3.2)$$

where h_r is the effective heat transfer coefficient between the ceiling and the floor surfaces through radiation.

The emissions and reflections from the wall surface to the ceiling / floor are not considered in this estimation since the view factor from the floor to ceiling dominates other view factors. Q_c is the solar radiation and internal heat gain transferred to the ceiling surface. Q_f is the solar radiation and internal heat gain transferred to the floor surface.

The incoming solar is absorbed and reflected multiple times inside the space before gaining an equilibrium distribution. Since the absorptance of the floor and ceiling for the solar is in the range of 0.65 – 0.80 (ASHRAE [6]), the solar is almost absorbed after two incidences. Therefore only one reflection was considered. The infrared radiation is also estimated. The guideline used in internal load calculation by ASHRAE [6] was applied to split the convective and radiation components. A split of 50% convective, 50% radiative was recommended for equipment, while a split of 40% convective, 60% radiative was recommended for occupant sensitive heat. Similarly to solar consideration, only the first bounce is considered. Since the internal gain is much smaller than the solar gain in general, for simplicity, the radiation to the walls and windows is also neglected and thus an equal distribution between the ceiling and the floor is assumed. With these approximations, the term Q_c and Q_f used in Equations (3.1) and (3.2) can be approximated by

$$Q_c \approx \alpha_s(1 - \alpha_s)S_{sol} \cdot F_{fc} + \alpha_i(0.5S_{equ} + 0.6S_{occ})/2, \quad (3.3)$$

and

$$Q_f \approx \alpha_s S_{sol} + \alpha(0.5S_{equ} + 0.6S_{occ})/2, \quad (3.4)$$

where α_s is the absorbance of the floor/ceiling surfaces for solar radiation and α_i is for infrared radiation. F_{fc} is the view factor from the floor to the ceiling, which is about 0.75 according to the geometries of the office space.

In the solution of temperatures by CoolVent, the internal zone temperature T_i is solved at each time step by solving the airflow and thermal network. The sub-network in Figure 3-10 will be simultaneously solved for the ceiling surface temperature T_c and floor surface temperature T_f .

3.5.1.2 Roof transmittances and shading effect

Since the atrium roof is made of clear glass, there is significant sunlight coming from the atrium roof and incident on the floor of the second floor North office. This adds to additional heat gains to the North side office. In the same time, the vertical side walls of the roof also serve as a possible obstruction that may shade the second

floor office. Therefore, both of these two effects were considered by calculating the geometric projection position of the shadow of the second floor roof. The calculation results are shown in Figure 3-11. The shading fractions at the beginning and the end of August – Aug 1 and Aug 31 – are presented on the graph. Here we define the *shading fraction* on a (virtual) surface (the opening of the second floor to atrium) as the fraction of shadow caused on the surface by an obstruction object. The higher the shading fraction, the less solar radiation passes through the surface. Figure 3-11 shows that most of the shading occurs during very early in the morning, when the solar radiation is not strong. Shading time also changes with the date (in a month). For example, the period of shading is around 1.5 hours different for the beginning of August (1st) and the end of August (31st).

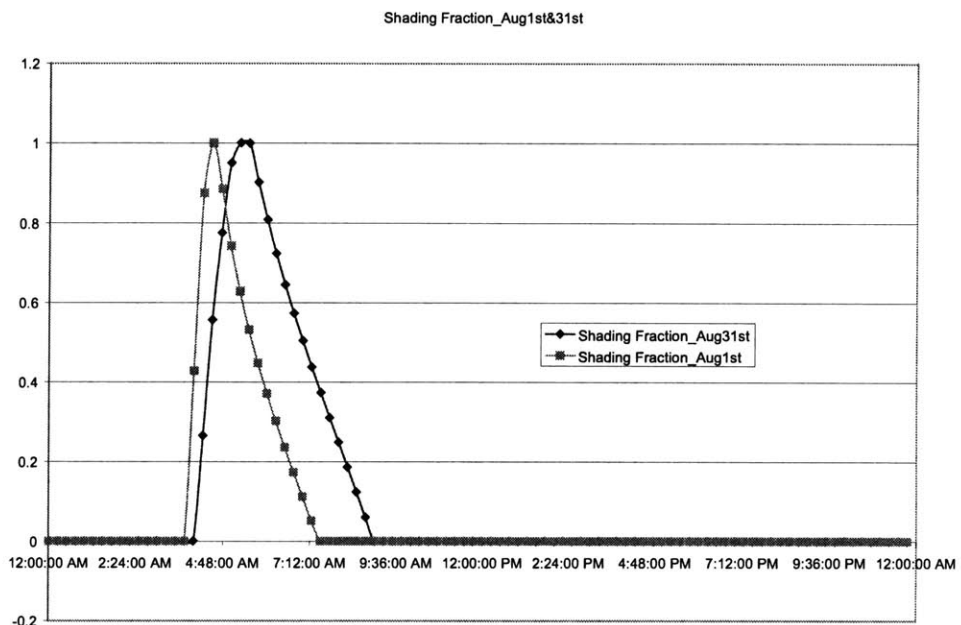


Figure 3-11: The shading fraction on the north office in the beginning and end of August (atrium side)

Other boundary conditions such as outdoor air temperature, wind velocity, and internal load profile during the monitoring period can be obtained from field measurement or the National Renewable Energy Lab (NREL, <http://www.nrel.gov/>) weather file. Based on the available information, the entire building was simulated by the developed program for a period of four weeks from early to late August, 2003.

3.5.2 Building monitoring data

Temperature

To validate the integrated model, the transient simulation results are compared with the field measurement data collected in August 2003, when the on-site temperatures

of the naturally ventilated building were logged at an interval of 15 minutes for a month by Walker et al. [62].

Solar radiation

Solar radiation through the windows, the most important heat source is calculated by the method illustrated by Duffie and Beckman [25]. The method takes the horizontal solar radiation (from measurement), time (month, hour, minute), and window orientation. The direct, diffuse, and reflective (by the ground) components of the solar radiation in the direction normal to the window are decomposed from horizontal radiation and the total incoming solar radiation is the sum of the three.

Occupant schedule

The building is operating from 8:30 am to 7:00 pm during each work day. The building is closed on weekends. The number of occupants was estimated based on the observations of Walker et al. [62] in August 2003. Table 3.1 lists the number of people in each office during different time of a particular day.

Table 3.1: Sample occupant schedule in August 2003

Date Day	Time (hh:mm)	Ground Floor	1 st Floor		2 nd Floor
			South	North	
Aug 1 Fri	10:15	15	17	13	7
	12:15	18	16	12	11
	14:15	16	21	8	6
Aug 6 Wed	10:00	13	16	12	6
	12:00	19	20	14	6
	14:00	11	15	15	7
Aug 14 Thu	11:30	19	23	12	11
	13:30	11	9	4	5
Aug 27 Wed	10:15	12	12	16	9
	12:15	23	14	11	8
	14:15	15	11	5	8

The above data provide a general profile about the number of people in the building during office hours. Since the occupant load is not as significant as the solar heat gains and equipment usage that will be discussed shortly, an average number of people at each zone is used and assumed constant during the business hours (8:30 am – 7:00 pm). Beyond the business hours, the number of occupants is assumed to be zero.

Electricity load

During the building monitoring period, the power usage of each floor was monitored for a period of two weeks in August, 2003 by Walker et al [62]. It shows a cyclic pattern

for each work day and weekend. The electricity consumption for a week is shown in Figure 3-12. The equipment load is estimated based on the power consumptions on each floor. For the first floor, the consumption is equally distributed to the North and South side offices.

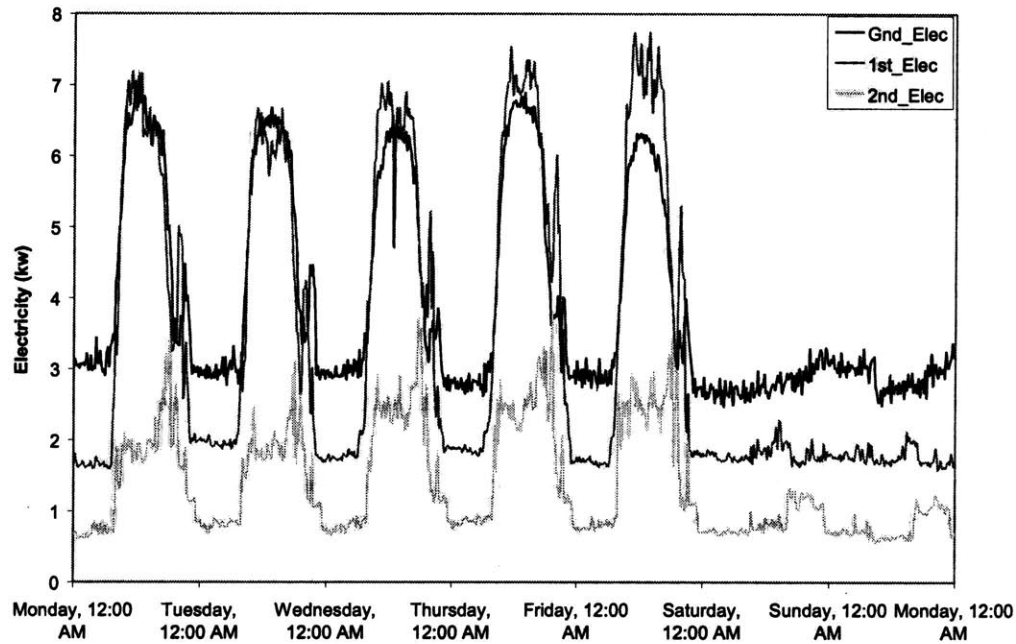


Figure 3-12: Monitored Electricity usage for a week during the validation period

Windows operation

The window operation also follows a regular pattern during the validation period. The upper windows were opened by the building manager in May and left open until October. The lower windows were closed every evening by 6pm and re-opened when occupants arrived starting at 8am. Even during the very hot weather, both sets of windows were open. Although not all the windows were actually open by the occupants, it was estimated that 60% of the windows were open. The occupants used personal fans to try to create a breeze to feel cooler. There were fewer occupants during extremely hot period (e.g. the heat wave on August 6, 2003), as the occupants tried to stay out of the office to keep cool.

On both the North side and the South side of the building, internal blinds are installed hanging from the top frame of the top vent. The blinds have a shading effect, especially when it is in a closed position. Part of the solar radiation will be shaded due to the blinds. There is not a good estimation on this effect. In real operation, people on the South side offices usually close the blinds more than the north side because the South side gets stronger direct solar radiation. In this study, we used a shading coefficient of 0.3 for the north side windows and 0.5 on the south side windows for to

account for the shading effect. Further, when the blinds are closed, they also provide a flow resistance across the upper window. This is also a parameter that is difficult to quantify. In the present study, we did not take it into account in the simulation, which could be a source of uncertainties and errors for the flow predictions.

3.5.3 Simulation results

The validation is run with the modeling details and the setup described above. The average temperatures for each of the three floors (ground, 1st, and 2nd) are compared to the field measurements data.

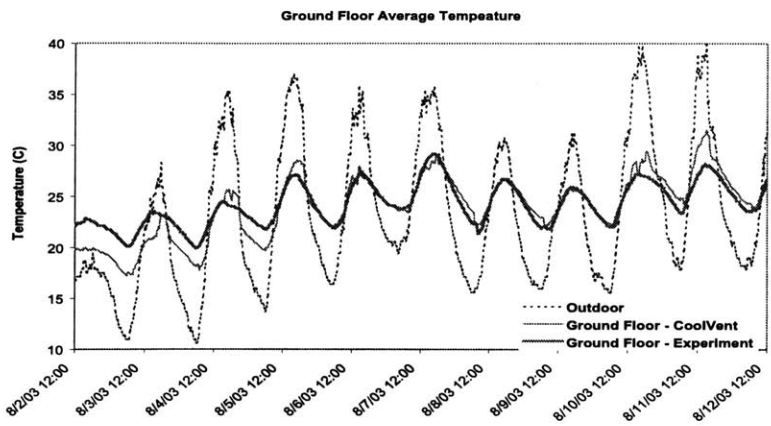
Figure 3-13 shows the simulation results vs. the measured average floor temperatures in the three floors for 10 days from August 2 to August 12. There are some larger discrepancies between predicted and measured data during the initial period (Aug 2 to Aug 4). This is mainly due to the initial thermal mass “warming up” (also described by Mehta [48]) because the simulation starts from a preset initial thermal mass temperature.

The results in Figure 3-13 show a general good agreement between the program predictions and the field measurements, especially for the first and the second floor. For these two floors, the differences between the CoolVent predictions and the field measurements are within ± 1 °C during most of the validation period. Figure 3-14 further shows the histogram of the prediction errors (discrepancies) for the three floors and Table 3.2 summarizes the means and the standard deviations of the errors. The results are reported in a 1.5-minute interval for the period of 10 days. For the ground floor, most of the errors are within ± 1 °C range. For the first floor, the error distribution is slight wider than the result for the ground floor, although most of the errors still fall in the range of ± 1 °C.

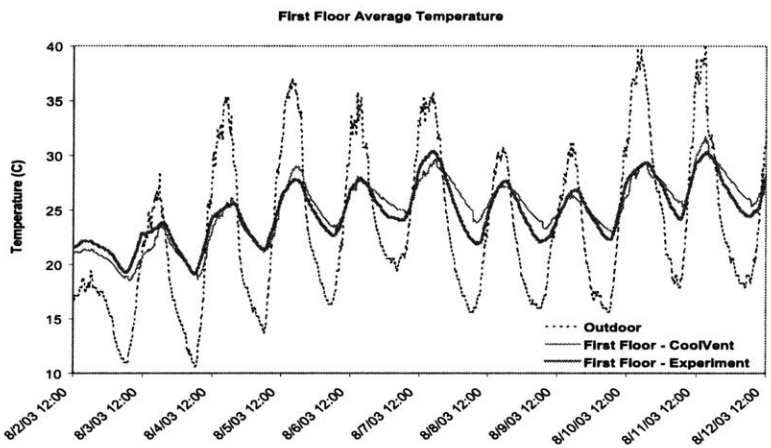
Table 3.2: Summary of the temperature prediction errors for the three floors

Floor	Ground	First	Second
Error Mean (°C)	-0.189	0.183	-0.0799
Error Std Dev (°C)	1.32	0.962	2.15

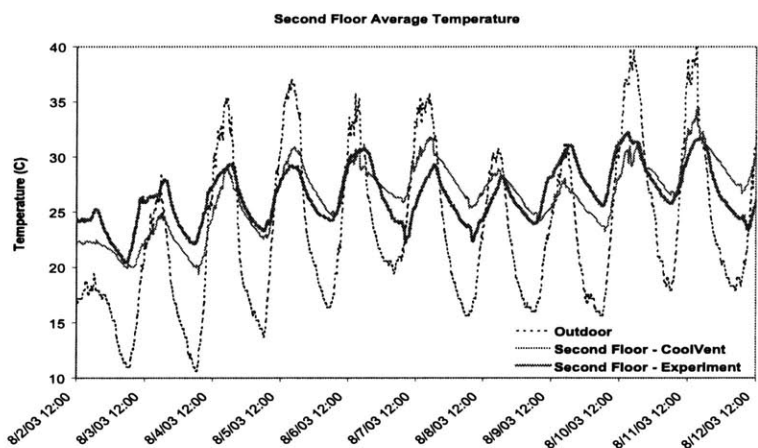
The errors for the second floor prediction have the widest distribution (Figure 3-14). The errors seem not to be centered near 0 but show a symmetric distribution with several major peaks. This means the predictions are sometimes (much) higher than the measured values and sometimes much lower than the measured values. Such a pattern can also be demonstrated in Figure 3-13(c). This large discrepancy is mainly due to the multi-zone models’ general weakness in handling the detailed air distribution inside a strongly stratified Second floor North (the upper-left) office. This weakness has already been discussed in previous validations with CONTAMW (§3.3) and CFD (§3.4.1.1).



(a) Ground Floor



(b) First Floor



(c) Second Floor

Figure 3-13: The floor-average temperatures in Luton building (Aug 2 to Aug 12)

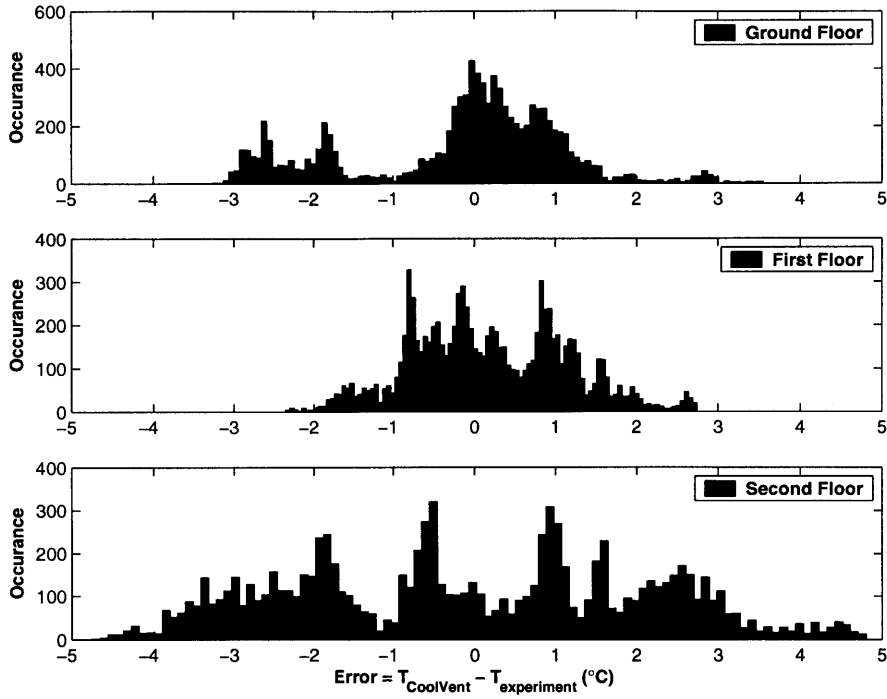


Figure 3-14: Distribution of prediction errors for the three floors

3.5.4 Possible uncertainties

In summary, the simulation and the field measurement data have a reasonable agreement in general. However, some discrepancies exist in the initial period due to the numerical effect of thermal mass “warming up”. Other discrepancies between the prediction and measurement data may be explained the window operations, blind effect, and other building operation details:

Windows operations. The windows in the offices are manually operated by the occupants. Although it is generally true that the windows were open in the working hours by the occupants, in hot days when the outdoor air temperature was relatively high, fewer windows were opened by the occupants during the day. It is, however, difficult to predict the random operations of the occupants when the building is occupied since too many factors may affect their decisions.

Blocking effect of window blinds. Other than the shading of sunlight, the blinds also act as a blockage to the wind flow, especially in the closed position. The blinds can also block the window openings areas and add more resistance for the airflow movement through the window. This will add more uncertainty in the airflow predictions.

Heating system operations. The heating system could be turned on at night in actual building operations when the outdoor air temperatures dropped too low

(e.g. $< 15^{\circ}\text{C}$). To further explain these discrepancies, more information on the building operations during the measurement period needs to be understood.

3.5.5 Summaries

In this section, results from a natural ventilated office building monitored over months were used to validate the accuracy of the CoolVent program. An internal radiation model is developed specially for this building geometry to consider the radiation distributions within the building.

The building monitoring details are reported and the methods to set up the boundary conditions for the simulation are discussed. The simulation results are compared with the monitoring data in terms of the averaged floor temperature for the three building floors.

The simulation and the field measurement data has a general good agreement but some large discrepancies exist in the initial period due to the numerical effect of thermal mass “warming up”. Other discrepancies between the prediction and measurement data were explained the window operations, blind effect, and other building operation details.

3.6 Conclusions

The CoolVent program is tested by three different methods ranging from steady state bulk flow program to transient field measurement. The results shows that the modules in the program are correctly implemented and the model assumptions are reasonable. Although differences exist when the model assumptions are violated, possible reasons for these discrepancies are discussed to provide information on how to compensate the disagreement between the model assumptions and the real conditions. The tests also examined the flexibility (or expandability) of the program to incorporate more complicated models in such as the internal radiation and solar calculation models. With this flexibility, more complicated models can be added to the program to conduct even more advanced simulations in the future.

Part II

Dynamical system analysis of multiple steady states

Chapter 4

Multiple steady states in a single zone natural ventilation system—A dynamical system analysis

Natural ventilation systems may have multiple steady states in the combined buoyancy and wind driven mode in a single space. In this chapter, dynamical system analysis is applied both graphically and quantitatively to investigate the multiple steady state behavior of such a natural ventilation system.

The necessary conditions for the system to have multiple steady states are derived for a single space combined wind and buoyancy driven natural ventilation system. Distinct from previous studies, the derivation comes from the transient dynamical system behaviors of the system rather than from the steady state equations, and it can be applied to more general cases.

Based on the dynamical system analysis, the quantitative relation between the initial temperature and the final steady state is investigated for the single space case. The unstable steady state, which cannot physically exist, is the critical point of the initial value in determining the final (steady) state of the system.

4.1 Introduction

Multiple steady state behavior occurs in many non-linear engineering dynamic systems (e.g., [3, 40]). Such multiple steady state behavior exists in some natural ventilation systems for buildings due to the non-linearity of the natural ventilation system dynamics. Linden [44] investigated a naturally ventilated system with floor heating and stated the possibility of hysteresis on the system when the boundary condition changes gradually. Further experimental studies were conducted by Hunt and Linden [37] both theoretically and experimentally. Li and Delsante [41] investigated a natural ventilation system where wind opposes buoyancy effects as shown in Figure 4-1. They solved the steady state equations that in some instances result in three possible mathematical solutions with the same boundary conditions. Similar results were also obtained by Gladstone and Woods [32] when investigating a naturally ven-

tilated space with a heated floor. Among the three steady states, one is unstable and does not exist in reality while the other two are stable for small scale disturbances. Later, Li et al. [42] demonstrated several more cases in which multiple steady states can exist. Reduced scale experiments was also carried out on a single zone with blocking ventilation to prove the existence of two steady states. Heiselberg et al. [35] conducted both experimental and CFD simulations on the single space natural ventilation and proved the multiple steady states do occur in reality under certain conditions. Livermore and Woods [45] discovered the existence of three steady states in a two-variable buoyancy driven natural ventilation system, among which two are shown to be locally stable and the other is not.

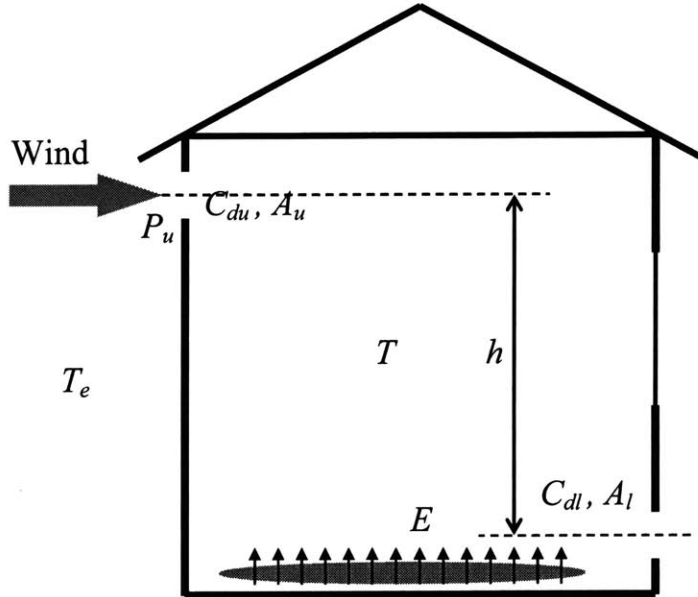


Figure 4-1: Configuration of a single-zone combined buoyancy and wind driven natural ventilation system

An example of multiple steady state systems is the single zone natural ventilation system with opposing buoyancy and wind forces, shown in Figure 4-1. Solving the steady state equations may result in three different mathematical solutions under the same boundary conditions. Among the three steady state solutions, one is mathematically unstable while the other two are stable. The conditions for the multiple steady states to exist were also expressed for a special case where the wall is adiabatic ($UA = 0$) to the outdoor air in a previous study [42]. The initial conditions of the nonlinear system were found important to the final state of the natural ventilation system when different steady states exist (e.g., [35, 42, 44]). For the system shown in Figure 4-1, if the initial room temperature is relatively low, the final steady state of the system will be wind-dominated downward ventilation. If the initial room temperature is relatively high, the final state of the system may be buoyancy-dominated upward ventilation.

However, in the previous studies, only steady state equations were used to derive the conditions for the existence of multiple steady states. These studies, therefore, did not systematically consider the transient dynamics of the system, which are critical to the system's behavior. In this chapter, the transient dynamics of the system are

investigated by a dynamical system method and their applications are demonstrated. For example, the dynamical system analysis can be used as a new method to study necessary conditions for the existence of multiple steady states, which were previously studied by solving steady state equation and can only easily applied to a special $UA = 0$ case. This dynamical system method reflects the underlying governing dynamics and can be conveniently applied to the more general cases of $UA \geq 0$.

More importantly, the dynamical system analysis quantitatively reveals the impact of the system's initial values on its final steady state. The "relatively low" or "relatively high" initial temperature argument about the initial values in the previous studies was a vague assertion, which did not demonstrate how exactly the initial temperature values can determine the final steady state. In this chapter, we find the critical point of the initial temperature values that can determine the final steady state of the system. If the initial temperature is lower than this critical temperature, the system will go to one steady state (wind-dominated downward); if it is higher than the critical temperature, the system will go to another steady state (buoyancy-dominated upward). As will be shown in later sections, this critical temperature point is exactly the unstable steady state of the system, which was generally viewed as of no practical use in previous studies.

In summary, the dynamical system analysis in this chapter will provide explanations on the existing conditions of multiple steady states and the dynamics mechanism of the initial value's impact on the final steady state of the system. The conclusions in this chapter will provide guidelines for the explanations on the multiple steady states phenomena in airflow and thermal models such as multi-zone, zonal, and Computational Fluid Dynamics (CFD) models. Further more, the dynamical system analysis in this chapter also builds the foundations for a further study on the state transitions behaviors between the multiple steady states under "strong" perturbations [77].

4.2 System equations

The basic configuration of a single zone with wind opposing buoyancy is shown in Figure 4-1. Two openings are located at different heights and enable both wind-driven flows introduced by the external wind and buoyancy-driven flows introduced by the heat source. If the wind force is greater than the buoyancy force, the airflow will be wind-dominated and downward. Otherwise, the airflow will be buoyancy-dominated and upward. In this case we assume well-mixed air within the single space and power-law flow relations for the two openings. The thermal mass is assumed to be at the same temperature as the air if any is considered. Applying energy balance and empirical flow equations to the system yields:

Energy balance:

$$Mc_p \frac{dT}{dt} = q \cdot \rho_a c_{pa} \cdot (T_e - T) + UA \cdot (T_e - T) + E. \quad (4.1)$$

Flow component:

$$q = \overline{C_d A} \cdot \sqrt{\left| 2gh\beta \cdot (T - T_e) - 2 \frac{P_w}{\rho_a} \right|}. \quad (4.2)$$

The symbols are defined as follows: M is the total thermal mass (including the air) in kg. t is the time in s. q is the volume flow rate of the air in m³/s. ρ_a is the air density in kg/m³ (assume constant). c_p is the specific heat of the thermal mass (including the air) in J/kg-K. c_{pa} is the specific heat of the air in J/kg K. T is the indoor temperature in K. T_e is the outdoor temperature in K. UA is the total conductance of the enclosure system in W/K. If the enclosure system is adiabatic, $UA = 0$; otherwise, $UA > 0$ in general cases. h is the height difference between the upper and the lower openings in m. g is acceleration of gravity and is assumed to be constant as 9.8 m/s². β is the thermal expansion coefficient of air in 1/K. For ideal gas, $\beta = 1/T$. P_w is the wind pressure difference between the inlet and outlet in Pa. P_w is the wind pressure difference between the two openings and is defined by

$$P_w = P_u - P_l = \frac{1}{2} \rho_a (Cp_u - Cp_l) \cdot v_{ref}^2. \quad (4.3)$$

Here P_u and P_l are the wind pressures (in Pa) at the upper and lower openings; Cp_u and Cp_l are the wind pressure coefficients for the two openings based on the reference velocity v_{ref} (in m/s) for the wind pressure coefficients.

Equation (4.1) describes the dynamics of the air temperature subjected to the external wind and the heat source. The term E in the equation is the sum of all the heat gains by heat transfer processes that are not related to the indoor temperature. For example, one way to express the term was given by Li and Delsante [41] as the sum of the internal heat gain, the direct radiation, and indirect solar gains through the building envelop.

Equation (4.2) describes the airflow rate by the combined interaction of the wind and buoyancy forces using the discharge coefficient expression of the Power-Law relationship. The term $\overline{C_d A}$ is given by

$$\frac{1}{\overline{C_d A}} = \sqrt{\frac{1}{(C_{du} A_u)^2} + \frac{1}{(C_{dl} A_l)^2}}, \quad (4.4)$$

where C_{du} , C_{dl} are the discharge coefficients and A_u and A_l are the areas of the top and bottom openings.

Substituting Equation (4.2) for the flow into Equation (4.1) yields a one dimensional first order differential equation where the indoor air temperature T is the only state variable:

$$\frac{dT}{dt} = f(T - T_e) = \frac{E}{M c_p} - \frac{T - T_e}{M c_p} \cdot \left(\overline{C_d A} \cdot \rho_a c_{pa} \sqrt{\left| 2gh\beta \cdot (T - T_e) - 2 \frac{P_w}{\rho_a} \right|} + UA \right). \quad (4.5)$$

Denote

$$T^* = T - T_e, \quad (4.6)$$

$$P^* = \frac{P_w}{\rho_a}, \quad (4.7)$$

$$T^{**} = \beta T^* = \beta(T - T_e), \quad (4.8)$$

$$P^{**} = \frac{P^*}{gh} = \frac{P_w}{\rho_a gh}, \quad (4.9)$$

where T^{**} and P^{**} become dimensionless.

T^{**} and P^{**} are dimensionless. The governing equation (4.5) can also be written as follows using the * or ** parameters:

$$f(T^*) = \frac{dT^*}{dt} = \frac{E}{Mc_p} - \frac{T^*}{Mc_p} \cdot \left(\overline{C_d A} \cdot \rho_a c_{pa} \sqrt{|2gh\beta \cdot T^* - 2P^*|} + UA \right), \quad (4.10)$$

or

$$f(T^{**}) = \frac{dT^{**}}{dt} = \frac{E}{Mc_p} - \frac{T^{**}}{Mc_p} \cdot \left(\overline{C_d A} \cdot \rho_a c_{pa} \cdot \sqrt{2gh} \cdot \sqrt{|T^{**} - P^{**}|} + UA \right). \quad (4.11)$$

4.3 System characteristics and solution behaviors

$f(T^{**})$ in Equation (4.11) is the derivative of T^{**} over time. It is a continuous function plotted in Figure 4-2. Two cases are included in the Figure: the special case of $UA = 0$, which is represented by the thick dashed curve; and the general case of $UA > 0$, which is represented by the thick solid curve. We will focus on the general case of $UA > 0$ in most part of the study. The curve stands for all the possible dynamical states (either transient or steady) that the system can undergo for a specific set of geometric and environmental parameters that appear in Equations (4.5), 4.10 or (4.11).

There are two special points on the system curve shown in Figure 4-2. The first one is point A denoted in Figure 4-2. At this point, the first derivative of the curve is not continuous. Physically, the wind pressure force and the buoyancy force are equal and the system flow rate q is zero at this point. On the left of point A, the system ventilation pattern is wind-dominated downward ventilation; on the right, the pattern is buoyancy-dominated upward ventilation. The values of T^{**} and $f(T^{**})$ at point A can be found as

$$T_A^{**} = P^{**} = \frac{P^*}{gh}, \quad (4.12)$$

and

$$f(T_A^{**}) = \frac{\beta E}{Mc_p} - \frac{P^{**} \cdot UA}{Mc_p}. \quad (4.13)$$

The other special point on the curve is the local minimum point B of the left section. At this point, the first order derivative of $f(T^{**})$ with respect to T^{**} equals

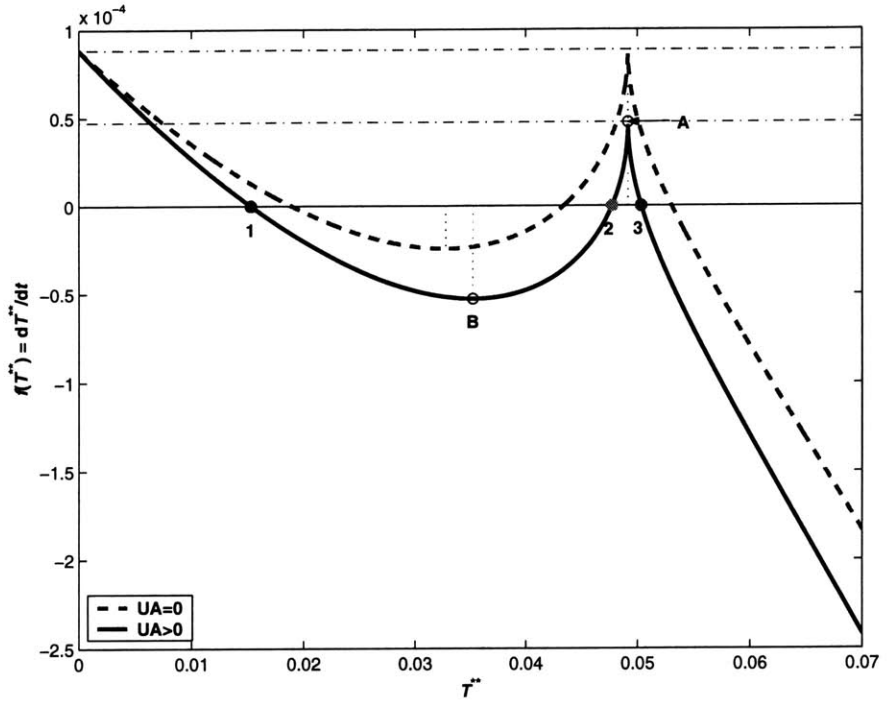


Figure 4-2: Dynamics behavior of the system: $f(T^{**}) = dT^{**}/dt$ vs. T^{**} for $UA > 0$ (solid line) and $UA = 0$ (dashed line)

zero. The corresponding T^{**} and $f(T^{**})$ for this point are:

$$T_B^{**} = P^{**} - \left(\frac{\sqrt{X^2 + 3P^{**}} - X}{3} \right)^2, \quad (4.14)$$

and

$$f(T_B^{**}) = \frac{\beta E}{Mc_p} - \frac{T_B^{**}}{Mc_p} \cdot \left(\overline{C_d A} \cdot \rho_a c_{pa} \cdot \sqrt{2gh} \sqrt{P^{**} - T_B^{**}} + UA \right), \quad (4.15)$$

where

$$X = \frac{UA}{\overline{C_d A} \cdot \rho_a c_{pa} \cdot \sqrt{2gh}}. \quad (4.16)$$

The expressions in Equations (4.14) – (4.16) are composed of known parameters and T_B^{**} can therefore be easily calculated. In the special case when $UA = 0$ (which leads to $X = 0$), Equations (4.14) and (4.15) can be simplified as

$$T_B^{**} = \frac{2}{3} P^{**}, \quad (4.17)$$

and

$$f(T_B^{**}) = \frac{\beta E}{Mc_p} - \overline{C_d A} \cdot \left(\frac{2}{3} P^{**} \right)^{\frac{3}{2}} \cdot (gh)^{\frac{1}{2}} \cdot \frac{\rho_a c_{pa}}{Mc_p}. \quad (4.18)$$

Equation (4.14) shows that when $X \rightarrow 0$, $T_B^{**} \rightarrow \frac{2}{3}P^{**}$, and when $X \rightarrow \infty$, $T_B^{**} \rightarrow P^{**}$. Therefore, the system always has a local minimum point T_B^{**} residing between $\frac{2}{3}P^{**}$ and P^{**} for any positive value of X , which is proportional to the UA value according to Equation (4.16).

The solid curve shown in Figure 4-2 has three points (denoted as 1, 2 and 3 in the figure) that intersect the x-axis, which are the steady states of the system where dT^{**}/dt equals to 0. Physically, the system gains an energy balance at these three points. At other points where there is not an energy balance, the temperature will change over time. Therefore the system is not in steady state at either point A or B because the derivative of the temperature (vertical axis value in Figure 4-2) is generally not zero there. For example, at point A, the buoyancy force is equal to the wind force and there is no flow. Therefore the system temperature will rise due to the heat source E , which makes the buoyancy force overwhelm the wind force and induces airflow again.

The three steady states (or roots) correspond to two distinct types of ventilation patterns. Steady states 1 and 2 reside on the left of point A and correspond to the wind-dominated downward flow pattern; Steady state 3 resides on the right of A and corresponds to the buoyancy-dominated upward flow pattern. However, states 1 and 3 are mathematically stable but state 2 is unstable to infinitesimal perturbations. This can be quickly demonstrated by inspecting Figure 4-2. Starting from state 1, if the system temperature T^{**} is perturbed a little bit off from its steady state value, it can still move back to T_{ss1}^{**} when the disturbance is gone because the derivative of T^{**} over time (i.e., $f(T^{**})$) acts against the change of T^{**} . For example, when T^{**} increases a little bit from root 1, $f(T^{**})$ becomes negative. T^{**} will decrease until it returns to T_{ss1}^{**} . Therefore, the system is able to resist small perturbation in the vicinity of state 1. This is also true in the vicinity of root 3. However, near steady state 2, the system is unstable because $f(T^{**})$ facilitates the temperature divergence from T_{ss2}^{**} under any infinitesimal perturbation. No matter how small the system temperature changes from T_{ss2}^{**} , this offset will always be immediately magnified until the system gains stable equilibrium again at either state 1 or state 3. Therefore, steady state 2 is unstable and cannot be observed in a real dynamical system because the system will always switch to one of the stable states.

The stability of the three steady states can also be physically explained by following the behavior of the flow rate through the building. The signed net flow rate \hat{q} is shown in Figure 4-3, as a function of the interior air temperature. The upward buoyancy-dominated direction is defined as positive and the downward direction is defined as negative. Around root 1, the flow is wind-dominated downward. If the system temperature increases above T_{ss1} , the flow rate decreases slowly but the term, $-|\hat{q}|(T - T_e)$ in Equation (4.1) increases in magnitude; there is larger energy loss from the building and its temperature decreases back toward T_{ss1} . In contrast at root 2, the flow rate decreases drastically with a small increase in temperature. In this case,

if the temperature increases slightly, the magnitude of the convective term decreases, causing the interior temperature to continue to rise and move further away from T_{ss2} . Finally, at the buoyancy-dominated steady state root 3, the flow rate increases as the system temperature increases. Thus, with a temperature increase above T_{ss3} , the magnitude of the convective term, $-|\hat{q}|(T - T_e)$ again increases causing the system temperature to return towards T_{ss3} .

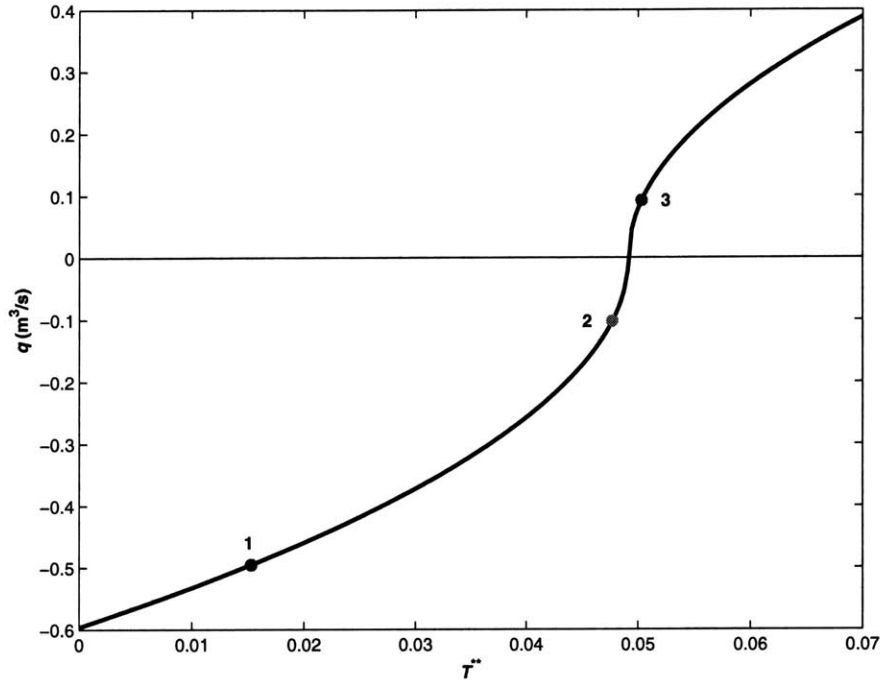


Figure 4-3: The flow rate q vs. dimensionless zone temperature T^{**} ($q > 0$ stands for upward buoyancy-dominated flow)

The temperatures of the three steady states can be obtained analytically. However, it is not necessary to know their explicit mathematical expressions in the present analysis. With a simple computer algorithm (e.g. bisectional search), the values of the three steady state roots can be easily calculated. Therefore, the temperature value of steady states 1, 2, and 3 are simply denoted by T_{ss1} , T_{ss2} , and T_{ss3} instead of their complete analytical expressions. The five points: point A, point B, and roots 1, 2, 3 will be used in the following sections to derive the conditions for multiple steady states to exist and the initial conditions for different steady states to be achieved.

4.4 Conditions for the system to have multiple steady states

In this section, the boundary conditions requirement for the system to achieve multiple steady states is presented from the analysis of the dynamical system characteristics of

the system. This method is different from the steady state equation solving method used in previous studies and it can be applied to more general cases of $UA \geq 0$.

4.4.1 General cases of $UA \geq 0$

A major concern for designers is the conditions in which the multiple steady states can exist, in order to avoid or take advantage of these multiple solutions in building design. These conditions can be derived by checking the positions of points A and B. Since points A and B are in the same smooth curve and B is the local minimum of the curve, the relationship $f(T_A^{**}) \geq f(T_B^{**})$ is automatically guaranteed.

From Figure 4-4, a general system shown in Figure 4-2 can have one of the three possible scenarios on its steady states:

- If $f(T_B^{**}) \geq 0$, then $f(T_A^{**}) \geq 0$. The system can have only one steady state solution corresponding to buoyancy-dominated upward ventilation pattern. This scenario is shown as the top curve in Figure 4-4.
- If $f(T_A^{**}) \leq 0$, then $f(T_B^{**}) \leq 0$. The system can have only one steady state solution corresponding to wind-dominated downward ventilation pattern, which is shown as the bottom curve in Figure 4-4.
- If $f(T_A^{**}) \geq 0$ and $f(T_B^{**}) \leq 0$ are simultaneously satisfied, the system can have three steady states, shown as the middle curve in Figure 4-4.

Therefore, in order to have multiple steady states, the system has to satisfy the following conditions:

$$f(T_A^{**}) \geq 0 \text{ and } f(T_B^{**}) \leq 0. \quad (4.19)$$

Substituting Equations (4.12) and (4.14) into Equation (4.19), we get the following expression:

$$P^{**} \cdot UA \leq \beta E \leq T_B^{**} \cdot \left(\overline{C_d A} \cdot \rho_a c_{pa} \cdot \sqrt{2gh} \cdot \sqrt{P^{**} - T_B^{**}} + UA \right), \quad (4.20)$$

where T_B^{**} is given by Equations (4.14) and (4.16).

Equation (4.19) or (4.20) describes the conditions for the system to have multiple steady states. As shown in Figure 4-4, if the term βE is smaller than the value of $P^{**} \cdot UA$, the system will have only one steady state on the left of point A (and B), which indicates the final steady state flow can only be downward and wind-dominated. If βE is greater than the value of $T_B^{**} \cdot (\overline{C_d A} \cdot \rho_a c_{pa} \cdot \sqrt{2gh} \cdot \sqrt{P^{**} - T_B^{**}} + UA)$, the system will have only one steady state on the right of point B, which indicates the final steady state flow can only be upward and buoyancy-dominated.

4.4.2 Special case of $UA=0$

For an ideally insulated building, the heat conduction through the enclosure may not be significant compared to the advection and heat source gain. Therefore, the

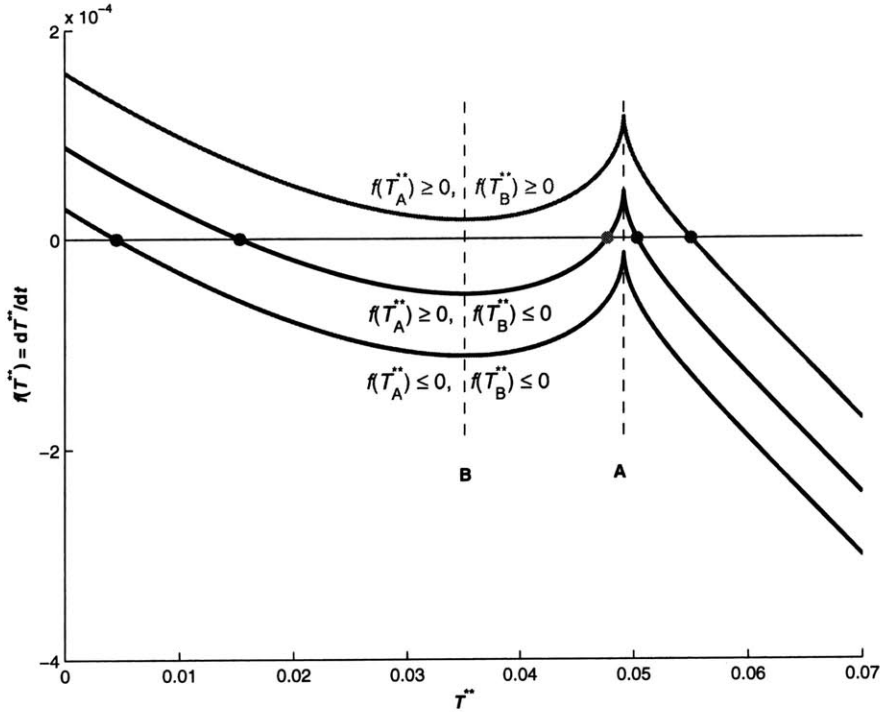


Figure 4-4: Three possible scenarios of the steady state solutions of the system

necessary condition given by Equation (4.20) can be further simplified by assuming $UA = 0$. The system curve is shown as the dashed curve in Figure 4-2. In this case,

$T_A^{**} = P^{**}$ and $T_B^{**} = \frac{2}{3}P^{**}$. The necessary condition for multiple steady states described in Equation (4.20) can be simplified as

$$0 \leq \beta E \leq \overline{C_d A} \cdot \rho_a c_{pa} \cdot \left(\frac{2}{3}P^{**}\right)^{\frac{3}{2}} \cdot \sqrt{gh}. \quad (4.21)$$

The left half of Equation (4.21) is automatically satisfied when $E \geq 0$, which is generally true, except when there is a cooling source that exceeds the internal heat gain. For the right half, it can be formulated as a ratio:

$$r = \frac{\beta E}{\overline{C_d A} \cdot \rho_a c_{pa} \cdot \left(\frac{2}{3}P^{**}\right)^{\frac{3}{2}} \cdot (gh)^{\frac{1}{2}}} \leq 1. \quad (4.22)$$

Therefore the necessary condition can be written as $0 \leq r \leq 1$ for the system to have multiple steady states in the special $UA = 0$ case. This result is identical to the results found by Li and Delsante [41] for the $UA = 0$ case by solving the steady state equation. In the original study [41] a variable that is identical to $\sqrt[3]{r}$ was used to describe the conditions for the steady state equation to have three solutions. However, the general cases of $UA > 0$ were not quantitatively solved with an explicit formula in that study. In this chapter, the conditions for the general cases ($UA >$

0) can be quantitatively presented by Equation (4.19) or (4.20) using the dynamical system analysis.

4.4.3 Graphical representation

Reorganizing Equation (4.22), we can get the following expression:

$$r = \frac{\frac{\beta E \cdot gh}{\rho_a c_{pa}}}{\overline{C_d A} \cdot \left(\frac{2}{3} P^*\right)^{\frac{3}{2}}} = \frac{\frac{\beta E \cdot gh}{\rho_a c_{pa}}}{\overline{C_d A} \cdot \left(\frac{1}{3}\right)^{\frac{3}{2}} (C_{pu} - C_{pl})^{\frac{3}{2}} \cdot v_{ref}^3}. \quad (4.23)$$

The two variables: $\frac{\beta E \cdot gh}{\rho_a c_{pa}}$ and $\overline{C_d A} \cdot \left(\frac{1}{3}\right)^{\frac{3}{2}} (C_{pu} - C_{pl})^{\frac{3}{2}} \cdot v_{ref}^3$ are proportional to the strength of the buoyancy force and wind force, respectively. Figure 4-5 shows the relation between the two variables for different UA values. For each UA value, there are two “demarcation” lines that are the critical conditions of multiple steady states in Equation (4.20) (or (4.21) for the $UA = 0$ case). The bounded region by the two “demarcation” lines is the multiple-solution region where the system can have three mathematical steady states. Above that bounded region, the system has only one buoyancy-dominated steady state. Below the region, the system has only one wind-dominated steady state.

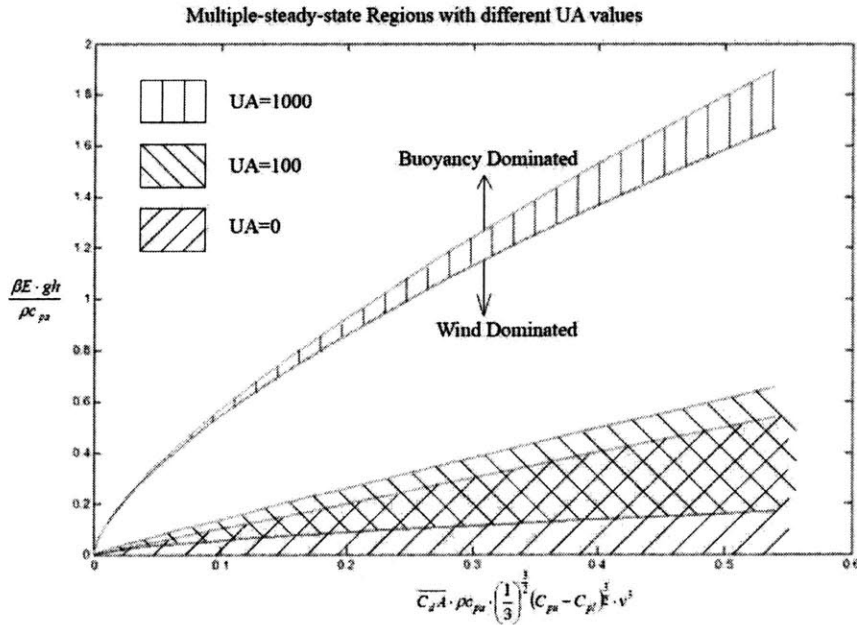


Figure 4-5: Multiple steady states regions for different UAs

Since the UA value also influences the multiple-solution region according to Equation (4.20), Figure 4-5 shows the regions for three different UA values. For $UA = 0$ case, the boundary are two linear boundaries. When UA increases (corresponding to $UA = 100W/K$ in this example), the boundaries become curved and approach each

other. The region for wind-dominated solution will expand. If UA increases even higher (to 1000 W/K), the boundaries are more non-linear; the multiple-solution region becomes very small as the wind-dominated solution region gets wider. Therefore, as UA value increases, the multiple-solution behavior will become less possible and the wind-dominated (downward flow) steady state will be more likely (if the outdoor conditions are random) to happen.

4.5 Critical point of the initial temperature

This section presents the mechanism of how exactly the initial temperature value determines the final steady state of the system. In this single zone system, the final steady state of the system is determined by the initial temperature of the system if multiple steady states exist. By examining the transient behaviors of the system through the dynamical system equations, a critical point for initial temperature is determined.

4.5.1 Theoretical critical point

When the conditions in Equation (4.19) or (4.20) are satisfied, three steady state solutions can be found mathematically by solving the steady state equations. Starting from an initial condition (temperature), the system will go to one of the steady states (roots 1 and 3) if a fixed boundary condition is given. However, the unstable steady state root 2 cannot be observed as a steady state in an actual system since it cannot survive infinitesimal perturbations. In a previous section (see §4.3) it was briefly demonstrated that the system will move toward either root 1 or root 3 from the unstable root 2. This implies that root 2 will be an important point in determining how the system reaches different steady states when multiple ones are possible.

Indeed, steady state 2 is the critical point in determining the final state of the system when an initial value of the temperature is given. At an initial state where the system has not gained equilibrium, if the initial system temperature is below T_{ss2} , the system will move toward root 1 since dT/dt is negative at the initial point (according to Figure 4-2). In the interval of (T_{ss1}, T_{ss2}) , the dT/dt is always negative and the system temperature T continues to decrease until it reaches T_{ss1} . This is true even if the system starts from an initial temperature below T_{ss1} . The system will finally reach root 1 as well because dT/dt maintains positive and makes the system temperature increases until it reaches T_{ss1} . Therefore, as long as the system starts from an initial temperature lower than T_{ss2} (root 2), the final steady state will be state 1. On the other hand, similar analysis can be applied to root 3 and we can conclude that the final steady state of the system will be state 3 if the system starts from an initial temperature higher than T_{ss2} .

Therefore, we have found a way of determining the final steady state and airflow pattern of the system at by examining the relation between the initial temperature T_0 and the unstable steady state temperature T_{ss2} . If the initial temperature T_0 is lower than T_{ss2} , the system will reach the steady state point 1 (T_{ss1}). The airflow

pattern will be wind-dominated downward. On the other hand, if the system starts from an initial temperature higher than T_{ss2} , it will finally reach the steady state 3. The airflow pattern will be buoyancy-dominated upward. The value of the critical temperature T_{ss2} can be easily obtained through a simple computer algorithm, as was discussed in Section §4.3.

4.5.2 Practical point of view on the initial conditions

According to the previous subsection (§4.5.1), in order to achieve the buoyancy-dominated steady state, the temperature of the space at some point has to be higher than the unstable steady state temperature T_{ss2} . In reality, if the unstable steady state of the system is at a very high temperature which is not likely to happen naturally (say, 40 °C), the system temperature will never increase over that critical point to achieve an even hotter buoyancy-dominated steady state. In this scenario, the system will practically have only one steady state, which corresponds to a wind-dominated downward flow pattern.

To demonstrate the scenario described above from a practical point of view, we will do a rough estimation the temperature of the system required to achieve buoyancy-dominated flow. According to Figure 4-2, the unstable steady state T_{ss2}^{**} will always reside between T_B^{**} and T_A^{**} . Therefore the relation $T_B^{**} \leq T_{ss2}^{**} \leq T_A^{**}$ will always hold if a real T_{ss2}^{**} exists. According to Equations (4.14), T_B^{**} is between $\frac{2}{3}P^{**}$ and P^{**} for all cases. Therefore, T_{ss2}^{**} is always greater than $\frac{2}{3}P^{**}$ (if a real T_{ss2}^{**} exists). Based on this relation, we can estimate a lower bound of T_{ss2}^{**} for the buoyancy-dominated steady state using the following expression:

$$\beta(T_{ss2} - T_e) \geq \frac{2}{3} \frac{P^*}{gh}. \quad (4.24)$$

Substituting $\beta \approx 1/T_e$ for β and Equations (4.3) and (4.9) for P^* into Equation (4.24), we obtain

$$T_{ss2} - T_e \geq \frac{T_e}{3} \frac{v_{ref}^2 (Cp_u - Cp_l)}{gh}. \quad (4.25)$$

For typical buildings, the value $Cp_u \approx 0.6 - 0.7$ and $Cp_l \approx -0.3$ to -0.4 can be used for an estimation (ASHRAE [6]). With $T_e = 280 - 300\text{K}$, a typical wind speed $v_{ref} = 3\text{m/s}$, and a typical room height $h = 3\text{m}$, the inside air temperature must exceeds the outside temperature by at least 30 °C in order to have an initial value for the buoyancy-dominated flow according to the estimation of Equation (4.19). This is very unlikely to occur naturally during moderate weather conditions unless the wind speed is well below 3m/s. The space is most likely to have only one wind-dominated steady state with the preset parameters.

The estimation from Equation (4.25) provides a lower bound for the minimum initial temperature the system should achieve in order to reach the buoyancy driven steady state if multiple-solution conditions are met. The lower bound estimated this way is independent of other parameters such as wall conductance (UA), opening discharge coefficients (C_d), opening areas (A), and heat source strength (E).

According to Equation (4.25), the most influential parameters on the lower bound of T_{ss2} is v_{ref}^2/h . As v_{ref}^2/h becomes smaller, the buoyancy-dominated steady state is easier to achieve. For example, in the above case, if $h = 10$ m, buoyancy-dominated flow can occur when the initial system temperature is at least 9 °C above the ambient.

The exact value of $T_{ss2} - T_e$ can be found for a given set of parameters of C_d , A , h , and E . The actual $T_{ss2} - T_e$ values are plotted in Figure 4-6 as a function of v_{ref}^2/h . The dashed line is the estimation made by Equation (4.25), which serves as a lower bound for $T_{ss2} - T_e$ (or $T_{ss2}^*; T_{ss2}^{**}$). The solid lines are the T_{ss2}^{**} values for three cases from the bottom to the top, respectively: $UA = 0$, UA = a finite value, and $UA \rightarrow \infty$. The top solid line (for $UA \rightarrow \infty$) is linear and has the slope exactly $\frac{3}{2}$ times of that of the dash line below. It can be seen that as UA increases, it is harder to achieve buoyancy-dominated solutions. However, UA plays a minor role at high value of v_{ref}^2/h . When v_{ref}^2/h exceeds about 1.5 m/s², buoyancy-dominated flow will require unrealistically high interior temperature (as initial value).

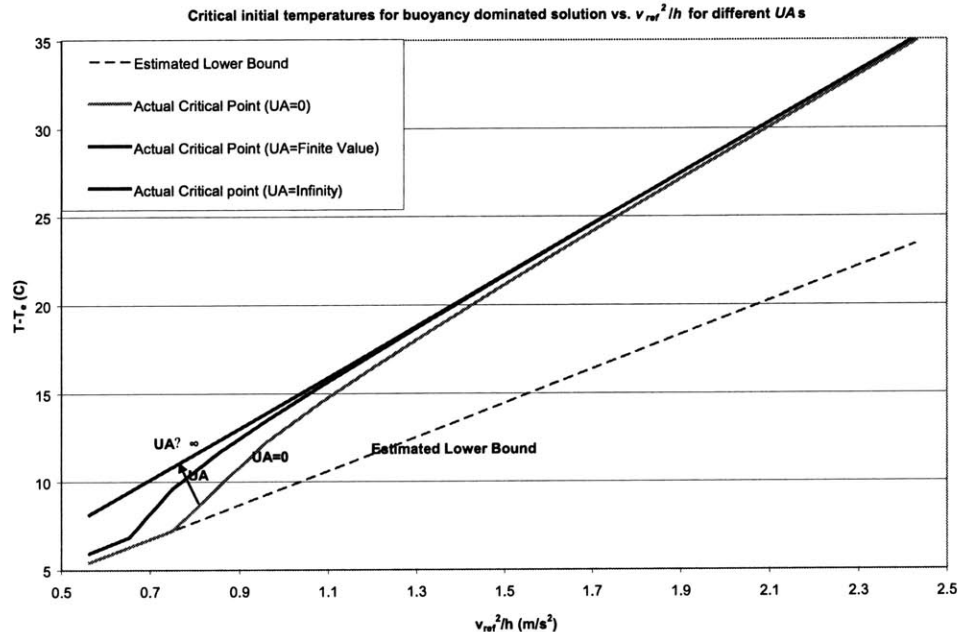


Figure 4-6: Buoyancy dominate conditions for different UA values

4.6 Discussions and potential applications

In this chapter, the mathematical models are built on the assumption of full mixing within a single space. The critical point may be different if stratification inside the room is considered. However, the unstable steady state solution can still provide a useful estimation on whether the steady state will be buoyancy or wind-dominated.

The dynamical system analysis of the multiple steady states behaviors can be

helpful to both the ventilation designers and the control engineers. In reality, due to the varying initial conditions in actual systems, the desired ventilation pattern may not be achieved under design condition due to the initial temperature in the multiple-solution region. To be trouble free, the designers may want to avoid the multiple steady state regions in their natural ventilation designs. Therefore, understanding the conditions for the multiple steady states to exist will potentially help the designer to avoid such multiple-solution regions.

On the other hand, for control engineers, knowledge of multiple-solution behavior may help them to take advantage of the multiple steady states phenomenon in ventilation controls. For example, if the system is in the multiple-solution region, one can change the initial conditions of the room to direct it toward another steady state ventilation mode. During the summer, switching from the hotter buoyancy-dominated steady state to the cooler wind-dominated steady state might be more desirable. To achieve the pattern change, a fan or a cooling source can be applied for a short while until the room temperature has reduced below the critical point. The magnitude and the time required for such a change are the subject of Chapter 7.

4.7 Conclusions

A single zone with combined wind and buoyancy driven natural ventilation can exhibit three steady states when certain conditions are satisfied. Among the three steady states (roots), two of the steady states are mathematically stable, while the other steady state is unstable even to infinitesimal disturbances. The conditions can be graphically and quantitatively derived by the relative positions of two special points on the dynamic system curve. When the system has three steady states (roots), two of them are mathematically stable, while the other is unstable even to infinitesimal disturbances.

The unstable steady state point is a critical point in determining the final (steady) state of the multiple steady state system. When the system initial temperature is lower than this unstable steady state temperature, the final steady state of the system will be in the wind-dominated downward flow pattern; when the initial temperature is higher than this unstable steady state temperature, the final steady state of the system will be in the buoyancy-dominated upward flow pattern. Based on this initial condition criteria and the realistic indoor temperature range, simpler criteria can also be used to determine the minimum interior temperature required to achieve buoyancy-dominated steady state flow.

The dynamical system method used in this study is important to building airflow simulations, natural ventilation designs, and ventilation control strategies. For example, it enables the designers to avoid the complexities of multiple solutions as much as possible by carefully choosing relevant parameters. More importantly, as a positive application, ventilation control strategies may be developed to switch the system from one (undesirable) steady state to another (desirable) steady state by altering the initial values of the system.

Chapter 5

Multiple steady states in a single-zone natural ventilation system with thermal mass—Dynamical system analysis

In this chapter, a mathematical model is developed to investigate the nonlinear dynamics behavior of a natural ventilation system with thermal mass. The impact of thermal mass on the multiple steady states is quantitatively investigated by a dynamical system method. Thermal mass is shown to have no effect on some static characteristics on the systems, for example, the values of the steady states, the conditions for multiple steady states to exist, and the solution bifurcation procedures. However, the thermal mass can have significant impacts on the dynamical behaviors of the system, for example, how the system reaches different steady states starting from different initial values. Nevertheless, the systems with mass and without mass have an intrinsic connection in the local stability properties of the steady states. The stabilities of steady states, which are determined by the eigenvalues of the linearized system around the steady states, were found to share a common pattern regardless of the thermal mass parameters. A further study on the impact of thermal mass on the system's nonlinear behaviors will be provided in Chapter 6.

5.1 Introduction

Multiple steady state behavior occurs in many natural ventilation systems. For example, Chen and Jiang [21] summarized the experiences in room airflow CFD simulations and found it was difficult to deal with cases with multiple solutions. In such cases, a typical observation was that the solutions jumped between different steady states as the iterations went on. Linden [44] investigated a naturally ventilated system with floor heating and reported the hysteresis in the system when the boundary condition changes gradually in experiments.

Past studies on the multiple steady state phenomena have mainly targeted the

behaviors of the fluid (air), with a general practice of solving either the steady-state or transient equations of the air energy balance. For example, Li and Delsante [41] investigated the single-zone natural ventilation system where wind opposes the buoyancy force (similar to the system in [44]), by assuming full-mixing in the space. They showed that the steady state equations may yield three possible solutions under the same boundary conditions. Later, Livermore and Woods [45] demonstrated the possible existence of three steady states in a two-variable natural ventilation system. The (local) stabilities of system at these steady states were investigated by the eigenvalues of the linearized system. More recently, a dynamical system method was used by Yuan and Glicksman ([70, 74]) to investigate the nonlinear behaviors of a single-zone natural ventilation system similar to that in [41, 44]. The mechanism of how the system reaches different steady states was explained by its dynamical system characteristics. Similar dynamical system methods were applied in a two-zone building by Yang et al. [67], where different airflow bifurcation phenomena were discussed in detail.

In all the previous studies, however, the thermal mass in buildings was either not considered or assumed to have the same temperature as the air. This is generally not true: the mass is generally much slower in responding to boundary condition changes than the air, due to the larger heat capacity of the mass. Therefore, significant convective heat transfer can occur between the air and the thermal mass (such as the wall, the floor, the ceiling, or even the furniture), especially in buildings that actively use thermal mass for night cooling. In this scenario, the heat transfer between the air and the thermal mass may substantially affect the transient behaviors of the system. For example, the air temperature rise due to the heat transfer from the thermal mass will affect the buoyancy force in the system. Since the transient behavior of a system is critically important to the multiple steady state phenomena, it is necessary to adequately consider the influence of the thermal mass in investigating the multiple steady state behaviors in building ventilation systems.

In this study, a mathematical model is developed to incorporate thermal mass into a combined wind and buoyancy-driven natural ventilation system that may have multiple steady states. The interactions between the air and the thermal mass are investigated using a dynamical system approach. Based on the governing dynamics, several important issues related to the multiple steady states will be addressed, for example, the conditions for the existence of multiple steady states and the influences of the initial values on the final steady states. We will also generalize the local stabilities of the steady states and develop an effective computational technique based on the characteristics of linearized systems around these steady states. Throughout the study, systems with and without thermal mass will be compared and their similarities and differences in multiple steady state behavior will be discussed.

In Chapter 6, the quantitative impact on the dynamics of the thermal mass will be further investigated. A dynamical system analysis will be used to explain more physical phenomena in the system with thermal mass. These two studies will also serve as the foundation of Chapter 8, which presents the state transition dynamics between the multiple steady states in a system with thermal mass. For a system without thermal mass, such state transition dynamics were investigated in a previous

study (Yuan and Glicksman [77]) that showed their importance in determining the actual stabilities of the locally stable steady states. With the presence of thermal mass, the state transitions within the system can be very different from those within a system without thermal mass.

5.2 Mathematical Models

Figure 5-1 shows the configurations of the system to be investigated. It is the same building investigated in some previous studies (e.g., [41, 44, 70, 74, 77]), except that thermal mass is now included in the present study. A subtle notational difference is that in several of the previous studies ([70, 74, 77]), the height difference between the upper and the lower openings was denoted by lower-case h ; while in the present study this height difference is denoted by capital H since the lower-case h is used for heat transfer coefficient.

In the single-zone building shown in Figure 5-1, two openings are located at different heights and enable both wind-driven flow introduced by the external wind that opposes buoyancy-driven flow introduced by the heat source. If the wind force is greater than the buoyancy force, the airflow will be wind dominated and downward. If the buoyancy force is greater than the wind force, the airflow will be buoyancy dominated and upward. Major assumptions for the mathematical model are:

- the air is well-mixed;
- the two openings follow power-law flow relations;
- the thermal mass only exchanges heat with the indoor air;
- the thermal mass is assumed to be at a lumped uniform temperature.

5.2.1 Governing equations

The mathematical model is built on a combination of several previous models (e.g., van der Mass and Roulet [60] for the air-mass interaction; and Li and Delsante [41] for airflow) with minor revisions. The following differential equations are applied to describe the temperature dynamics in the system:

For the air:

$$M_a c_a \frac{dT_a}{dt} = E - \rho_a c_a q(T_a - T_e) - UA(T_a - T_e) - hA_m(T_a - T_m). \quad (5.1)$$

For the thermal mass:

$$M_m c_m \frac{dT_m}{dt} = -hA_m(T_m - T_a). \quad (5.2)$$

In the above equations, T_a and T_m are the state variables of the system (which are shown in bold face font in Figure 5-1). Two equations are coupled through the heat transfer term $hA_m(T_a - T_m)$ between the air and the thermal mass. The heat transfer

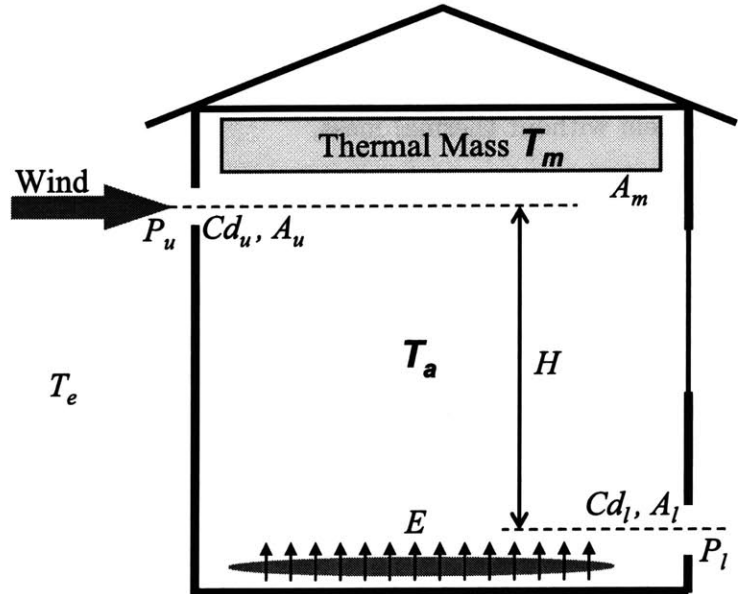


Figure 5-1: Configurations of a single-zone natural ventilation system with thermal mass

coefficient h in is the (effective) convection heat transfer coefficient between the air and the thermal mass. Here we also assumed a heat transfer term $UA(T_a - T_e)$ between the interior and outdoor air through the building enclosures, where UA stands for the conductance of the enclosure.

The volumetric flow rate q in Equations (5.1) is the airflow rate under the combined wind and buoyancy (heat source) forces, which can be obtained modeled by

$$q = \overline{C_d A} \sqrt{|2gH\beta(T_a - T_e) - 2P_w/\rho_a|}, \quad (5.3)$$

where β is the thermal expansion coefficient of the air. For ideal gas, β can be approximated as $1/T$. In this study, we used a constant $\beta = 1/T_e$. P_w is wind pressure difference between the inlet and outlet defined as

$$P_w = P_u - P_l = \frac{1}{2}\rho_a v_{ref}^2 \cdot (Cp_u - Cp_l), \quad (5.4)$$

where Cp_u and Cp_l are the Wind Pressure Coefficients (WPC) for the two openings, and v_{ref} is the reference wind velocity for the WPC.

In Equation (5.3), we assumed an empirical power-law relation using the discharge coefficient. $\overline{C_d A}$ is the effective product of the discharge coefficients and the areas of the two openings in m^2 , which is defined as

$$\frac{1}{\overline{C_d A}} = \sqrt{\frac{1}{(C_{du}A_u)^2} + \frac{1}{(C_{dl}A_l)^2} + \frac{1}{(C_{di}A_i)^2}}, \quad (5.5)$$

where C_{du} , C_{dl} are the discharge coefficients for the top and bottom openings respectively, and A_u and A_l are the areas of these two openings. Rigorously, an effective internal flow resistance term described by resistance C_{di} and A_i is also included in

Equation (5.5). However, this internal resistance term is usually small (since A_i is large) compared to those of the two actual openings so that it can be neglected in the single-zone configuration shown in Figure 5-1.

As a specific example in this study, we assigned some typical numerical values to the above parameters (except the state variables T_a and T_m) to hypothetically configure a $10\text{m} \times 10\text{m} \times 6\text{m}$ single space (i.e., total volume $V = 600 \text{ m}^3$, floor area = 100 m^2). The height difference H between the upper and the lower windows is set to 5 m and an effective $\overline{C_dA}$ of 0.35 m^2 is used for airflow calculation. The wind velocity is set to 2.2 m/s and the difference in the wind pressure coefficients for windward and leeward sides is set to 1. The heat source E is assumed to be 5000 W based on a per square meter strength of 50 W/m^2 . The outdoor air temperature T_e is set to 10°C . We also set the total enclosure conductance UA as 60 W/K . We also define a base case where the thermal mass is a 2.5 cm thick concrete slab with a density of $2,500 \text{ kg/m}^3$ covering the entire floor (or ceiling) area (100 m^2). The weight of the thermal mass M_m is thus 6250 kg in total. The contact area A_m between the air and the thermal mass is set to 100 m^2 (equal to the floor area, one sided) and the effective heat transfer coefficient h is set to $5 \text{ W/m}^2\text{-K}$. The *Biot number* of the thermal mass can also be calculated by

$$Bi = hl/k, \quad (5.6)$$

where l is the characteristic thickness of the thermal mass and k is the thermal conductivity of the thermal mass materials. For single-sided thermal mass, the actual thickness of the thermal mass is be used for l and we used 1.28 W/m-K for k . The Biot number with the presented thermal mass parameters is 0.098, which satisfies the empirical lumped-sum assumption requirement ($Bi < 0.2$).

Table 5.1 summarizes the parameters above for later references. Most of these parameters are kept constant in later sections unless specially noted for change.

Table 5.1: Major parameters used in the example cases

Parameter	Value	Unit	Parameter	Value	Unit
V	100	m^3	T_e	10	$^\circ\text{C}$
H	6	m	UA	60	$\text{W/m}^2\text{-K}$
h	5	$\text{W/m}^2\text{-K}$	M_m	6250	Kg
A_m	100	m^2	E	5000	W
$\overline{C_dA}$	0.35	m^2	Floor Area	100	m^2
v_{ref}	2.2	m/s			

The selection of the above parameters is primarily to make the building reasonably configured for clearer illustration. Nevertheless, the generality of the building representation is not lost since the mathematical derivations in the study can be applied to any set of parameters. In later sections, we will also see that the dynamical system behavior will also have a general pattern regardless of the actual numerical values of these parameters.

5.2.2 Solution behaviors

For the conciseness of mathematical notations, we define two new state variables (T_a^* , T_m^*) as the corresponding (T_a , T_m) less the outdoor air temperature T_e :

$$T_a^* = T_a - T_e, \quad (5.7)$$

and

$$T_m^* = T_m - T_e. \quad (5.8)$$

Substituting Equation (5.3) for the flow into Equations (5.1) and (5.2) yields two first-order ordinary differential equations (using the T_a^* and T_m^* expression):

$$\begin{aligned} f_a(T_a^*, T_m^*) = \frac{dT_a^*}{dt} &= \frac{E}{M_a c_a} - \frac{\rho_a c_a}{M_a c_a} \overline{C_d A} \sqrt{\left| 2gH\beta T_a^* - 2\frac{P_w}{\rho_a} \right|} \cdot T_a^* \\ &- \frac{UA}{M_a c_a} T_a^* - \frac{hA_m}{M_a c_a} (T_a^* - T_m^*), \end{aligned} \quad (5.9)$$

and

$$f_m(T_a^*, T_m^*) = \frac{dT_m^*}{dt} = -\frac{hA_m}{M_m c_m} (T_m^* - T_a^*). \quad (5.10)$$

Figure 5-2 shows the changes of T_a^* and T_m^* with time after a sudden change in ambient temperature, starting from a common initial value. Due to the large time constant of the thermal mass, the entire system requires a long time to reach steady states. In the initial stage (the top plot in Figure 5-2), the air temperature increases quickly and thereafter both the air and the thermal mass change in moderate pace until finally reaching the steady state temperature. In Chapter 6 (or [76]), we will provide an explanation for this initial increase phenomenon by the eigen characteristics of the system.

Due to the possible existence of multiple steady states, the final steady state of the system can be sensitive to the initial values. Figure 5-3 shows these two possibilities for two different initial temperature values when wind forces oppose buoyancy forces as shown in Figure 5-1. The first case is shown in the lower two (heavier lines) curves in Figure 5-3. The air and the thermal mass start from a lower initial temperature (the same as that in Figure 5-2) and finally reach a wind-dominated steady state (SS1¹). The second case is shown in the upper set of (lighter) curves in Figure 5-3. The air and the thermal mass now start from a much warmer initial temperature. They finally reach another warmer buoyancy-dominated steady state (SS3). These two cases indicate that the system has at least two possible steady states: a cooler SS1 and a warmer SS3. In Figure 5-3, a third steady state (SS2) is also marked there, which is locally unstable and the system will not permanently stay there. More details about this unstable steady state will be discussed in later sections.

Mathematically, the steady states temperatures can be obtained by simultaneously setting the time derivatives of the air and the thermal mass temperatures (Equations

¹SS1 is the short for Steady State 1. Similarly, SS2 is Steady State 2 and SS3 is Steady State 3.

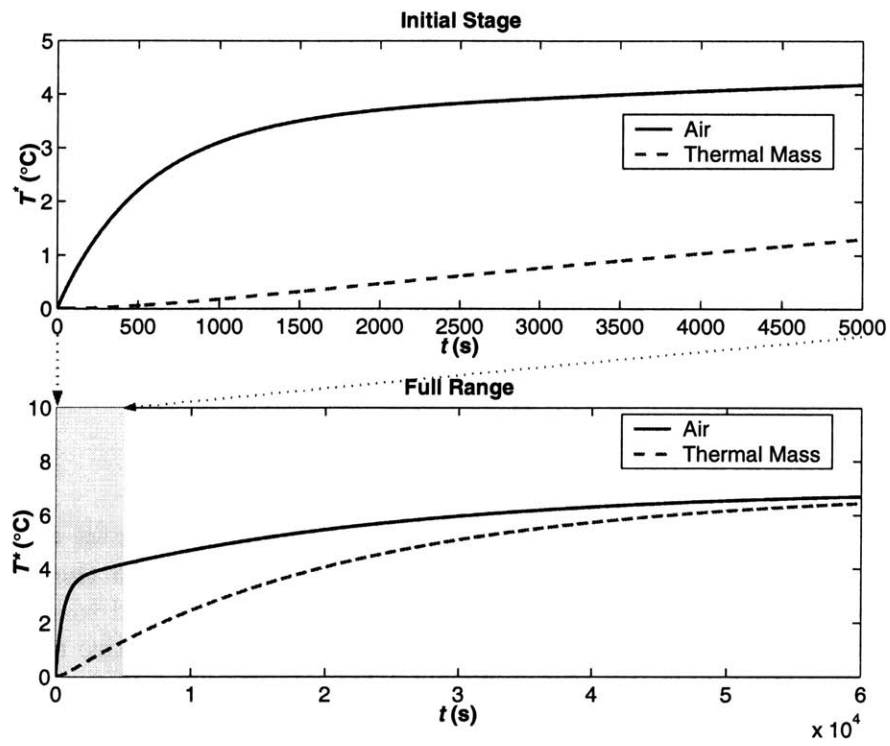


Figure 5-2: The air and the thermal mass temperatures vs. time: initial stage and full range

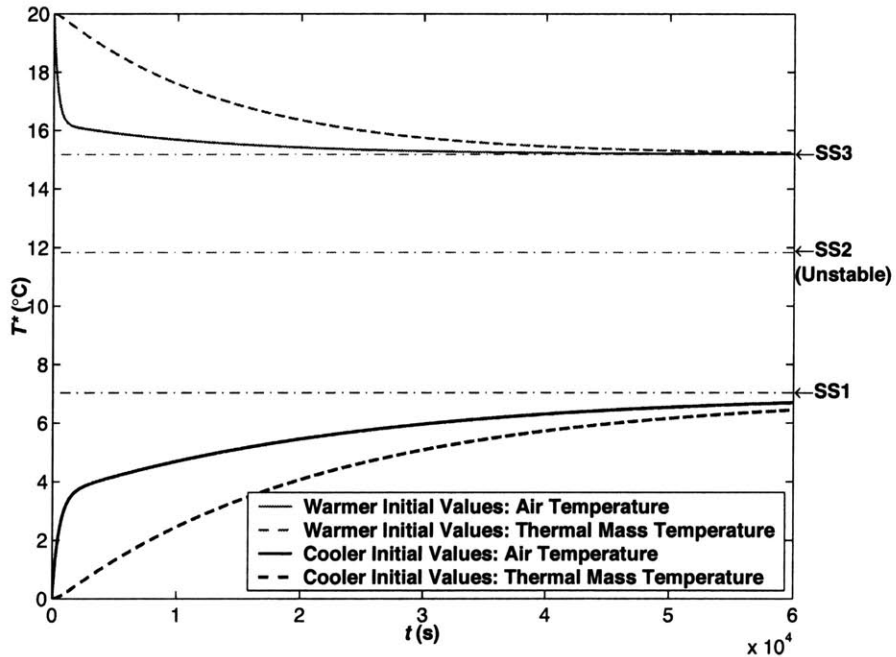


Figure 5-3: Two steady states the system can reach starting from two different initial values

(5.9) and (5.9)) to zero, which leads to $T_a^* = T_m^*$ at the steady states. The thermal mass temperature is thus canceled out in the steady state equations and we obtained a steady state equation that is the same as that for a system without thermal mass as follows:

$$E - \rho_a c_a \cdot \overline{C_d A} \cdot \sqrt{|2gH\beta T_a^* - 2P_w/\rho_a|} T_a^* - UA \cdot T_a^* = 0. \quad (5.11)$$

Equation (5.11) can have three solutions if certain conditions are satisfied. Such conditions are derived in Chapter 4. Since the systems with and without thermal mass share the same steady state equation, the values of the steady states of the two systems are the same.

5.2.3 Two extreme cases

The multiple steady states behaviors of a single-zone system without thermal mass have been discussed in several previous studies (e.g. [70, 74]). For the system with thermal mass, there are two special cases where it can be converted to a system that can be represented only by a single temperature. These are the two extreme cases where the convective heat transfer coefficient h between the air and the thermal mass is 0 and $+\infty$, respectively. For an existing system, the surface area A_m of the thermal mass is usually fixed and thus the hA_m value is proportional to h . Therefore we have $hA_m \rightarrow 0$ and $hA_m \rightarrow \infty$, respectively, for the two extreme cases.

In the special case of $hA_m \rightarrow 0$, there is nearly no heat exchange between the air and the thermal mass. The thermal mass temperature will neither change with time nor affect the air temperature. In other words, the thermal mass is completely disconnected from the system and will always be at its initial temperature. Therefore, the system can be treated as a single variable system where the air temperature is the only state variable, and the heat capacity of the air is the only heat capacity that will affect the system. The governing equation for the system is

$$f_0(T_a^*) = \frac{dT_a^*}{dt} = \frac{S}{M_a c_a} - \frac{\rho_a c_a}{M_a c_a} \overline{C_d A} \sqrt{|2gH\beta T_a^* - 2P_w/\rho_a|} \cdot T_a^* - \frac{UA}{M_a c_a} T_a^*. \quad (5.12)$$

In the other special case of $hA_m \rightarrow \infty$, the air and the thermal mass will have a strong heat transfer between them even for a small temperature difference so that they will have nearly identical temperatures at any time. Therefore the system also reduces to a single variable system. The system equation is similar to Equation (5.11) except for a larger thermal heat capacity $M_a c_a + M_m c_m$:

$$f_\infty(T^*) = \frac{dT^*}{dt} = \frac{S - \rho_a c_a \overline{C_d A} \sqrt{|2gH\beta T_a^* - 2P_w/\rho_a|} \cdot T_a^* - UA \cdot T_a^*}{M_a c_a + M_m c_m}. \quad (5.13)$$

Usually $M_a c_a + M_m c_m$ (total thermal mass and air heat capacity) is at least one order of magnitude higher than $M_a c_a$ (air heat capacity). Therefore, in the $hA_m \rightarrow \infty$ case, the air temperature changes very slowly due to the much larger active heat capacity. In contrast, the air changes very fast when $hA_m \rightarrow 0$. These two extreme

cases in the temperature changes can be shown by the magnitudes of $f_0(T_a^*)$ (for $hA_m \rightarrow 0$) and $f_\infty(T^*)$ (for $hA_m \rightarrow \infty$) in Figure 5-4: the absolute magnitude of $f_\infty(T^*)$ is much smaller than that of $f_0(T_a^*)$. The two extreme cases can be treated as the lower and upper bounds of the air temperature responses of an arbitrary system with $0 < hA_m < \infty$ (a finite hA_m value).

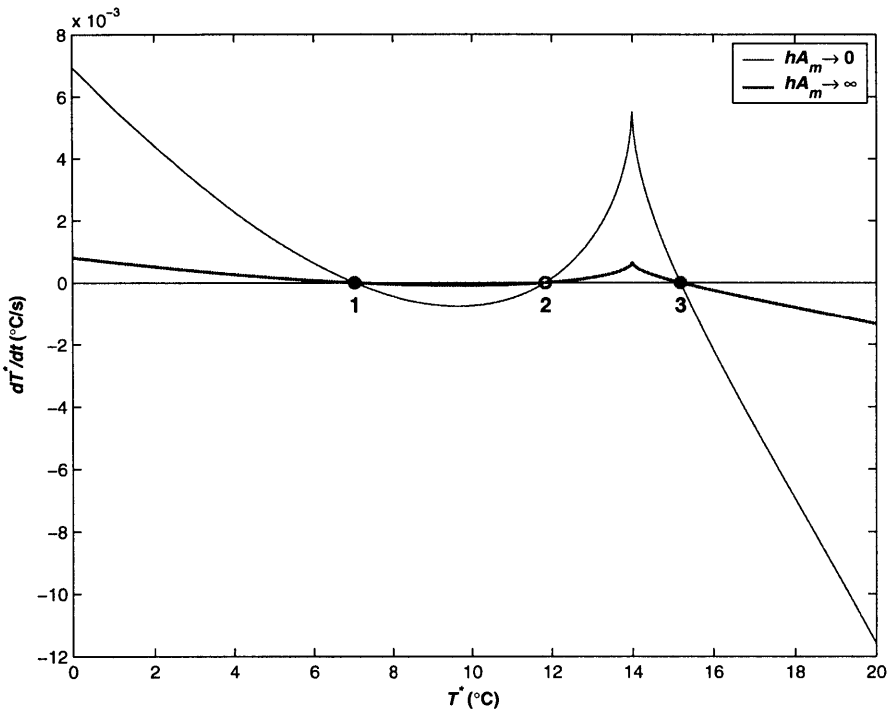


Figure 5-4: $f_0(T_a^*)$ and $f_\infty(T^*)$ for the two extreme cases

For the two extreme single-state cases, the stabilities of the three steady states can be obtained from Figure 5-4 as well. By examining the sign of dT^*/dt at a steady state, the direction the system will move when it is perturbed by an infinitesimal distance from the steady state can be determined (also see [74]). For SS1 and SS3, the system temperature will move back since dT^*/dt is positive at a lower temperature (than the steady state) and negative at a higher temperature. The temperature T^* will tend to move back to the same steady state when the system is perturbed from the SS1 or SS3, which indicates that these two steady states are stable. For SS2, when the system temperature is perturbed away from the steady state, it will either continuously decrease or increase since dT^*/dt is negative at a lower temperature (than the steady state) and positive at a higher temperature. Therefore SS2 is an unstable steady state. The knowledge about the sign of dT^*/dt and the stability of a single-variable system can be used to simplify the mathematical derivations in later sections when we systematically examine the stability of the more general two-variable air-mass systems.

5.3 Conditions for multiple steady states to exist

5.3.1 A similar system view

There are different ways to examine the conditions for the multiple steady states to exist. The simplest way is to use the property that the systems with and without thermal mass share the same steady state equation (Equation (5.11)). Therefore they will also have the same requirements for multiple steady states to exist. For a system without thermal mass, the conditions were investigated in previous studies ([70, 74]) as follows:

$$P^{**}UA \leq \beta S \leq \left(P^{**} - \left(\frac{\sqrt{X^2 + 3P^{**}} - X}{3} \right)^2 \right) \left(\rho_a c_a \bar{C}_d A \sqrt{2gH} \frac{\sqrt{X^2 + 3P^{**}} - X}{3} + UA \right), \quad (5.14)$$

where P^{**} is defined as

$$P^{**} = \frac{P_w}{\rho_a g H}, \quad (5.15)$$

and X is defined as

$$X = \frac{UA}{\rho_a c_a \bar{C}_d A \sqrt{2gH}}. \quad (5.16)$$

Since no thermal mass parameters (e.g. h , A_m , M_m , c_m) appears in Equations (5.14) to (5.16), the presence of the thermal mass will not affect the existence of multiple steady states. Physically, since the air and the thermal mass will finally settle at the same temperature (to reach a steady state), there will be no heat transfer between the air and the thermal mass at steady state. Therefore, the thermal mass will not affect the static behavior of the system at these steady state points. However, once the system starts to deviate from a steady state, the thermal mass will immediately have an impact. One impact will be the way the system converges to a steady state from an initial value, which will be discussed in later sections.

5.3.2 A parameter-dependency view

The conclusion obtained from Equation (5.14) and from [70, 74] was derived through a more general method—examining the dependence of solution behaviors (i.e. the number of steady states) on parameters. In this subsection we will apply such a method to examine the conditions for multiple steady states to exist in the air-mass system presented in this study.

By continuously changing a parameter, which is usually named a *control parameter*, we will observe the change in the system's steady state solution behaviors. For example, we can define a control parameter as follows:

$$r = \frac{\beta E}{Z}, \quad (5.17)$$

where Z is defined as (according to Equation (5.14))

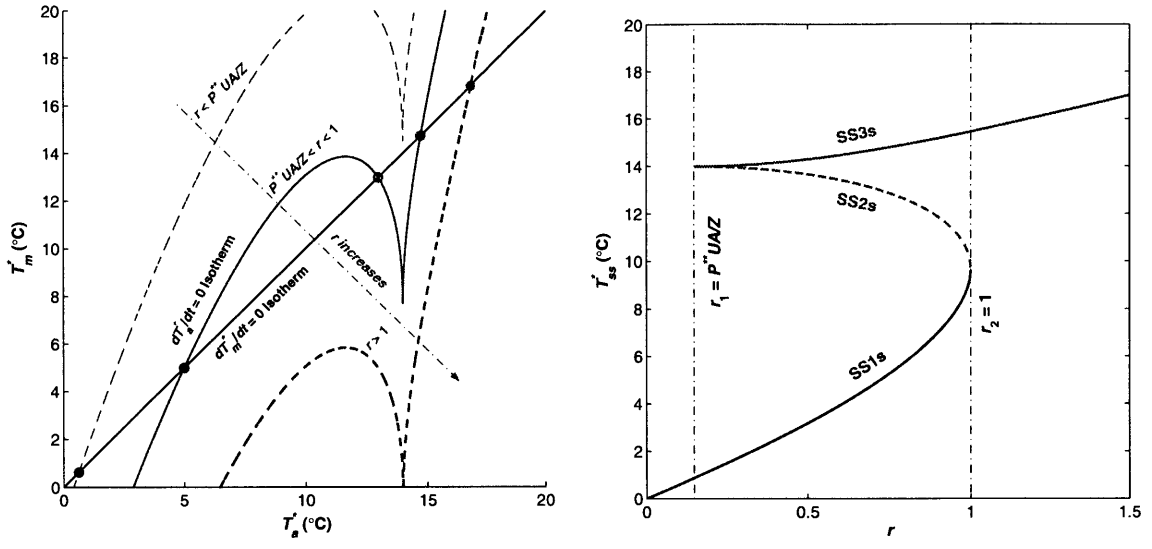
$$Z = \left(P^{**} - \left(\frac{\sqrt{X^2 + 3P^{**}} - X}{3} \right)^2 \right) \left(\rho_a c_a C_d A \sqrt{2gH} \frac{\sqrt{X^2 + 3P^{**}} - X}{3} + UA \right). \quad (5.18)$$

For different r values, the number of steady states the system can have will also be different. This process can be shown in Figure 5-5(a). Two *nullclines*—defined as the two lines where $dT_a^*/dt = 0$ and $dT_m^*/dt = 0$ on the phase plane, respectively—are plotted on the figure. The intersections of isotherms are the steady states (sometimes called *fixed points* in nonlinear dynamics) of the system. In the mathematical model presented in this study, the nullcline for $dT_m^*/dt = 0$ is a straight line whose position is fixed for all r values; while the nullcline for $dT_a^*/dt = 0$ changes with r values. Three sets of nullclines are plotted in Figure 5-5(a) for three different r values. When r is small so that $r < P^{**}UA/Z$, the two nullclines intersect only once and the system has only one steady state (SS1). When $P^{**}UA/Z < r < 1$, the two nullclines intersect three times and the system will have three steady states. As r increase further to $r > 1$, the two nullclines again intersect only once at the steady state (SS3). Therefore, at $r = P^{**}UA/Z$ and $r = 1$, the solution properties will change, which is called *bifurcation* in nonlinear dynamics. Bifurcation is usually associated with the creation, destruction, or stability property changes of fixed points. Figure 5-5(b) shows a bifurcation diagram that plots the steady states (fixed points) the system can have against the r values, which summarizes the process shown in Figure 5-5(a). The bifurcation processes shown in Figure 5-5 at the two bifurcation points (at $r_1 = P^{**}UA/Z$ and $r_2 = 1$) are typically called *saddle-node bifurcations*, which involves the collision and mutual annihilation of two fixed points when r changes. At a saddle-node bifurcation point, two fixed points collide with each other or one fixed point splits into two depending on the direction r moves.

Again, the mathematical derivations above shows that the thermal mass parameters (h , A_m , M_m , c_m) do not appear in the control parameter or the bifurcation points. This means the solution bifurcation of the system with thermal mass is the same as that of a system without thermal mass. The latter was presented in several previous studies in different contexts such as hysteresis [44], solution dependency [41], and dynamical system characteristics [70, 74]. On the other hand, this similarity between the systems with and without thermal mass indicates that a bifurcation analysis cannot completely explain the difference between the two systems. In the next sections, we will explore the differences between the system with and without thermal mass from other aspects.

5.4 Initial values and dynamical system characteristics

When multiple steady state can occur in a system with thermal mass (i.e. it satisfies the condition described by Equation (5.11)), the initial air temperature is not the sole



(a) Bifurcation process on the phase plane (b) Bifurcation diagram
Figure 5-5: The change of the steady states of the system for different r values

variable that determines the final steady state. The thermal mass temperature can be important as well. For example, if the system starts from a low air temperature (much lower than the unstable steady state temperature) but a very high thermal mass temperature, the thermal mass may gradually heat up the air and the system may still possible to reach the buoyancy dominated upward SS3. On the other hand, if it starts from a high air temperature but an extremely low thermal mass temperature, it is also possible for the system to reach the wind dominated downward SS1. However, the air and the thermal mass are coupled so that when the air is heated or cooled by the thermal mass, the thermal mass temperature will also change. Therefore, a quantitative description of the interactions between the air and the thermal mass is important in investigating the way the system converges to different steady states.

In previous studies ([70, 74]), it was found that the temperature of the unstable steady state (SS2) is the critical value in determining the final steady state of the system. For a system without additional thermal mass other than the air, if the initial air temperature is higher than the temperature of SS2, the system will finally reach the buoyancy dominated upward SS3. If it starts from a lower value than SS2, the system will finally reach the wind dominated downward SS1. This conclusion is also valid for the system with thermal mass as is shown in Figure 5-3, when we assume the air and the thermal mass start from the same initial temperature. However, in reality, the air and the thermal mass almost never start from the same initial temperatures. In this section, we will investigate the general scenarios where the air and the thermal mass start from any arbitrary combinations of initial values.

5.4.1 Mechanisms for the system to reach different steady states

With the governing dynamics described by Equations (5.9) and (5.10), the interactions between the air and the thermal mass can be quantitatively described by plotting the trajectories of the state variables on the phase plane, a plane for all the system (both steady and unsteady) states. Figure 5-6 shows some of the system trajectories starting from different initial values (points). The x-axis is the air temperature (less the outdoor temperature); and the y-axis is the thermal mass temperature (also less the outdoor temperature). The solid lines are the trajectories starting from a series of points. At these starting points, a few arrows are also plotted. They are generally called *vectors*, whose directions and (relative) lengths are determined by dT_a^*/dt and dT_m^*/dt : dT_a^*/dt is the x-component and dT_m^*/dt is the y-component of the vector at a particular point; and $\sqrt{(dT_a^*/dt)^2 + (dT_m^*/dt)^2}$ is (the relative) length of the vector. At any point on the phase plane we can plot a vector; and all the vectors in the phase plane form a vector *field* (although, we only plotted the vectors at the starting points of some selected trajectories). At any point on the phase plane, the vector is always tangential to the trajectory passing through that point.

Figure 5-6 shows that all the trajectories will finally end at one of the two stable steady states – SS1 and SS3. A dividing line (the heavy dashed line in Figure 5-6) separates the phase plane into two regions in which the trajectories converge to two different steady states. In the lower-left region (shaded), all the trajectories reach SS1, which represents a wind-dominated downward flow steady state. In the upper-right region (unshaded), all the trajectories finally reach SS3 — the buoyancy-dominated upward flow steady state.

Steady State 2 (SS2) is essentially on the dividing line because the system can reach either SS1 or SS3, starting an infinitesimal displacement from SS2, depending on the direction of the displacement. There are, indeed, two special trajectories that can temporarily reach SS2. However, they cannot stably stay there. The trajectories will continue to move towards either SS1 or SS3 under infinitesimal perturbations. In Chapter 6 we will investigate these two special trajectories in detail, and shown that they are exactly the dividing line between the two attraction regions in Figure 5-6.

In traditional nonlinear dynamics [57], SS1 and SS3 are also called *attractors* due to their properties of attracting the trajectories, and the two corresponding regions for the attractors on the phase plane are called their *basins of attractions*. This dividing line of the two basins of attractions is composed of two special trajectories, which are traditionally called the *separatrices*.

Figure 5-6 shows that the thermal mass will have an impact on how the system reaches the final steady states. For example, the upper-left corner of the phase plane is a region where the thermal mass is at a high initial temperature but air is at a low one. In this region, for a system without thermal mass (see [74]), the system will reach SS1 since the initial air temperature is much lower than the temperature of SS2, the critical temperature required to obtain the buoyancy dominated SS3. However, for the system with thermal mass in this study, although the initial air temperature is

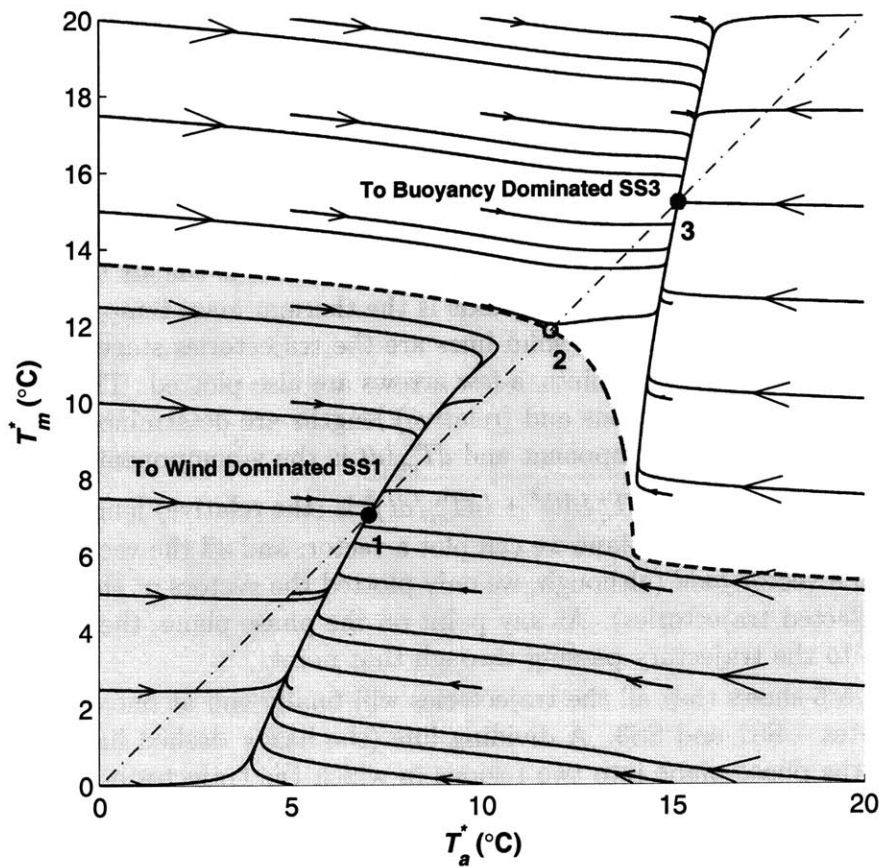


Figure 5-6: Trajectories, fixed points, attraction regions, and separatrices on the phase plane (parameters in Table 5.1)

much lower than the critical SS2 temperature, the system will still reach the buoyancy-dominated SS3 due to the warmer thermal mass. Similarly, starting from the vicinity of the lower-right corner of the phase plane on Figure 5-6, the system with thermal mass will reach the wind-dominated SS1 instead of SS3 due to a low initial thermal mass temperature, even though the initial air temperature is high enough for a similar system without thermal mass to reach the buoyancy-dominated SS3.

Figure 5-6 also shows a “central” region (where $T_a^* = \sim 10$ °C to 14 °C) on Figure 5-6) on the separatrices around SS2, where the separatrices are relatively steep. Physically, the air temperature is more dominant in determining the system’s final steady state in this region. Beyond the “central” region on the two “wings”, the separatrices are much flatter, which indicates that thermal mass temperature is more important in determining the system’s final steady state.

5.4.2 Systems that have only one steady state

When conditions for multiple steady states to exist in Equation (5.11) are not satisfied, the system can only have one steady state. In this scenario, the system will reach the

same steady state from any combination of initial air and thermal mass temperatures. Figure 5-7 shows two such systems that have only one steady state. For the system shown in Figure 5-7(a), the system has only one wind-dominated steady state (see the upper curve in Figure 5-5(a)). All the trajectories will converge to SS1 finally, starting from any combination of the initial air and thermal mass temperatures. For the system shown in Figure 5-7(b), the system has only one buoyancy-dominated steady state. All the trajectories will converge to SS3, starting from any initial values.

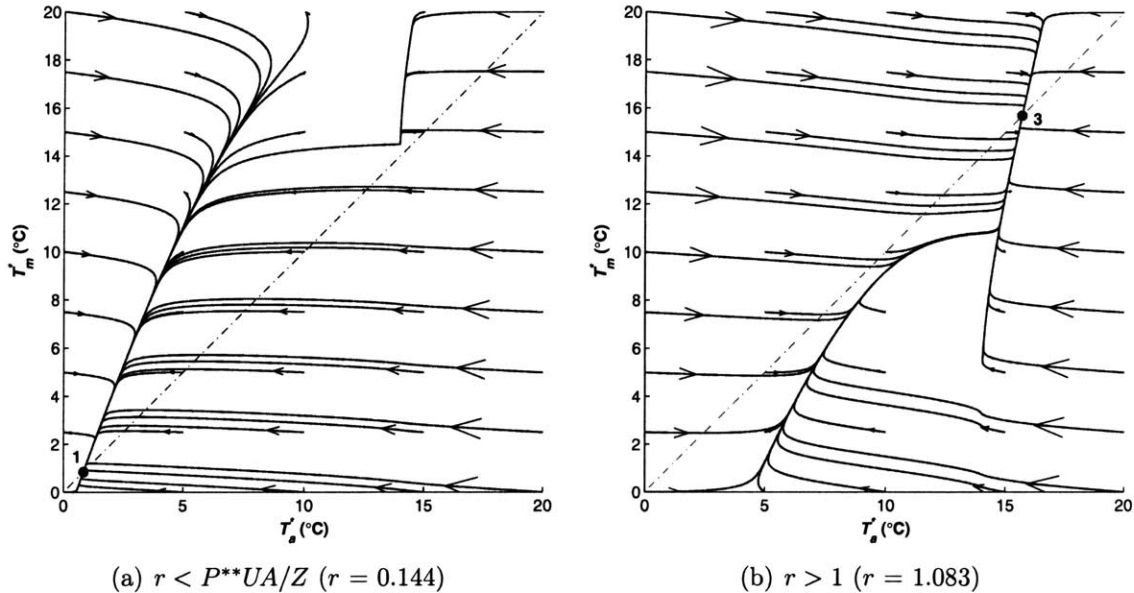


Figure 5-7: The trajectories for systems that have only one steady state: a). $r < P^{**}UA/Z$ (only has SS1); b). $r > 1$ (only has SS3)

From the parameter dependence analysis in a previous section we have shown that two steady states will mutually disappear when the control variable r moves out of the multiple steady states region. However, there is a “ghost” effect which makes the annealed steady states (fixed points) still affecting the trajectories in the system. For example, in Figure 5-7(a), SS3 (and SS2) is (are) destroyed since $r < P^{**}UA/Z$; however, the trajectories of the upper-right corner of the phase plane are still temporarily attracted by an imaginary SS3 (or a ghost SS3) as if they have to pass a *bottleneck*. Similarly, in Figure 5-7(b), although SS1 (and SS2) is (are) destroyed since $r > 1$, the trajectories in the lower-left corner of the phase plane are still affected by a “ghost” steady state.

This process of passing the bottleneck usually takes a long time since the time derivatives of the state variables are small there (close to the original steady states). Figure 5-8(a) illustrates the time the system spend to pass this bottleneck starting from a high thermal mass and high air temperature to reach the only steady state SS1 when $r < r_1$. The system will have to spend a long time (nearly 1/3 of the total time) to pass through the affected bottleneck region (“ghost”). Similarly Figure 5-8(b) provides the information about the “bottleneck” passing of the system from a

cold thermal mass and air temperature to its only (hot) steady state SS3. The system will also need to pass a bottleneck region to before entering the track that converges to SS3. In this case, the time to pass the bottleneck is even longer—it accounts for nearly 60% of the total time to reach the steady state.

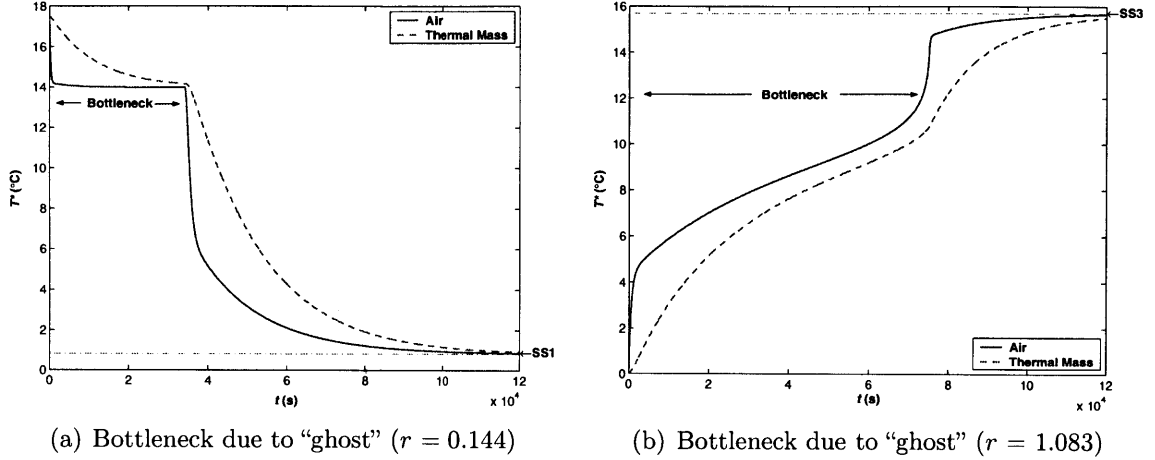


Figure 5-8: Bottleneck the system encounter due to a “ghost” fixed point

As r increases or decrease further away from the two bifurcation points, the “ghost” effect will be gradually weakened. The trajectories are less influenced by the “ghost” when r moves further away from the bifurcation points.

5.5 Local stability analysis of the three steady states

In this section, we will provide a formal local stability analysis on the three steady states, which are mathematically determined by the eigenvalues of the linearized system matrix. More importantly, we will generalize the stability properties of the steady states for the systems with thermal mass, regardless of the amount of thermal mass or the strength of the interaction between the air and the thermal mass. Through the presented analysis, we expect to provide a general description about systems regardless of the amount of the thermal mass and the strength of the air-mass interaction.

5.5.1 Generalize the dynamical system characteristics

By linearizing the system equations at any of the three steady states, a linear matrix is obtained as follows:

$$\begin{bmatrix} \frac{d(T_a^* - T_{ssi}^*)}{dt} \\ \frac{d(T_m^* - T_{ssi}^*)}{dt} \end{bmatrix} = \begin{bmatrix} a & b \\ c & d \end{bmatrix} \begin{bmatrix} T_a^* - T_{ssi}^* \\ T_m^* - T_{ssi}^* \end{bmatrix}, \quad (5.19)$$

where $i = 1, 2, 3$ for the three steady states, respectively; the four real numbers a , b , c , and d in the matrix are given by

$$\begin{aligned} a &= \frac{\partial f_a}{\partial T_a^*} \Big|_{T_{ssi}^*, T_{ssi}^*} & b &= \frac{\partial f_m}{\partial T_m^*} \Big|_{T_{ssi}^*, T_{ssi}^*} \\ c &= \frac{\partial f_a}{\partial T_a^*} \Big|_{T_{ssi}^*, T_{ssi}^*} & d &= \frac{\partial f_m}{\partial T_m^*} \Big|_{T_{ssi}^*, T_{ssi}^*}, \end{aligned} \quad (5.20)$$

where functions f_a and f_m are given by Equations (5.9) and (5.10).

The stability of the system around any Steady State i (1, 2 or 3) is then determined by the two eigenvalues of the Jacobian matrix $\mathbf{J} = \begin{bmatrix} a & b \\ c & d \end{bmatrix}$ (denote as \mathbf{J}), which are given by

$$\lambda_{1,2} = \frac{a+d}{2} \pm \frac{\sqrt{(a-d)^2 + 4bc}}{2}. \quad (5.21)$$

Different eigenvalues obtained in Equation (5.21) indicate different local stabilities of a steady state. If both eigenvalues have negative real parts, the linearized system (and the steady state) will be stable. Further, if both eigenvalues are real (no imaginary part) and negative, the steady state is called a *stable node*. The properties of a stable node are similar to those of SS1 and SS3. In the system presented in this study, SS1 and SS3 are indeed stable nodes. The rigorous proof of the stable node properties for SS1 and SS3 will be presented in the next section.

If for a steady state, either of the two eigenvalues has a positive real part, the linearized system (and the steady state) will be unstable. Further, if both of the eigenvalues are real, and one is positive and the other is negative, the steady state is called a *saddle point*. In the system presented in this study, SS2 is indeed a saddle point because the corresponding linearized system has exactly one positive eigenvalue and one negative eigenvalue. The rigorous proof will be presented in the next section as well.

5.5.2 Demonstrate the eigen characteristics

From this subsection we will start to rigorously demonstrate the dynamical system characteristics (e.g. why Steady States 1 and 3 are stable nodes and Steady State 2 is a saddle point) of the system around the three steady states. Further, we also intend to answer another question about the system Eigen characteristics: are the Eigen characteristics of the system always true for any parameters (e.g. hA_m and M_mc_m) given that multiple steady states can exist in the system.

In the following subsections, we will prove that: a.) for the Jacobian matrix \mathbf{J} obtained at Steady States 1 or 3, both of the two eigenvalues of matrix \mathbf{J} are negative; and b.) for the Jacobian matrix \mathbf{J} obtained at Steady States 2, one of the two eigenvalues of \mathbf{J} is negative and the other is positive. Further, to prove the above two claims, we will not use a brute-force method of completely expanding the expressions in Equation (5.20). Rather, we will make full use of the existing knowledge about the system without thermal mass, and only partially expand Equation (5.20).

First we will partially expand the expressions in Equation (5.20). The terms b , c , and d are relatively easy to expand since only linear terms are involved. To obtain the term a , we can first decompose Equations (5.9) into two parts denoted as

$$f_a(T_a^*, T_m^*) = \frac{dT_a^*}{dt} = \underbrace{\frac{S}{M_a c_a} - \frac{\rho_a c_a}{M_a c_a} \overline{C_d A} \sqrt{\left| 2gH\beta T_a^* - 2\frac{P_w}{\rho_a} \right| T_a^* - \frac{UA}{M_a c_a} T_a^*}}_{f_0(T_a^*), \text{ Air term}} - \underbrace{\frac{hA_m}{M_a c_a} (T_a^* - T_m^*)}_{\text{Air-mass interaction}}, \quad (5.22)$$

The first part of Equation (5.22) is exactly the state equation for a system without thermal mass (also see [70, 74]). The term was denoted as $f_0(T_a^*)$ in Equation (5.12). The second part is a linear term that describes the thermal mass and air interactions. With the expression in Equation (5.22), we can express the term a in the Jacobian matrix \mathbf{J} as

$$a = \frac{\partial f_0(T_a^*)}{\partial T_a^*} - \frac{hA_m}{M_a c_a} \frac{\partial (T_a^* - T_m^*)}{\partial T_a^*} = \frac{df_0(T_a^*)}{dT_a^*} - \frac{hA_m}{M_a c_a}, \quad (5.23)$$

where $\frac{df_0(T_a^*)}{dT_a^*}$ is plotted in Figure 5-4. From Figure 5-4 we can also obtain its sign at all the three steady states: at SS1 and SS3, $\frac{df_0(T_a^*)}{dT_a^*}$ is negative; and at SS2, $\frac{df_0(T_a^*)}{dT_a^*}$ is positive. We will show that this information will be sufficient to determine the sign of the eigenvalues calculated by Equation (5.21). Recalling Equations (5.9) and (5.10) we obtain all the elements in the Jacobian matrix \mathbf{J} as

$$\mathbf{J} = \begin{bmatrix} a & b \\ c & d \end{bmatrix} = \begin{bmatrix} \frac{df_0(T_a^*)}{dT_a^*} - \frac{hA_m}{M_a c_a} & \frac{hA_m}{M_a c_a} \\ \frac{hA_m}{M_m c_m} & -\frac{hA_m}{M_m c_m} \end{bmatrix}. \quad (5.24)$$

Prior to showing the stable node or saddle point behavior of the three steady states, here we will show that the eigenvalues of the linearized system will always be real values (i.e. no imaginary parts) for the system investigated in the present study. Whether the eigenvalues are real or complex (with an imaginary part) depends on the whether the term $(a - d)^2 + 4bc$ in Equation (5.21) is nonnegative or not. It is obvious that $(a - d)^2$ is always nonnegative. Further, according to Equation (5.24), $4bc$ is also nonnegative, which leads to that the sum $(a - d)^2 + 4bc$ will always be nonnegative, too. Therefore the linearized system can only have real eigenvalues at any of the three steady states.

5.5.3 Steady States 1 and 3

Now we will show that for the system linearized at Steady States 1 and 3 will have two negative eigenvalues. We will look at the term $(a - d)^2 + 4bc$ again. This time we will compare it with the term $(a + d)^2$, which is equal to $(a - d)^2 + 4ad$. Therefore,

the relationship between the values of bc and ad will determine which one will be larger: $(a - d)^2 + 4bc$ or $(a + d)^2$. To do that, recall Equation (5.24), from which we can obtain the values of bc and ad as:

$$bc = \left(-\frac{hA_m}{M_a c_a} \right) \left(-\frac{hA_m}{M_m c_m} \right) = \frac{hA_m}{M_a c_a} \cdot \frac{hA_m}{M_m c_m}, \quad (5.25)$$

and

$$ad = \left(\frac{df_0(T_a^*)}{dT_a^*} - \frac{hA_m}{M_a c_a} \right) \left(-\frac{hA_m}{M_m c_m} \right) = -\frac{hA_m}{M_m c_m} \cdot \frac{df_0(T_a^*)}{dT_a^*} + \frac{hA_m}{M_m c_m} \cdot \frac{hA_m}{M_a c_a}. \quad (5.26)$$

Now we will use the fact that $\frac{df_0(T_a^*)}{dT_a^*} < 0$ at SS1 and SS3 (obtained from Figure 5-4). From Equations (5.25) and (5.26), we can obtain that $ad > bc$ when $\frac{df_0(T_a^*)}{dT_a^*} < 0$. Therefore we have $(a - d)^2 + 4bc < (a - d)^2 + 4ad = (a + d)^2$. The following statement immediately follows:

$$\sqrt{(a - d)^2 + 4bc} < \sqrt{(a - d)^2 + 4ad} = \sqrt{(a + d)^2} = |a + d| = -(a + d), \quad (5.27)$$

where the last part $|a + d| = -(a + d)$ comes from the fact that at SS1 and SS3 (use Equation (5.24)),

$$a + d = \underbrace{\frac{df_0(T_a^*)}{dT_a^*}}_{<0} - \frac{hA_m}{M_a c_a} - \frac{hA_m}{M_m c_m} < 0. \quad (5.28)$$

Using this relationship in Equations (5.21), (5.27), and (5.28), we can obtain the sign of the two eigenvalues of the system linearized at SS1 and SS3 as

$$\lambda_1 = \frac{a + d}{2} + \frac{\sqrt{(a - d)^2 + 4bc}}{2} < \frac{a + d}{2} + \frac{-(a + d)}{2} = 0, \quad (5.29)$$

and

$$\lambda_2 = \underbrace{\frac{a + d}{2}}_{<0} - \frac{\sqrt{(a - d)^2 + 4bc}}{2} < 0. \quad (5.30)$$

Since both of the eigenvalues are real and negative ($\lambda_2 < \lambda_1 < 0$), Steady States 1 and 3 are indeed stable nodes. This statement is valid for any values of hA_m and $M_m c_m$, which means the interaction between the air and the mass do not change the local stability properties of these two steady states (SS1 and SS3). On the phase plane (Figure 5-6), the stable nodes are the points to which all the trajectories will finally converge.

5.5.4 Steady State 2

For the system linearized at SS2, we will show that $\lambda_1 > 0$ and $\lambda_2 < 0$. We will continue to use the relation between ad and bc . However, different from the linearized

system obtained at SS1 and SS3, the linearized system obtained at SS2 has $\frac{df_0(T_a^*)}{dT_a^*} > 0$ (see Figure 5-4). According to the expressions of bc and ad in Equations (5.25) and (5.26), we have $bc > ad$ in this case. Therefore, the following relation immediately follows:

$$\sqrt{(a-d)^2 + 4bc} > \sqrt{(a-d)^2 + 4ad} = \sqrt{(a+d)^2} = |a+d|. \quad (5.31)$$

Using this relation, we have the following relation

$$\lambda_1 = \frac{a+d}{2} + \frac{\sqrt{(a-d)^2 + 4bc}}{2} > \frac{a+d}{2} + \frac{|a+d|}{2} \geq 0, \quad (5.32)$$

and

$$\lambda_2 = \frac{a+d}{2} - \frac{\sqrt{(a-d)^2 + 4bc}}{2} < \frac{a+d}{2} - \frac{|a+d|}{2} \leq 0. \quad (5.33)$$

In Equations (5.32) and (5.33) we used the fact that for any real number y ,

$$y - |y| \leq 0, \text{ and } y + |y| \geq 0. \quad (5.34)$$

Substituting y with $a+d$ will yield the second half of Equations (5.32) and (5.33).

Therefore, one of the eigenvalues of the linearized system at SS2 is negative and the other one is positive ($\lambda_2 < 0 < \lambda_1$), for any hA_m and M_mc_m values. This means that SS2 is indeed a saddle for any parameters, regardless of the interactions between the air and the thermal mass, provided that the system does have multiple steady states (i.e., the parameters satisfy Equation (5.14)).

5.5.5 Summary on eigenvalues

In the previous subsections we have provided an analysis on the eigenvalues of the linearized systems at the three steady states, which determines the local stabilities of the three states. In general, since we only care about the sign of the eigenvalues (also whether they are real or complex), we strategically used the properties of a single-variable system that we have known well from previous studies ([70, 74] to reduce the complexity of mathematical derivations.

The signs of the eigenvalues of the linearized systems at the three states are shown to have a general pattern for the system, dependent of the thermal mass parameters. Namely, changing the amount of the thermal mass (M_m, c_m) or the strength of the air-mass interactions capabilities (h, A_m) will not (mathematically) make a stable solution unstable or an unstable solution stable. However, the thermal mass parameters do affect the magnitudes of the eigenvalues and the directions of the corresponding eigenvectors, which are important to the shapes of the trajectories in the system. Details about these effects will be discussed Chapter 6.

5.6 Discussion

An important computational issue is how to obtain the values of the three steady states. There are several methods to for this purpose. The first method is to resort to an analytical solution or analytically solve the steady state Equation (5.11), which can be easily converted to a cubic equation. For example, such a method was used in a system without thermal mass in [41] to obtain the three steady state flow rate, from which the steady state temperatures can be derived. The second method is to use a root search algorithm, such as a standard line search or Newton method ([51]) to solve Equation (5.11). A standard line search is especially effective for simple cases when the solution characteristics of the system are already known (for example, in [70, 74]), while a Newton type method is a more standard method for complex flow network (e.g. multi-zone network [30]). For both of these two methods, an additional procedure is needed to distinguish the stable and the unstable steady states, which still requires knowledge about the dynamical system behaviors. Therefore they are more useful only when the dynamical system characteristics of the solutions are known or can be obtained by other methods.

The third method (to find only the stable steady states) is to solve the dynamical state system Equations (5.9) and (5.10) to reach a steady state from different initial values, which is generally referred as an Initial Value Problem (see Strang [56]). Since the steady states are the same for the systems with and without thermal mass, it will be more efficient to solve the dynamical state Equation (5.12) for a system without thermal mass to obtain the stable steady states. In terms of computational time, this method of solving dynamical system equations is not as efficient as the previous two methods of solving steady state equations; nevertheless, it can automatically exclude the unstable solutions since the system cannot permanently stay at an unstable steady state. More importantly, this method can be generalized and applied to a more complex system (e.g. with multiple zones) to explore the possible steady states, which is the topic of Chapter 10.

5.7 Conclusions

In this chapter, we investigated the multiple steady-state behavior in a single-zone natural ventilation system with thermal mass. A mathematical model is presented to describe the underlying driven dynamics of the system. The dynamical system characteristics were compared with those of a similar system without thermal mass.

A system with thermal mass shows some similarities to an otherwise equivalent system without thermal mass. For example, both systems can obtain the same three steady states under the same boundary conditions; the bifurcation procedures are the same for both systems; and the steady states in both systems show similar (qualitative) local stability properties.

An intrinsic linkage between the systems with mass and without mass was established by the similarities of the two systems. In particular, in a generalization of the local stabilities of the steady states, which are determined by the signs of the two

eigenvalues of the linearized system, we strategically used the existing knowledge on an otherwise equivalent system without thermal mass. The derivation shows that the signs of the eigenvalues of the linearized system are largely determined by the properties of the governing differential equation of the air.

However, there are also differences between a system with thermal mass and a similar system without thermal mass, especially on the transient features of how the system reach different steady states. With the existence of thermal mass, the final steady state of the system is not solely determined by the initial air temperature. Rather, it is determined by the combination of the initial air and mass temperatures. This initial temperature dependency property is quantitatively explained by the trajectory properties on a phase plane that was divided into two distinct attraction regions by the separatrices. The position of the air-mass initial temperature combination relative to the separatrices on the phase plane determines the final steady state of the system.

The nonlinear behavior of the system even has an impact when there is only a single steady state, through a “bottleneck” trajectory attraction and time delay effect due to a “ghost” steady state. This phenomenon, together with other findings presented in this study, will expect to provide new knowledge about the nonlinear dynamics behaviors of an air-mass system; and to promote the understanding of possible computational issues in actual air-mass systems that can have multiple steady states.

Nomenclature

A_i = (effective) internal area (in m^2) for air flow resistance	Cp_u = Wind Pressure Coefficient for the upper openings
A_l = area of the lower opening in m^2	E = heat gain of the space in W
A_m = area of the thermal mass surface that contacts with the air in m^2	g = gravitational acceleration in m/s^2
A_u = area of the upper opening in m^2	H = height difference between the upper and the lower openings in m
c_a = (constant pressure) specific heat of the air in $J/kg\cdot K$	h = effective convection heat transfer coefficient between the air and the thermal mass in $W/m^2\cdot K$
c_m = specific heat of the thermal mass in $J/kg\cdot K$	l = characteristic thickness of the thermal mass in m
$\overline{C_d A}$ = effective product of the discharge coefficient and the opening area in m^2	M_a = mass of the space air in kg, which equals to $\rho_a V$
C_{di} = (effective) discharge coefficient for the internal airflow resistance	M_m = mass of the thermal mass in kg
C_{dl} = discharge coefficient for the lower opening	P_l = wind pressure at the upper opening in Pa
C_{du} = discharge coefficient for the upper opening	P_u = wind pressure at the upper opening in Pa
C_{pl} = Wind Pressure Coefficient for the lower openings	P_w = wind pressure difference between the inlet and outlet in Pa

P^{**} = non-dimensional wind pressure difference between the inlet and the outlet
 q = volumetric air flow rate in m^3/s
 r = a defined boundary condition variable
 t = time in s
 T_a = (indoor) air temperature in $^\circ\text{C}$
 T_e = outdoor temperature in $^\circ\text{C}$
 T_m = thermal mass temperature in $^\circ\text{C}$
 T_a^* = (indoor) air temperature less the outdoor air temperature in $^\circ\text{C}$, i.e. $T_a - T_e$
 T_m^* = thermal air temperature less the outdoor air temperature in $^\circ\text{C}$, i.e. $T_m - T_e$
 UA = total conductance of the building enclosure system in W/K
 V = volume of the space (air) in m^3
 v_{ref} = reference wind velocity in m/s for Wind Pressure Coefficients
 X = an intermediate variable
 y = a real number
 Z = an intermediate variable

Greek

β = thermal expansion coefficient of the air in K^{-1}
 ρ_a = density of air in kg/m^3
 λ_1, λ_2 = eigenvalues of the Jacobian matrix \mathbf{J}

Matrix

\mathbf{J} = Jacobian matrix of the linearized system
 a, b, c, d = the elements of the Jacobian matrix \mathbf{J}

Subscript

a – for air
 m – for thermal mass

Chapter 6

Multiple steady states in a single-zone natural ventilation system with thermal mass—Transient behaviors and impact of mass

In Chapter 5, a mathematical model was introduced to investigate the generalized multiple steady state behaviors of a natural ventilation system with thermal mass. The present part focuses on the transient behaviors and the time characteristic of the system, especially under the condition that the thermal mass parameters vary. The transient interactions between the thermal mass and the air interact are demonstrated and explained by the system's linear and nonlinear dynamical system features. The response time characteristics related to the trajectories in the bottleneck effect discussed in Chapter 5 are further investigated through the system's eigen characteristics. The nonlinear dynamics behaviors related to the unstable steady state and the separatrices on the phase plane was explained by the eigen characteristics of the system. An efficient computational method was developed to compute the attraction region boundaries—the critical initial values in determining the long-term behaviors of the system. Finally, the impact of thermal mass on the transient dynamical system behaviors, such as the attraction regions on the phase plane, the characteristics of the system's trajectories, are investigated by the eigen system characteristics. The related thermal mass parameters, such as the heat transfer rate between the air and the thermal mass and the amount of thermal mass, were found to have significant impacts on the trajectory shapes and the boundary of basin of attractions, which are important to the short-term and long-term behaviors of the system.

6.1 Introduction

In Chapter 5, we developed a dynamical system model for an air-thermal-mass (briefed as air-mass hereafter) system that may exhibit multiple steady states. We generalized the common behaviors of systems with regardless the thermal mass pa-

rameters such as the mass weight and the air-mass interaction strength. For example, the thermal mass will affect neither the number of steady states the system can have nor the numerical values of these steady states. Further, the bifurcation procedures were also shown to be unaffected by the thermal mass. Mathematically, we demonstrated that the qualitative local stability characteristics of the system at the steady states can also be generalized by the signs of the eigenvalues of the linearized system near the steady states, regardless the amount of thermal mass, the strength of air-mass interaction, and even the existence of the thermal mass.

Nevertheless, in Chapter 5 we also demonstrated that there were behaviors that can be affected by the thermal mass (parameters). One of the affected behaviors is the outcome of which steady state the system will reach starting from different combinations of air-mass initial temperatures, when multiple steady states can exist. For example, starting from a low initial air temperature but a high initial thermal mass temperature but, the system can still reach a warmer steady state that would otherwise requires a much higher initial air temperature in a similar system without thermal mass [74]. These results indicate that the transient behaviors of the system should be further examined and the impact of thermal mass parameters on the transient behaviors should be examined further in the present study.

Further, in Chapter 5 (or [75]), we also illustrated the how the system reaches different steady states through the trajectories on the phase plane. A trajectory on the phase plane traces the changes of the state variables when starting from an initial temperature. However, the trajectory itself does not reveal the underlying time characteristics associated with them. In this study, we will further investigate the associated time characteristics with the trajectories and show the characteristics change with different thermal mass parameters. More importantly, we will demonstrate that the time characteristics can be used to further explain a nonlinear remnant (or “ghost”) effect discussed in Chapter 5, which is important to nonlinear systems that have only one steady state as well.

Another objective of the present study is to demonstrate how the multiple steady state behaviors can be important to the system behaviors. Although there were numerous previous studies on air-mass system using “state-space” type dynamical system models, none of them have considered the impact of the multiple steady states in the system. In later section, we will demonstrate that the existence of the nonlinear behaviors will have great impact to the dynamical behaviors of the system. Even when the conditions for the multiple steady states are not met, there is a remnant effect of the multiple steady state behaviors, which was described shortly as a “ghost” effect in Chapter 5 of this study. In this study, we will further demonstrate the time characteristics associated with this “ghost” effect. These results are expect to provide new knowledge to the applications of thermal mass in buildings (e.g. Rabl and Norford [52], Braun et al [15]) and optimal controls of building thermal mass (e.g., Armstrong et al [5]).

In this study, we will also explain the nonlinear dynamics behaviors of the air-mass system in more details with the consideration of both the time characteristics and the eigen characteristics of the system. The characteristics of the unstable steady states and the manifolds associated with them will be used to develop a computational

method to compute the boundaries of the attraction regions of the system on the phase plane. The boundaries are important in determining how the combination of thermal mass and air initial temperatures affects the final steady state of the system. Further, we will demonstrate how the thermal mass parameters, such as the amount of thermal mass and the interaction strength between the air and the thermal mass can affect the shape of the boundaries (separatrices).

Again we used the same parameters for plotting, unless specially noted in later studies. These parameters are listed in Table 1.

6.2 Transient behaviors

In Chapter 5 we have developed the dynamical system model of the system that is governed by the following equations:

$$f_a(T_a^*, T_m^*) = \frac{dT_a^*}{dt} = \frac{E}{M_a c_a} - \frac{\rho_a c_a}{M_a c_a} \overline{C_d A} \sqrt{\left| 2gH\beta T_a^* - 2\frac{P_w}{\rho_a} \right|} \cdot T_a^* - \frac{UA}{M_a c_a} T_a^* - \frac{hA_m}{M_a c_a} (T_a^* - T_m^*), \quad (6.1)$$

and

$$f_m(T_a^*, T_m^*) = \frac{dT_m^*}{dt} = -\frac{hA_m}{M_m c_m} (T_m^* - T_a^*). \quad (6.2)$$

where T_a^* and T_m^* are defined as the corresponding air and thermal mass temperatures T_a and T_m less the outdoor air temperature T_e :

$$T_a^* = T_a - T_e, \quad (6.3)$$

and

$$T_m^* = T_m - T_e. \quad (6.4)$$

Equation (6.1) is a coupled equation of the airflow and thermal phenomenon. The fluid flow in the system is assumed to be quasi-static since the airflow changes (pressure wave propagation process) much faster than the air temperature (thermal diffusion process). The flow rate is driven by the combination of opposing wind and buoyancy forces, which is given by

$$q = \overline{C_d A} \sqrt{|2gH\beta(T_a - T_e) - 2P_w/\rho_a|}, \quad (6.5)$$

In Equation (6.1), this expression for q was already expanded.

In Chapter 5 (or [75]), we have demonstrated that the system may reach two different steady states (SS1 and SS3) starting from different initial temperatures (if certain conditions are met) by examining the trajectories on the phase plane shown in Figure 6-1. However, an observation of the trajectory characteristics near SS1 and SS3 on the phase plane is that they seem to follow a pattern of first going through a relative horizontal line before gathering at another relative vertical direction to reach the steady state point. Especially, the later direction has a very dense collection of trajectories.

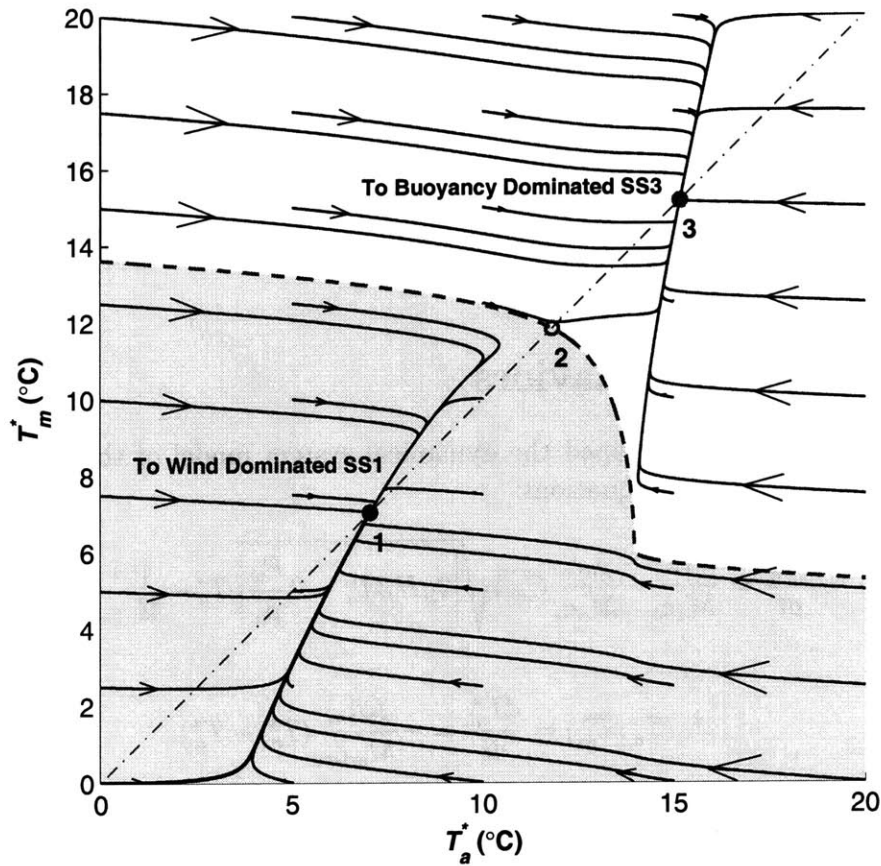


Figure 6-1: The trajectory characteristics of a system with multiple steady states on the phase plane ($h = 5 \text{ W/m}^2\text{-K}$, and $M_m = 6250 \text{ kg}$)

We also mentioned a general pattern of how the air and thermal mass temperatures change with time: a very fast initial change of the air temperature, and a moderate rate change of both air and thermal mass temperature thereafter. One example of the air and thermal mass temperatures change is shown in Figure 6-2 when the system starts from an initial temperature to reach one of the steady states (SS1). Due to the large time constant of the thermal mass, the entire system requires a long time to reach steady states. However, the air temperature increases quickly in the initial stage (the top plot in Figure 6-2). After the initial stage, both the air and the thermal mass temperatures change in a much slower pace before reaching the steady state. We will start explaining this issue while continuing our discussion of the eigen system characteristics generalized in Chapter 5.

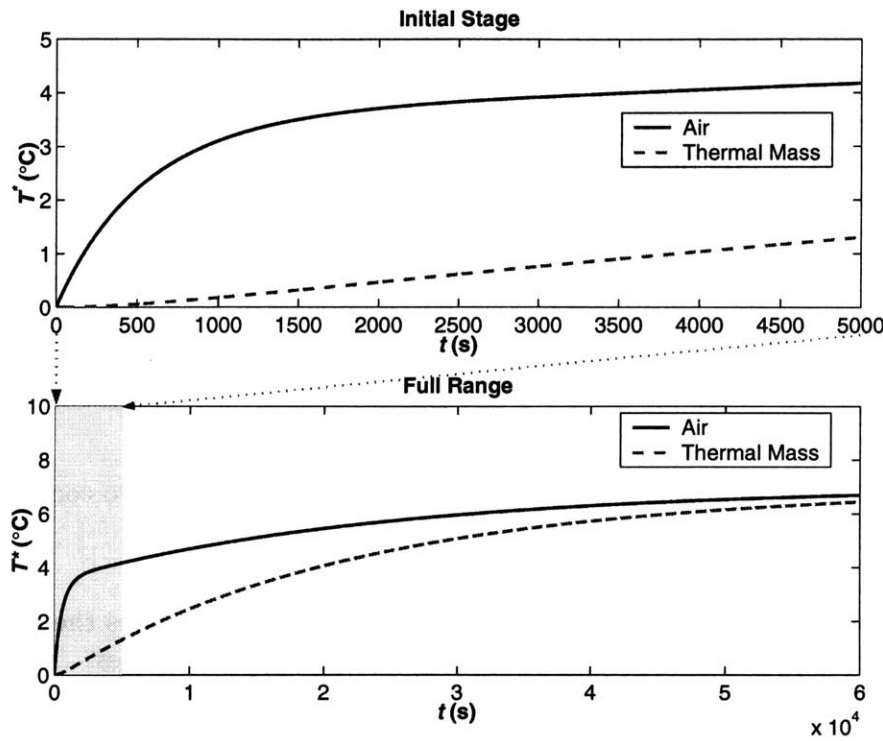


Figure 6-2: The air and the thermal mass temperatures vs. time: initial stage and full range

6.3 Trajectory characteristics near Steady States 1 and 3

In Chapter 5 (or [75]) of this study we have demonstrated that the eigenvalues of the Jacobian matrix determine the local stability of the steady states. SS1 and SS3 are stable nodes where the Jacobian matrix of the linearized system has two negative eigenvalues.

In this section, we will further examine the trajectories near the three steady states using a linearized system approximation and explain their time characteristics by the eigenvectors of the linearized system. Using the trajectory characterizes and the eigenvectors, the different rates of change of the air temperature in the initial stage and the stage thereafter shown in Figure 6-2 will be explained.

More importantly, we will explain the change of the linear system characteristics as influenced by the nonlinear dynamics associated with multiple steady states. The linear system approximation will be further used to explain a “ghost” fixed point phenomenon stated in Chapter 5.

6.3.1 Trajectories near SS1 and SS3

The directions of the two linear system manifolds can be determined by the *eigenvectors* of the Jacobian matrix. In Chapter 5 (or [75]), we have derived that the linearized system at SS1 or SS3 has two eigenvalues λ_1 and λ_2 that satisfy $\lambda_2 < \lambda_1 < 0$. The two corresponding eigenvectors \vec{v}_1 and \vec{v}_2 for λ_1 and λ_2 are defined as vectors that satisfy

$$\mathbf{J}\vec{v}_1 = \lambda_1\vec{v}_1, \text{ and } \mathbf{J}\vec{v}_2 = \lambda_2\vec{v}_2. \quad (6.6)$$

The two directions along the lines spanned by \vec{v}_1 and \vec{v}_2 respectively are called the *eigendirections* of the linearized system. The solution of the linear system is characterized by

$$\mathbf{T} = c_1\vec{v}_1 e^{-\lambda_1 t} + c_2\vec{v}_2 e^{-\lambda_2 t}, \quad (6.7)$$

where \mathbf{T} denotes the temperature vector $[T_a^*, T_m^*]^t$; c_1 and c_2 are two constants determined by the initial values:

$$\mathbf{T}_0 = c_1\vec{v}_1 + c_2\vec{v}_2. \quad (6.8)$$

For the stable node SS1 and SS3, the eigenvectors also indicate the two eigendirections by which the trajectories converge to these stable nodes. For SS1 and SS3, we have derived from previous sections that the eigenvalues λ_1 and λ_2 satisfies $\lambda_2 < \lambda_1 < 0$. Figure 6-3 shows the two eigendirections (the dashed lines) at stable nodes SS1 and SS3 respectively. Since $|\lambda_2| > |\lambda_1|$, the exponential decay term of \vec{v}_2 in Equation (6.7) decays with faster rate of $e^{-\lambda_2 t}$ and the exponential decay term of \vec{v}_1 decays with a slower rate of $e^{-\lambda_1 t}$. The eigendirection determined by the eigenvector \vec{v}_2 is called the *fast eigendirection*, and the eigendirection determined by the eigenvector \vec{v}_1 is called the *slow eigendirection*. The system converges at a faster rate to SS1 (or SS3) along the fast eigendirection and a slower rate along the slow eigendirection as is shown in Figure 6-3 (and Figure 6-1).

A general pattern for the trajectories in Figure 6-1 to Figure 6-3 is that they first quickly progress in the direction of the fast eigendirection \vec{v}_2 and then gather along the slow eigendirection \vec{v}_1 . Graphically, the trajectories are sparser along the fast eigendirection and are denser along the slow eigendirection and denser along the slow eigendirection, especially when the magnitudes of λ_1 and λ_2 are significantly different, for example, different in orders of magnitude.

The slow and fast eigendirections can be used to explain the physical process of how the system approaches a steady state. In this air-mass system, the fast eigendirection is shown to be more horizontal which indicates a direction where air temperature changes much faster than the thermal mass temperature changes only in a much slower pace. The slow eigendirection is more vertical which indicates a direction where both the air and the thermal mass temperatures change in a closer pace. Therefore, the fast moving of the trajectories in the fast eigendirection corresponds to the very fast air temperature change in the initial stage (similar to that in the initial stage of Figure 6-2). After the initial stage the system will gradually enter the slow eigendirection, where the air and the thermal mass temperatures change together in a closer pace (similar to the process after the initial stage in Figure 6-2). However, this process along the slow eigendirection takes much longer time than the initial stage along the

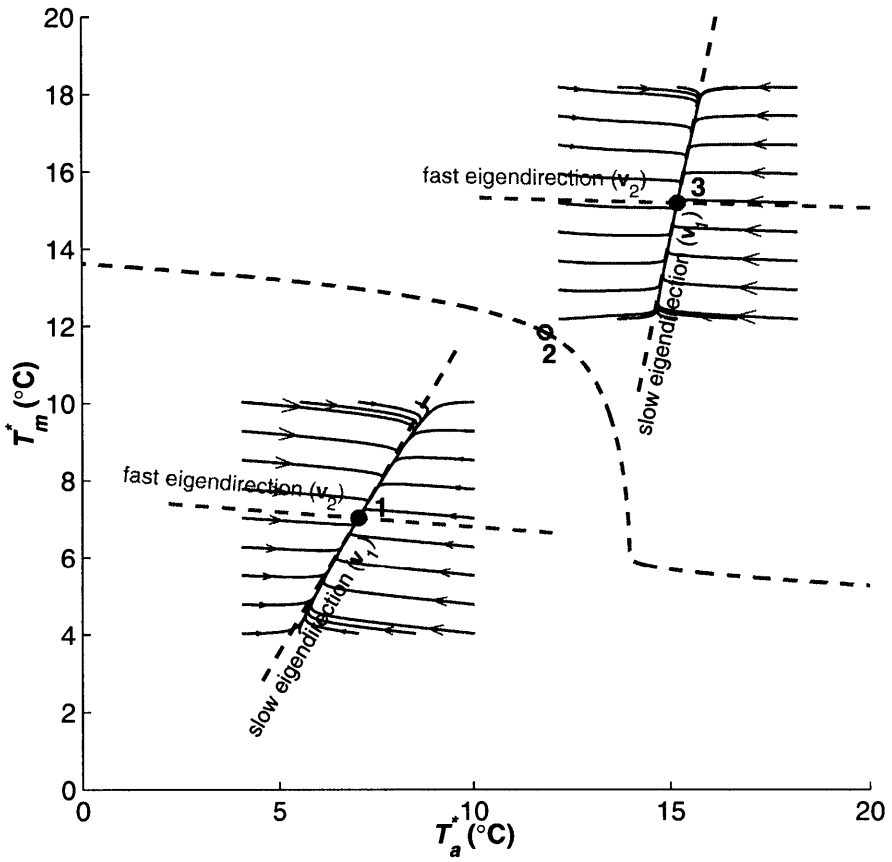


Figure 6-3: Fast and slow eigendirections of the linearized system near SS1 and SS3

fast eigendirection.

6.3.2 Applications of linear approximations

Strictly speaking, the system is not linear around either SS1 or SS3, although the system characteristics can be explained by the eigen characteristics of the linear system. However, as was shown in previous sections, the linear system approximation does explain the time characteristics of the system temperature changes around SS1 and SS3. In Chapter 5, the local stabilities of the system at different steady states were also explained by the linear system approximation argument. Further, the eigenvector explanation of the system behaviors near the steady states can also be applied to the systems that have only one steady state (e.g. the systems in Figure 5). In both Figure 5a and Figure 5b, most of the trajectories also move (approximately) along the fast eigendirection and finally gather along the slow eigendirection before finally reaching the only steady state of the system (SS1 for Figure 5a or SS3 for Figure 5b, respectively). This pattern generally indicates that the air temperature will change very fast in an initial stage and both the air and the thermal mass temperatures will change in a slower pace thereafter to reach the steady state.

6.3.3 Nonlinear effect—Bottleneck effect revisit

Although the linear approximation is generally valid for the air-mass system, the nonlinear effect can still affect it in at least two scenarios. The first scenario is when multiple steady states exist. The phase plane is divided into two attraction regions and the system needs to be treated differently in the two regions for the two possible steady states (SS1 and SS3), respectively.

The second scenario is even more important. Even when the system has only one steady state (see Figure 6-4(b)), the nonlinear behaviors of the system may still affect the linear approximation, for example, by the bottleneck effect caused by a “ghost” steady state discussed in Chapter 5. In this section, we will provide a further explanation to the time delay effect of the bottleneck and “ghost” and demonstrate how it can affect the system from the linear approximation aspect.

Using the linear approximation conclusions obtained from previous sections, we can demonstrate associated time features in the trajectories that are affected by the “ghost”. The entire process that a particular trajectory (that is affected by the ghost) undergoes can be roughly divided into four stages:

1. In the first stage, the system will go through the “virtual” fast eigendirection of the “ghost” steady state. Although the steady state does not really exist, its attraction features make it still like a steady state fixed point that can attract trajectories. The system will first go through a “virtual” fast eigendirection of the “ghost” and the time associated with that period is relatively small (in the order of 10^3 s). In about 1000s the air temperature will drop about $3.5\text{ }^\circ\text{C}$ but the thermal mass temperature only changes less than $0.5\text{ }^\circ\text{C}$.
2. In the second stage, the system will pass the “virtual” slow eigendirection of the “ghost”. This process will last for about 4×10^4 s, which is about $1/3$ of the total time (to reach the steady state). During this period, the total change in the air temperature is small; but the total change in the thermal mass temperature is relatively large, which is about $3.5\text{ }^\circ\text{C}$ in this case. Essentially, at the end of this stage, the thermal mass catches up with the air temperature change, yielding almost identical thermal mass and air temperatures at the end of the stage. It is similar to going along a “slow” eigendirection track of a “ghost” SS3 (which does not really exist), although in reality there is not a steady state (or fixed point) there.
3. In the third stage, the system enters the fast eigendirection of SS1, the air temperature drops very fast again in a short time period (in the order of 10^3 s) with little thermal mass temperature change. In this stage, the system is going on a fast eigendirection tract of the real steady state (SS1), which is similar to the initial stage of Figure 6-2 except in an opposite direction.
4. In the fourth stage, the system will again enter the slow eigendirection of SS1. The thermal mass and the air temperatures change concurrently with a moderate pace, until finally reaching the steady state SS1. This is similar to the stage after the initial stage in Figure 6-2 except in an opposite direction.

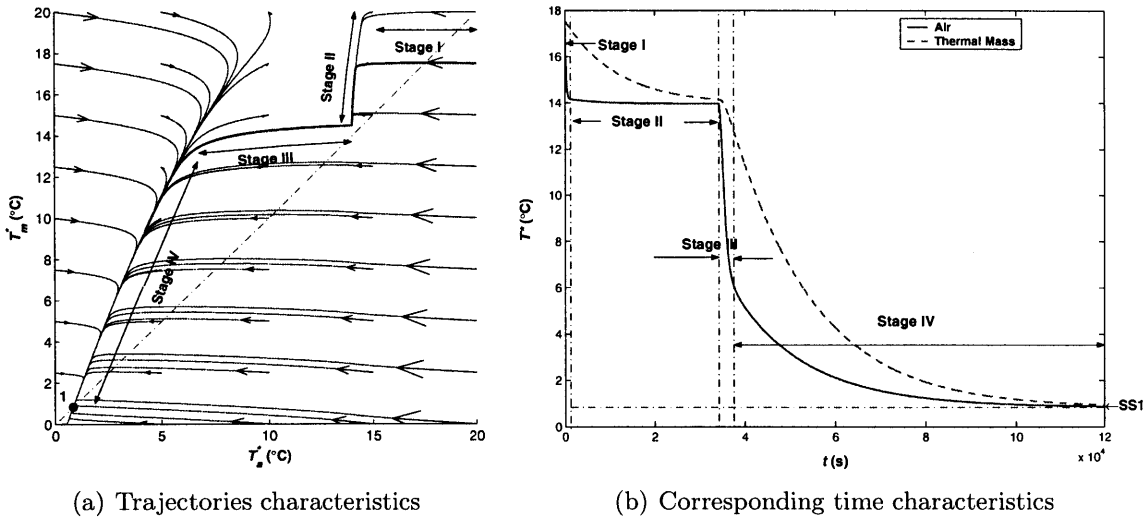


Figure 6-4: Trajectories and time characteristics for a system that has only one steady state (SS1)

Similarly, the process to reach another higher steady state (SS3) from a lower initial temperature can also be roughly divided into four stages, as is shown in Figure 6-5(b). The time spent on the bottleneck stages (Stages I and II) is even longer in this scenario, mainly due to the fact that the thermal mass temperature needs to undergo a larger change when passing the bottleneck in Stage II.

In summary, the process for the system to reach a steady state from a system that have only one steady state may be affected by the nonlinearity of the system, especially the remnant effect of a “ghost” steady state. They may first pass a bottleneck where both the air and the thermal mass temperature derivatives (over time) are very small. This is somehow similar to a system that has to “reach” another “ghost” steady state before finally settling down to the real steady state.

6.4 Trajectory characteristics near Steady State 2

The trajectories near the unstable steady state SS2 are important to determine the long-term dynamics behaviors of the system. For example, the separatrices, dividing lines that divide the phase plane into two attraction regions in which trajectories converge to two different steady states (SS1 and SS2), passes this unstable steady state. In Chapter 5, we have proved mathematically that that SS2 is a saddle where the linearized system matrix has one negative eigenvalue and one positive eigenvalue regardless of the value of the thermal mass parameters. In this section we will demonstrate that the important trajectory properties determined by the eigen characteristics of the linearized system at SS2. These properties are useful in explaining the dynamical behaviors of the unstable steady state and the shape of the separatrices on the phase plane. Further, an effective computational method can be developed to compute the separatrices, based on the theoretical analysis.

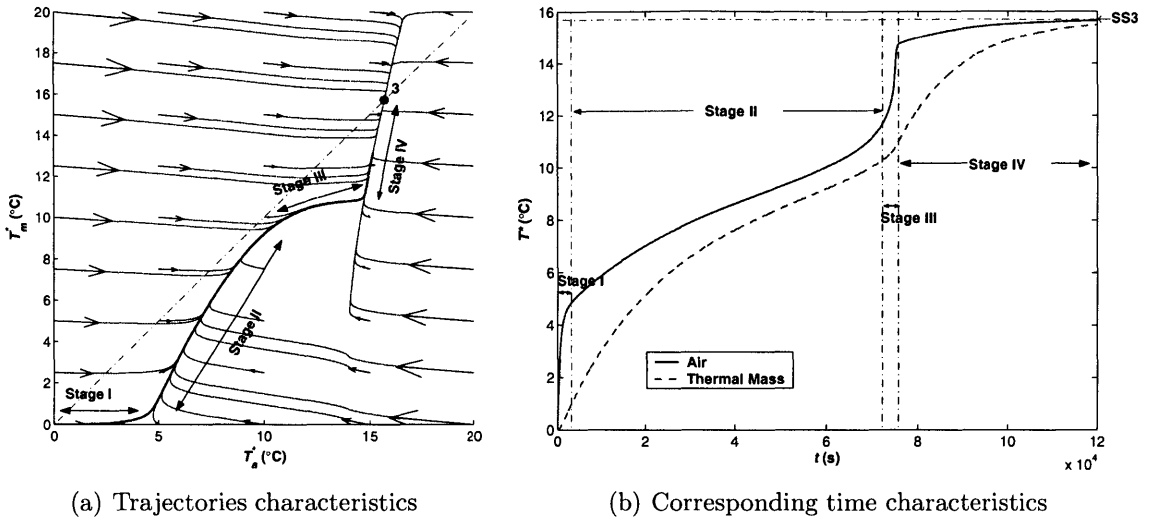


Figure 6-5: Trajectories and time characteristics for another system that has only one steady state (SS3)

6.4.1 Eigen characteristics

As is shown in Chapter 5, at the saddle SS2, the two eigenvalues λ_1 and λ_2 satisfy $\lambda_2 < 0 < \lambda_1$. The two eigendirections determined by the corresponding eigenvectors \vec{v}_1 and \vec{v}_2 have special meanings as well. Since $\lambda_2 < 0$, the corresponding eigenvector \vec{v}_2 will determine the direction that the trajectories converge to the saddle SS2. Similarly, since $\lambda_1 > 0$, the corresponding eigenvector \vec{v}_1 will determine the direction that the trajectories diverge from SS2. These two eigendirections are also shown as the two dashed lines passing through SS2.

Since SS2 is a saddle, two special trajectories will converge to it temporarily and then quickly diverge to either the stable nodes SS1 or SS3, depending on the directions of the infinitesimal perturbations. Figure 6-6 shows the incoming trajectories to and the outgoing trajectories from SS2. In dynamical systems, the two incoming trajectories are called *stable manifolds* of a saddle and the two outgoing saddles are named the *unstable manifolds* of the saddle.

For the linearized system at SS2, the eigendirection determined by \vec{v}_2 in Figure 6-6 is (and should be) tangent to the stable manifolds nonlinear system at SS2 on the phase plane. The eigendirection spanned by \vec{v}_1 is also tangent to the unstable manifolds of the nonlinear system at SS2. Essentially, the two eigendirections are the stable and unstable manifolds the linear system linearized at SS2.

6.4.2 Compute the separatrices

The stable manifolds are important since they form the boundaries (separatrices) of the basin attractions, which is very useful to determine the long-term behaviors of the system starting from an initial value. The separatrices can be obtained through calculating the stable manifolds of the saddle. Indeed, the separatrices in Figure 6-1

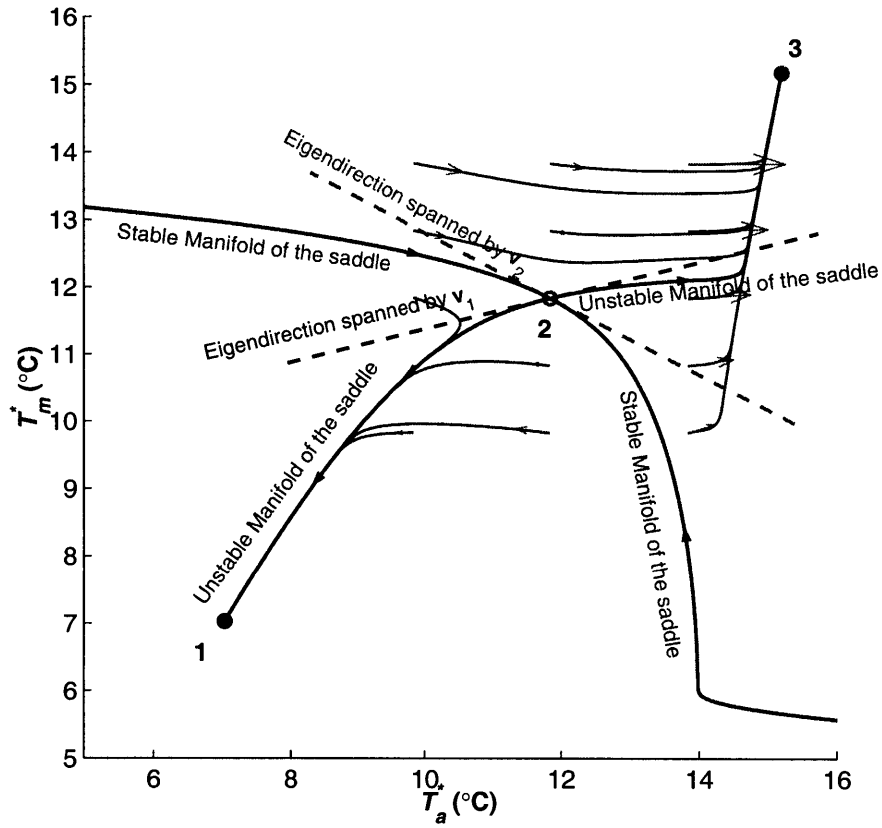


Figure 6-6: Stable and unstable manifolds of the saddle point (Steady State 2)

were calculated by this method. In this section, we will discuss the details of this computational method.

As was discussed in previous subsections, the separtrices are the stable manifolds of the saddle SS2. The stable manifolds can thus be obtained by reversing the time of the dynamical system starting from SS2. That is, we track the incoming trajectories back from SS2. To do this, we replace the term t in Equations (6.1) and (6.2) by $-t$. At the same time, the initial conditions will be set at $[T_{ss2}^*, T_{ss2}^*]'$. With this approach, the system will automatically diverge from SS2 along one of the stable manifolds shown in Figure 6-6, depending on the direction of the initial perturbation. Practically, in order to obtain both unstable manifolds, we can start the reversed time system start from an infinitesimal offset from $[T_{ss2}^*, T_{ss2}^*]'$ along the eigendirection determined by \vec{v}_2 , which means

$$\mathbf{T}_0 = \begin{bmatrix} T_{ss2}^* \\ T_{ss2}^* \end{bmatrix} \pm \varepsilon \frac{\vec{v}_2}{\|\vec{v}_2\|}, \quad (6.9)$$

where $\|\vec{v}_2\|$ is the norm (or length) of the vector \vec{v}_2 , and ε is an infinitesimal positive number. In actual computation, a reasonably small number (e.g. 10^{-3} °C) can be used for ε to account for numerical errors (e.g. round-off and truncation errors).

6.5 Impact of thermal mass parameters on separatrices shapes

The separatrices, which are two special trajectories on the phase plane, will also be different when the hA_m value changes. In this section, we will investigate the change of the system due to hA_m – an indication of the strength of the air-mass interactions.

6.5.1 Impact of hA_m values

6.5.1.1 General pattern

Figure 6-7(a) shows a case with a lower hA_m value (only half of that in the base case shown in Figure 6-1). As the hA_m decreases, the “central” part (where $T_a^* \approx 10 - 14$ °C) of the separatrices becomes more “vertical”, which indicates the air temperature is more dominant in determining the final steady state of the temperature. Figure 6-7(b) shows an example with a higher hA_m value that is twice the hA_m in the base case in Figure 6-1. As is expected, the “central” part of the separatrices becomes flatter and narrower, which indicates that the initial thermal mass temperature becomes more important as the convective heat transfer strength between the air and the thermal mass becomes stronger. Physically, as the interactions between the air and the thermal mass become stronger, the air temperature follows the thermal mass temperature more closely. Therefore, the air temperature is closer to the thermal mass temperature when hA_m values increases, which makes the thermal mass more dominant in determining the system’s final steady state.

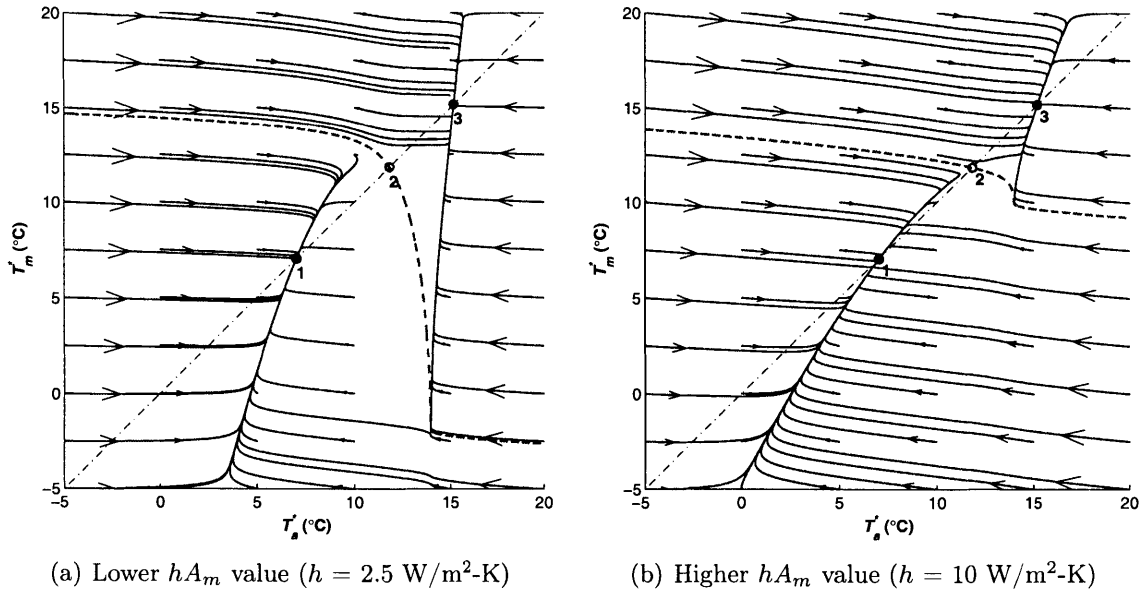


Figure 6-7: Trajectories and separatrices for two different hA_m values ($A_m = 100 \text{ m}^2$)

For different hA_m values, the shapes of the separatrices are also different on the

two “wings”, especially on the lower-right “wing”. For example, to achieve a wind-dominated SS1 from a relatively high air temperature (e.g. a T_a^* of 15 °C), the system with a lower hA_m value (Figure 6-7(a)) requires the thermal mass to be initially chilled down to at least 2 °C below the outdoor air temperature (i.e., $T_m^* \approx -2$ °C on the separatrices). However, for the system with the system with a higher hA_m value (Figure 6-7(b)), the system can achieve SS1 for a much higher thermal mass temperature range (i.e., as far as $T_m^* < \sim 10$ °C according to the separatrices on Figure 6-7(b)).

6.5.1.2 Variations of the separatrices

Since the separatrices is very important in determining the long-term (steady state) behaviors when the system starts from an initial combination of temperatures, the separatrices variations should be carefully studied when the thermal mass parameters vary. In the previous subsection we have demonstrated the differences of the differences of the separatrices for two different hA_m values. In this subsection, we would examine the trend of the separatrices variations for more hA_m values.

The differences in the separatrices for different hA_m values are further demonstrated in Figure 6-8. Figure 6-8 shows the separatrices for a series of hA_m values including the two extreme cases ($hA_m \rightarrow 0$ and $hA_m \rightarrow \infty$) discussed in a previous section. When the $hA_m \rightarrow 0$ (or a tiny value), the separatrices shown in Figure 6-8 become almost a vertical line passing through SS2. This indicates that the air temperature becomes the only factor that determines the final steady state and its critical point is SS2. This agrees with the single zone case where $hA_m \rightarrow 0$ discussed in Chapter 5 (or[75]).

When the hA_m value increases toward ∞ , the separatrices shown in Figure 6-8 will approach a line passing through SS2 with a slope of $-\frac{M_a c_a}{M_m c_m}$. The explanation to this observation requires a further examination on the physical processes in this scenario. When $hA_m \rightarrow \infty$, the heat transfer between the air and the thermal mass will be so strong that the process is essentially adiabatic. Therefore, from an arbitrary initial point (T_{a0}^*, T_{m0}^*) , the air and the thermal mass will first reach a common temperature through an adiabatic heat transfer process. The temperature is represented by

$$T^* = \frac{M_a c_a}{M_m c_m + M_a c_a} T_{a0}^* + \frac{M_m c_m}{M_m c_m + M_a c_a} T_{m0}^*. \quad (6.10)$$

If the mixed temperature T^* is higher than T_{ss2}^* (the temperature of SS2), according to the system curve of the extreme case of $hA_m \rightarrow \infty$ discussed in Chapter 5, the system will finally reach the buoyancy-dominated SS3. If T^* is lower than T_{ss2}^* , the system will finally reach the wind-dominated SS1. Therefore the separatrices on the phase plane are described by

$$\frac{M_a c_a}{M_m c_m + M_a c_a} T_a^* + \frac{M_m c_m}{M_m c_m + M_a c_a} T_m^* = T_{ss2}^*. \quad (6.11)$$

which is a line that passes (T_{ss2}^*, T_{ss2}^*) with a slope of $-\frac{M_a c_a}{M_m c_m}$.

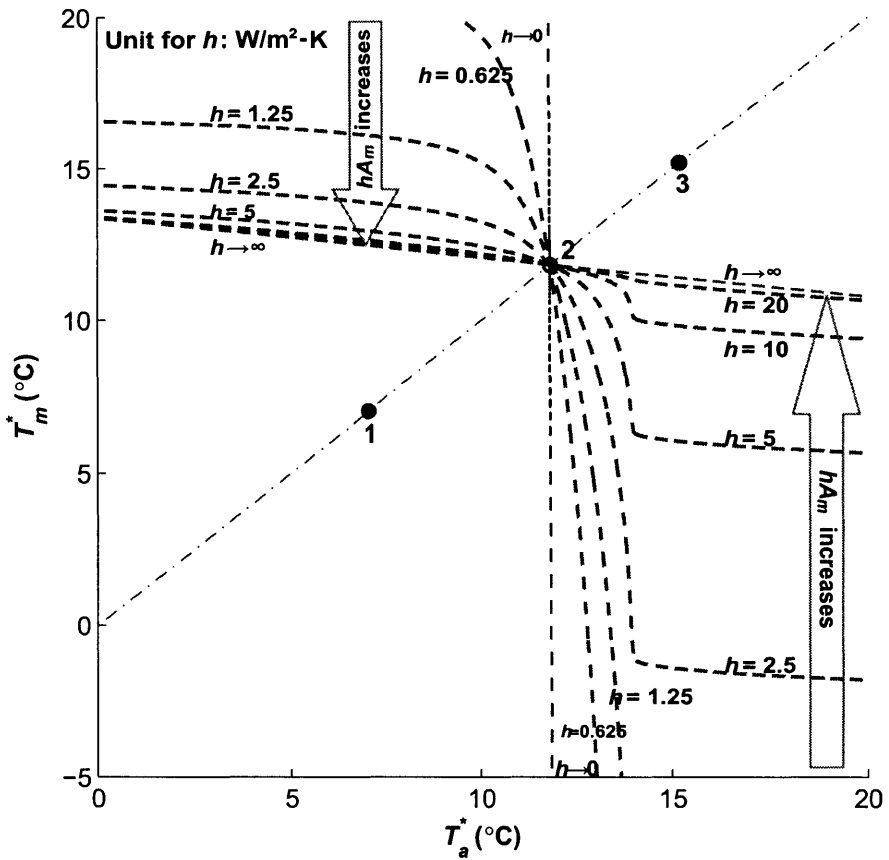


Figure 6-8: The separatrices for different hA_m values ($A_m = 100 \text{ m}^2$)

6.5.2 Impact of $M_m c_m$ on the separatrices

6.5.2.1 General pattern

For different $M_m c_m$ values, the separatrices and the attraction regions differ as well, especially on the two “wings”. For example, Figure 6-9(a) shows the separatrices of a system with only half of thermal mass in the base case shown in Figure 6-1. With lighter thermal mass ($M_m = 3,125 \text{ kg}$), the trajectories and arrows (which stands for the rate of the changes of the air and thermal mass temperatures) in Figure 6-9(a) have gained larger vertical components, which means the thermal mass temperature is now easier to change due to the smaller heat capacities. Therefore the separatrices become more downward inclined on the two “wings” and the air temperature gains more weight in determining the final steady state of the system. The system with heavier thermal mass shown in Figure 6-9(b) shows the opposite trend in shapes of the trajectories and the arrows. With a heavier thermal ($M_m = 12,500 \text{ kg}$), the slope of the two “wings” becomes flatter and the air temperature gains less weight in determining the final steady state.

Physically, since heavier thermal mass represents larger heat capacities, a system

with heavier thermal mass will thus have more potential to consistently affect the air temperature. Therefore, the thermal mass becomes more dominant especially when the temperature difference between the air and the thermal mass is initially large. These correspond to the two “wings” on the separatrices, where the differences between the air and thermal mass temperatures are large.

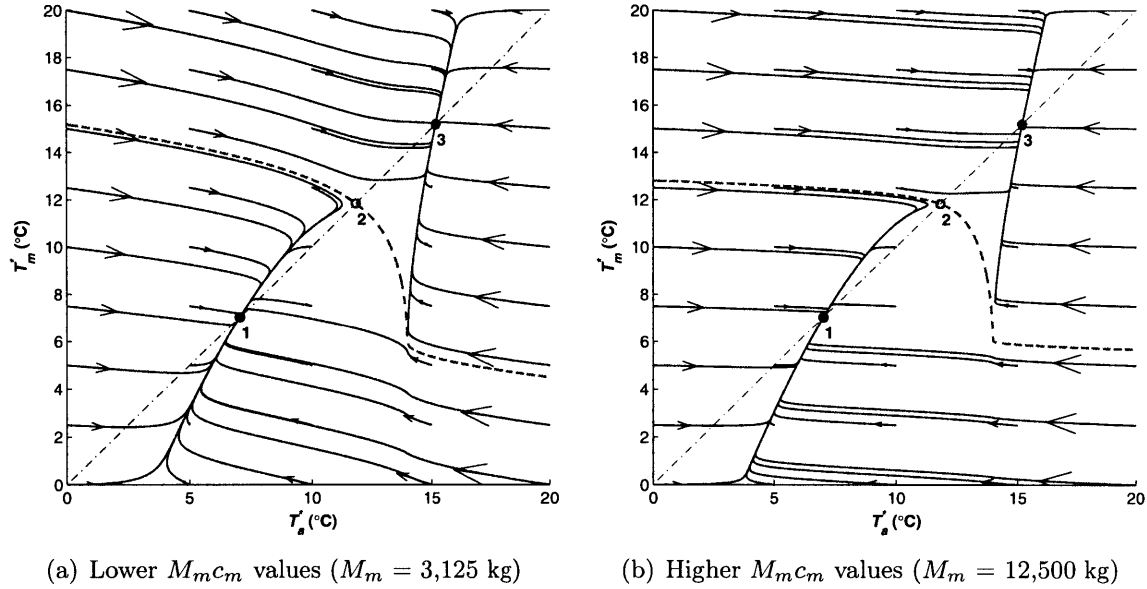


Figure 6-9: Separatrices and attractions regions on the phase plane when for two different M_m values

6.5.2.2 Variations on the separatrices

The impact of thermal mass weight on the separatrices for more M_{mc_m} values is further demonstrated in Figure 6-10. In the special case of $M_m \rightarrow 0$, the separatrices becomes vertical, where the thermal mass interaction becomes negligible. An increase of M_m tends to flatten the two “wings” of the separatrices since the thermal mass weights more in determining the final steady state of the system. In the special case of $M_m \rightarrow \infty$, the two “wings” of the separatrices flatten toward horizontal but the center part (near SS2) still keeps part of the vertically curved shape. This means the air temperature keeps its influence on the final steady state of the system in the center region. In this region, the final steady states will be determined by both the air and the thermal mass initial temperatures. However, as M_m increases, it will take much longer time for the thermal mass temperature to change. For the $M_m \rightarrow \infty$ case, although theoretically it will finally reach a steady state, the vertical movement of the thermal trajectory on the phase plane (which means change in thermal mass temperature) will tend to take infinite time.

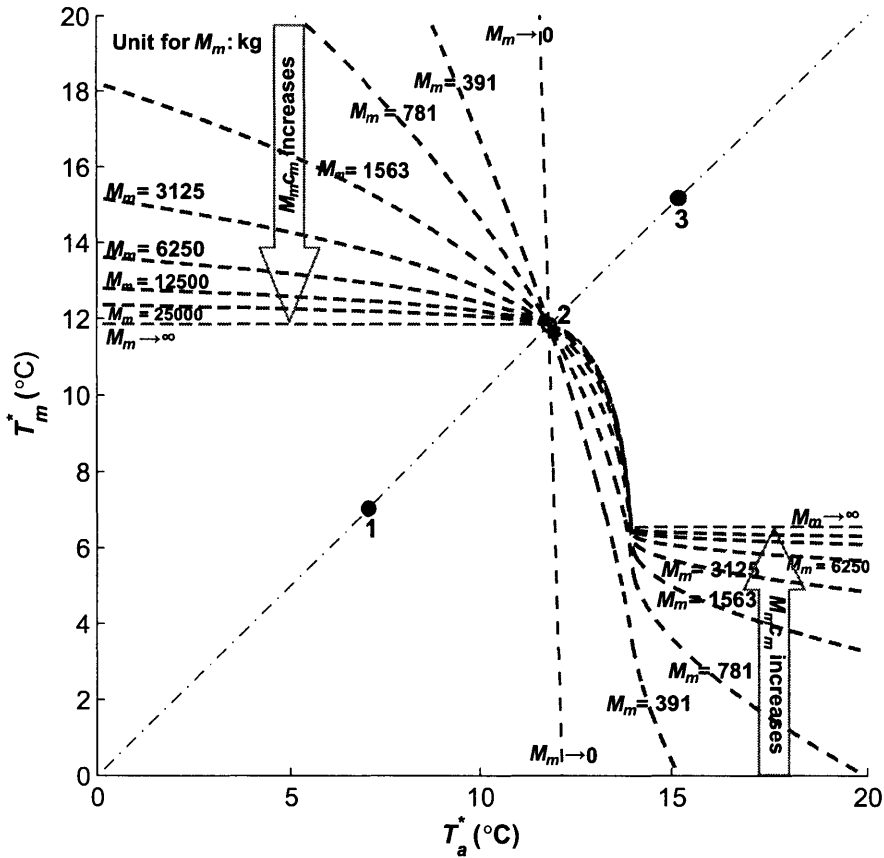


Figure 6-10: The separatrices for different thermal mass weights

6.6 Factors that affect the shape of the separatrices

The separatrices are important to the dynamical system features of the system. Different separatrices shapes will result in different divisions of the attraction regions, and thus different long-term (steady state) behaviors of the system. Although we provided a computational method in a previous section, here we will provide an analysis of the (qualitative) factors that can affect (or determine) the shape of the separatrices to understand the mechanism of how the separatrices are affected by the thermal mass parameters. In this section, we will single out at least three factors that can affect the shape of the trajectories: the position of a special point, the eigendirection near SS2, and the vector flow direction.

6.6.1 Special point O

The first important parameter is a special point O on the nullcline. Figure 6-11 shows the relation between the nullclines and the separatrices. The special point O on the nullcline is a point where the airflow rate $q = 0$ and $dT_a^*/dt = 0$. Physically, at this point, the air is at a temporary equilibrium state while the system has no air flow

exchange with the exterior. This equilibrium is temporary because the thermal mass does not gain an energy balance. The mass temperature will still change over time and the temporary energy equilibrium for the air will be broken. Nevertheless, the air and the thermal mass temperatures of the system at point O can be calculated by

$$T_{ao}^* = \frac{P_w}{\rho_a g H \beta} = P^{**}/\beta, \quad (6.12)$$

and

$$T_{mO}^* = \left(1 + \frac{UA}{hA_m}\right) T_a^* - \frac{E}{hA_m} = \left(1 + \frac{UA}{hA_m}\right) \frac{P^{**}}{\beta} - \frac{E}{hA_m} = \frac{P^{**}}{\beta} - \frac{E - UA \cdot P^{**}/\beta}{hA_m}, \quad (6.13)$$

where P^{**} is defined as

$$P^{**} = \frac{P_w}{\rho_a g H}. \quad (6.14)$$

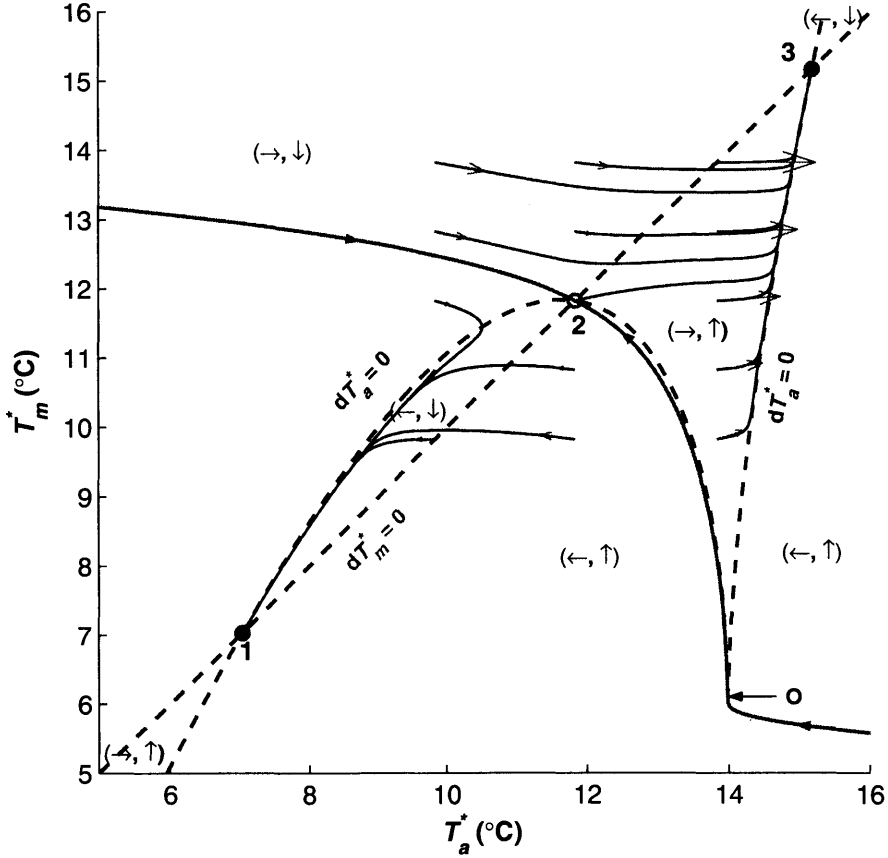


Figure 6-11: Separatrices vs. Nullclines on phase plane

According to the condition we derived for the system to have multiple steady states in Chapter 5 (or [75]), the term $\frac{E - UA \cdot P^{**}/\beta}{hA_m}$ in Equation (6.13) is always greater or equal than zero when multiple steady state exist since $UA \cdot P^{**} < \beta E$ is one of the

conditions for the system multiple steady states. Therefore, the point O is always below the diagonal line of $T_a^* = T_m^*$ when the system has multiple steady states. The term $\frac{E - UA \cdot P^{**}/\beta}{hA_m}$ represents the temperature differences between the air and the thermal mass at the special point O.

Starting from the special point O, the system will always reach the SS3 when multiple steady states exist in the system. More generally, on the $dT_a^*/dt = 0$ nullcline, starting from all the points to the right of SS2, the system will also converge to SS3. Therefore, on the phase plane, the right half of separatrices (where $T_a^* > T_{ss2}^*$) must always be lower than the $dT_a^*/dt = 0$ nullcline. This is determined by the vector flow directions on the phase plane. We can use a $(+/-, +/-)$ notation to indicate the signs of dT_a^*/dt and dT_m^*/dt . A corresponding $(\rightarrow / \leftarrow, \uparrow / \downarrow)$ will indicate the vector direction. For example, a $(+, +)$ stands for $dT_a^*/dt > 0$ and $dT_m^*/dt > 0$, thus leading to a (\rightarrow, \uparrow) type vector direction on the phase plane. Similarly, a $(-, +)$ stands for $dT_a^*/dt < 0$ and $dT_m^*/dt > 0$, thus leading to a (\leftarrow, \uparrow) type vector direction notation on the phase plane. Using this notation, the phase plane is divided into different regions with different vector directions by the two nullclines, as are shown in Figure 6-11.

The separatrices (or stable manifolds) are special incoming trajectories to SS2, which means the stable manifolds must have a negative x-component and a positive y-component on the lower branch (the part below the diagonal $T_a^* = T_m^*$ line). Since the nullcline that connects SS2 and point O satisfies $dT_a^*/dt = 0$, the stable manifolds must be below the SS2-O nullcline section. Therefore the position of the point O is an important point that roughly “pinpoints” (and affects) the rough position and shape of the stable manifolds (the separatrices) when multiple steady states exist in the system. With other parameters fixed, the position of the point is influenced by the hA_m value as is shown in Equation (6.13), although it is independent of the thermal mass weight M_m . The larger the hA_m value, the closer the air and the thermal mass temperatures at this point. On the phase plane, this means the point O is closer to the diagonal line (or SS2) when hA_m is larger. The point O will be in the attraction region of SS3 when multiple steady states exist. This partially explains the differences in the lower half of the separatrices in Figure 6-8: the positions of point O are different on the phase plane for different different hAm values, which makes the separatrices “turn” right at different thermal mass temperature values. One clarification is that although the point O looks very close to the turning point of the separatrices, it not exactly the point, especially when hA_m value is large. When hA_m is large, the correspoing point O is very close to the diagonal $T_a^* = T_m^*$ line on the phase plane. However, the separatrices turning point is far below the diagonal line. In this scenario, although the relation between point O and the turning point of the separatrices is not violated, they are not so close to each other. Therefore, the relation between the separatrices and the point is just a rough constraint that the separatrices should satisfy. Nevertheless, the point O and the turning point of the separatrices are generally close for non-so-extreme hA_m values.

6.6.2 Vector directions on phase plane

The vector direction is the direction of the flow vectors in the field, namely, the tangency of the trajectories. Since the separatrices are two special trajectories (the stable manifolds), the shape of the separatrices will be affected by also the directions of the flow vectors, especially those on the two “wings”. The rational behind it is the ratio of the x-component of the vector described by Equation (6.1) and the y-component of the vector described by Equation (6.2). On the far-ends of the two “wings”, the temperature difference between the air and the thermal mass become very large and the direction is largely affected by the ratio of the x-component over y-component as follows:

$$\theta = \frac{dT_a^*/dt}{dT_m^*/dt} = \frac{M_m c_m}{M_a c_a} \frac{1}{hA_m} \frac{E - (\rho_a c_a \bar{C}_d A \sqrt{|2gH\beta \cdot T_a^* - 2P_w/\rho_a|} + UA) T_a^*}{T_a^* - T_m^*} - \frac{M_m c_m}{M_a c_a}. \quad (6.15)$$

From Equation (6.15), the thermal mass parameters (e.g., $M_m c_m$, hA_m) are shown to be able to affect the vector directions on the phase plane. Since the separatrices are also special trajectories, the shape of the separatrices will also be affected by the thermal mass parameters.

For example, when hA_m value increases, the absolute value of θ will generally tend to decrease. This means the slope of the trajectories will tend to become flatter on the two “wings” with the increase of hA_m . Similarly, when $M_m c_m$ values decrease, the absolute value of θ will decrease as well. These variations explained the variation of the slopes with different hA_m values in Figure 6-8 and with different $M_m c_m$ values in Figure 6-10.

6.6.3 Eigenvector direction at SS2

The second important parameter that affects the shape of the separatrices is the eigenvector of the linearized system near SS2, namely, the tangent direction of the stable manifolds of the nonlinear dynamical system at SS2. The eigendirection \vec{v}_2 determines how the separatrices approaches SS2, which is the basis of the computational algorithm discussed in previous sections. This parameter will change with different thermal mass parameters as well.

In general different eigen characteristics will result in not only different separatrices, but also different trajectory shapes. A general pattern of the variation of the trajectories characteristics with different thermal mass parameters will be discussed in the next section.

6.7 Impact of thermal mass parameters on other dynamical behaviors

The dynamical system characteristics are dependent on various parameters, one of which is the hA_m value, which presents the potential strength of the heat transfer

between the air and the thermal mass. Another important factor that affects the system is the amount of thermal mass. For example, intuitively, with more thermal mass, the system will experience longer time in the “slow” eigendirection track. In this section, we will investigate the impact of the two important parameters — hA_m and M_mc_m respectively.

6.8 Impact of hA_m on dynamical behaviors

In Chapter 5, we have concluded that the change of hA_m value will not fundamentally change the signs of the eigenvalues of the linearized system at the three steady states, which means the qualitative stability characteristics of the steady states will not be affected by the variation of hA_m . However, the magnitudes of the eigenvalues do vary with hA_m , which indicates different time properties of the system. For example, the time the system spends on the fast eigendirection stage and the slow eigendirection stage will change when the magnitudes the eigenvalues change. Further, with different hA_m values, the eigenvector directions will also be different, which may indicate different trajectory shapes near the steady states, especially for the extreme cases (of $hA_m \rightarrow 0$ and $hA_m \rightarrow \infty$).

6.8.0.1 Eigenvalue and eigendirection variations

The eigenvalues of the system near the steady states will change with hA_m values. We will first examine the eigenvalue changes at the two stable steady states SS1 and SS3. Figure 6-12(a) and Figure 6-12(b) show changes of $\lambda_{1,2}$ with different hA_m values (A_m is set to constant as 100 m^2). For both of the two steady states (SS1 in Figure 6-12(a) and SS3 in Figure 6-12(b)), the linerized systems have two eigenvalues that satisfy $\lambda_2 < \lambda_1 < 0$ for all hA_m values, which agrees with the theoretical generalization in Chapter 5 (or [75]).

When hA_m is small ($h \rightarrow 0$), λ_2 (the larger eigenvalue in absolute magnitude) tends to reach a constant value (at $\sim -5 \times 10^{-4}$); while λ_1 (the smaller eigenvalue in absolute magnitude) continuously to decrease to zero. In this situation, the time the system spent on the fast eigenvalue track changes little, while the time spent on the slow eigenvalue track will increase when hA_m decreases.

The eigenvectors \vec{v}_1 and \vec{v}_2 also follows a gradual trend of changes when hA_m changes. For example, when hA_m is small, the (fast) eigenvector \vec{v}_2 is almost parallel to the x-axis on the phase plane. This means in the fast eigendirection stage, only the air temperature changes. The slow eigendirection \vec{v}_1 becomes vertical in this case. This is exactly what we have talked about that the thermal mass is “disconnected” from the system. Since the eigenvalue λ_1 is very close to zero (very small absolute magnitude), the time spent on the slow eigendirection will goes to infinity as $hA_m \rightarrow 0$. Physically, the thermal mass cannot follow the change of the air temperature to reach the steady state point. Rather, the thermal mass will tend to take infinitely long time to reach the steady state temperature.

When hA_m is large ($\rightarrow \infty$), the air and the thermal mass will have very strong heat

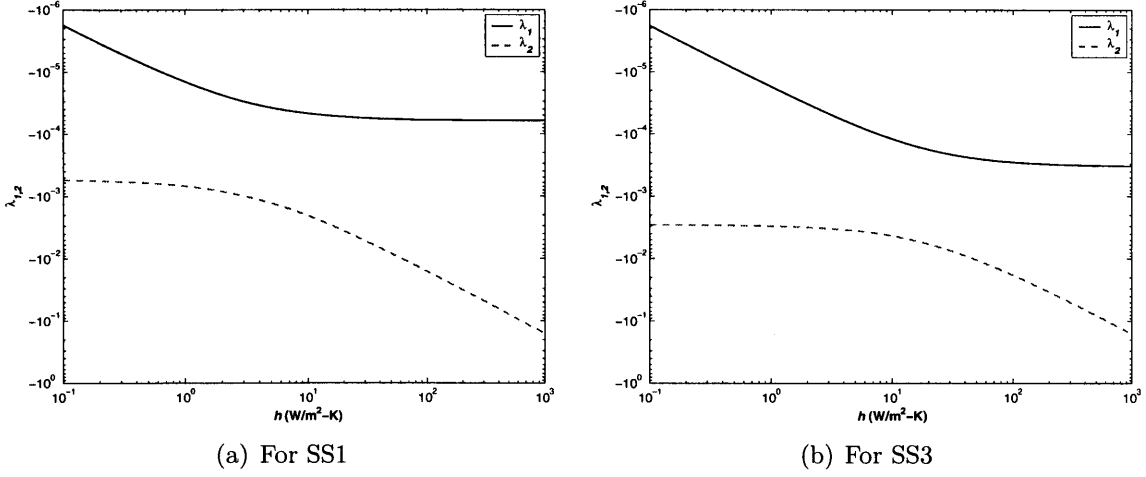


Figure 6-12: The change of the eigenvalues with hA_m values at SS1 and SS3 ($A_m = 100 \text{ m}^2$)

transfer in between for even a small temperature difference. As is shown in Figure 6-12, (the magnitude of) the larger eigenvalue λ_2 grows larger and larger as hA_m increases. This indicates that the time a trajectory spends on the fast eigendirection track will be very short as hA_m is large ($\rightarrow \infty$). Physically, in this large hA_m scenario, the fast eigendirection stage will be an ideal mixing between the air and the thermal mass to reach a common temperature. The eigendirection is therefore a line on the phase plane with a slope of $-\frac{M_{aca}}{M_m c_m}$. The larger hA_m is, the shorter this mixing process (on the fast eigendirection) will take. After the fast eigendirection stage, the air and the thermal mass temperature will almost kept the same at all time and evolve together (with time) to reach the steady state (SS1 or SS3) along the slow eigendirection, which is very close to the $T_a^* = T_m^*$ line (the diagonal line) on the phase plot.

Now we will examine the change of the eigen characteristics near SS2 when hA_m values changes. The values of two eigenvalues λ_1 and λ_2 for different hA_m values are plotted in Figure (6-13). The positive eigenvalue λ_1 increases to a value of $\sim 10^{-3}$ when hA_m approaches 0, and decreases to a value of $\sim 10^{-4}$ as hA_m value increases to $+\infty$. The corresponding eigendirection \vec{v}_1 for $hA_m \rightarrow 0$ is along the horizontal direction, which means the air temperature will change but the thermal mass temperature will hardly change, starting from SS2. As $hA_m \rightarrow \infty$, the eigendirection \vec{v}_1 will be suppressed to the diagonal line on the phase plane, which indicates that the air and the thermal mass will almost always keep the same when evolving to a stable steady state (SS1 or SS3).

6.8.1 Impact of $M_m c_m$ on dynamical behaviors

In this subsection, we will investigate the mechanism of how the thermal mass weight influences the dynamical system behaviors. In order to do this, we will keep the

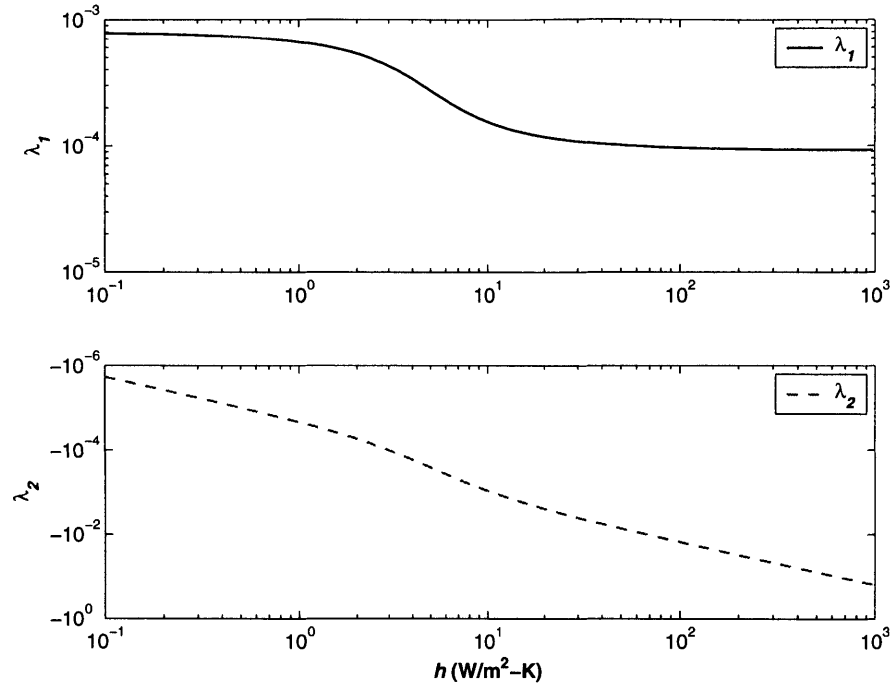


Figure 6-13: Variations of the two eigenvalues of the linearized system at SS2 with different hA_m values

hA_m value constant and vary the M_mc_m value. The shape of the trajectories and the time associated with different parts of the trajectories will expect to be different with different thermal mass weight.

6.8.1.1 Variations on eigen characteristics

The differences in the trajectories for different M_mc_m values can be explained by the eigenvalues and the eigenvectors of the linearized system around its steady state. Figure 6-14 shows the eigenvalues for different M_mc_m values for the linearized systems at SS1 and SS3. The general pattern is exactly opposite to the hA_m variation case. The magnitude of eigenvalue λ_2 will increase when $M_mc_m \rightarrow 0$ and decrease to a relative constant value when $M_mc_m \rightarrow \infty$. This means the time the system spend on the fast eigendirection \vec{v}_2 will become very short when $M_mc_m \rightarrow 0$ and relatively constant when $M_mc_m \rightarrow \infty$. On the other hand, the magnitude of eigenvalue λ_1 will increase to a moderate value when $M_mc_m \rightarrow 0$ and decrease asymptotically toward zero as $M_mc_m \rightarrow \infty$. This indicates that the time the system spends on the slow eigendirection (\vec{v}_2) track will reduce become infinite when $M_mc_m \rightarrow \infty$. Physically, with infinite thermal mass, the time for the thermal mass to reach a steady state will become infinity.

For the system linearized at SS2, the eigenvalues for different M_mc_m values are plotted in Figure 6-15. Different from the trend with varying hA_m case presented in previous section, when M_mc_m increases, the (absolute) magnitudes of both of the

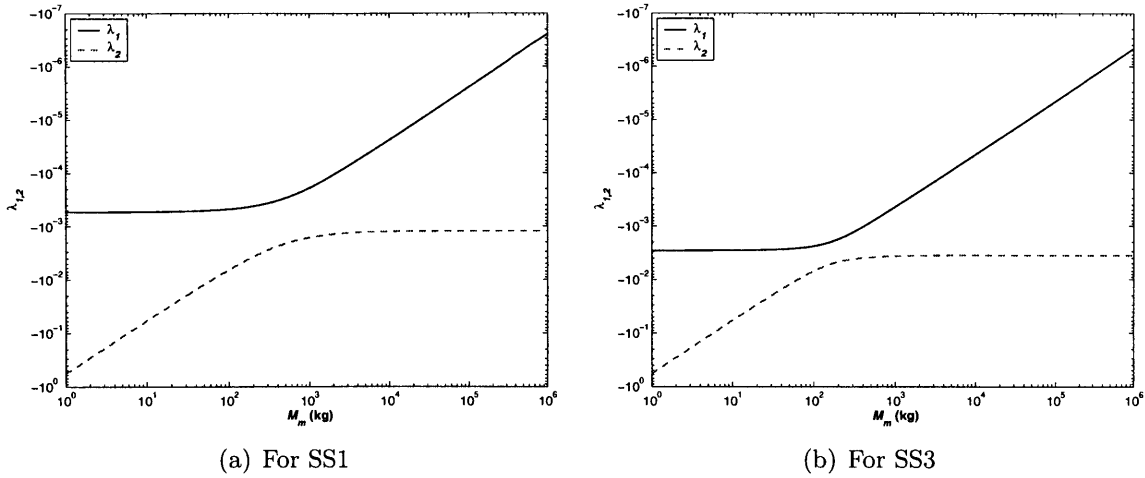


Figure 6-14: Eigenvalues of the linearized system for different $M_m c_m$ values: a.) at SS1; b.) at SS3

eigenvalues will decrease in this case. This indicates both the trajectories that enter and leave SS2 will take much longer time when $M_m c_m$ increase. When $M_m c_m \rightarrow \infty$, the time to reach SS2 along the eigendirection \vec{v}_2 will increase to infinity.

6.9 Conclusions

In this chapter, we investigated the transient dynamical system behaviors in a natural ventilation system with thermal mass, with the possibility of multiple steady states. Further, the impact of thermal mass in the linear and nonlinear system characteristics was quantitatively investigated.

For a system near a steady state, linear approximation is generally a very valid approximation to the system behaviors. The two eigenvalues and the eigenvectors determine how the air and thermal mass temperature change with time. When multiple steady states exist, linear system approximations are generally valid near each of the steady states.

However, there is an important nonlinear effect that is caused by the nonlinear system behaviors, even when only one steady state can actually exist in the system. When an air-thermal-mass system starts from an initial temperature, it will sometimes be first attracted to another region close to a “ghost” steady state before reaching a real steady state. The “ghost” effect causes a time delay in the time to reach the real steady state of the system.

We further investigated the nonlinear characteristics near the unstable steady state (SS2) of the system. Two special trajectories passing through SS2 are demonstrated to be exactly the boundaries of two attraction regions when multiple steady states exist. A computational method was proposed to compute the boundary (separatrices) between the two attraction regions on the phase plot.

The variations of the linear and nonlinear system behaviors are found to be sensi-

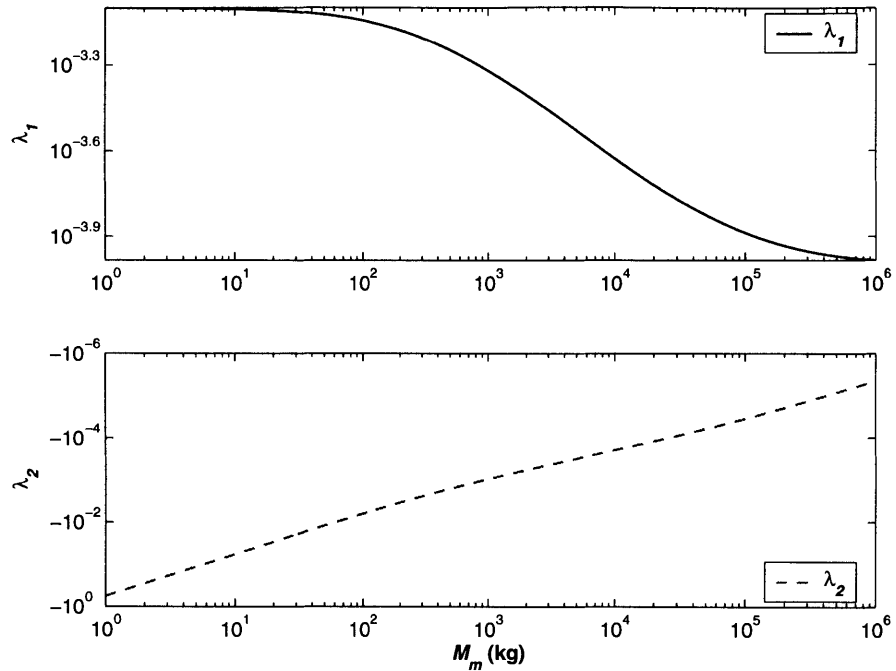


Figure 6-15: Eigenvalues of the system linearized at SS2 for different $M_m c_m$ values

tive to the thermal mass parameters, such as hA_m and $M_m c_m$ values. With different hA_m and $M_m c_m$ values, the system trajectories will demonstrate different shapes, which stand for different time characteristics of the system. The shape of the separatrices is also found to be sensitive to hA_m and $M_m c_m$. The trend of the trajectories and separatrices changes is carefully explained with the analysis of the eigen characteristics of the system.

Nomenclature

A_m = area of the thermal mass surface that contacts with the air in m^2	efficient between the air and the thermal mass in $\text{W}/\text{m}^2\text{-K}$
c_a = (constant pressure) specific heat of the air in $\text{J}/\text{kg}\text{-K}$	l = characteristic thickness of the thermal mass in m
c_m = specific heat of the thermal mass in $\text{J}/\text{kg}\text{-K}$	M_a = mass of the space air in kg , which equals to $\rho_a V$
$C_d A$ = effective product of the discharge coefficient and the opening area in m^2	M_m = mass of the thermal mass in kg
E = heat gain of the space in W	P_w = wind pressure difference between the inlet and outlet in Pa
g = gravitational acceleration in m/s^2	P^{**} = non-dimensional wind pressure difference between the inlet and the outlet
H = height difference between the upper and the lower openings in m	q = volumetric air flow rate in m^3/s
h = effective convection heat transfer co-	r = a defined boundary condition variable

t = time in s

T_a = (indoor) air temperature in °C

T_e = outdoor temperature in °C

T_m = thermal mass temperature in °C

T_a^* = (indoor) air temperature less the outdoor air temperature in °C, i.e. $T_a - T_e$

T_m^* = thermal air temperature less the outdoor air temperature in °C, i.e. $T_m - T_e$

UA = total conductance of the building enclosure system in W/K

V = volume of the space (air) in m³

v_{ref} = reference wind velocity in m/s for Wind Pressure Coefficients

Greek

β = thermal expansion coefficient of the air in K⁻¹

ρ_a = density of air in kg/m³

λ_1, λ_2 = eigenvalues of the Jacobian matrix \mathbf{J}

ε = an infinitesimal positive real number

Matrix

\mathbf{J} = Jacobian matrix of the linearized system

\vec{v}_1, \vec{v}_2 = the eigenvectors of the Jacobian matrix \mathbf{J}

Part III

Transition dynamics between multiple steady states

Chapter 7

Transitions between the multiple steady states in a natural ventilation system with combined buoyancy and wind driven flows

Natural ventilation systems may have multiple steady states in the combined buoyancy and wind driven mode due to the nonlinearity of the systems. Previous studies have shown that some of the steady states are locally stable for small disturbances. However, the system can flip over from one stable steady state to another under sufficiently strong perturbations. In this chapter, the mechanism of such state transitions is quantitatively investigated by a dynamical system approach.

The transition dynamics between the stable steady states is examined by the system's responses to two types of perturbations—heat source fluctuations and wind variations. Two important parameters—the minimum perturbation magnitude and the minimum perturbation time to switch from one stable steady state to another—are defined to describe the transition requirements. The result from a previous experimental study was discussed and explained by these state transition behaviors.

The transition dynamics between two stable steady states under perturbations are found important to the robustness of the stable steady states, which can be quantitatively described by the minimum perturbation time and the minimum perturbation magnitude. The experimental and numerical simulation results from another existing study are successfully explained by these two parameters. The applications of the developed perturbation method are further discussed.

7.1 Introduction

In natural ventilation systems, multiple steady states can sometimes be found in either numerical simulations or in reduced scale model experiments. A typical example is the single zone system with opposing wind and buoyancy forces shown in Figure 7-1. Linden [44] reviewed such a system and found two different steady state flow

patterns following different flow histories. If the wind was applied to the system gradually, the system finally reached a buoyancy dominated upward flow pattern. However, if the wind was applied abruptly, the system could reach a wind dominated downward flow pattern. Li and Delsante [41] investigated this system by solving the steady state equations. Three mathematical solutions are found to be possible when certain conditions were met. Among those solutions, one is unstable and the other two are stable under infinitesimal disturbances. Heiselberg et al. [35] conducted both experimental and CFD simulations on the same system and showed that two stable steady states do occur in reality.

More recently, the transient behaviors in the system's underlying driven dynamics are found to be important to the mechanisms for the system to achieve multiple steady states. For example, Yuan and Glicksman [70, 74] investigated transient behaviors of the system shown in Figure 7-1 by a dynamical system approach. The conditions for multiple steady states to exist and the local stabilities of the steady states were investigated by examining the transient characteristics of the system. Through the dynamical system analysis, the exact mechanism of how the system reaches different steady states from different initial temperatures was further investigated. The unstable steady state is found to be the critical point for the initial temperature to determine the system's final steady state.

In this chapter, the state transition dynamics between the stable steady states are investigated using the dynamical system approach. Although the system is locally stable to infinitesimal disturbances at a stable steady state, it still can be perturbed to another stable steady state when a sufficiently large perturbation is applied. Both the magnitude and the duration of the perturbation are important. As will be shown in later sections, the differences in the system's responses to different perturbation magnitudes provide an explanation to the experiment observation reported by Linden [44] where different ways to apply a wind force could cause different final steady states.

Further mathematical analysis is conducted to link the minimum perturbation magnitude and time requirements with the robustness of the stable steady states. The result gives important implications on the actual stabilities of the mathematically stable steady states. It can be used to quantitatively explain the experiment/CFD simulation results found in another existing study [35], where a theoretically (locally) stable buoyancy dominated steady state was not observed under certain boundary conditions.

In Section §7.1, the mathematical derivations and major conclusions from the dynamical system analysis in [70, 74] are briefly summarized because the present studies are largely built on these results. Section §7.2 discusses the system's responses to two different perturbations-heat source fluctuations and wind variations. Section §7.3 examines the perturbation magnitude requirements for the state transitions between two stable steady states and defines the concept of the minimum perturbation magnitude. The experimental result reported by Linden [44] is explained by the state transition behaviors under perturbations. Section §7.4 examines the perturbation time requirements for the state transitions between two stable steady states and defines the concept of the minimum perturbation time. Section §7.5 links the minimum perturbation magnitude and the minimum perturbation time to the robustness of the

mathematically stable steady states. The CFD predictions and experiment results by Heiselberg et al. [35] are quantitatively explained. Section §7.6 extends the results of the minimum perturbation time to the stability of a steady state in actual systems. Potential applications of the developed methods to other solution multiplicity problems are discussed.

7.1.1 Dynamical system analysis of the system

This subsection introduces the major mathematical deviations and conclusions in two previous studies [70, 74] that will be applied in this study.

7.1.1.1 Configuration

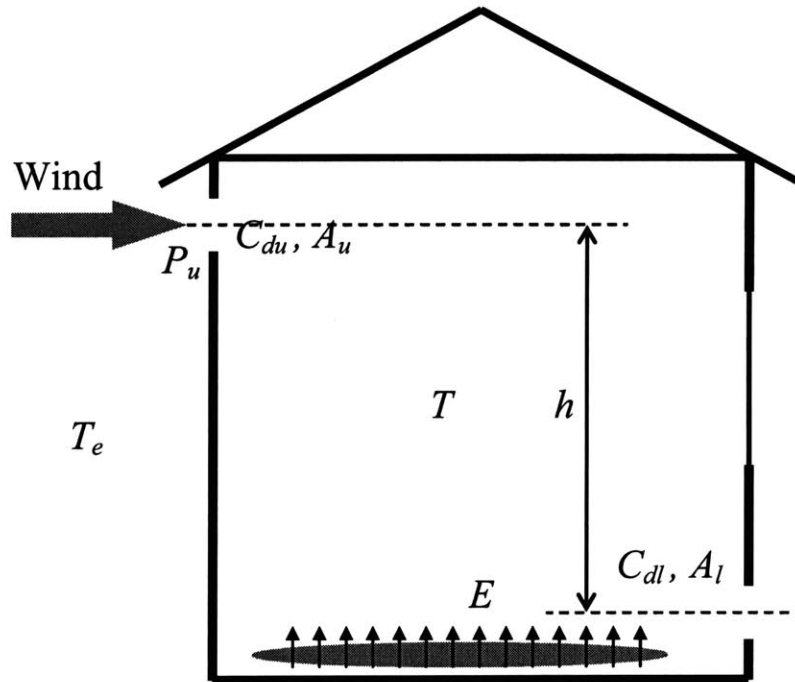


Figure 7-1: A single zone natural ventilation system with opposing wind and buoyancy forces

The basic configurations of a single variable natural ventilation system with combined wind and buoyancy forces are shown in Figure 7-1. A simple mathematical model was built by applying mass balance and empirical flow equations.

Energy Balance:

$$Mc_p \frac{dT}{dt} = q \cdot \rho_a c_{pa} \cdot (T_e - T) + UA \cdot (T_e - T) + E. \quad (7.1)$$

Flow Rate:

$$q = \overline{C_d A} \cdot \sqrt{\left| 2gh\beta \cdot (T - T_e) - 2 \frac{P_w}{\rho_a} \right|}. \quad (7.2)$$

Where

M is the total thermal mass (including the air) in kg,

t is the time in s,

q is the volume flow rate of the air in m^3/s ,

ρ_a is the air density in kg/m^3 (assume constant),

c_p is the specific heat of the thermal mass (including the air) in $\text{J}/\text{kg}\cdot\text{K}$,

c_{pa} is the specific heat of the air in $\text{J}/\text{kg}\cdot\text{K}$,

T is the indoor temperature in K,

T_e is the outdoor temperature in K,

UA is the total conductance of the enclosure system in W/K ,

β is the thermal expansion coefficient of the domain fluids in $1/\text{K}$. For ideal gas, β can be approximated as $1/T$. In Equation (7.2), β is assumed to be constant based on the ambient air temperature T_e with the relation $\beta = 1/T_e$.

P_w is the wind pressure difference between the inlet and outlet in Pascal, which is given by

$$P_w = P_u - P_l = \frac{1}{2} \rho_a (Cp_u - Cp_l) \cdot v_{ref}^2. \quad (7.3)$$

where P_u and P_l are the wind pressures (in Pascal) at the upper and the lower openings, respectively; Cp_u and Cp_l are the wind pressure coefficients for the two openings. v_{ref} (in m/s) is the reference wind velocity for the wind pressure coefficient. E is a lumped sum (in W) of all the heat gains through heat transfer processes that are not directly related to the indoor air temperature. One possible way to compose this term was given by Li and Delsante [41] as the sum of internal, direct solar, and solar-air heat gains.

$\overline{C_d A}$ is defined by:

$$\frac{1}{\overline{C_d A}} = \sqrt{\frac{1}{(C_{du} A_u)^2} + \frac{1}{(C_{dl} A_l)^2}}, \quad (7.4)$$

where C_{du} , C_{dl} are the discharge coefficients for the upper and lower openings respective, and the A_u and A_l are the areas of the two openings.

7.1.1.2 System characteristics and solution behavior

Substituting Equation (7.2) for the flow into Equation (7.1) yields a one dimensional first-order differential equation where the indoor air temperature T is the only state variable

$$\frac{dT}{dt} = f(T - T_e) = \frac{E}{Mc_p} - \frac{T - T_e}{Mc_p} \cdot \left(\overline{C_d A} \cdot \rho_a c_{pa} \sqrt{\left| 2gh\beta \cdot (T - T_e) - 2 \frac{P_w}{\rho_a} \right|} + UA \right). \quad (7.5)$$

Denote

$$T^* = T - T_e, \quad (7.6)$$

$$P^* = \frac{P_w}{\rho_a}, \quad (7.7)$$

$$T^{**} = \beta T^* = \beta(T - T_e), \quad (7.8)$$

$$P^{**} = \frac{P^*}{gh} = \frac{P_w}{\rho_a g h}, \quad (7.9)$$

T^{**} and P^{**} are dimensionless. The governing Equation (7.5) can also be written as follows using the * or ** parameters:

$$f(T^*) = \frac{dT^*}{dt} = \frac{E}{Mc_p} - \frac{T^*}{Mc_p} \cdot \left(\overline{C_d A} \cdot \rho_a c_{pa} \sqrt{|2gh\beta \cdot T^* - 2P^*|} + UA \right), \quad (7.10)$$

or

$$f(T^{**}) = \frac{dT^{**}}{dt} = \frac{E}{Mc_p} - \frac{T^{**}}{Mc_p} \cdot \left(\overline{C_d A} \cdot \rho_a c_{pa} \cdot \sqrt{2gh} \cdot \sqrt{|T^{**} - P^{**}|} + UA \right). \quad (7.11)$$

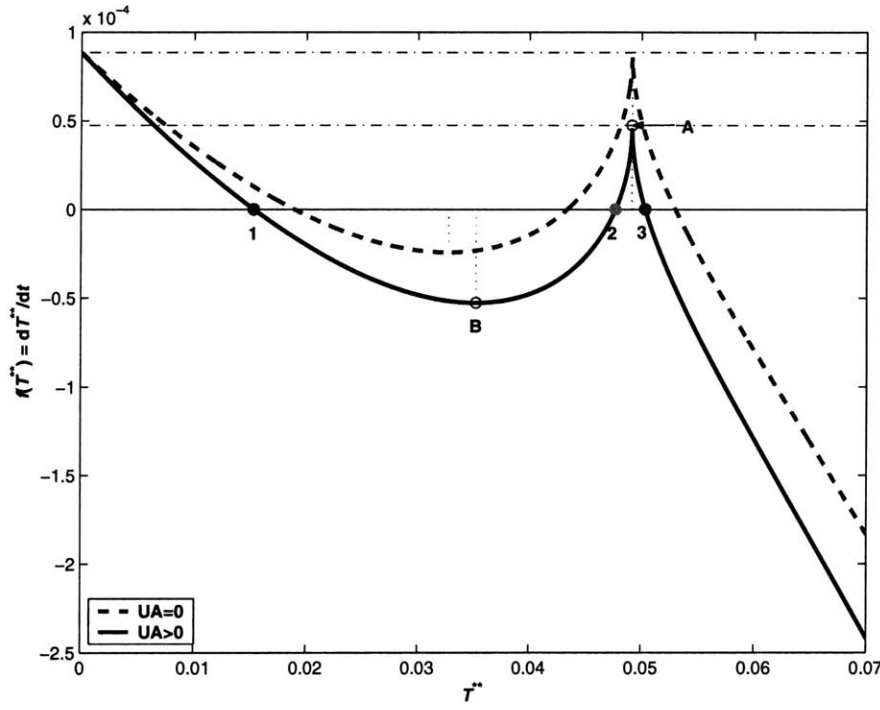


Figure 7-2: Solution characteristics of the system: dT^{**}/dt vs. T^{**}

The function $f(T^{**})$ versus T^{**} is plotted on Figure 7-2 for two different cases. The solid curve stands for the general cases of $UA > 0$. The dashed curve is for the special case of $UA = 0$.

There are two special points on the $f(T^{**})$ curve. The first one is point A where the system flow rate q equals zero. The values of T_A^{**} and $f(T_A^{**})$ are:

$$T_A^{**} = P^{**} = \frac{P^*}{gh}, \quad (7.12)$$

and

$$f(T_A^{**}) = \frac{\beta E}{Mc_p} - \frac{P^{**} \cdot UA}{Mc_p}. \quad (7.13)$$

The other special point is the local minimum point B, which can be found by

$$T_B^{**} = P^{**} - \left(\frac{\sqrt{X^2 + 3P^{**}} - X}{3} \right)^2, \quad (7.14)$$

and

$$f(T_B^{**}) = \frac{\beta E}{Mc_p} - \frac{T_B^{**}}{Mc_p} \cdot \left(\overline{C_d A} \cdot \rho_a c_{pa} \cdot \sqrt{2gh} \sqrt{P^{**} - T_B^{**}} + UA \right), \quad (7.15)$$

where

$$X = \frac{UA}{\overline{C_d A} \cdot \rho_a c_{pa} \cdot \sqrt{2gh}}. \quad (7.16)$$

If $UA = 0$, Equation (7.14) and (7.15) can be simplified as follow:

$$T_B^{**} = \frac{2}{3} P^{**}, \quad (7.17)$$

and

$$f(T_B^{**}) = \frac{\beta E}{Mc_p} - \overline{C_d A} \cdot \left(\frac{2}{3} P^{**} \right)^{\frac{3}{2}} \cdot (gh)^{\frac{1}{2}} \cdot \frac{\rho_a c_{pa}}{Mc_p}. \quad (7.18)$$

Equation (7.14) shows that the system has a local minimum point T_B^{**} residing between $\frac{2}{3}P^{**}$ and P^{**} for any X value from 0 to $+\infty$.

7.1.1.3 Conditions for multiple steady states to exist

Figure 7-3 graphically illustrated the relationship between the $f(T^{**})$ curve and the number of steady state solutions the system have. In order to have multiple steady states, the system needs to satisfy the following conditions shown in the middle curve in Figure 7-3:

$$f(T_A^{**}) \geq 0 \text{ and } f(T_B^{**}) \leq 0. \quad (7.19)$$

or

$$P^{**} \cdot UA \leq \beta E \leq T_B^{**} \cdot \left(\overline{C_d A} \cdot \rho_a c_{pa} \cdot \sqrt{2gh} \cdot \sqrt{P^{**} - T_B^{**}} + UA \right), \quad (7.20)$$

where T_B^{**} is given by Equation (7.14) and (7.16).

For a system with adiabatic wall ($UA = 0$), the necessary condition for multiple

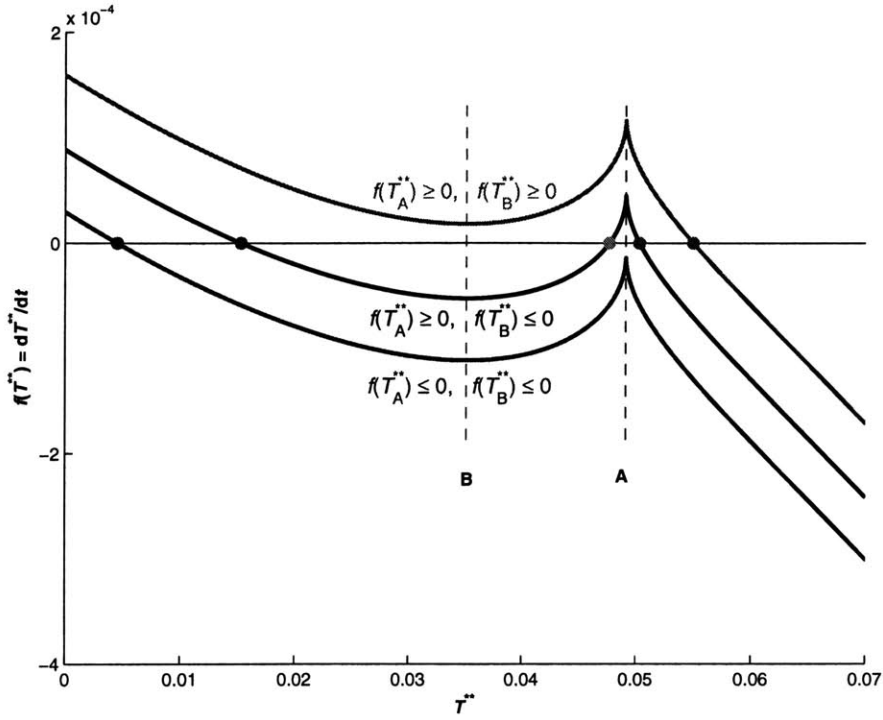


Figure 7-3: Three possible scenarios of the steady state solutions of the system

steady states to exist, described in Equation (7.19) or (7.20), can be simplified as:

$$0 \leq \beta E \leq \overline{C_d A} \cdot \rho_a c_{pa} \cdot \left(\frac{2}{3} P^{**} \right)^{\frac{3}{2}} \cdot \sqrt{gh}. \quad (7.21)$$

For a system with positive heat source ($E \geq 0$), the right half of Equation (7.21) can be rewritten as a ratio as follow:

$$r = \frac{\beta E}{\overline{C_d A} \cdot \rho_a c_{pa} \cdot \left(\frac{2}{3} P^{**} \right)^{\frac{3}{2}} \cdot (gh)^{\frac{1}{2}}} \leq 1. \quad (7.22)$$

7.1.1.4 Local stability of the three steady states

The three steady states (or solutions, roots) in Figure 7-2 have different local stabilities. Steady state 1 and 3 are stable but steady state 2 is unstable to infinitesimal perturbations. This can be quickly demonstrated by inspecting Figure 7-2. Starting from steady state 1, if the system temperature T^{**} is perturbed a little bit off from this state, it can move back to T_{ss1}^{**} because the derivative of T^{**} over time ($f(T^{**})$) acts against the change of T^{**} . For example, when T^{**} increases from state 1, $f(T^{**})$ becomes negative. T^{**} will decrease until it returns to T_{ss1}^{**} . Therefore, the system is able to resist small disturbances at steady state 1. This is also true at steady state 3. However, at steady state 2, the system is unstable because $f(T^{**})$ facilitates the

temperature divergence from T_{ss2}^{**} under any infinitesimal perturbation. No matter how small the system temperature changes from T_{ss2}^{**} , this offset will always be immediately magnified until the system gains stable equilibrium again at either state 1 or 3. Therefore, steady state 2 is unstable and can not be observed in an actual dynamical system. The system will always move toward one of the two stable steady states (1 or 3) from there.

Stability shown at steady states 1 and 3 is defined as local stability in nonlinear dynamics texts [57]. In the following sections, this local stability is sometimes referred as mathematical stability to distinguish from the actual robustness of the stable steady states. Similarly, throughout the chapter, “steady state” is sometimes referred as “steady state solution”, “steady state root”, “solution” or “root”, from the equation-solving point of view.

7.1.1.5 Critical point of the initial temperature

The value of the initial system temperature T_0^{**} relative to T_{ss2}^{**} , the temperature of the unstable steady state 2, distinguishes the final (steady) state of the system. If the initial temperature T_0^{**} is lower than T_{ss2}^{**} , the system will reach the steady state 1 (T_{ss1}^{**}) in the absence of further perturbations; otherwise, if T_0^{**} is higher than T_{ss2}^{**} , the system will reach the steady state 3 (T_{ss3}^{**}).

In this mathematical model, the temperatures of all the system states (the x-axis in Figure 7-2) are divided into two regions by the unstable steady state solution. Starting from the left of the unstable solution, the system will finally reach the steady state 1. Starting from the right of the unstable solution, the system will finally reach steady state 3. The unstable steady state 2 is the dividing point of the two regions.

7.2 System responses under strong perturbations

Although the system shown in Figure 7-1 is locally stable to infinitesimal perturbations at steady states 1 and 3, it can still switch from 1 to 3 or from 3 to 1 when sufficient perturbations exist. Here a large scale boundary condition change is called a “strong perturbation”, which is distinguished from the infinitesimal disturbances used in the local stability analysis. The strong perturbation can either be a sudden or a gradual/smooth change of the environmental parameters. The perturbations in this chapter are generally assumed a square shape unless otherwise specified. At one stable steady state, the system is assumed to be subjected to a sudden step change ΔW in a certain parameter that lasts for a time span t_s shown in Figure 7-4. After time t_s , the perturbation is immediately removed and the parameter changes back to its original value.

Both the magnitude and the duration of the perturbation are important factors for the system responses. Here the task is to find the minimum required magnitude and time that can lead to the transition between the two stable steady states. Since two major types of perturbations – heat source fluctuations and wind variations – may exist in the system, the system responses under these two types of disturbances

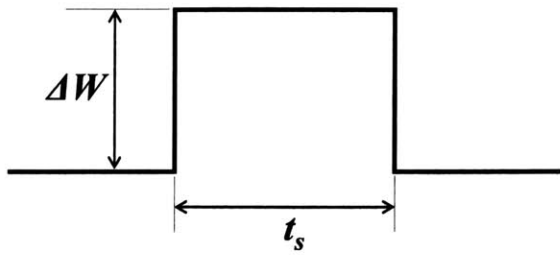


Figure 7-4: A strong perturbation acting on the system

are discussed in detail.

7.2.1 Heat source perturbation

In this chapter, a heat source perturbation is denoted as ΔE and can be either positive or negative as the result of the increase or decrease in the heat source strength. Under the perturbation ΔE , the $f(T^*)$ curve is shifted upward or downward by a uniform magnitude $\frac{\Delta E}{Mc_p}$. Figure 7-5 shows the change in the system curves $f(T^*)$ under a positive ΔE . The lower curve is the original system curve $f(T^*)$ and the upper one is the new system curve under perturbation. When only a heat source perturbation applies, the values of T_A^* and T_B^* do not change since the curve only vertically shifts upward or downward. This can also be seen from Equations (7.12) and (7.14).

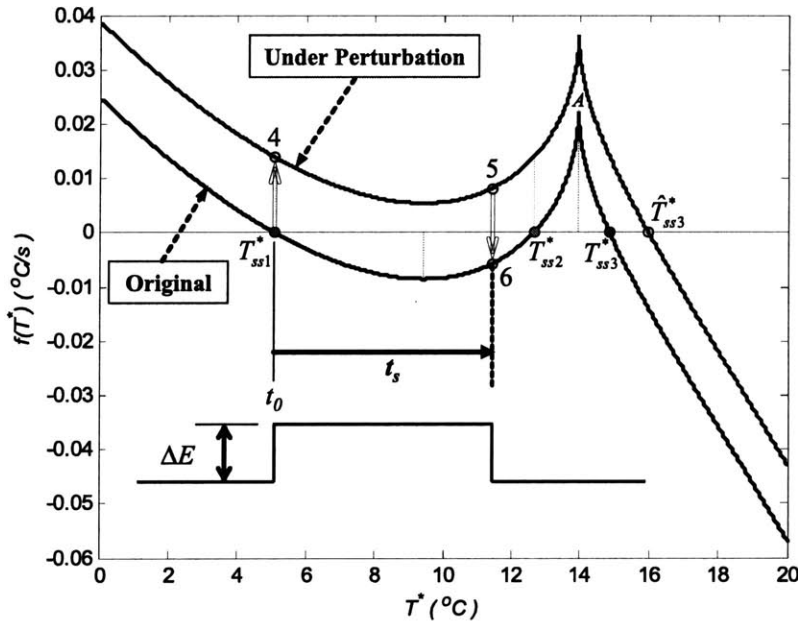


Figure 7-5: System under a heat source increase perturbation ($\Delta E/E = 55.7\%$)

7.2.2 Wind velocity perturbation

Another important perturbation is the change in the wind velocity (or direction). The change of wind velocity will cause variations in the pressure difference P^* between the two openings in Figure 7-1. For a wind velocity perturbation, the variation in wind velocity v_{ref} is denoted as Δv_{ref} . The corresponding variation in pressure P^* is denoted as ΔP^* . The change in the system curve is shown in Figure 7-6 when a decrease in wind velocity occurs.

The $f(T^*)$ curve also changes under a perturbation. The value of T_A^* changes (e.g. when $UA = 0$, its position is determined by $T_A^{**} = P^{**}$) in proportional to P^* . The value of T_B^* also changes when P^* changes (e.g. $T_B^{**} = \frac{2}{3}P^{**}$ when $UA = 0$). The values of $f(T_A^*)$ and $f(T_B^*)$ change with P^* according to Equations (7.13) and (7.15).

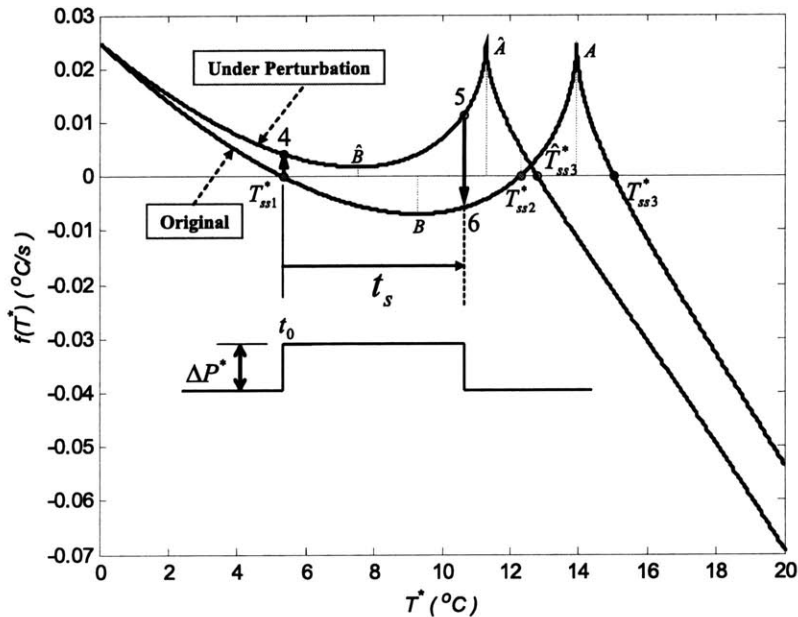


Figure 7-6: System under a wind velocity decrease perturbation ($\Delta v_{ref}/v_{ref} = -10\%$)

7.3 Minimum perturbation magnitude

We assume that starting from a stable steady state, an environmental parameter suddenly changes by a magnitude of ΔW and remains active for a period of time t_s . Since the steady states 1 and 3 are stable to infinitesimal perturbations, if the perturbation is not strong enough, the system can still return to its original steady state when the perturbation is removed. Therefore, there is a minimum perturbation magnitude that has to be met in order to perturb the system over to the other steady state when the perturbation can be applied for a sufficiently long time.

7.3.1 Heat source perturbation

Figure 7-5 illustrates the system's transition from steady state 1 to steady state 3 under a heat increase perturbation. Assume the system has reached the steady state 1 (Figure 7-5) before time t_0 . At time t_0 , a square heat source perturbation ΔE is suddenly applied to the system by a change in the direct solar gain, for example. Now the system curve will shift upward shown as the "Under Perturbation" curve in Figure 7-5. Since the new system curve has a positive value of dT^*/dt at point 4, the temperature will start to increase. Over time t_s , its temperature changes from T_4^* ($=T_{ss1}^*$) to T_5^* . When the perturbation is removed at time $t_0 + t_s$, the system returns to the original curve with a new initial temperature at time $t_0 + t_s$, shown as T_6^* ($=T_5^*$) in Figure 7-5. If the current temperature T_6^* is lower than the unstable root temperature T_{ss2}^* on the original system curve, the system will change back to the original steady state 1. To enable the system to move towards the other stable steady state T_{ss3}^* when the perturbation is removed, the temperature T_6^* at time $t_0 + t_s$ has to be greater than T_{ss2}^* . Similarly, if the original steady state of the system starts from steady state 3 in Figure 7-5, the temperature at the end of the perturbation must be lower than T_{ss2}^* of the original system curve to enable the system to switch toward the new steady state 1.

Now consider an infinite perturbation time. Given the assumption that t_s can be as long as needed (e.g., $t_s \rightarrow +\infty$), the system starting from state 1 can reach a new steady state under the perturbed curve $\hat{f}(T^*)$ as shown in Figure 7-5. In order to switch the system state from steady state 1 to steady state 3, the minimum magnitude of the perturbation has to raise the value of $f(T_B^*)$ at the local minimum point B above zero as is shown in Figure 7-5. Otherwise, the new steady state of the perturbed system will be trapped into a steady state temperature below T_{ss2}^* . Similarly, in order to change the flow pattern from steady state 3 to 1, the minimum perturbation magnitude (negative in this case) has to be able to shift point A below zero.

Mathematically, in order to perturb the system from a downward flow pattern to an upward flow pattern (steady state 1 to 3) by a square heat source perturbation, the perturbation has to satisfy (use Equation (7.15))

$$\frac{\beta(\Delta E + E)}{Mc_p} - \frac{T_B^{**}}{Mc_p} \left(\overline{C_d A} \cdot \rho_a c_{pa} \sqrt{2gh} \cdot \sqrt{P^{**} - T_B^{**}} + UA \right) \geq 0. \quad (7.23)$$

Reorganizing Equation (7.23), it becomes

$$\beta(\Delta E + E) \geq T_B^{**} \left(\overline{C_d A} \cdot \rho_a c_{pa} \sqrt{2gh} \cdot \sqrt{P^{**} - T_B^{**}} + UA \right) \geq 0. \quad (7.24)$$

where $E + \Delta E$ represents the total heat source in the building under perturbation. Therefore, the minimum heat source perturbation has to be large enough to shift the system curve upward enough to break the necessary conditions for the existence of multiple steady states in this scenario. Figure 7-5 shows an example of a perturbed curve that has only one steady state root.

Following the same analysis, in order to perturb the system from the buoyancy dominated steady state 3 to the wind dominated steady state 1 by a square heat source perturbation, the minimum perturbation magnitude has to make the system satisfy the following:

$$\beta(E + \Delta E) \leq P^{**}UA. \quad (7.25)$$

For the special case where $UA = 0$, the transition from state 3 to state 1 requires the perturbation to satisfy the simplification of Equation (7.25) as follow:

$$E + \Delta E \leq 0. \quad (7.26)$$

This means the perturbation ΔE has to be so negative that the total heat source $E + \Delta E$ under perturbation becomes a cooling source if everything else does not change.

As a summary, in order to perturb the system either from steady state 1 to 3 or from 3 to 1 by a square heat source perturbation, the perturbation has to be able to break the existence conditions for multiple steady states described in Equation (7.19) or (7.20). If the magnitude of the perturbation cannot achieve that, the final state will not be able to switch when the perturbation is removed, no matter how long the perturbation lasts.

7.3.2 Wind velocity perturbation

The minimum perturbation magnitude required for a state transition under a square wind velocity perturbation can also be derived. However, under wind perturbations, the switch from state 1 to 3 and the switch from 3 to 1 need to be analyzed differently.

7.3.2.1 Switch from steady state 1 to 3 under wind perturbations

Under a square wind velocity decrease perturbation, one of the conditions for a switch is almost the same as that for a heat source increase perturbation case. As is shown in Figure 7-6, the perturbed function $\hat{f}(T_B^*)$ has to be raised above zero at the local minimum point \hat{B} on the perturbed curve. From Equation (7.15), this is,

$$\beta E \geq T_{\hat{B}}^{**} \left(\overline{C_d A} \cdot \rho_a c_{pa} \cdot \sqrt{2gh} \cdot \sqrt{(P^{**} + \Delta P^{**}) - T_{\hat{B}}^{**}} + UA \right), \quad (7.27)$$

where $P^{**} + \Delta P^{**}$ and $T_{\hat{B}}^{**}$ are the new values in the perturbed system. Only sufficiently large decreases in velocity (pressure) will make a transition from state 1 to state 3 possible.

However, even if the condition in Equation 7.27 is satisfied, the temperature of the perturbed system may still not be able to reach above T_{ss2}^* , the critical temperature for the switch from state 1 to 3. Figure 7-7 shows such an example where the wind velocity decrease is too large. The system cannot switch from steady state 1 to 3 after the perturbation is removed no matter how long ($t_s \rightarrow \infty$) the perturbation endures. For the perturbed system shown in Figure 7-7, the highest temperature it can achieve is T_{ss3}^* , the steady state solution in the perturbed system. Since T_{ss3}^* is lower than

the unstable steady state temperature T_{ss2}^* of the original system, the state transition cannot be accomplished when the perturbation is removed. Therefore, although the flow pattern can change (to buoyancy dominated upward) when the perturbation exists, this change cannot be sustained when the perturbation is removed. When the perturbation is removed, the system will go back to its original state. Therefore, satisfying Equation 7.27 alone is not sufficient to perturb the system from state 1 to 3 even under infinite time.

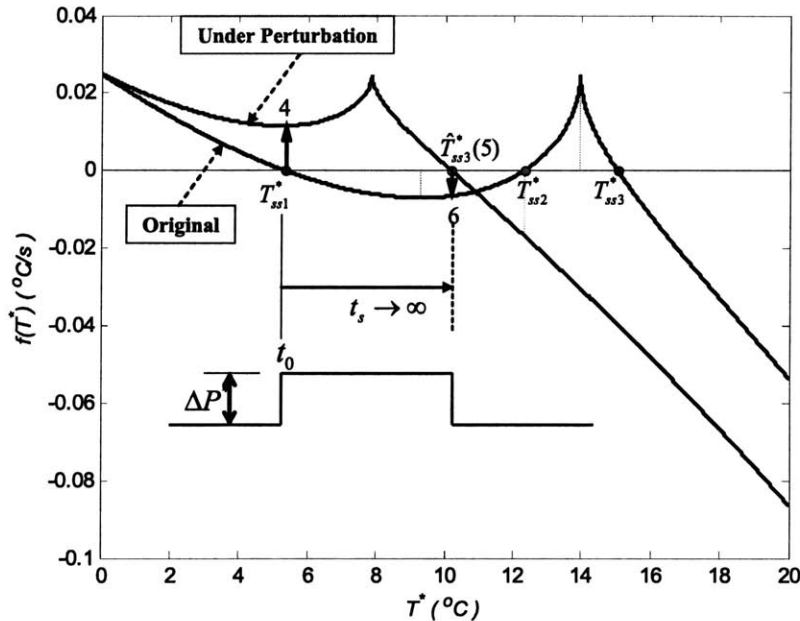


Figure 7-7: Unsuccessful flow pattern switch under stronger wind perturbations ($\Delta v_{ref}/v_{ref} = -25\%$)

A $4m \times 5m \times 5m$ space is selected to demonstrate the perturbation requirements in Equation 7.27 and the unsuccessful switch scenarios stated above under wind perturbations. The two openings (see Figure 7-1) are 0.8 m^2 . The wind velocity is 1.6 m/s and the heat source strength is 3.0 kW . Using a wind velocity decrease perturbation ($\Delta v_{ref}/v_{ref} < 0$), we try to perturb the system from state 1 to 3. When the perturbation is not strong enough ($|\Delta v_{ref}|/v_{ref} < 8\%$), the transition cannot be completed after the perturbation removal because Equation 7.27 is not satisfied. However, if the square perturbation is too strong (say $|\Delta v_{ref}|/v_{ref} > 12\%$), the situation illustrated in Figure 7-7 will take place. The system cannot switch from root 1 to 3 when the perturbation is removed because \hat{T}_{ss3}^* is lower than T_{ss2}^* and the switch is not self-sustainable.

The physical explanation for this “stronger square wind decrease perturbations cannot make the switch” phenomenon is as follow: When the wind velocity decreases substantially during the perturbation period, buoyancy force becomes dominant and strong upward flow is formed in the perturbed system. However, at a low wind ve-

lacity, the resulting buoyancy dominated upward flow rate is so high that the interior temperature cannot rise high enough (according to the energy conservation equation) to reach T_{ss2}^* , the minimum temperature to initiate a transition to the buoyancy dominated steady state 3 upon the perturbation removal. Therefore, the system can only go back to its original steady state (root 1, downward ventilation) because it now starts from a temperature lower than the critical unstable root 2 temperature.

In this “stronger square wind decrease perturbations cannot make the switch” scenario, the way (or process) that the perturbation is applied or removed can affect the state transition outcome significantly. We have only assumed a square perturbation in our study, which means that the perturbation is applied suddenly at t_0 and is removed immediately at $t_0 + t_s$. If the perturbation is removed gradually and smoothly as is shown in Figure 7-8, it is possible for the system to switch from state 1 to 3 under a wind velocity decrease perturbation. In this scenario, a gradually changing perturbation forms a series of perturbed curves and the steady state roots of these curves will gradually approach and exceed the unsteady state root T^{*ss2} of the original system to enable the final state to switch towards state 3. The solid line shows one possible actual system curve the system undergoes during and after the perturbation.

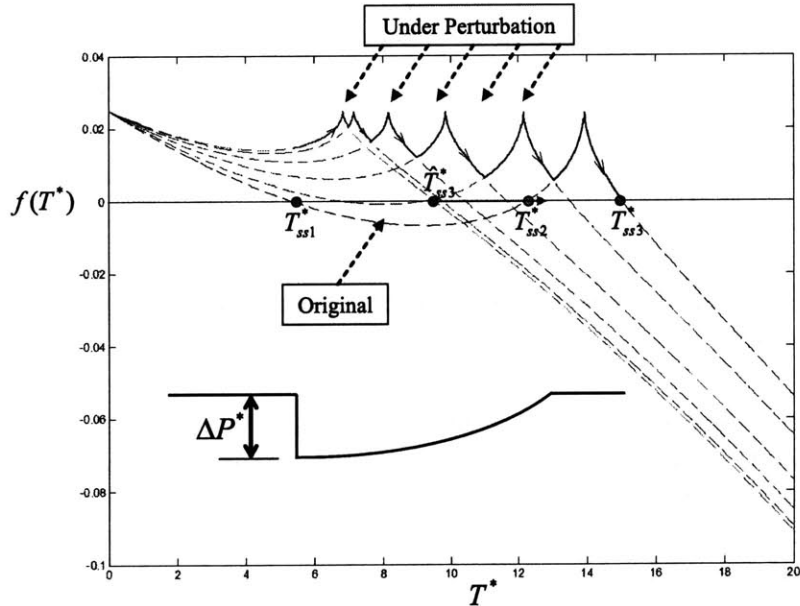


Figure 7-8: Transitions between steady states under a gradually reducing wind velocity decrease perturbation

7.3.2.2 Switch from steady state 3 to 1 under wind perturbations

The switch from the buoyancy dominated steady state 3 to the wind dominated steady state 1 is slightly different. When the wind velocity increases, multiple steady

states will always appear in the perturbed system if the original system has multiple steady states. The perturbed curve $\hat{f}(T^*)$ is shown in Figure 7-9 when a wind velocity increase perturbation is applied at time t_0 . The system starts from point 4 ($T_4^* = T_{ss3}^*$) on the perturbed curve $\hat{f}(T^*)$. Since $\hat{f}(T_4^*) > 0$ the system temperature will increase and gain another steady state ($\hat{T}_{ss3}^*(5)$) under sufficient long time. When the perturbation is removed, the system will move back towards the original steady state (T_{ss3}^*) because $T_6^* > T_{ss3}^*$.

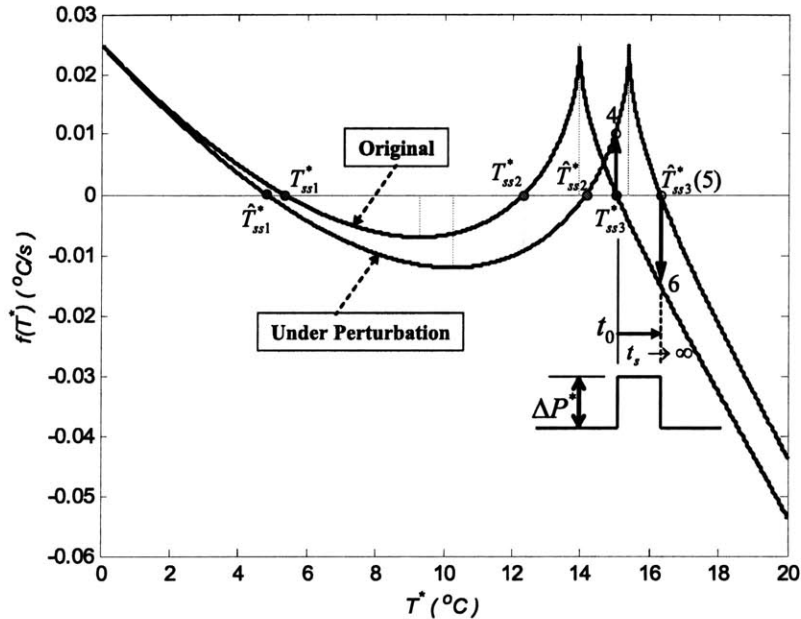


Figure 7-9: System under wind velocity increase perturbation ($\Delta v_{ref}/v_{ref} = 5\%$)

The minimum perturbation magnitude can be derived from Figure 7-10. In order to perturb the system from the steady state 3 to 1 by a wind velocity increase perturbation, the temperature T_4^* ($= T_{ss3}^*$) at point 4 on the perturbed system curve has to be lower than \hat{T}_{ss2}^* (the unstable steady state temperature of the perturbed system) to enable the system temperature to drop under perturbation. Therefore, the minimal square perturbation magnitude for a solution switch must ensure that the temperature T_{ss3}^* of the stable steady state 3 on the original system curve $f(T^*)$ is lower than the temperature \hat{T}_{ss2}^* of the unstable steady state on the perturbed curve $\hat{f}(T^*)$. The relation can be formulated as:

$$T_{ss3}^* < \hat{T}_{ss2}^*. \quad (7.28)$$

7.3.3 Explanation to a previous study

The transitions shown in Figures 7-9 and 7-10 can also partly explain an experimental result stated by Linden [44]. Different outcomes were observed depending on whether

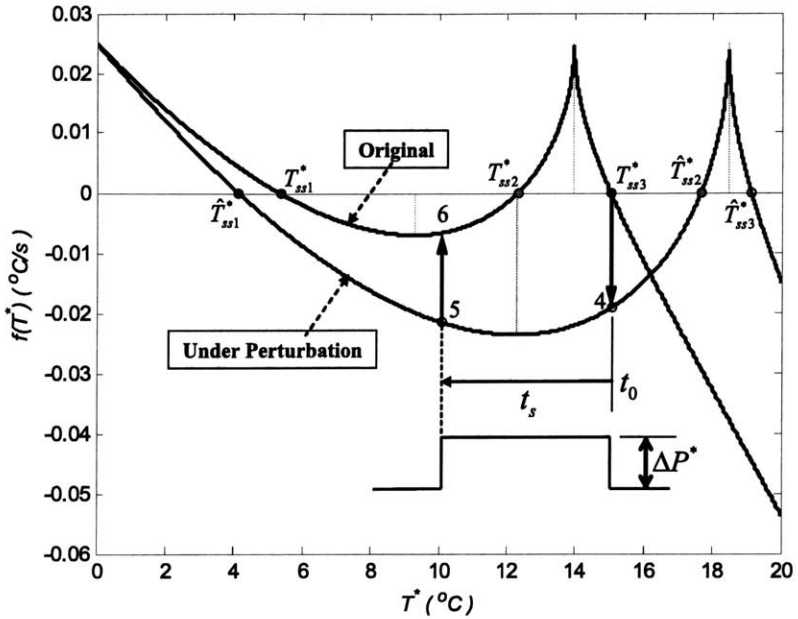


Figure 7-10: The change of the system curve and the steady state solutions when velocity increases ($\Delta v_{ref}/v_{ref} = 15\%$)

a wind force was added quickly or gradually. The experiment started from a buoyancy dominated upward flow generated by a point source on the ground. Wind forces were introduced to oppose the buoyancy to change the flow pattern. The results showed that when the wind force was added quickly, the system could gain a downward mixing flow (similar to state 1, wind dominated). However, if the wind force was added gradually, the system gains an upward displacement flow (similar to state 3, buoyancy dominated). However, no detailed quantitative explanation was provided in the original study.

Although in the above experiment the wind forces (which are called perturbations in this study) were not removed once being added, the transition analysis in our study still can explain to this phenomenon. The perturbed curve in Figure 7-10 corresponds to the quick wind enforcement case (15% wind increment all at once). Therefore the system can finally reach a new wind dominated steady state 1, which is shown in Figure 7-10 as \hat{T}_{ss1}^* . For the gradual wind enforcement (e.g. three 5% increments in series, or fifteen 1% increments in series, or other combinations), the system can be viewed as continuously undergoing a series of smaller square perturbations. Since the wind enforcement is gradual, we can assume each of the smaller perturbations lasts for a reasonably long time. Thus, each of the smaller perturbations in this series has the effect similar to that in Figure 7-9. Therefore none of them can actually move the system to a wind dominated steady state 1 on the perturbed curve (in Figure 7-9). After the entire series of perturbations are applied in a gradual manner, the transition to steady state 1 can never happen. Therefore the final perturbed system

is still in a buoyancy dominated state 3, at a temperature equals to the \hat{T}_{ss3}^* in Figure 7-10.

7.3.4 Summary on the minimum perturbation magnitude

As is stated in the introduction section (§7.1), all the system states (temperature) are divided into two regions by the unstable solutions. The minimum requirement to perturb the system from one steady state to the other is to move the system temperature out of its original region to the other region. The minimum perturbation magnitude measures this requirement in an infinite time base. If the minimum perturbation magnitude remains active for sufficiently long time, the system will exactly reach the unstable root of the originally unperturbed system, the critical point to move forwards into the other region.

The minimum perturbation magnitude required to switch from one stable steady state to another is also depended on the shape of the perturbation. The minimum perturbation magnitude for a square shape perturbation can be mathematically derived. In some cases, especially the wind perturbation case, a smooth removal or addition of a perturbation can make a gradual transition to another steady state. Therefore, the way the perturbation is added or removed can also be important to the state transitions. The system transitions under an arbitrary perturbation can be views as a series of square perturbations acted on the system. The square perturbation analysis can still be applied on each of the small sections (e.g. Figure 7-8).

7.4 Minimum perturbation time

In this section we will investigate the minimum time t_{smin} to trigger a state transition under a square perturbation ΔW that is greater than the minimum perturbation magnitude ΔW_{min} . To restate, we are looking for the minimum duration of perturbations that can result in a permanent change in the final steady state of the system. For example, at time t_0 the system is in a wind dominated steady state 1 and suddenly the perturbation ΔW is applied. When the perturbation is removed at time $t_0 + t_{smin}$, the system is able to move towards the buoyancy dominated steady state 3 and finally reach there. If ΔW lasts shorter than t_{smin} , the system will not be perturbed enough to reach the critical temperature and will finally return to the original steady state 1, even though ΔW is greater than the minimum perturbation magnitude ΔW_{min} .

The conclusion that the unstable steady state is the critical initial temperature point in determining the system's final steady state will be again applied here. Take the transition from steady state 1 to 3 as an example. The system is originally at the stable steady state 1. At time t_0 , when a positive heat source ΔE is applied, the $f(T^*)$ curve shifts upward and forms a new curve $\hat{f}(T^*)$ (see Figure 7-5). Starting from point 4 ($T_4^* = T_{ss1}^*$), the system will reach point 5 (T_5^*) at the end of the perturbation at time $t_0 + t_s$. Now, the perturbation is suddenly removed and the system will follow the original curve $f(T^*)$ again from point 6 ($T_6^* = T_5^*$). If at this moment the temperature T_5^* is greater than the unstable steady state temperature

T_{ss2}^* of the original system, the system will switch over toward steady state 3. The final state will be the buoyancy dominated steady state 3.

A similar scenario occurs to the wind velocity (pressure) perturbations. Figure 7-6 shows an example where the wind decrease perturbation time t_s is not long enough for T_5^* to exceed T_{ss2}^* of the original curve. Therefore, the system cannot switch from 1 to 3 when the perturbation is removed. However, if t_s is increased so that T_5^* exceeds T_{ss2}^* when the perturbation is removed, the system will finally reach steady state 3.

Therefore, the unstable steady state temperature T_{ss2}^* plays an important role in determining the minimum perturbation time $t_{s\min}$ for a specific perturbation magnitude. The minimum perturbation time for the system to trigger a state transition can be calculated by the following analysis.

During the minimum perturbation time $t_{s\min}$, the system temperature needs to be increased from T_{ss1}^* to T_{ss2}^* along the new system curve $\hat{f}(T^*)$. Therefore, the following equation holds:

$$T_{ss2}^* - T_{ss1}^* = \int_{t_0}^{t_0 + t_{s\min}} \hat{f}(T^*) dt. \quad (7.29)$$

Reformulation of Equation (7.29) leads the explicit formula to calculate $t_{s\min}$:

$$t_{s\min} = \int_{T_{ss1}^*}^{T_{ss2}^*} \frac{1}{\hat{f}(T^*)} dT^*, \quad (7.30)$$

where the values of T_{ss1}^* , T_{ss2}^* can be calculated either analytically or numerically and the function $\hat{f}(T^*)$ is determined once the perturbation magnitude is known.

The same building example illustrated in the minimum perturbation magnitude analysis is used here to illustrate the minimum perturbation time calculation results. Again, the building is $5m \times 5m \times 4m$ with two $0.8m^2$ openings, 1.6 m/s wind, and $3000W$ heat source. The walls are assumed adiabatic and only the mass of the interior air is considered. Figure 7-11 shows the minimum perturbation time under different heat perturbation magnitudes ranging from $1,700$ to $17,000W$. At low perturbation strength (e.g. a $\Delta E/E$ just above the minimum requirement), the rate of temperature change with time dT^*/dt is small during the change especially near the local minimum point B on the perturbed curve shown in Figure 7-5. In particular, dT^*/dt near point B is only marginally above zero in the perturbed system, requiring a long time for the room temperature to change. Therefore, it requires a long time to raise the temperature to exceed the unstable steady state point T_{ss2}^* of the original system. When the perturbation magnitude increases, the minimum perturbation time decreases as is expected. As the value of $\Delta E/E$ becomes larger and larger, the minimum perturbation time asymptotically approaches 0.

Similar analysis can be used to find the minimum perturbation time required to perturb the system from steady state 3 to 1. In this scenario, the perturbation needs to decrease the system temperature below T_{ss2}^* during at the end of the perturbation period. By almost the same analysis as the transition from state 1 to 3, the minimum perturbation time $t_{s\min}$ for the state transition from state 3 to 1 can be calculated by

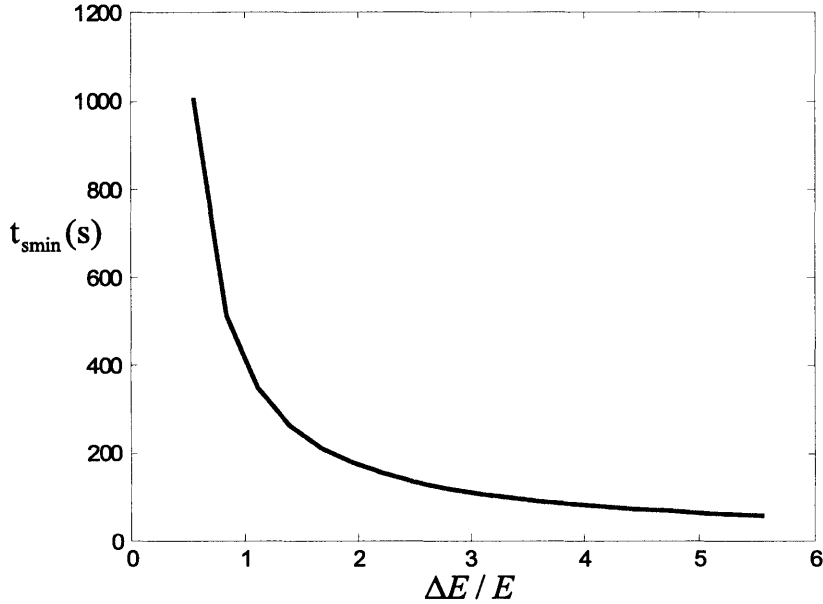


Figure 7-11: The minimum perturbation time (s) vs. heat source perturbation $\Delta E/E$ for transition from wind dominated to buoyancy dominated flow

the formula

$$t_{s\min} = - \int_{T_{ss3}^*}^{T_{ss2}^*} \frac{1}{\hat{f}(T^*)} dT^* = \int_{T_{ss2}^*}^{T_{ss3}^*} \frac{1}{\hat{f}(T^*)} dT^*. \quad (7.31)$$

Equations (7.30) and (7.31) can be applied in the state transitions perturbed by either heat source perturbation or wind velocity perturbation. For example, when a wind velocity decrease perturbation meets the minimum perturbation magnitude requirements, Equation (7.30) can be used to determine the minimum perturbation time for this perturbation to trigger the state transition from state 1 to 3. Equation (7.31) can be applied as well when the system switches from steady state 3 to 1 under a qualified wind increase perturbation.

Figure 7-12 shows the minimum perturbation times calculated by Equation (7.30) under the different perturbation magnitudes $|\Delta v_{ref}|/v_{ref}$ in a transition from state 1 to 3 under wind velocity decrease perturbations. Due to the “stronger square wind decrease perturbations cannot make the switch” effect discussed in the minimum perturbation magnitude section (§7.3.2.2), the state transition can only accomplished with a square perturbation when the velocity perturbation is greater than 8% and less than 12%. Therefore, only the results in this range are reported. As is expected, the minimum perturbation time decreases as the perturbation magnitude increases.

Figure 7-13 shows the minimum perturbation times calculated by Equation (7.31) under different wind velocity increase perturbations $\Delta v_{ref}/v_{ref}$ in the switch from steady state 3 to 1. As is expected as well, the minimum perturbation time decreases when the perturbation magnitude increases. One noticeable fact is that the vertical

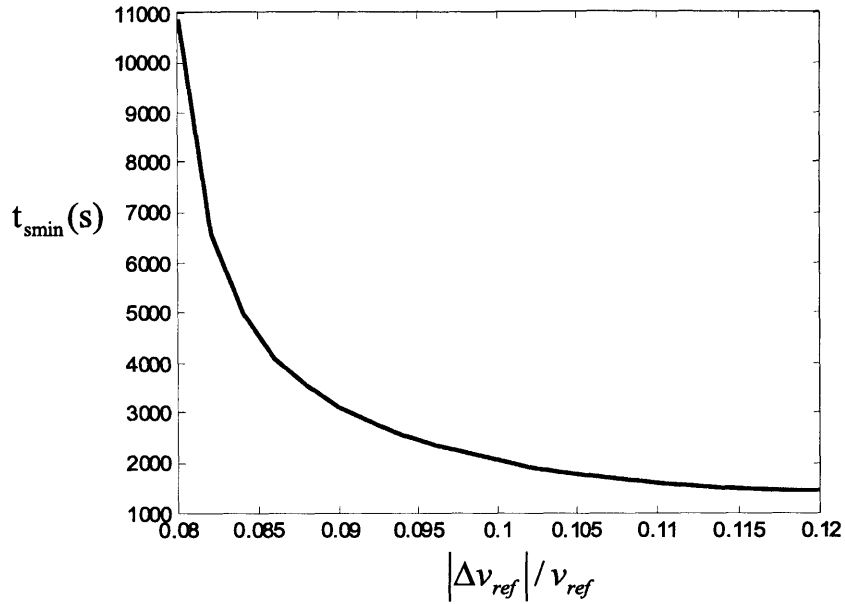


Figure 7-12: Minimum perturbation time (s) vs. wind velocity decrease perturbation $\Delta v_{ref}/v_{ref}$ for transition from steady state 1 to 3

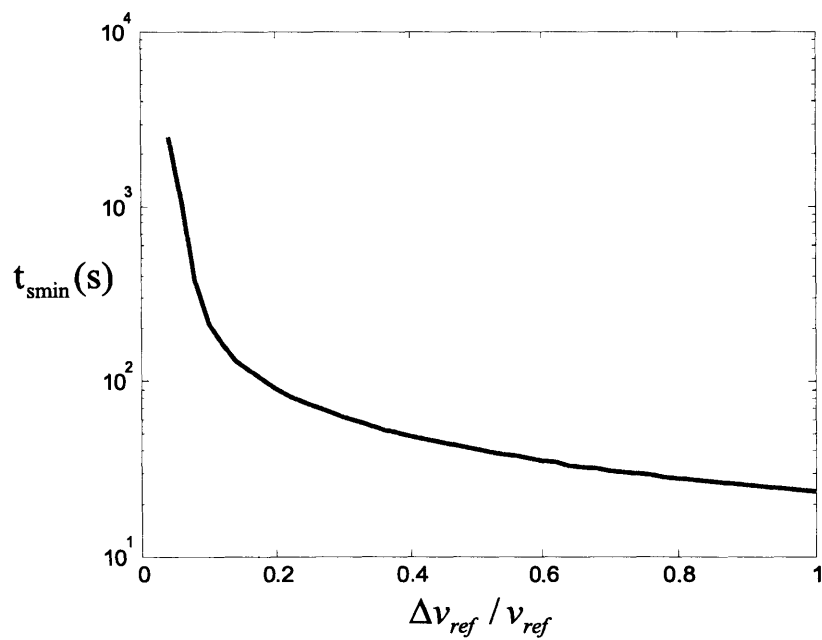


Figure 7-13: Minimum perturbation time vs. wind velocity increase perturbation $\Delta v_{ref}/v_{ref}$ for transition from steady state 3 to 1

axis is in logarithmic scale. This indicates that the perturbation time decreases very fast when the wind (or pressure) perturbation magnitude increases.

7.5 Robustness of the stable steady states

The minimum perturbation magnitude and the minimum perturbation time can be used to quantify the robustness of the stable steady states. The robustness of a stable steady state can be inspected in two aspects: (a) the minimum perturbation magnitude required to switch to another steady state; (b) the minimum perturbation time required to trigger the state switch under a qualified perturbation. For a stable steady state, the larger the minimum perturbation magnitude required for the transition to another steady state, the more robust the steady state is. Under the same qualified perturbation magnitude, the larger the minimum perturbation time required for triggering the state switch, the more robust the steady state is.

In actual systems, all kinds of stochastic perturbations exist in the boundary conditions, such as the fluctuations in wind velocities, air temperatures, and wind directions. If the minimum perturbation magnitude for the transition from one mathematically (or locally) stable steady state to another is very small, the system is potentially easy to be perturbed toward the other stable steady state under these stochastic perturbations. Further, if the minimum perturbation time for switching from a mathematically stable steady state to another state is very short, this mathematically stable steady state may not be actually observed in reality. In the following subsections, such an example is discussed and explained by the minimum perturbation magnitude and the minimum perturbation time.

7.5.1 Case introduction

By solving the steady state equation for the $UA = 0$ case, Heiselberg et. al [35] plotted the relationship (Figure 7-14) between the non-dimensional steady state flow rate $q (\overline{C_d A})^{-\frac{2}{3}} \left(\frac{\beta Egh}{\rho_a c_{pa}} \right)^{-\frac{1}{3}}$ and the boundary condition parameter ξ , which defines the relative magnitude of buoyancy to wind forces by

$$\xi \equiv \sqrt[3]{r}. \quad (7.32)$$

Here q is the real flow rate described in Equation (7.2); r is given by Equation (7.22).

Although Figure 7-14 looks similar to Figure 7-2, it has different meaning. Figure 7-2 shows the details of two values of ξ from the transient system Equation (7.1). It has both the steady states (equilibria) and the intervening non-equilibrium states. Most importantly, they are under the same boundary conditions. Figure 7-14 is obtained solving steady state equations as the boundary conditions are varied. The boundary conditions are represented by the values in the x-axis, which is the relative strength of the buoyancy force to the wind force. The y-axis is the dimensionless flow rate obtained from the steady state equation solution. From Figure 7-14, the observed range for multiple solutions is between $\xi = 0$ and 1, which is the same with

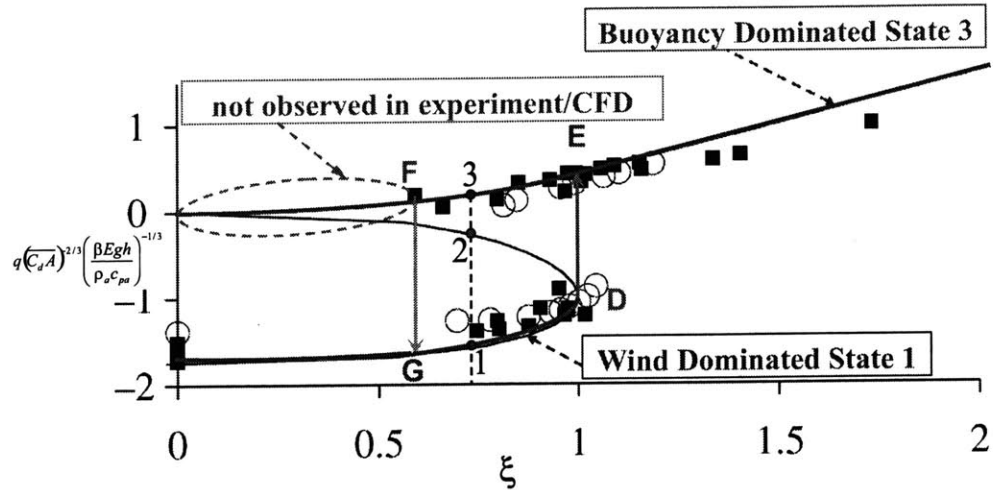


Figure 7-14: Observed behavior of the steady state of the system (Superimposed on the experimental results by Heiselberg et. al [35])

Equation (7.19) — the special case where $UA = 0$. For each ξ , in the range of 0–1, three mathematical solutions (or roots) of the steady state equation can be found. On the upper branch of the curve, the flow rate is upward and the points on it correspond to the buoyancy dominated patterns. On the lower branch of the curve, the flow is downward and the points on it correspond to the wind dominated patterns. The solutions in the upper branch and the lower branch are mathematically stable while the ones in the middle (the thinner curve) are not. Only those steady states on the upper or the lower branch can be observed in reality. The ones on the middle curve cannot be observed in reality due to their sensitivity to infinitesimal perturbations.

Although mathematically a buoyancy dominated stable solution exists for each of the ξ -values between 0 and 1, it is not observed in the scaled experiments and numerical CFD simulations by Heiselberg et al. [35] when ξ is below ~ 0.6 – 0.7 (Figure 7-14). This discrepancy between theoretical model and experimental/CFD results was explained only in a qualitative way in the original study [35].

However, with the minimum perturbation magnitude and the minimum perturbation time concepts developed in our study, this phenomenon can be quantitatively explained by differences in the state transition requirements of the two stable steady states. The explanations are provided in the following two subsections.

7.5.2 Minimum perturbation magnitude explanation

Since the system can have two stable steady states when $0 < \xi < 1$ (e.g. 1 and 3 in Figure 7-14 for a specific ξ), the minimum perturbation magnitudes for these two steady states can be calculated. Again based on the $5\text{m} \times 5\text{m} \times 4\text{m}$ sample building used in the previous sections (but with a series of different heat source and wind velocity combinations), the minimum perturbation magnitudes for different ξ -values are shown in Figures 7-15 and 7-16.

Figure 7-15 shows the minimum heat source perturbation required for two different types of solution switches: from solution 1 (wind dominated) to 3 (buoyancy dominated) and from solution 3 to 1. When the ξ -value is below ~ 0.8 , the switches from solution 1 to 3 need much higher heat source perturbations (the y-axis is in logarithmic scale) than the switches from 3 to 1. When ξ is greater than (~ 0.8), the opposite is true.

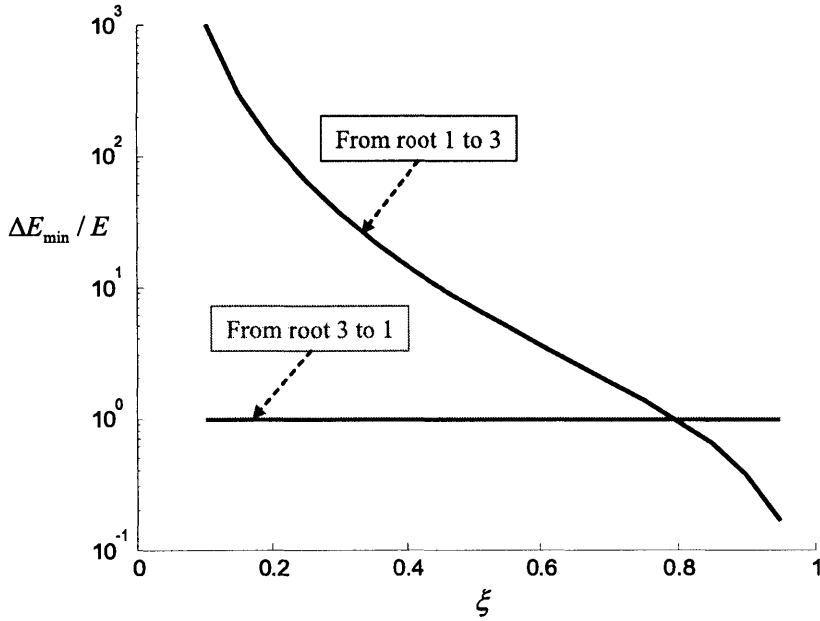


Figure 7-15: Minimum perturbation magnitude $\Delta E_{\min}/E$ vs. ξ for transitions between two stable steady states

Similar scenario happens for wind velocity (or pressure) perturbations. Figure 7-16 plots the minimum pressure (or velocity) perturbation magnitude for the two types of switches. When ξ is below ~ 0.9 , the switches from solution 1 to 3 need higher wind perturbations than the switches from 3 to 1 do. As ξ approaches unity, switches in the opposite direction are easier to happen under pressure perturbations.

More importantly, below approximately $\xi = 0.7$ (Figure 7-16), a small pressure perturbation (e.g. $< 5\%$) will enable the switch from buoyancy steady state 3 to wind dominated state 1. When ξ is below 0.6–0.7, the buoyancy dominated steady state 3 is very sensitive to pressure perturbations. Even a few percent of wind pressure increase may potentially cause the final state to switch over (if the perturbation lasts long enough). This minimum perturbation magnitude result partly explains why the steady state solution 3 is not likely to exist when ξ is below ~ 0.6 in the experiments and CFD simulations [35].

In summary, for both the heat source and the wind perturbations in this example, the transition from the buoyancy dominated state 3 to the wind dominated state 1 is more likely to occur when ξ is in small ($\leq \sim 0.8$), whereas the opposite is true when ξ grows larger near unity ($\geq \sim 0.9$). In other words, solution 1 is more stable than

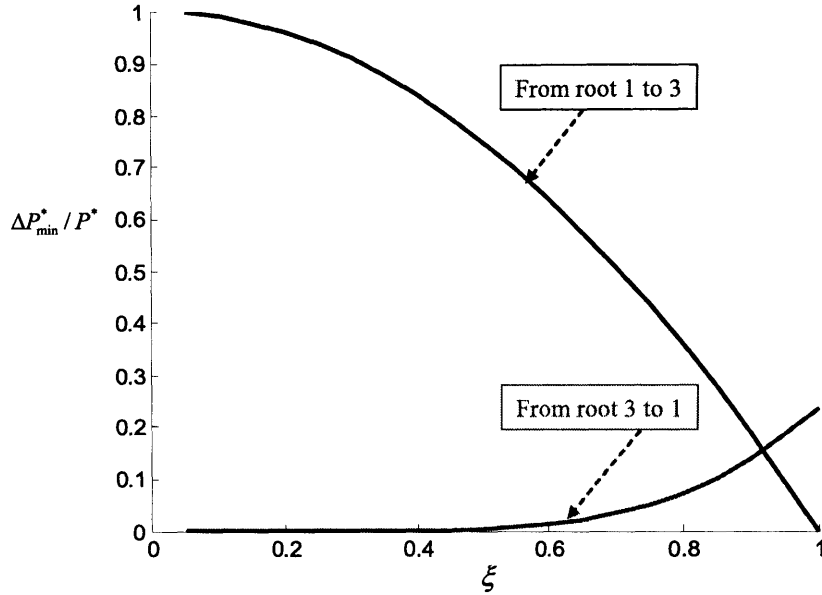


Figure 7-16: Minimum perturbation magnitude $|\Delta P^*| / P^*$ vs. ξ for transitions between two stable steady states

solution 3 in the range where x is small (e.g. $\leq \sim 0.8$), while solution 3 is more stable as ξ approaches unity.

7.5.3 Minimum perturbation time explanation

Along with the magnitude of the perturbation, the minimum time required for triggering the state transition under a certain perturbation can also be calculated to explain the phenomenon.

Figure 7-17 shows the minimum perturbation time for a switch from buoyancy dominated state 3 to the wind dominated state 1 under a 10% wind velocity increase perturbation for different ξ -value in our sample building ($5\text{m} \times 5\text{m} \times 4\text{m}$). The increase in the minimum perturbation time is extremely fast as ξ grows larger. However, when $\xi < \sim 0.7$, the minimum perturbation time is less than 10 seconds. When ξ becomes even smaller, the minimum perturbation time is less than 1 second. In this situation, any small wind gust will cause a buoyancy dominated steady state pattern to switch very quickly to the more stable wind dominated state. However, the same perturbation magnitude in the other direction (several percent wind decrease) is still much smaller than the minimum perturbation magnitude required to perturb the system from wind dominated state 1 to buoyancy dominated state 3 (Figure 7-16).

The results in Figures 7-16 and 7-17 together provide the explanation why buoyancy dominated flows are not observed in previous experiments and CFD simulations [35] when ξ is low ($< \sim 0.6-0.7$). In such a situation, a small pressure perturbation (several percent wind increase) can enable the switch from the buoyancy dominated

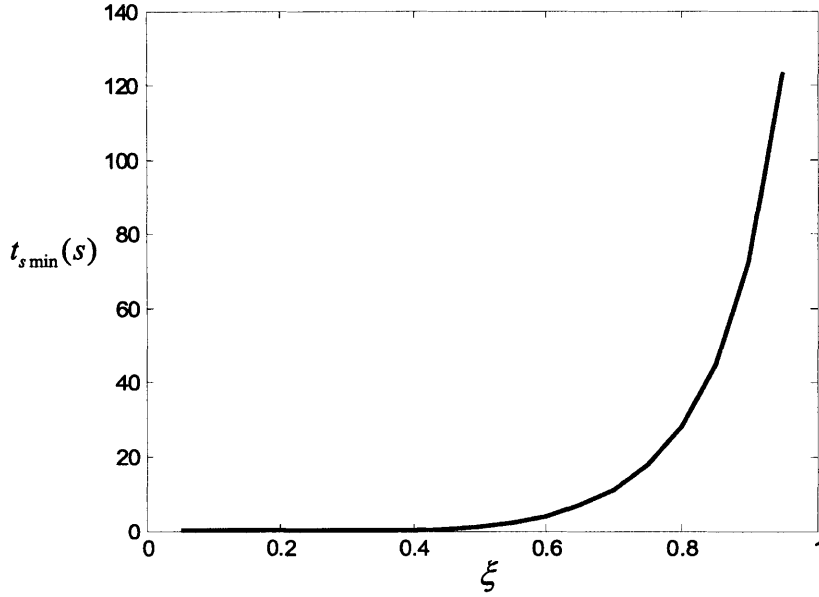


Figure 7-17: Minimum perturbation time vs. ξ ($\Delta v_{ref}/v_{ref} = 10\%$) for transition from the buoyancy dominated steady state 3 to the wind dominated steady state 1

solution 3 to the wind dominated solution 1 (the minimum perturbation magnitude, Figure 7-16) and trigger that switch in a very short time (the minimum time, Figure 7-17) such as a few seconds. Both the intrinsic fluid turbulences and the external stochastic environmental disturbances can be the sources of the small perturbations. Therefore, although it is mathematically possible and locally stable, the buoyancy dominated solution will not be observed in practice when ξ is less than ~ 0.6 .

For the same pressure perturbation magnitude, the minimum perturbation times for the transitions from steady state 1 to 3 and from 3 to 1 are compared in Figure 7-18. For the switch from 1 to 3, a negative 25% pressure perturbation ($\sim 10\%$ velocity decrease) is applied. For the switch from 3 to 1, a positive 25% pressure perturbation ($\sim 10\%$ velocity increase) is applied. In the $5m \times 5m \times 4m$ building example used in our study, the switch from 1 to 3 takes much longer time than that from 3 to 1 does when ξ is below ~ 0.97 . Beyond that ξ -value, the minimum perturbation time for the state switch from 3 to 1 becomes longer.

Figure 7-18 also shows that the wind dominated downward pattern is strengthened when ξ decreases. As ξ decreases, the minimum perturbation time for a switch from 1 to 3 will increase and make the switch from wind dominated flow to buoyancy dominated flow less likely. However, the minimum perturbation time for the switch from 3 to 1 becomes smaller as ξ decreases, which makes the wind dominated solution 1 more robust.

In contrast, the buoyancy dominated downward pattern is strengthened when ξ increases. As ξ increases, the minimum perturbation time to switch from 1 to 3 decreases. This makes the buoyancy dominated solution more robust as ξ approaches

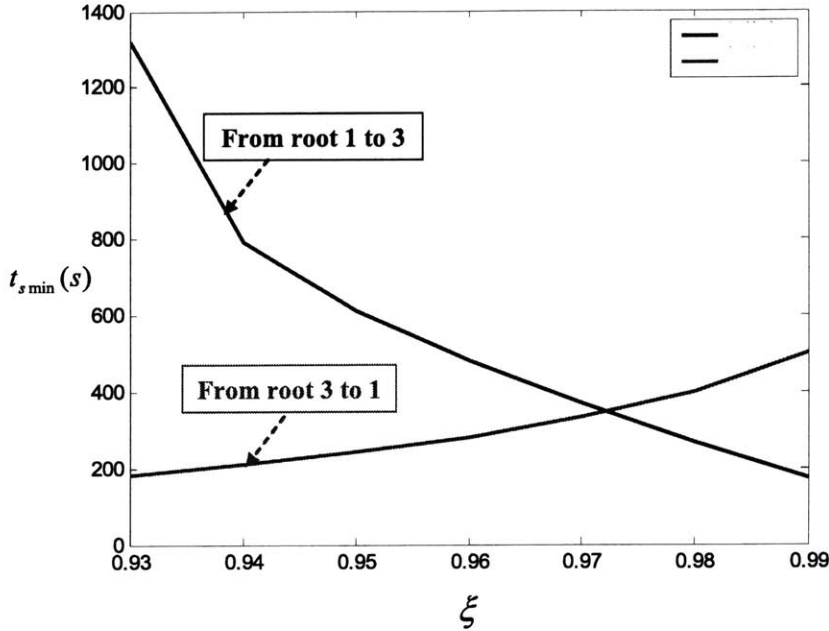


Figure 7-18: Minimum perturbation time vs. ξ under pressure (wind velocity) perturbations ($|\Delta P_{min}^*| / P^* = 0.25$)

unity. This trend can also be found in Figure 7-19 under a 50% heat source increase perturbation. When ξ approaches unity, the transition from wind dominated state 1 to buoyancy dominated state 3 under the heat source increase perturbation becomes easier and easier because the minimum perturbation time decreases toward zero.

Since the minimum perturbation time is a function of the perturbation magnitude, the influence of $\Delta v_{ref}/v_{ref}$ on the transition from buoyancy dominated (state 3) to wind dominated (state 1) flows is investigated in Figure 7-20. When ξ decreases, the perturbation time for such a switch quickly becomes smaller. When $\xi = \sim 0.6$, the time is less than 1 s, which means the system can be easily toppled by a very small perturbation (e.g. 5% of wind velocity increase).

Figure 7-21 illustrates the influence of heat source perturbation magnitude on the switching from state 1 to state 3 with different values of ξ . When ξ increases, the perturbation time decreases. The minimum perturbation time is also a function of the perturbation magnitude. However, the rate of change of the minimum perturbation time with ξ is much slower than that in Figure 7-20.

7.6 Applications of minimum perturbation time

Since the minimum perturbation time quantitatively indicates of the robustness of a stable steady state, it can be used to determine the actual existence of a specific stable steady state in an actual system. If the minimum perturbation time required for solution switch is too small, the theoretically (locally) stable solution will become

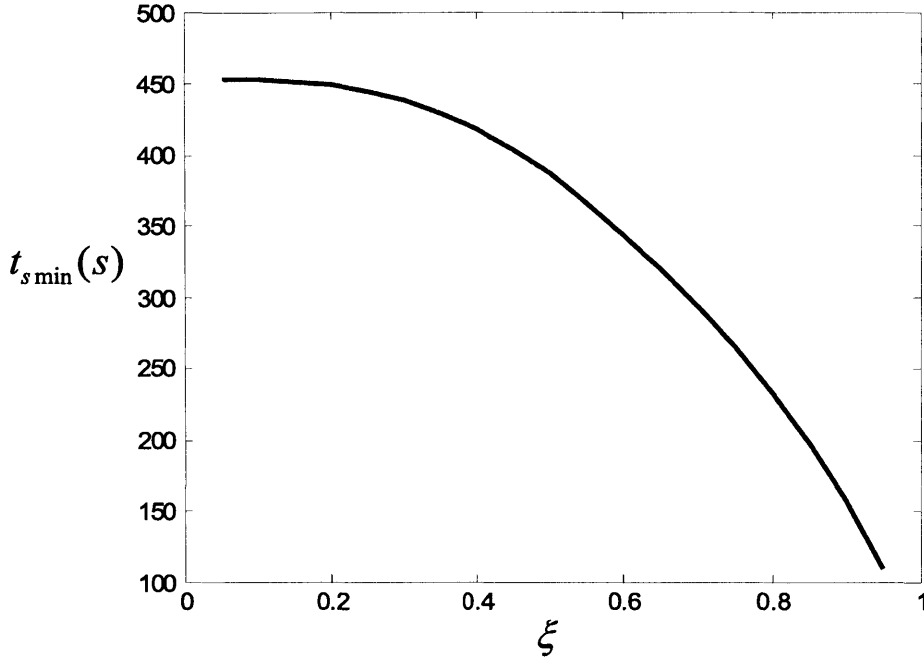


Figure 7-19: Minimum perturbation time vs. ξ ($\Delta E/E = 0.5$) for transition from wind dominated steady state 1 to buoyancy dominated steady state 3

unstable in actual systems where small perturbations always exist. An example will be presented in Section §7.6.1 .

Further, since the minimum perturbation time analysis is derived from the dynamical system differential equations, it can be a better indication of the actual existence of a solution than a single ξ value. A sensitivity study that shows the advantage of this analysis will be presented in Section §7.6.2.

Finally, Section §7.6.3 will discuss the potential application of the developed method in other solution multiplicity problems in building simulations and general dynamical systems.

7.6.1 Determination of the actual existence of a steady state in actual systems

The minimum perturbation time analysis is applied to the water bath experimental system used in a previous study [35]. Figure 7-22 shows the minimum perturbation time for the water bath system to switch from the buoyancy dominated steady state 3 to the wind dominated steady state 1 under a 10% velocity increase perturbation. In this case, the minimum perturbation time is shorter than a few seconds when ξ is ~ 0.6 or less. Therefore when ξ is smaller than ~ 0.6 , the buoyancy dominated steady state 3 can not be observed in the water bath experiment.

Figure 7-23 shows possible steady state solutions then can be plotted based on the

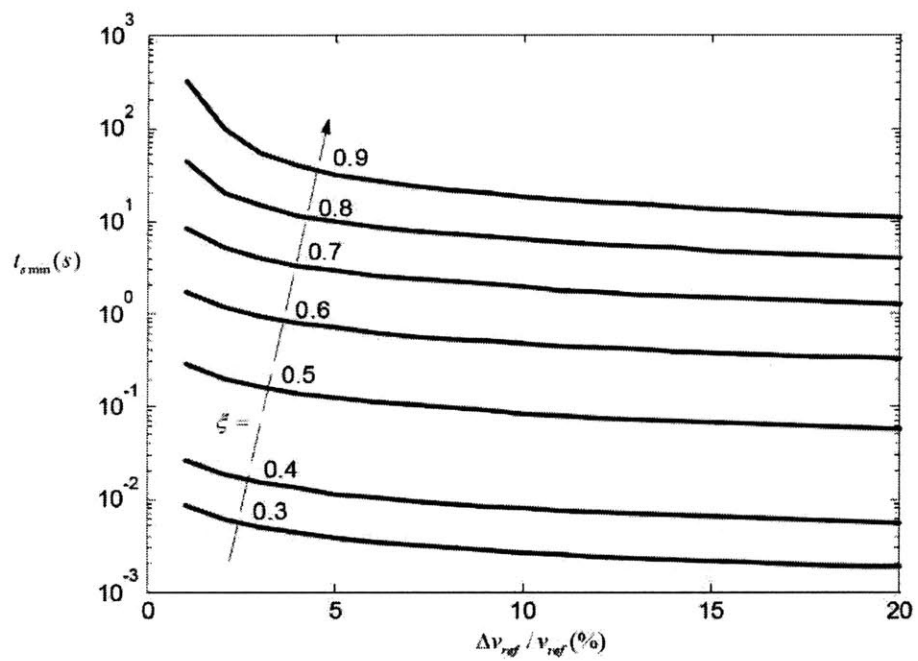


Figure 7-20: Minimum perturbation time (s) vs. Wind velocity perturbations for different ξ values from 0.3 to 0.9 (switch from buoyancy dominated state 3 to wind dominated state 1)

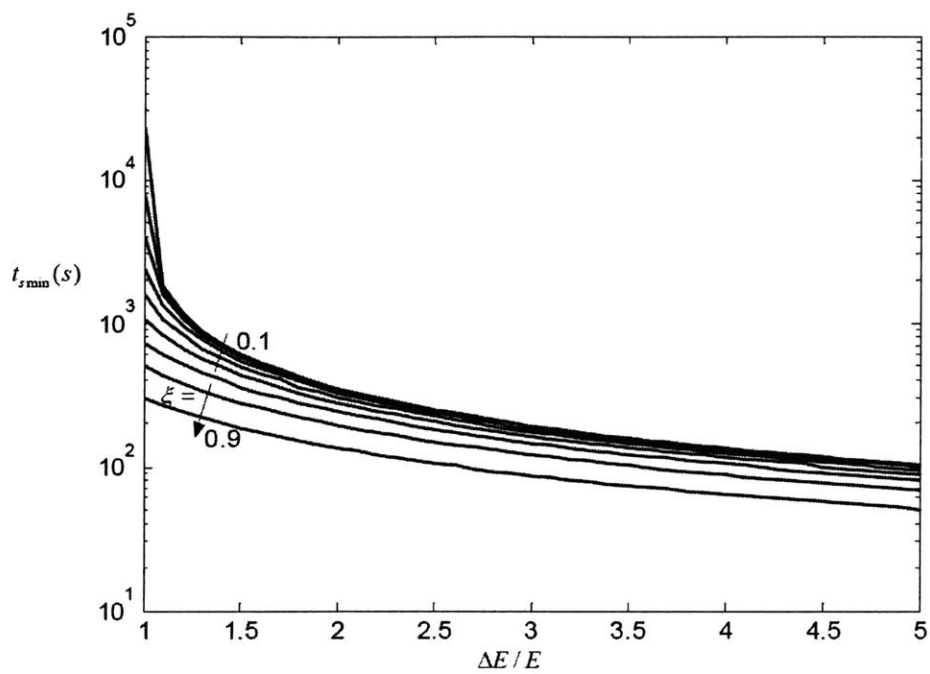


Figure 7-21: Minimum perturbation time (s) vs. heat source perturbations for different ξ values from 0. 1 to 0.9 (switch from wind dominated state 1 to buoyancy dominated state 3)

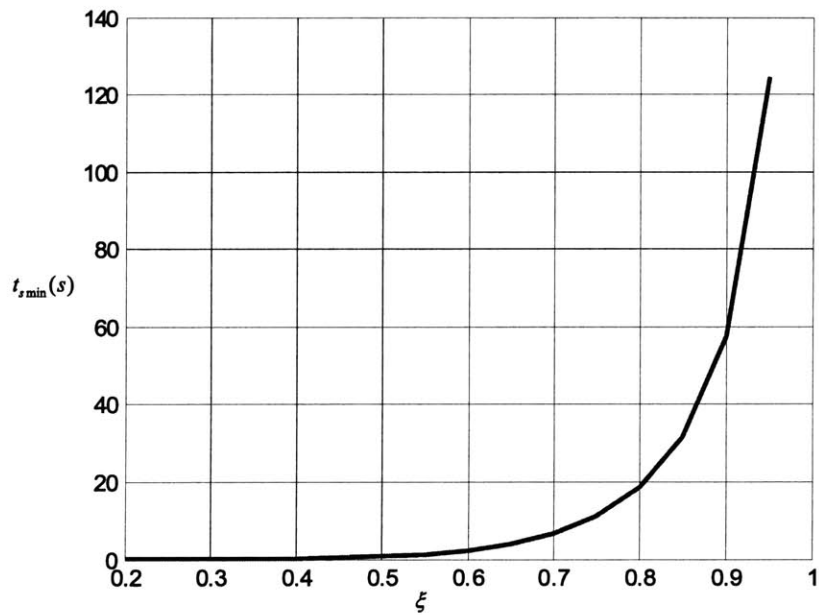


Figure 7-22: Minimum perturbation time for different ξ values under a 10% velocity increase perturbation (transition from buoyancy to wind dominated states) for water bath experiment in Heiselberg et. al [35])

minimum perturbation time calculation. Here 10 s is used as the cut-off minimum perturbation time that distinguishes whether or not a mathematically stable steady state can exist in an actual system under a 10% velocity variation. An air filled room of dimensions $5\text{m} \times 5\text{m} \times 4\text{m}$ is used for this example. The solid lines indicate the stable and observable steady states, while the dashed lines stand for the steady states that are either mathematically unstable or practically unobservable (the minimum perturbation time < 10 s). The segment of the dashed line marked as “mathematically unstable” stands for the locally unstable steady state solutions 2. The segments of the dashed line marked as “not robust enough” stands for the steady state solutions whose minimum perturbation time to switch to another steady state under a 10% wind velocity perturbation is shorter than 10 s. By this criterion, the points that are not stable or not robust enough will both be categorized as unobservable solutions in actual systems. Starting from the buoyancy dominated steady state 3, as ξ decreases, the solution is not stable in actual systems when ξ drops below ~ 0.6 . Starting from the wind dominated steady state 1, as ξ increases, the solution is stable up to a ξ -value very close to unity. Therefore, there is a region of hysteresis as ξ is reduced in state 3 and then ξ is increased in state 1 between ξ of ~ 0.6 and unity.

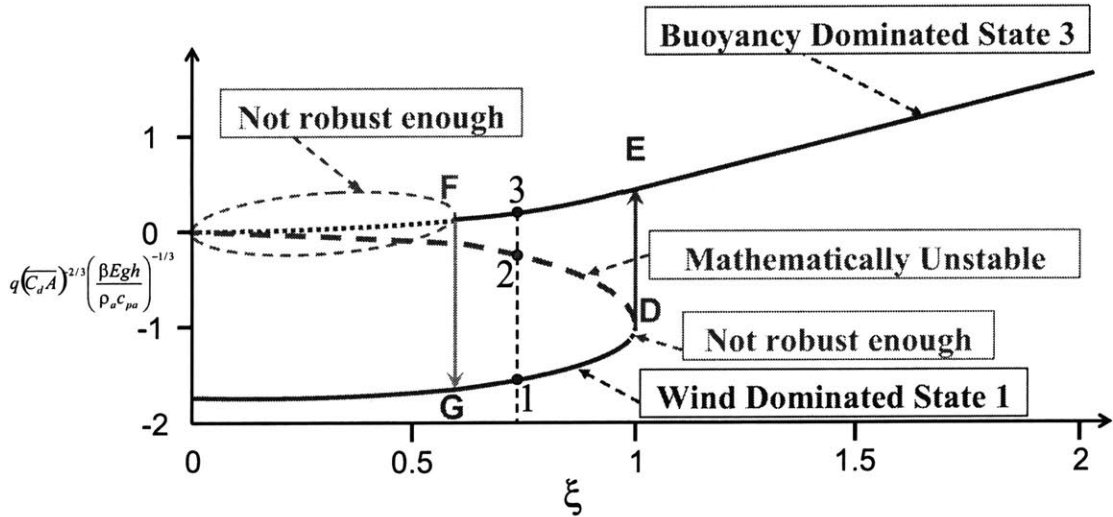


Figure 7-23: Stable steady states for with both stability and robustness of steady state solutions

7.6.2 Sensitivity studies on other parameters

The minimum perturbation time is a function not only of ξ and the perturbation magnitude, but essentially of all other parameters that appear in Equations (7.5), (7.30), and (7.31). Therefore, a single value of ξ may not be enough to determine the actual stability of the system. For example, the graph shown in Figure 7-23 stands for only one set of parameters such as the room dimensions, the opening sizes, wind velocity and heat source magnitudes. The following sensitivity test will show

the advantages of the minimum perturbation methods in considering all the other parameters in actual system.

A sensitivity study on the wind velocity's (one of the parameters used in Equation (7.5)) influence on the minimum perturbation time is shown in Figure 7-24. The minimum perturbation time versus ξ is plotted on four curves for four different velocities (v_{ref}): v_0 ($=1.7\text{m/s}$), $1.1v_0$, $1.2v_0$, and $1.3v_0$. For the same ξ -value, the minimum perturbation time is dependent on the wind velocity v_{ref} . Especially when ξ increases, the impact of v_{ref} becomes larger. Other than v_{ref} , other parameters in Equation (7.5) can also affect the solution transition behaviors. Their effects on the solution transition dynamics may not be accurately captured by a single ξ -value, while it can be accurately captured by the minimum perturbation time calculated by Equations (7.30) and (7.31).

Therefore, the minimum perturbation time is a more quantitative and accurate measure to the stability for a stable steady state in actual systems. Although the ξ -value can be useful in qualitatively distinguishing mathematically stable steady states for a special case of $UA = 0$ (e.g. in [35]), the minimum perturbation method more accurately reflects the underlying state transition dynamics and can be used for more general cases of $UA \geq 0$. Thus, the minimum perturbation analysis can be a more reliable and applicable method in determining the actual existence of a mathematically stable steady state.

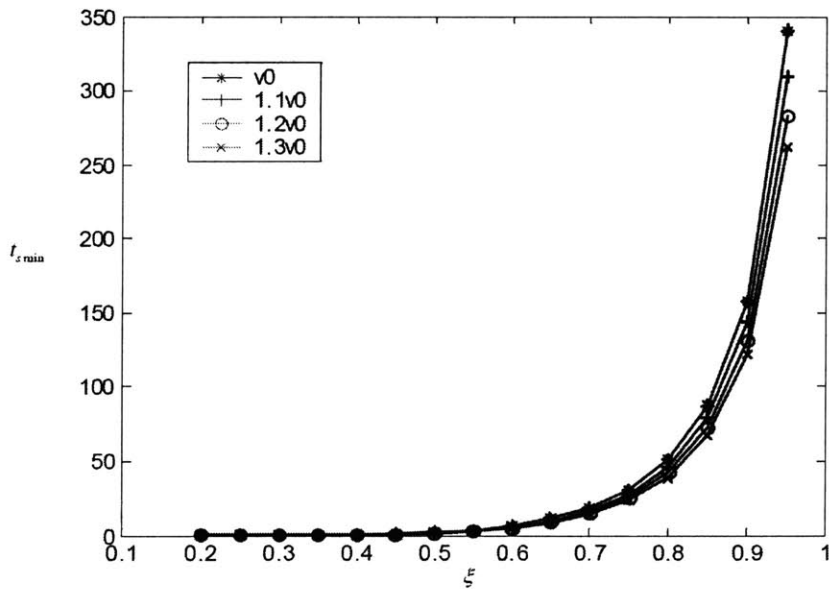


Figure 7-24: Minimum perturbation time vs. ξ with different initial wind velocities for transition from buoyancy dominated to wind dominated states

7.6.3 Discussion on more general applications

The perturbation method can be applied to more general solution multiplicity problems in natural ventilation systems (e.g. [22, 45]). In these systems, the stochastic components of the environmental variables such as the heat source and wind velocity fluctuations can still be the sources of perturbations. Special attention should be paid to the wind velocity (pressure) perturbations in pure buoyancy driven natural ventilation systems that have multiple steady states. In those systems, pressure perturbations due to small wind motions can exist in reality and greatly affect the flows. In such systems, the minimum perturbation magnitude and the minimum perturbation time under perturbations can also be calculated by analytical or numerical methods to check the stability of a mathematically stable steady state in reality.

For dynamical systems that are described by one-dimensional (or even higher dimensional) ordinary differential equations, the perturbation analysis presented in our study can also be applied analytically or numerically to examine the robustness of the locally stable steady states. A key point is to identify possible disturbances in the actual system and use them as perturbations, which in our study are the heat source and pressure (velocity) disturbances.

7.7 Conclusions

A naturally ventilated building with opposing wind and buoyancy forces can exhibit two mathematically stable steady states when certain conditions are satisfied.

However, the system can switch from one stable steady state to another when the environment conditions change. In this chapter, these environmental conditions change were defined as strong perturbations. Two types of practical perturbations-heat source fluctuations and wind variations- and their impact on the dynamical characteristics of the system were discussed. Situations where the system goes back to the original steady state or switches to the other steady state are related to both the magnitude and the duration of the perturbation.

The minimum perturbation magnitude must be able to perturb the system across the unstable steady state in an infinite time to enable a state switch. For a square perturbation, the minimum perturbation magnitude for a state transition can be mathematically derived. For the case of an arbitrary shape perturbation, it can be reviewed as a series of small square perturbations. Based on this principle, the experimental phenomenon observed by Linden [44] was successfully explained.

A minimum perturbation time is required for the system to switch to the other stable steady state when a qualified perturbation is applied. This time can be mathematically calculated by integration when a qualified perturbation is given.

The minimum perturbation time is an important parameter in describing the robustness of a mathematically (or locally) stable steady state. If the perturbation time required to switch to another stable steady state is too short under a small perturbation, this steady state is practically unstable. This conclusion successfully explains the experiment/CFD results reported in another existing study [35], where

the buoyancy dominated steady state cannot be observed with a low ξ -value. The minimum perturbation magnitude and the minimum perturbation time calculations show that when ξ is small, a small wind perturbation may trigger a rapid permanent transition from the buoyancy dominated state to the wind dominated state. On the other hand, when ξ approaches very close to unity, transition from the wind dominated state to the buoyancy dominated state is more likely.

Finally, the concepts of the minimum perturbation magnitude and the minimum perturbation time may also be applied in buoyancy driven systems with multiple steady states, where heat source and pressure perturbations are important as well. Further, the mathematical derivations of the minimum perturbation time can also be applied to a general one-dimensional dynamical system represented by a first-order differential equation.

Chapter 8

Transitions between the multiple steady states in a single-zone natural ventilation system with thermal mass

Previous studies have shown that a.) a natural ventilation system with thermal mass (air-mass system) can have multiple (stable) steady states (see Chapters 5 and 6 or [75, 76]) due to nonlinearities of the system; and b.) the system can transit from one stable steady state to another under sufficient “strong” perturbations. In this chapter, we investigate the transitions between the multiple (stable) steady states in a natural ventilated building with thermal mass. First, mathematical models and methodologies are introduced for the transition dynamics between the transitions between the multiple steady states in the air-mass system. Two indicative parameters—the minimum perturbation magnitude and the minimum perturbation time—are further quantitatively investigated in the system with mass; and compared with those in an otherwise equivalent system without thermal mass (air-only system). It is found in an air-mass system, the transitions between two stable steady states are much more difficult than in the air-only system. The transitions in the air-mass system will need much longer minimum perturbation time to occur due to the time-lag effect of the thermal mass. The minimum perturbation time is also sensitive to the thermal mass parameters such as the air-mass heat transfer coefficient (hA_m) and the heat capacities of the thermal mass. With larger heat transfer capabilities (hA_m) between the air and the thermal mass, or larger heat capacity of the thermal mass ($M_m c_m$), the state transition is more difficult. The results indicate that the thermal mass tends to make a steady state in a nonlinear system more stable and more resistant to the stochastic disturbances in actual systems.

8.1 Introduction

In a natural ventilation system with multiple steady states, the transition dynamics between the stable steady states are important to the actual stability of those steady states. For example, in Chapter 7 (or [77]), the transition dynamics between the

multiple steady states in a system (similar to Figure 8-1) without thermal mass (air-only) was investigated. The study showed that a *minimum perturbation magnitude* is required to enable the state transitions between two mathematically stable steady states, assuming that there is no time limit of applying the perturbation. Further, given a perturbation that is strong enough, the system also requires a *minimum perturbation time*—the shortest time the perturbation need to be applied—to transform from one stable steady state to another. Both the minimum perturbation magnitude and the minimum perturbation time can be quantitatively computated and can serve as indicative parameters for the actual stability of the (mathematically) stable steady states in a natural ventilation system. If the two indicative parameters are too small, the system may be easily perturbed from one steady state to another under small (but not infinitesimal) perturbations that exist in reality.

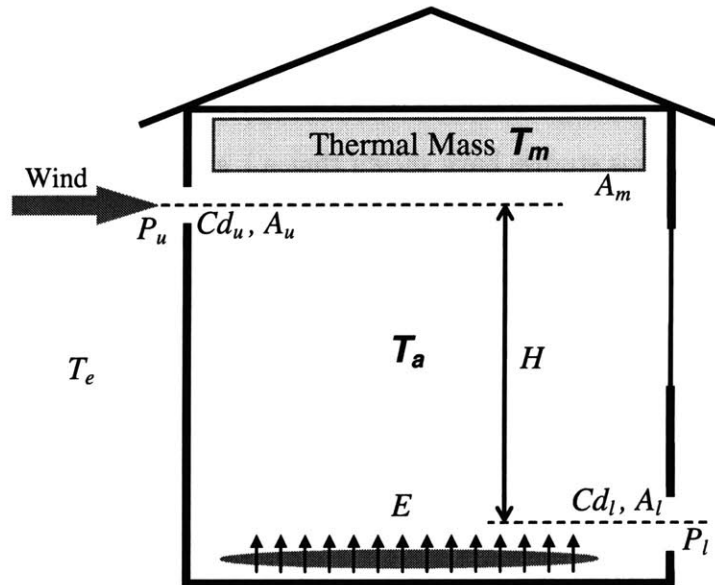


Figure 8-1: A single-zone air-mass natural ventilation system with opposing wind and buoyancy forces

However, the state transition study above does not consider the impact of thermal mass during the transitions. Generally, thermal mass can have a strong impact on the dynamical system behaviors of a ventilation system. An obvious effect of thermal mass is its time-delay effect on the response on the parameters change (e.g., the outdoor air temperature), which sometime are positively used for storing heat, shifting peaks, and achieving energy-bill savings (e.g., Rabl and Norford[52]). In particular, for the natural ventilation systems that may exhibit multiple steady states, thermal mass can have significant impact on the nonlinear behaviors of the system, as was investigated in Chapters 5 and 6 (or [75, 76]). In a natural ventilation system with thermal mass shown in (Figure 8-1), although the thermal mass does not affect the existence of the multiple steady states, it has significant impacts on determining the final steady state of the system. When the system contains additional thermal mass (other than the air), the initial air temperature is no longer the sole decision variable that determines the final steady state of the system. Even more importantly, the initial thermal mass temperature can even be a more important factor than the initial air temperature in

determining the final steady states of the system if the inter-air-mass heat transfer rate and the mass heat capacity are high enough.

The impact of thermal mass on the dynamical system behaviors in ventilation system poses a challenge to the state transitions in a system with thermal mass. Since the state transition dynamics is closely related to the dynamical system behaviors of a ventilation system (see Chapter 7 or [77], thermal mass models, essentially, should be adequately incorporated into a state transition model that transition dynamics between multiple steady states.

In this chapter, we will build the models for the state transitions between the multiple steady states in a single-zone natural ventilation system with thermal mass. Similar to the methodology used in Chapter 7, we will analyze the behaviors of the (air-mass) system under strong perturbations, which are defined sudden boundary parameter changes of a finite magnitude, as is shown in Figure 8-2. Two types of perturbations we will use are the heat source perturbation and the wind pressure perturbation.

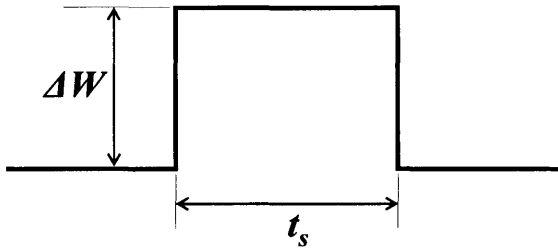


Figure 8-2: A “strong” perturbation

8.2 Mathematical models

The single zone system with thermal mass shown in Figure 8-1 is again studied in this chapter. The mathematical model to describe the dynamical system behaviors of the system developed in Chapter 5 is also used here. The governing equations of the air and thermal mass dynamics are shown in Equations (8.1) to (8.5).

For the air:

$$f_a(T_a^*, T_m^*) = \frac{dT_a^*}{dt} = \frac{E}{M_a c_a} - \frac{\rho_a c_a}{M_a c_a} q \cdot T_a^* - \frac{UA}{M_a c_a} T_a^* - \frac{hA_m}{M_a c_a} (T_a^* - T_m^*), \quad (8.1)$$

and for the thermal mass:

$$f_m(T_a^*, T_m^*) = \frac{dT_m^*}{dt} = -\frac{hA_m}{M_m c_m} (T_m^* - T_a^*). \quad (8.2)$$

where T_a^* and T_m^* are defined by

$$T_a^* = T_a - T_e, \quad (8.3)$$

$$T_m^* = T_m - T_e. \quad (8.4)$$

Flow Component:

$$q = \overline{C_d A} \cdot \sqrt{\left| 2gH \cdot \beta(T_a - T_e) - 2 \frac{P_w}{\rho_a} \right|}, \quad (8.5)$$

where β is thermal expansion coefficient of the air in $1/K$. For ideal gas, β can be approximated as $1/T$. In Equation (8.5), the expansion coefficient is assumed a constant based on the temperature of the outdoor air T_e . Therefore $\beta = 1/T_e$. P_w is the wind pressure difference between the inlet and outlet in Pa. The relationship is defined by

$$P_w = P_u - P_l = \frac{1}{2} \rho_a (Cp_u - Cp_l) \cdot v_{ref}^2. \quad (8.6)$$

where Cp_u and Cp_l are the wind pressure coefficients for the two openings, and v_{ref} is the reference velocity for wind pressure coefficient.

Equations (8.1) and (8.2) describe the dynamics of the air and thermal mass temperature subjected to the ventilation flow rate and heat source. The term E in this equation is a lumped sum which is composed of all the heat gains by heat transfer processes that are not related to the indoor temperature. Equation (8.6) describes the airflow rate by the combined interaction of the wind-driven and buoyancy-driven forces. The term $\overline{C_d A}$ is the product of effective flow discharge coefficient and the effective area of the two openings in m^2 . The complete reference explanation and references of the system equation are available in Chapters 5 and 6.

As was demonstrated in Chapter 5, the system can have three steady states when certain conditions are satisfied. Figure 5-6 shows the three steady states on the *phase plane*, where the two state variables— T_a^* and T_m^* —are plotted against each other. We denote the three steady states as SS1, SS2, and SS3, from low to high temperature values. SS1 and SS3 are the two stable steady states, and SS2 is the unstable one. Physically, SS1 is a wind-dominated steady state where the flow travels downward in Figure 8-1; while SS3 is a buoyancy-dominated steady state where the flow travels upward in Figure 8-1. SS2 is an unstable steady state, where the system may approach from two special trajectories on the phase plane but cannot permanently stay. For the stability details of the three steady states, refer to Chapters 5 and 6.

8.3 System behavior under strong perturbations—minimum perturbation magnitude

Although the system exhibits stable equilibrium at the stable Steady States 1 and 3, it can still switch between SS1 and SS3 when there is sufficient perturbation of the boundary conditions (see also Chapter 7 or [77]). Here we again use the square “strong perturbation” defined in Chapter 7 (or [77]) as is shown in Figure 8-2. It is assumed that starting from one of the system’s stable steady state conditions, a sudden change in the amount of ΔW in the wind pressure (velocity) or the heat load acts on the system and lasts for a time span of t_s . After time t_s , the perturbation is removed and

the parameter change back to its original value (before the perturbation).

Two important factors—the magnitude of the perturbation ΔW and the duration of the perturbation t_s —are important to the system's behavior under the perturbation. Here the task is to find requirements for the magnitude and duration that can cause a state transition between the two stable steady states—SS1 and SS3. In Chapter 7 (or [77]), these minimum requirements were investigated for a heat source perturbation and a wind velocity (pressure) perturbation. With the existence of thermal mass, the situation is more complicated since the mass will also play an active role in the transition dynamics. In the following text, the perturbation requirement will be investigated under two different types of perturbations — heat source perturbations and wind velocity (pressure) perturbations.

For the heat source perturbation, the only way to transform the system from SS1 to SS3 or from SS3 to SS1 is to break the necessary condition for the existence of multiple steady states during the perturbation. Therefore, all the conclusions from Chapter 7 (or [77]) regarding the minimum heat source perturbation magnitude can still be applied. This necessary condition for the minimum heat source perturbation magnitude is independent of the thermal mass parameters. (However, the duration of a perturbation that causes a switch between steady states is a function of the thermal mass. If the perturbation lasts long enough, it will finally switch to the other steady state. We will discuss the time requirement issues in the later sections.)

For example, a transition from SS1 to SS3 under a heat source perturbation requires the minimum perturbation magnitude to satisfy

$$\beta(\Delta E + E) \geq T_B^{**} \left(\overline{C_d A} \cdot \rho_a c_a \sqrt{2gH} \cdot \sqrt{P^{**} - T_B^{**}} + UA \right) \geq 0, \quad (8.7)$$

where

$$T_B^{**} = P^{**} - \left(\frac{\sqrt{X^2 + 3P^{**}} - X}{3} \right)^2, \quad (8.8)$$

where X is defined by

$$X = \frac{UA}{\overline{C_d A} \cdot \rho_a c_a \cdot \sqrt{2gH}}. \quad (8.9)$$

A transition from SS3 to SS1 requires the minimum heat source perturbation to satisfy

$$\beta(E + \Delta E) \leq P^{**} \cdot UA. \quad (8.10)$$

The condition described in Equations (8.7) and (8.10) are also sufficient conditions to switch the solution if the perturbation time is long enough.

The minimum perturbation requirements for the pressure perturbation are slightly more complex. The minimum pressure perturbation magnitude for a transition from SS1 to SS3 still obey the rule of “destroy the necessary condition for multiple steady states”, although it might not be a sufficient condition even when the perturbation time is long enough. This issue is discussed in Chapter 7 and will not be repeated here. Here will just introduce the minimum pressure perturbation magnitude requirement

for transitions from SS1 to SS3 as

$$\beta E \geq T_{\hat{B}}^{**} \left(\overline{C_d A} \cdot \rho_a c_a \cdot \sqrt{2gH} \cdot \sqrt{(P^{**} + \Delta P^{**}) - T_{\hat{B}}^{**}} + UA \right), \quad (8.11)$$

where $T_{\hat{B}}^{**}$ is defined the same way as by Equations (8.8) and (8.9), except that we need to use $P^{**} + \Delta P^{**}$ to replace P^{**} for computing of $T_{\hat{B}}^{**}$.

The minimum pressure perturbation requirement for the transition from SS3 to SS1 is slightly different from that for the transition from SS1 to SS3. Nevertheless, the systems with thermal mass and without thermal mass still share the same requirements for the transition from SS3 to SS1. This requirement was developed in Chapter 7 as

$$\hat{T}_{ss2}^* > T_{ss3}^*, \quad (8.12)$$

which means that the minimum perturbation should be strong enough to the extent that the temperature of SS3 in the original system is below the temperature of the unstable steady state SS2 in the perturbed system.

8.4 System behavior under strong perturbations—minimum perturbation time

When the thermal mass exists in a system, the system generally becomes more sluggish in responding to the boundary parameter changes due to the increased heat capacity of the system. Here we conducted a preliminary case of state transitions in an air-mass system under a heat source perturbation similar to a previous study (Yuan and Glicksman [77]). The test building is a $5\text{m} \times 5\text{m} \times 4\text{m}$ ($\text{W} \times \text{L} \times \text{H}$) single room. The heat source perturbation is $\Delta E/E = 1.1137$ and $hA_m = 840 \text{ W}/^\circ\text{C}$. If air is the only thermal mass, the minimum perturbation time for the system to switch from the cooler Steady State 1 ($\sim 15^\circ\text{C}$) to the warmer Steady State 3 ($\sim 25^\circ\text{C}$) is around 303s. However, when the thermal mass is incorporated into the system, a similar duration is far from enough to make the system solution to switch (Figure 8-3(a)). The air temperature increases during the perturbation but the cooler thermal mass reverses the air temperature again at the end of the perturbation. Only when the perturbation time is more than 4046s can the system solution switch from the pressure dominated lower solution to the buoyancy dominated higher solution (Figure 8-3(b)). This allows enough time for the thermal mass temperature to increases near the new steady state temperature.

The same “sluggish” behavior occurs when pressure perturbations are applied to the system. Therefore, the convective heat transfer between the air and the thermal mass plays an important role in the speed of the system response when subjected to a perturbation that can switch the solution. However, for this two-variable system, no explicit formula can be derived as for the single variable system (Yuan and Glicksman [77]) to calculate the minimum perturbation time. A step perturbation of magnitude of ΔW (either heat source or wind) that lasts a time span t_s is used here. In the succeeding sections, the minimum perturbation time is obtained by numerical meth-

ods in an automatic bisectional trial-and-error way. The accuracy of the minimum perturbation time calculation is set to 10s since most of the values are in the order of hundreds to thousands of seconds.

8.5 Impact of hA_m on state transitions

8.5.1 Heat source perturbations

To investigate the impact of hA_m on the solution switching, the case of switching from the lower temperature wind dominated solution 1 to the higher temperature buoyancy dominated solution 3 is investigated using the same room dimensions as used for Figure 8-3.

Under a heat source perturbation, the minimum perturbation time is bounded by the two extreme cases. When $hA_m = 0$, the solution switch needs the shortest time. When $hA_m \rightarrow \infty$, the system needs the longest perturbation time to switch from the lower solution 1 (wind dominated) to the upper solution 3 (buoyancy dominated). For the tested perturbation magnitude ($\Delta E/E = 1.1137$), the minimum perturbation time is listed in Table 8.1 and plotted in Figure 8-4. The minimum perturbation time under this condition is bounded between 302.82s and 5867.8s.

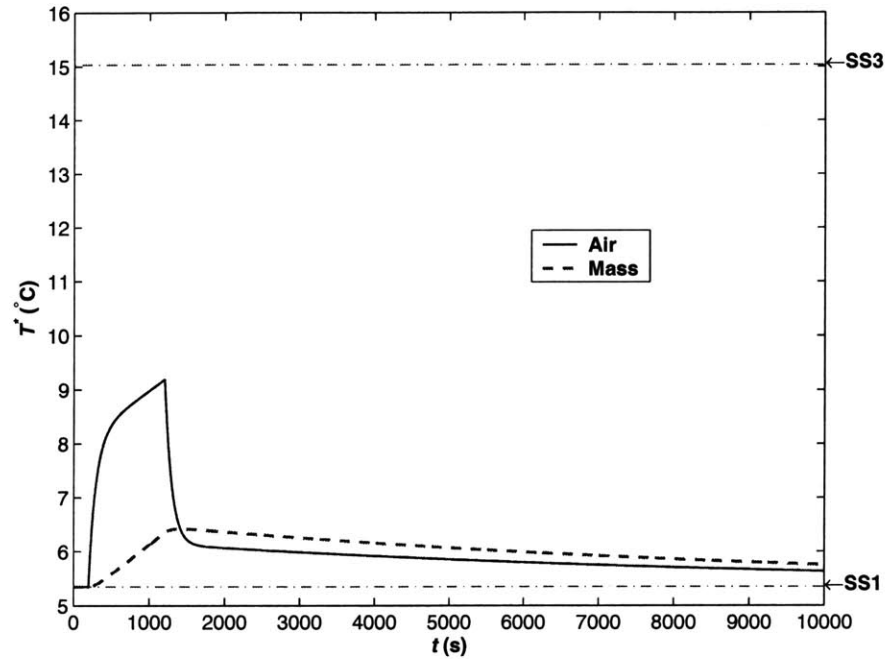
Table 8.1: Minimum perturbation times vs. hA_m value for the transitions from wind dominated SS1 to buoyancy dominated SS3 under heat source perturbation ($\Delta E/E = 1.1137$)

hA_m (W/ $^{\circ}$ C)	∞	3360	2520	1680	1470	1260	1050	840
$t_{smin}(s)$	5868	5584	5494	5250	5155	4994	4630	4046
hA_m (W/ $^{\circ}$ C)	630	420	210	105	52.5	26.25	0	
$t_{smin}(s)$	3130	1399	494.4	385.7	339.5	320.5	302.8	

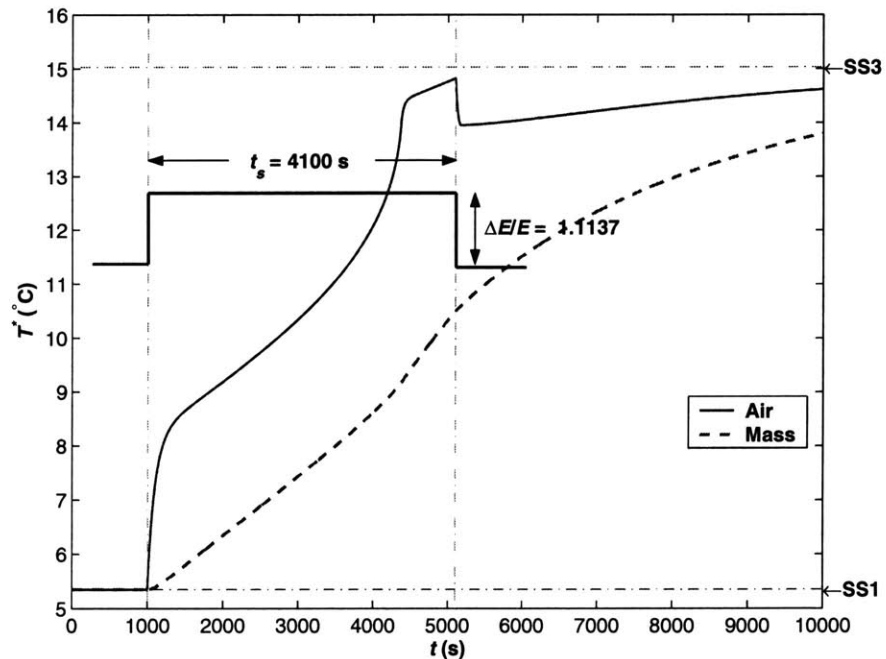
For the switch from the buoyancy dominated solution 3 to the wind dominated solution 1, the necessary condition is to reduce the heat source below zero, i.e. cooling as is discussed in the previous study (Yuan and Glicksman [77]). The minimum perturbation time can be investigated in the same way. Since such a situation is not usual (the heat source inside becomes a cooling source), the test case is not conducted in detail here. However, since the system becomes more sluggish when the thermal mass is incorporated, it would also take much longer perturbation time than a single variable system for the same solution switch.

8.5.2 Pressure perturbations

Under certain pressure perturbation, the system can switch from one steady state to the other steady state. Table 8.2 and Figure 8-5 show the relation between different hA_m values and the minimum perturbation time for the switch from buoyancy dominated solution 3 to the wind dominated solution 1 under a 20% pressure increase. The two extreme cases are still the longest and shortest time required for the system



(a) $t_s = 1000\text{s}$



(b) $t_s = 4100\text{s}$

Figure 8-3: Responses of the system to heat source perturbations of two different durations ($\Delta E/E = 1.1137$, $hA_m = 840 \text{ W}/^\circ\text{C}$)

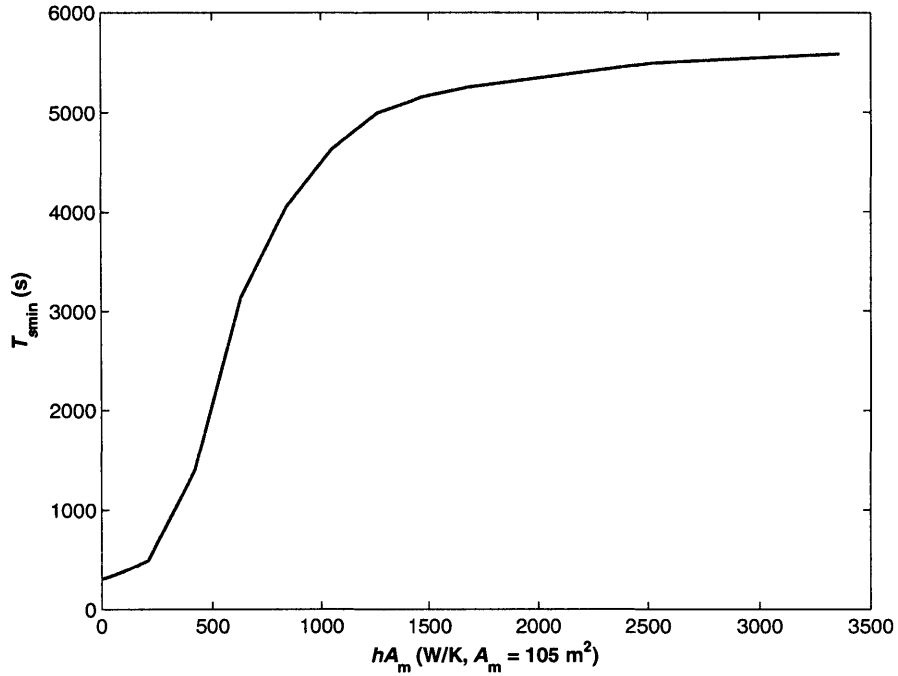


Figure 8-4: Minimum perturbation time vs. hA_m value under heat source perturbation ($\Delta E/E = 1.1137$) for transition from SS1 to SS3

to switch solution. When hA_m is given as a finite value, the minimum perturbation time is in between the two extreme cases.

Table 8.2: Minimum perturbation times vs. hA_m value for transition from SS3 to SS1 under pressure perturbation ($\Delta P/P = 0.2$)

hA_m (W/ $^{\circ}$ C)	∞	3360	1680	1260	840	630	420	315
t_{smin} (s)	4462	3936	3554	3367	3121	2943	2561	2026
hA_m (W/ $^{\circ}$ C)	262.5	210	157.5	105	78.75	52.5	26.25	0
t_{smin} (s)	1485	650.0	358.0	290.0	268.4	251.5	243.0	230.2

With negative pressure perturbations on the system causing it to switch from solution 1 to 3, the system would be expected to show the same behavior as the previous cases. However, it is more complicated and unusual as shown on Table 8.3 and Figure 8-6. The bounding values of the minimum transition time are not the same as the heat source perturbation. For the test case, the pressure perturbation is taken as a 20% decrease in the original pressure difference (the corresponding velocity decrease is $\sim 10\%$).

Table 8.3 lists the minimum perturbation time for the switch from the downward flow pressure dominated solution 1 to the upward flow buoyancy dominated solution 3 under a 20% pressure decrease. Unlike the previous result for the pressure perturbation, the minimum perturbation time for different hA_m value is not exactly bounded

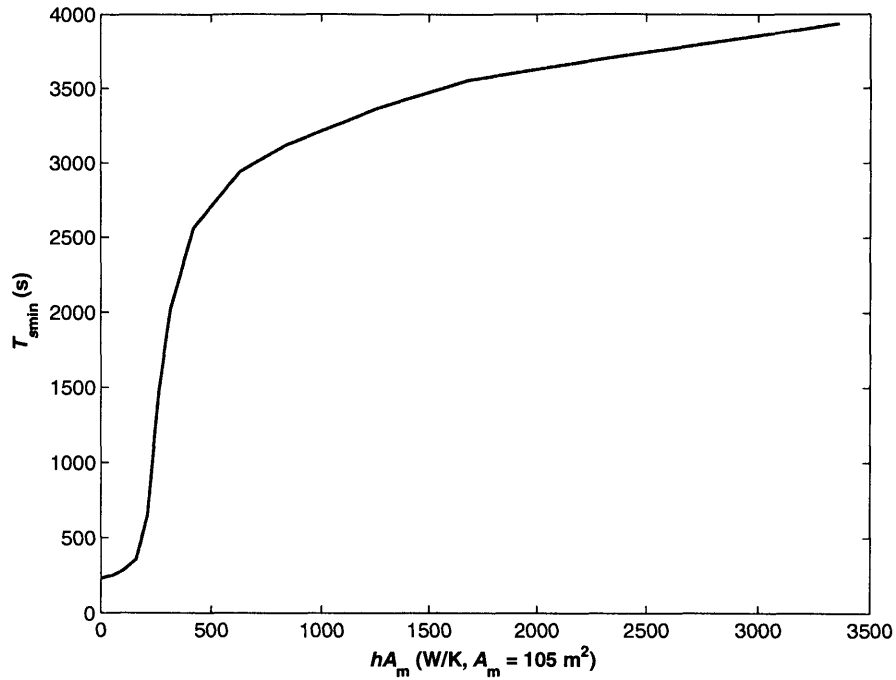


Figure 8-5: Minimum perturbation time vs. hA_m for transitions from SS3 to SS1 under pressure perturbation ($\Delta P/P = 0.2$)

by the two extreme case.

Table 8.3: Minimum perturbation times vs. hA_m values for transitions from SS1 to SS3 under pressure perturbation ($\Delta P/P = -0.2$)

hA_m (W/ $^{\circ}$ C)	∞	3360	1680	1260	840	630	420	210
t_{smin} (s)	34048	34277	34675	35012	35723	36317	37040	37990
hA_m (W/ $^{\circ}$ C)	157.5	105	78.75	52.5	39.375	26.25	13.125	0
t_{smin} (s)	37941	37144	37763	37022	32181	13151	1980.8	1757.1

This phenomenon is mainly due to the trajectory the system follows in a phase plane. The trajectory of the system variables (T_a , T_m) under a heat source perturbation can be very different from that of the system under a pressure perturbation. A possible explanation is that the trajectory depends largely on where the system crosses the separatrices (see Chapters 5 and 6) on the phase plot upon the removal of the perturbation. However, further investigations are still needed to further explain this phenomenon.

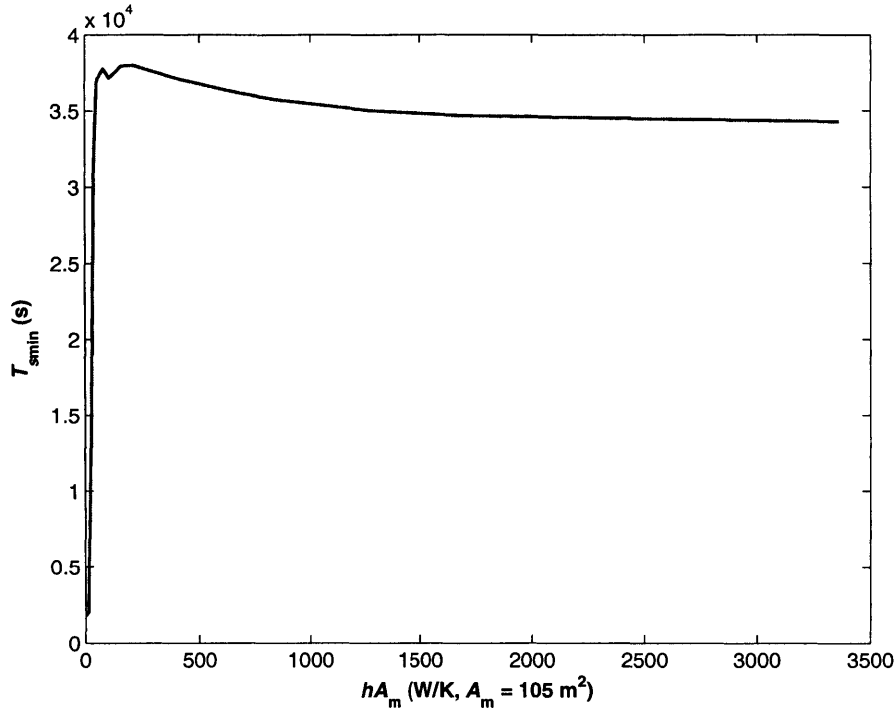


Figure 8-6: Minimum perturbation time vs. hA_m for transitions from SS1 to SS3 under pressure perturbation ($\Delta P/P = -0.2$)

8.6 Effect of air to mass heat capacity ratio

The air to thermal mass ratio, which is defined as

$$r = \frac{M_a c_a}{M_m c_m}, \quad (8.13)$$

is also an important parameter influencing the system response. For a specific hA_m value and fixed air mass, smaller r means heavier thermal mass in the system and thus slower system response to the environment changes.

Table 8.4 lists the minimum perturbation time for the switch from the downward wind dominated solution 1 to the upward buoyancy dominated solution 3 under an increase perturbation that is 1.1137 times the original heat source strength E for different r values. As an opposite solution switch, the minimum perturbation time for the switch from the upward buoyancy dominated solution 3 to the downward pressure dominated solution 1 under 20% pressure increase for three different r values is listed in Table 8.5.

For the same hA_m value, the minimum perturbation time for a specific perturbation increases as the air to thermal mass ratio decreases due to an increase in the thermal mass. This is expected under the assumption that the thermal mass has a uniform temperature distribution, because more thermal mass participates in the response to the environmental changes. Strictly, the assumption is valid only for small

Table 8.4: Minimum perturbation times to switch from solution 1 to 3 vs. r value (under heat source perturbation, $\Delta E/E = 1.1137$, $hA_m = 840$) for fixed air mass

r	0.544	0.0544	0.00544
t_{smin} (s)	775.68	4045.9	36783

Table 8.5: Minimum perturbation times to switch from solution 3 to 1 vs. r value (under pressure perturbation, $\Delta P/P = 0.2$, $hA_m = 840$) for fixed air mass

r	0.544	0.0544	0.00544
t_{smin} (s)	537.21	3120.7	29868

*Biot number*¹ of the thermal mass. In other words, the system becomes more sluggish when the thermal mass fraction increases. The switch from one steady state to the other will take much longer time under the same perturbation.

8.7 Conclusions

In this chapter, we investigated the state transitions between the two stable steady states in a natural ventilation system with thermal mass. The perturbation magnitude and the perturbation time requirements for the system to switch from one stable steady state to another in this air-mass system were quantitatively investigated and compared to those in an otherwise equivalent system without mass.

The minimum perturbation magnitudes under two different types (wind; heat source) of perturbations for different transition directions (SS1 to SS3; SS3 to SS1) in the air-mass system were mathematically derived. The magnitude requirements for transitions were found to be no different from those of similar transition in an otherwise equivalent system without thermal mass.

However, the minimum perturbation times for a system with mass and for an otherwise equivalent system without mass can be very different. With thermal mass, the state transitions need the perturbation to last a much longer period; otherwise the system will still return to its original steady state even the time is much longer than the minimum perturbation time requirement for the equivalent system without thermal mass.

The minimum perturbation times are sensitive to the thermal mass parameters, for example, the inter-air-mass heat transfer coefficient and the air-mass heat capacity ratio. With larger heat transfer coefficient or smaller air-mass heat capacity ratio, the minimum perturbation times become longer and the state transitions become more difficult to occur.

Nomenclature

¹Biot number is defined as $Bi = hl/k$, where l is the characteristic thickness of the solid slab and k is the thermal conductivity of the slab material.

A_m = area of the thermal mass surface that contacts with the air in m^2	P_w = wind pressure difference between the inlet and outlet in Pa
c_a = (constant pressure) specific heat of the air in $\text{J/kg}\cdot\text{K}$	P^{**} = non-dimensional wind pressure difference between the inlet and the outlet
c_m = specific heat of the thermal mass in $\text{J/kg}\cdot\text{K}$	q = volumetric air flow rate in m^3/s
$\overline{C_d A}$ = effective product of the discharge coefficient and the opening area in m^2	r = air-mass heat capacity ratio
C_{pl} = Wind Pressure Coefficient (WPC) for the lower openings	t = time in s
C_{pu} = Wind Pressure Coefficient (WPC) for the upper openings	T_a = (indoor) air temperature in $^\circ\text{C}$
E = heat gain of the space in W	T_e = outdoor temperature in $^\circ\text{C}$
g = gravitational acceleration in m/s^2	T_m = thermal mass temperature in $^\circ\text{C}$
H = height difference between the upper and the lower openings in m	UA = total conductance of the building enclosure system in W/K
h = effective convection heat transfer coefficient between the air and the thermal mass in $\text{W/m}^2\cdot\text{K}$	V = volume of the space (air) in m^3
l = characteristic thickness of the thermal mass in m	v_{ref} = reference wind velocity in m/s for Wind Pressure Coefficients
M_a = mass of the space air in kg, which equals to $\rho_a V$	X = an intermediate variable
M_m = mass of the thermal mass in kg	
P_l = wind pressure at the upper opening in Pa	
P_u = wind pressure at the upper opening in Pa	

Greek

β = thermal expansion coefficient of the air in K^{-1}
ρ_a = density of air in kg/m^3
ΔE = heat source perturbation in W
ΔP = pressure perturbation in Pa

Subscript

a – for air
m – for thermal mass

Part IV

Applications of mutiple steady states in buildings

Chapter 9

Using the dynamical system characteristics to guide chimney and wind scoop designs—how to deal with the multiple steady states

In this chapter we investigate the multiple steady state behaviors in a two-zone building with the combined wind and buoyancy, which represents several widely used natural ventilation design prototypes such as solar chimney or wind scoop. With this configuration, two types of flow patterns can occur under the same set of boundary conditions. The steady state and transient behaviors of the system are investigated by a dynamical system analysis. The mechanism of how the system achieves different steady states is explained within the dynamical system context. The significance of the findings in actual ventilation applications was further discussed in the context of natural ventilation designs.

9.1 Introduction

Multiple steady state behavior can occur in natural ventilation systems. For example, Nitta [50] reported that multiple steady states can be found when different initial values are given to a multi-zone airflow model with coupled energy equation. Linden [44] investigated a naturally ventilated system with floor heating and stated the possibility of hysteresis on the system when the boundary condition changes gradually. Li and Delsante [41] further investigated natural ventilation when wind opposes buoyancy effects as shown in Figure 9-1. They showed that the steady state equations may yield three possible mathematical steady states with the same boundary conditions. Similar results were also obtained by Gladstone and Woods [32] in investigating the natural ventilation of a heated floor. Among the three steady states, one is unstable and does not exist in practical cases while the other two are stable and physical. In the same year, Li et. al [42] demonstrated two more cases in which multiple steady states can exist and reported a small scale experiments on a single zone

blocking ventilation to prove the existing of multiple steady states. Heiselberg et. al [35] conducted both experimental and CFD simulations on the single space blocking ventilation and showed the multiple steady states do occur in reality under certain conditions. Livermore and Woods [45] discovered the existence of three steady states in more complicated two-zone buoyancy driven natural ventilation system. Two of the three solutions are proved to be stable and the other is unstable.

More recently, dynamical system methods were used to investigate the system behavior of a natural ventilation system that has multiple steady states. Yuan and Glicksman [70, 74] investigated the nonlinear dynamics features of a single zone system by dynamical system analysis. The local (or mathematical) stabilities of different steady states were explained and the conditions for multiple steady states to exist were derived. It was shown that the value of the initial temperature relative to the temperature of the unstable steady state was a key factor in determining which steady state the system moved forward. Yang et al. [67] applied similar dynamical system method to a two-zone building with pure buoyancy driven forces and discussed the flow bifurcations in the system.

Further investigations along the dynamical system line were presented by Yuan and Glicksman [77] by examining the transitional dynamics between two stable steady states under perturbations. The study investigated the transition dynamics of two common perturbations—heat source fluctuation and wind variation. Experimental results found by Linden [44] were explained by this transition behavior. More importantly, the requirements for a perturbation to transform the system from one steady state to another are quantified by two parameters—minimum perturbation time and the minimum perturbation magnitude. These two parameters were found to be critical to the stability of the steady state and successfully explained the experimental and CFD results reported in Heiselberg et al [35].

In this chapter, the multiple steady state behaviors are investigated in a typical chimney type building under the wind and buoyancy forces. First, a steady state energy balance analysis is conducted to illustrate the two possible steady states. Secondly, the mathematical conditions for the multiple steady states to exist are explored based on the similarity between the present two-zone building and a single-zone building investigated in a previous study [74]. Further, through a dynamical system analysis, the mechanism of the initial value to affect the final steady states of the system is investigated. The eigen characteristics of the two steady states are demonstrated by linerizing the system around these two steady states.

The dynamical system analysis of the system can be applied to explain and guide the natural ventilation designs of a chimney type of buildings. In general, these two steady states stand for two typical types of ventilation design strategies—the wind scoop design and the (solar) chimney design. For two different designs, the analysis in the present study will help building ventilation designers to better choose the design parameters to achieve their intended objectives.

9.2 Dynamical system models

9.2.1 Building configuration

This building geometry is originated from a typical solar chimney design. The system consists of an occupied zone (Zone 1) and the chimney zone (Zone 2). The heat source is generated from the occupied zone with a rate of S and the chimney zone is assumed to have no heat source. This setup mimics the night mode of the operation of the system, where the occupied zone has a relatively constant internal generation and the chimney has nearly no solar gain. Another practical application of this geometry is the natural cooling towers used in power plants, which is generally huge and tall to introduce enough buoyancy. Similar design can be turned into a wind scoop is widely used in mid-east for natural ventilated buildings. In the wind scoop application, the wind scoop is usually used to induce a strong downward flow to cool the occupied space.

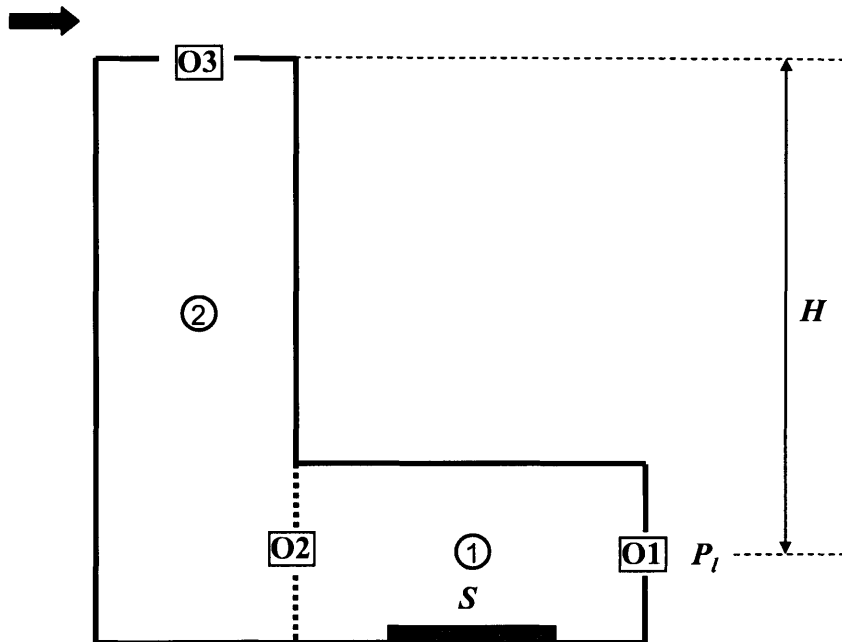


Figure 9-1: Configurations for a building with two zones in a typical atrium design

In this study we made some simplifications on such chimney designed buildings. We assumed that the zones are well-mixed and the building is well insulated. In spite of the simplifications, the major steady state and dynamical system characteristics of the system can be captured by the mathematical models presented in this study. A generalized model for complex buildings is presented in Chapter 10 (or [72]) based on the theoretical models developed in this study.

9.2.2 Governing equations

The two state variables are the zone temperatures T_1 and T_2 . The outdoor air temperature is assumed to be a constant as T_0 . We also define the upward (buoyancy) flow direction as positive (i.e. $q > 0$). Therefore, for buoyancy-dominated flow patterns where $q > 0$, the governing dynamical system equations of the two zones are:

$$\rho_a c_{pa} V_1 \frac{dT_1}{dt} = \rho_a c_{pa} q(T_0 - T_1) + S, \quad (9.1)$$

and

$$\rho_a c_{pa} V_2 \frac{dT_2}{dt} = \rho_a c_{pa} q(T_1 - T_2). \quad (9.2)$$

When $q < 0$, the flow is downward wind-dominated. In this scenario, the governing equations of the two zones are:

$$\rho_a c_{pa} V_1 \frac{dT_1}{dt} = -\rho_a c_{pa} q(T_2 - T_1) + S, \quad (9.3)$$

and

$$\rho_a c_{pa} V_2 \frac{dT_2}{dt} = \rho_a c_{pa} q(T_2 - T_0), \quad (9.4)$$

where S is the internal heat load (in W) inside the building. We assumed that the building enclosures are well thermally insulated so that the conductive heat transfer caused by the indoor and outdoor air temperature difference can be neglected. This is similar to the $UA = 0$ case in a previous study on a single-zone system [74].

Three flow resistances are assumed in this study: the opening in the occupied zone 1 (such as regular windows), the top window in the chimney Zone 2 (such as louvers), and the transitional resistance between Zone 1 and Zone 2. We consequently denote the three openings as O1, O2, and O3 in this order (also see Figure 9-1). Other internal flow resistances can be considered in the same fashion, although they are neglected in this study since they are much smaller compared to the three resistances at the three openings. Each of the three flow resistances is assumed to follow the power-law relationship of an orifice flow as

$$|q_i| = C_{di} A_i \cdot \sqrt{\frac{2\Delta P_i}{\rho_a}}, \quad (9.5)$$

where i stands for the index for the openings and $i = 1, 2$, and 3. ΔP_i is the pressure drop across the opening.

Since the three resistances are in series, the flow rate passes through them can be roughly assumed to be the same (within moderate air density variations in building ventilation applications). Therefore, an effective flow coefficient $\overline{C_d A}$ can be used in this system as

$$\frac{1}{\overline{C_d A}} = \sqrt{\left(\frac{1}{C_{d1} A_1}\right)^2 + \left(\frac{1}{C_{d2} A_2}\right)^2 + \left(\frac{1}{C_{d3} A_3}\right)^2}. \quad (9.6)$$

The flow rate induced by the combined buoyancy and wind forces can thus be expressed as

$$q = \overline{C_d A} \sqrt{\left| 2gh \cdot \beta(T_2 - T_0) - \frac{2P_w}{\rho_a} \right|} \cdot \text{sign} \left(2gh \cdot \beta(T_2 - T_0) - \frac{2P_w}{\rho_a} \right), \quad (9.7)$$

where the direction of the flow is denoted by the sign of the term $2gh \cdot \beta(T_2 - T_0) - \frac{2P_w}{\rho_a}$. PW is the wind pressure difference (in Pa) between the upper and the lower openings, which can be determined by the wind velocity and the wind pressure coefficient differences between the top opening (O3) and the bottom opening (O1).

There is a special point of $q = 0$, at which the flow changes directions. The corresponding temperature of Zone 2 (denote $T_{2c} - T_0$ as T_{2c}^*) can thus be calculated by

$$T_{2c}^* = T_2 - T_0 = \frac{P_w / \rho_a}{gh\beta} \approx \frac{T_0 P_w / \rho_a}{gh} = \frac{P_w}{\rho_a g h} T_0, \quad (9.8)$$

where h is the height difference of between the top and the bottom exterior openings. In this case, we assume that the openings O1 and O2 are at the same height. The top window in Zone 2 is in a position of h higher than those two openings.

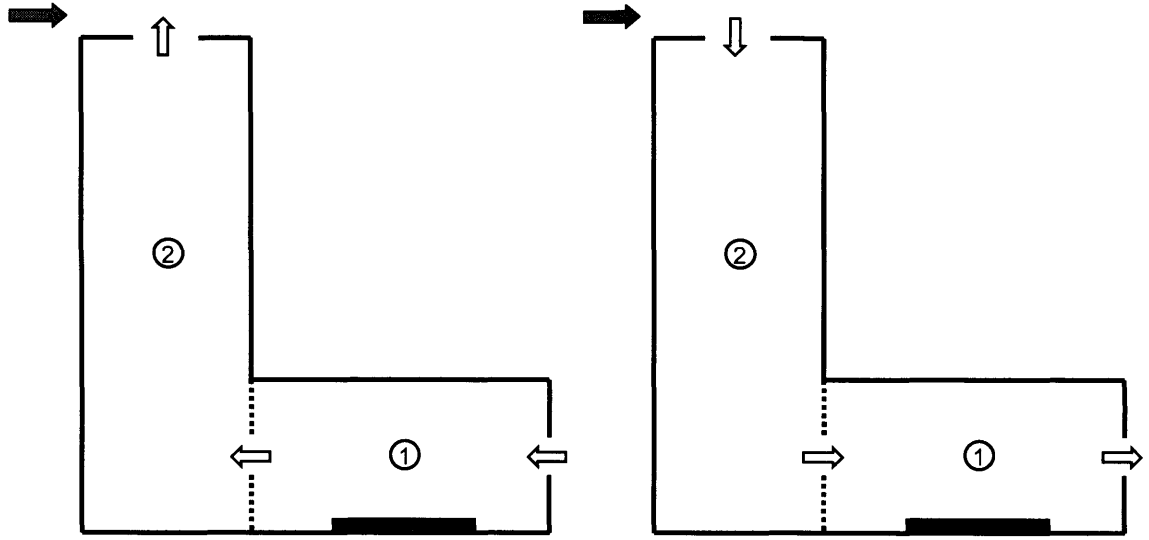
9.3 Steady state behaviors

Mathematically, the system can have two different steady states under the combination of a positive heat source and an opposing wind. The two steady states are shown in Figure 9-2. Figure 9-2(a) shows a buoyancy-dominated steady state where the outdoor air is sucked in from O1 by the chimney formed in Zone 2. In this scenario, reheat fresh air will enter Zone 2 from Zone 1 and the two zones will have exactly the same temperatures in steady state. Figure 9-2(b) shows a wind-dominated steady state where the outdoor air drills down from the top window and travels downward. Since we assumed no heat source in Zone 2, T_2 will be the same at the outdoor air temperature T_0 . The incoming air will be heated in Zone 1 thereafter and exit through the opening O1. In this section we will investigate the static features of these two possible steady states using the static energy balance relationship of the system.

9.3.1 Buoyancy-dominated steady state

When the airflow goes upward, this case is exactly the buoyancy-dominated state in a combined wind and buoyancy case investigated in several previous studies ([70, 74, 77]). In this case, the two zones are finally in the same temperature. The buoyancy-dominated steady state will be the solution for this system. The flow rate of the system can be obtained by a steady state energy balance

$$q_u = \frac{S}{\rho_a c_{pa}(T_{ssu} - T_0)} = \frac{S}{\rho_a c_{pa} T_{ssu}^*}, \quad (9.9)$$



(a) Buoyancy-dominated (upward flow) steady state
(b) Wind-dominated (downward flow) steady state

Figure 9-2: Two possible steady states of the system

where T_{ssu}^* can be determined by the unique real solution of the cubic equation

$$T_{ssu}^{*3} + pT_{ssu}^{*2} + r = 0. \quad (9.10)$$

The term p and r in Equation (9.10) are defined as

$$p = -\frac{P_w}{\rho_a g h \beta}, \quad (9.11)$$

and

$$r = \frac{S^2}{2gh\beta(C_d A \rho_a c_{pa})^2}. \quad (9.12)$$

Solve the cubic equation (9.10) for the temperature of Zone 2 and we obtain

$$T_{ssu}^* = \sqrt[3]{-\frac{1}{27}p^3 + \frac{1}{2}r + \sqrt{\frac{1}{27}p^3r + \frac{1}{4}r^2}} + \sqrt[3]{-\frac{1}{27}p^3 - \frac{1}{2}r - \sqrt{\frac{1}{27}p^3r + \frac{1}{4}r^2}} - \frac{p}{3}. \quad (9.13)$$

Therefore, the analytical close-form for the buoyancy-driven steady state flow rate is

$$q_u = \frac{S}{\rho_a c_{pa} T_{ssu}^*} = \frac{\frac{S}{\rho_a c_{pa}}}{\sqrt[3]{-\frac{1}{27}p^3 + \frac{1}{2}r + \sqrt{\frac{1}{27}p^3r + \frac{1}{4}r^2}} + \sqrt[3]{-\frac{1}{27}p^3 - \frac{1}{2}r - \sqrt{\frac{1}{27}p^3r + \frac{1}{4}r^2}} - \frac{p}{3}}. \quad (9.14)$$

Other than the analytical form, the values of T_{ss2} and q_u can also be easily found

by a computer algorithm such as a bisectional search ([70, 74]).

9.3.2 Wind-dominated state

When the initial flow is developed as downward flows, the temperature of Zone 2 is the same as outdoor air temperature because there is no heat source inside the space. In this case, it is a pure wind driven natural ventilation. If other friction flow resistances are neglected, the flow can be calculated by

$$q_d = -\overline{C_d A} \sqrt{\frac{2P_w}{\rho_a}}, \quad (9.15)$$

where we used the subscript d for flow rate to denote the downward wind-dominated steady state flows. Similarly, in the next subsection, we will use the subscript u to denote the upward buoyancy-dominated steady state flows.

The temperatures of the two spaces can be easily calculated under this condition. Zone 2 is in the same temperature as the ambient and steady state temperature of Zone 1 can be calculated as:

$$T_{1ssd}^* = T_{1ssd} - T_0 = \frac{S}{\rho_a c_{pa} |q_d|} = \frac{S}{\overline{C_d A} \sqrt{\frac{2P_w}{\rho_a}}}. \quad (9.16)$$

9.4 Conditions for multiple steady states to exist

Theoretically, the wind driven ventilation pattern always exists in this system. Given a relatively low initial temperature, a downward steady-state flow pattern can always occur in this case. However, in practical systems, when the pressure forces are small, the solution can become practically unstable following a perturbation analysis similar to that presented in Chapter 7.

The buoyancy-dominated ventilation pattern, however, cannot always happen mathematically. In Chapter 4 we provided the conditions for this buoyancy solution to exist. When the wind forces are strong, the conditions for the buoyancy-dominated solution to exist may not be satisfied. Use the same parameters, the condition for a buoyancy solution to exist can be mathematically described as follows:

$$\beta S - \frac{P_w}{\rho_a g h} \cdot UA > 0, \quad (9.17)$$

where UA is total conductance of the enclosure system. Since in this study we assume that $UA = 0$ (the enclosures are adiabatic), the above relation is reduced to

$$S > 0. \quad (9.18)$$

Therefore, theoretically, as far as a positive heat source S exists in the occupied space (Zone 1), a mathematically stable solution will always exist. However, in

practice, there are two arguments that can undermine the above statement that two steady states always exist for any $S > 0$. Firstly, in an actual building, the enclosure may not be adiabatic (i.e. $UA \neq 0$). In particular, for large buildings with relative high indoor and outdoor air temperature differences, the conductive heat transfer through enclosure system may be large so that the adiabatic assumption is undermined. Secondly, in Chapter 7, this buoyancy-dominated steady state was shown to be sensitive to perturbations and may switch to the other steady state in a very short time under small (but not infinitesimal) perturbations when the heat source S is small compared to the wind P_w . Therefore, there are still practical constraints for a buoyancy-dominated flow to actually exist in real systems.

9.5 Dynamical system analysis

Although in the previous sections we have successfully identified the two possible steady states and calculated their corresponding values, the question of how the system can reach each of the steady state cannot be adequately answered by the steady state analysis shown in the previous section. Such a question needs to be investigated by a dynamical system analysis (see [70, 74]). In this section, the dynamical system characteristic of the system will be investigated.

9.5.1 Impact of initial values

The dynamical system equations given in Equations (9.1) to (9.4) can be reorganized into a state space form. For example, for $q > 0$ (buoyancy-dominated flow), we have

$$f_1(T_1, T_2) = \frac{dT_1}{dt} = \begin{cases} \frac{1}{V_1}q(T_0 - T_1) + \frac{S}{\rho c_{pa}V_1}, & \text{for } q > 0; \\ -\frac{1}{V_1}q(T_2 - T_1) + \frac{S}{\rho c_{pa}V_1}, & \text{for } q < 0, \end{cases} \quad (9.19)$$

and

$$f_2(T_1, T_2) = \frac{dT_2}{dt} = \begin{cases} \frac{1}{V_2}q(T_1 - T_2), & \text{for } q > 0; \\ -\frac{1}{V_2}q(T_0 - T_2), & \text{for } q < 0, \end{cases} \quad (9.20)$$

where T_1 and T_2 are the state variables and $S, V_1, \rho_a c_{pa}$ are constants. The signed flow rate q is also a function of one of the state variables T_2 (see Equation (9.7)).

According to the above four equations, the trajectories of the system can be plotted on a phase plane shown in Figure 9-3. Starting from any initial temperature combinations T_1 and T_2 , the phase plots shows the temperatures the system will undergo and finally reach. The system is shown to have two mathematically stable steady states. From the trajectory plotting, the two steady states discussed in the previous sections are shown as two stable fixed points, where all the trajectories will converge to in an autonomous dynamical system.

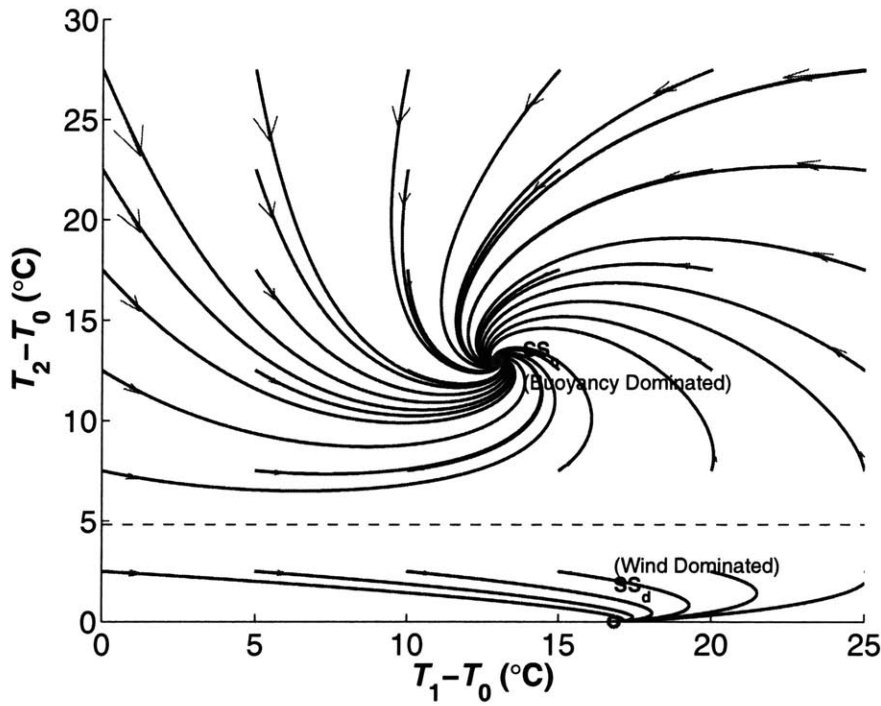


Figure 9-3: Dynamical system characteristics of the system shown on the phase plane

In this system, the final steady state will be solely determined by the temperature of Zone 2.

$$T_{2c}^* = T_{2c} - T_0 = \frac{P_w/\rho_a}{gh\beta} = \frac{P_w}{\rho_a gh \beta} \approx \frac{P_w}{\rho_a g h} T_0. \quad (9.21)$$

If the chimney temperature is below this critical temperature T_{2c}^* , the system will evolve towards a wind-dominated (downward flow) steady state. On the other hand, if the initial temperature of Zone 2 is higher than T_{2c}^* , the system will finally reach the buoyancy-dominated (upward flow) steady state.

For a typical building design, T_{2c}^* is always positive if the heat source is positive and the wind opposes the buoyancy force. As is shown in the equation above, it is in positive proportion to the wind pressure and negative proportion to the height of the chimney. When the wind force is strong, T_{2c}^* can be high, which may make the initial conditions to reach the buoyancy steady state very difficult to obtain. On the other hand, if the h is very high, T_{2c}^* will be very small so that the building has a lower chance to get a pure wind-dominated flow.

9.5.2 Eigen characteristics of the system at steady states

The local stabilities of the steady states are determined by the eigenvalues of the linearized system matrix. By linearizing the system equations at a steady state, a

linear system matrix is obtained as follows:

$$\begin{bmatrix} \frac{dT_1}{dt} \\ \frac{dT_2}{dt} \end{bmatrix} = \begin{bmatrix} a & b \\ c & d \end{bmatrix} \begin{bmatrix} T_1 \\ T_2 \end{bmatrix}. \quad (9.22)$$

where a , b , c , and d are four real numbers given by

$$\begin{aligned} a &= \left. \frac{\partial f_1}{\partial T_1} \right|_{T_{1ss}, T_{2ss}} & b &= \left. \frac{\partial f_1}{\partial T_2} \right|_{T_{1ss}, T_{2ss}} \\ c &= \left. \frac{\partial f_2}{\partial T_1} \right|_{T_{1ss}, T_{2ss}} & d &= \left. \frac{\partial f_2}{\partial T_2} \right|_{T_{1ss}, T_{2ss}}. \end{aligned} \quad (9.23)$$

The matrix $\begin{bmatrix} a & b \\ c & d \end{bmatrix}$ is called the Jacobian matrix (denote as \mathbf{J} hereafter). The stability of the linearized system at a particular steady state is determined by the eigenvalues of \mathbf{J} , which are given by

$$\lambda_{1,2} = \frac{a+d}{2} \pm \frac{\sqrt{(a-d)^2 + 4bc}}{2}. \quad (9.24)$$

The system is locally stable around a steady state point if the real parts of both eigenvalues are negative. If any eigenvalue of the system has a positive real part, the system will be locally unstable and will diverge to other steady states. For the two-zone system presented in Figure 9-3, both of the steady states are stable since the eigenvalues of the corresponding linearized systems do not have a positive real part.

9.5.2.1 Linearized system around the buoyancy-dominated steady state

For the buoyancy-dominated upward flow steady state, we will linearize the system around the steady state point $[T_{ssu}, T_{ssu}]$, where T_{ssu} can be obtained by Equation (9.13). Here in order to quickly demonstrate the eigenvalue characteristics of the system, we have temporarily assumed that $V_1 = V_2 = V$ in the above equation, which physically means that Zone 1 and Zone 2 are set to the same volume (and thus the same thermal capacity). Using Equation (9.23), the Jacobian matrix \mathbf{J} (denoted with a 'u' subscript to indicate upward flow pattern) in this case can be obtained as follows:

$$\mathbf{J}_u = \begin{bmatrix} -\frac{1}{V}q & -\frac{1}{V}(T_{ssu} - T_0) \left. \frac{dq}{dT_2} \right|_{T_{ssu}} \\ \frac{1}{V}q & -\frac{1}{V}q \end{bmatrix}. \quad (9.25)$$

The eigenvalues of such a system can thus be calculated as

$$\lambda_{1,2} = -\frac{1}{V}q \pm \frac{1}{V}\sqrt{-4q(T_{ssu} - T_0)} \left.\frac{dq}{dT_2}\right|_{T_{ssu}}. \quad (9.26)$$

We only need the sign of the terms in the above equation to know its possible values. In this case, q is positive (> 0) since the flow direction is upward in this case. For dq/dT_2 , it can be shown to be > 0 either by its mathematical expression (Equation (9.7)) or by its physical meaning: in the buoyancy driven flow pattern, when T_2 increase, the buoyancy effect also increases, which will lead the flow rate q increase as well; therefore dq/dT_2 is positive in this scenario.

Therefore the term under the square root is obtained a negative number. The two eigenvalues are complex numbers in the following form:

$$\lambda_{1,2} = -\frac{1}{V}q \pm \left(\frac{1}{V}\sqrt{-4q(T_{ssu} - T_0)} \left.\frac{dq}{dT_2}\right|_{T_{ssu}}\right)i. \quad (9.27)$$

Therefore the eigenvalues have negative real parts and an imaginary part. A steady state point that has an imaginary part is called a *spiral* in dynamical system. Physically, a spiral usually associates with an oscillation feature of the state variables, with a decreasing magnitude. It is different from the *stable node* presented in Chapter 5 where the eigenvalues are real numbers.

9.5.2.2 Linearized system around the wind-dominated steady state

For the wind-dominated (downward flow) steady state, we will linearize the system around the steady state point $[T_{1ssd}, T_0]$, where T_{1ssd} can be obtained by Equation (9.16). Again assuming $V_1 = V_2 = V$ and using Figure (9.23), the Jacobian matrix \mathbf{J} (denoted with a 'd' subscript to indicate downward flow pattern) in this case can be obtained:

$$\mathbf{J}_d = \begin{bmatrix} \frac{q_d}{V} & -\frac{q_d}{V} \\ \frac{q_d}{V} & \frac{q_d}{V} \end{bmatrix}. \quad (9.28)$$

where q_d is the steady state flow rate in the wind-dominated ventilation pattern. A special note here is that q_d is signed (see Equation (15)) and it is negative in this downward flow pattern.

The eigenvalues can again calculated as

$$\lambda_{1,2} = \frac{q_d}{V} \pm \frac{q_d}{V}i. \quad (9.29)$$

Therefore, both eigenvalues have a negative real part and an imaginary part. This steady state is again a *spiral* and it is locally stable.

9.6 Ventilation applications

In design of natural ventilation systems, the dynamical system characteristics investigated in the present study should be adequately considered. For building designs, the designer may consider only one type of design and conduct the steady state energy balance to check out the flow rate. However, the present study presents a challenge to this method: how does a designer know whether the building can actually stay at the designed pattern, with two possible steady states under the same design condition?

As is shown in Equation (9.21), the critical temperature which divides the phase plane will be the key control parameters. In a previous section we have found it is the critical point T_{2c}^* for the system to reach different steady states. Therefore the designers have to be careful about this value in considering their chimney or wind scoop designs.

9.6.1 Chimney designs

Through a chimney design, a designer expects to achieve the buoyancy-dominated steady states (or at least as much as possible). Further, it is also expected that under certain range of wind velocities (e.g., an increase in wind velocity), the buoyancy flow will not be interrupted.

From the previous sections we have known that to reach a buoyancy-dominated steady state, the chimney temperature has to be raised (or kept) to higher than this critical temperature T_{2c}^* . Otherwise the system may drop to a wind-dominated pattern and the desired design patterns are not achieved. Therefore we need to design the critical temperature T_{2c}^* to be as low as possible so that the building can be easily boosted to a buoyancy-dominated flow pattern. This can be shown in Figure 9-4. The critical point is designed to be a low value so that Zone 2 can easily achieve that temperature to develop the buoyancy flow pattern. In this design type, one should shift the critical line down (the dashed line in Figure 9-4) as low as possible.

The critical temperature is like a triggering point for the system to reach a buoyancy steady state (or a wind-dominated state in the next subsection). If the triggering point is set too high in buoyancy design, the design may encounter problems that the desired ventilation pattern will not be reached. An analogy is that it serves like a starter of a car: the engine will not start if the starter has not offered a certain initial torch.

The above conclusions about T_{2c}^* also agree with simple design intuitions. For example, within expectations, the critical temperature T_{2c}^* is a function of the chimney height h of Zone 2, and a function of wind pressure P_w : T_{2c}^* is proportional to the former and in reverse proportion to the later. For the chimney height h , one can choose to increase its height in buoyancy designs (that's essentially exactly how "chimney" should look like). In chimney design, the other factor that can affect the critical temperature—the wind pressure P_w , can be reduced by facing the top window upward. Indeed, almost every chimney is designed like that. The critical temperature, therefore, can also contribute to the simple question of why chimneys should be built high and open upward.

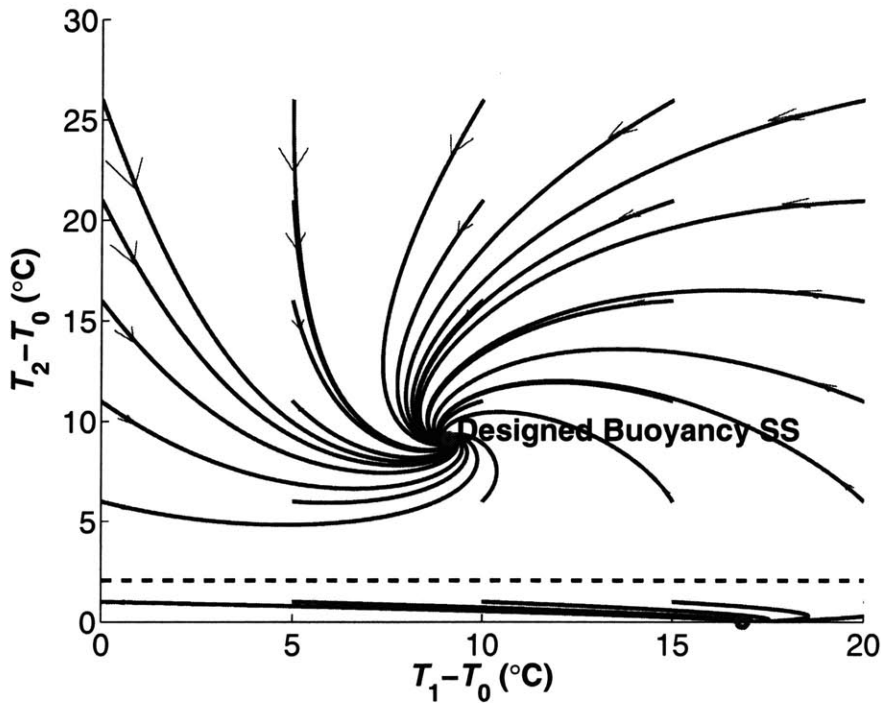


Figure 9-4: Buoyancy-dominated natural ventilation design consideration

9.6.2 Wind scoop designs

The wind scoop design is opposite to the chimney design, with a major objective of utilizing wind forces. The designer expects to achieve a wind-dominated pattern to induce as much outdoor airflow as possible. Similar to the wind design expectations, a good wind scoop design should enable the system to reserve its flow pattern under a certain range of parameter variations.

Opposite to the chimney designs, in the wind scoop design, the critical temperature T_{2c}^* should be designed as high as possible to eliminate the possibility to (wrongly) achieve a buoyancy-dominated flow pattern. This can be shown in Figure 9-5. The critical point is designed to be a high value so that Zone 2 will not easily achieve that temperature to develop the buoyancy forces. In this design type, one should raise the critical line up as high as possible.

Again, the above conclusions about T_{2c}^* agree with intuitions. With a wind scoop design, the height of the chimney should be reduced and the top opening should orient to face the wind to increase the P_w as much as possible.

9.7 Conclusions

In this study we provided a theoretical study to address the multiple steady states phenomenon's in building designs. A mathematical model was developed and the steady state and transient behaviors of the systems were investigated.

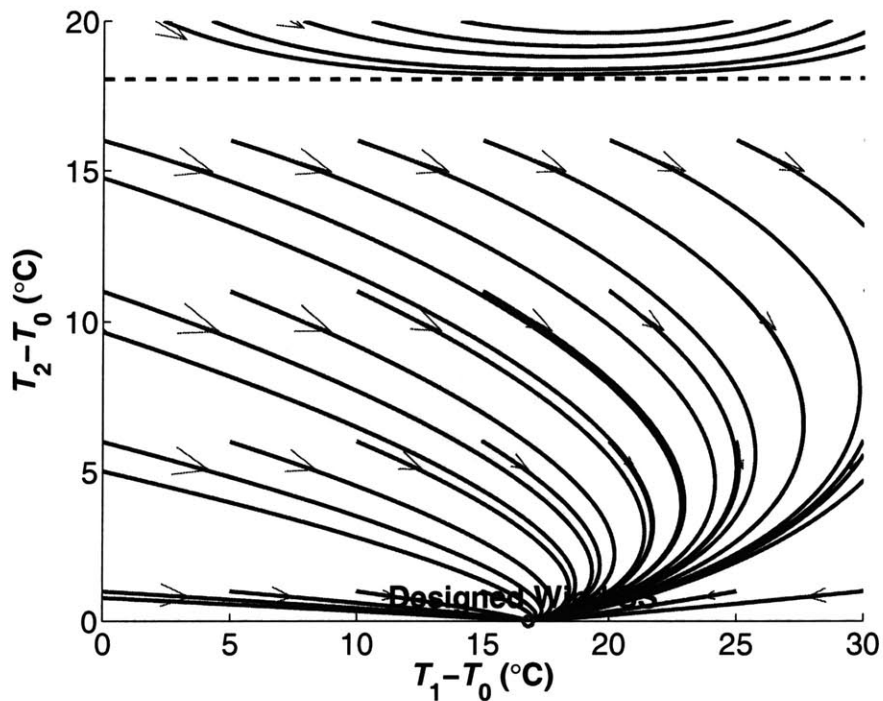


Figure 9-5: Wind-dominated ventilation design considerations

For such a chimney system with opposing wind, two possible steady states under the same boundary conditions could be found when certain conditions are met. Both steady states are locally stable and this stability was explained by the eigen characteristics of the linearized system equations near the steady states.

The analytical studies provide new knowledge to guide the natural ventilation design in system with similar geometries or functionalities. One design criterion applied to the chimney and wind scoop designs is the control of the critical temperature for the dynamical system to switch attraction regions. For chimney design, the critical temperature should be suppressed downward as much as possible; and for wind scoop design, the critical temperature should be raised as much as possible.

The theoretical derivations in this study relied on several simplifications. For a complex system that is beyond the configuration of the building presented in this study, a generalized method was developed in Chapter 10 (or ??).

Nomenclature

A_i = area of opening i in m^2

c_{pa} = (constant pressure) specific heat of the air in $\text{J}/\text{kg}\cdot\text{K}$

$\overline{C_d A}$ - effective product of the discharge coefficient and the opening area in m^2

g = gravitational acceleration in m/s^2

H = height difference between the upper and the lower openings in m

ΔP_i = pressure drop across opening i in Pa

P_w = wind pressure difference between the inlet and outlet in Pa

P^{**} = non-dimensional wind pressure difference between the inlet and the outlet
 p, r = intermediate variables used in solving cubic equations

q = volumetric air flow rate in m^3/s

S = heat gain of the space in W

t = time in s

T_1 = air temperature of Zone 1 in $^\circ\text{C}$

T_2 = air temperature of Zone 2 in $^\circ\text{C}$

T_0 = outdoor temperature in $^\circ\text{C}$

T_{2c} = the critical temperature of Zone 2

for initial values

UA = total conductance of the building enclosure system in W/K

V_1 = volume of Zone 1 (air) in m^3

V_2 = volume of Zone 2 (air) in m^3

v_{ref} = reference wind velocity in m/s for

Wind Pressure Coefficients (WPC)

Greek

β = thermal expansion coefficient of the air in K^{-1}

ρ_a = density of air in kg/m^3

$\lambda_{1,2}$ = eigenvalues of the linearized system

Matrix

\mathbf{J} = Jacobian matrix of the linearized system

Superscript

* – for temperature relative to the outdoor temperature (i.e., $T^* = T - T_0$).

Chapter 10

Identification of the multiple steady states in buildings with complex geometries by a computer model

In this chapter we investigate the multiple steady state behavior in buildings with complex geometries and the numerical method to identify these states. A generalized dynamical system model is developed based on the underlying governing air flow and thermal transport dynamics of the building ventilation systems. Three different search methods to determine the system's transient paths to reach different stable steady state are discussed. The dynamical system model and the search method are successfully applied to two natural ventilated buildings with complex geometries. Three different stable steady states are identified in one case and four are identified in another case. The validities of the obtained states were examined by model assumptions, the actual physical processes. Finally, the actually stabilities of the obtained steady states are quantitatively examined by an effective test method based on the system's responses to strong stochastic perturbations.

10.1 Introduction

Multiple-steady-state behavior in ventilation systems has been of increasing interest to researchers. Analytical models have been established to explore and explain the different possible steady states under the same boundary conditions (e.g. [41, 44, 45, 73]). Linden [44] investigated a naturally ventilated system with floor heating and reported the hysteresis on the system when the boundary condition changes gradually. Li and Delsante [41] further investigated the system by solving the steady state equations that may yield three possible mathematical steady states under the same boundary conditions. Moreover, Livermore and Woods [45] demonstrated the existence of three steady states in a simplified two-story building. More recently, Yuan and Glicksman [73] investigated the solution multiplicity problems in a ventilation system that actively uses thermal mass. The thermal mass was found to be important to the transient behavior of the system.

The methods used to investigate the simple systems above have also evolved in recent years. An early method was to set the steady state mass and energy balance equations and solve the steady state equation (e.g. in [41, 44]). With simple building geometries (e.g. single-zone), this method can usually provide an analytical solution by solving a nonlinear algebra equation. With two-zone buildings, a method of continuously solving the steady state system equations by saving some previous solution results was demonstrated as a means to search for the possible steady states in a system with multiple steady states (see [68]). The algorithm could find multiple steady states in a simple two-zone system, but was unable to distinguish dynamically stable solutions from those unstable ones. In order to explain the stability of different steady states obtained, the transient behaviors of the system has to be considered by further examining the dynamical characteristics of the system (see [70, 74]). For example, the dynamical system behavior of the system was found to be important in explaining how the initial value determines the final steady state of the system (e.g. [70, 74]). The dynamical system method also evolves further to explain the actual stability of the stable steady states using a perturbation method (see Chapter 7), which successfully explained two previous experiment studies [35, 44].

However, when it comes to buildings with complex geometries, the analytical models developed in the previous studies are either incapable or inefficient in identifying the possible multiple steady states. In this paper, we will develop a method to find all (or as many as possible) of the possible meaningful steady states in complex buildings based on a general dynamical system model. The developed method will be applied to two reasonably configured sample buildings with multiple zones to demonstrate the possible steady states found. Several important theoretical and empirical issues, such as the way to deal with thermal mass in simulation, the pros and cons of different search methods, and the way to analyze the validity of obtained results, will also be discussed in this study.

10.2 Dynamics model—a single-variable case

We will start with a single-zone building to demonstrate the dynamical system model. Figure 10-1 shows a naturally ventilated building with combined wind and buoyancy forces. The dynamical system equation of the system can be written as:

$$f_0(T) = \frac{dT}{dt} = \frac{S}{\rho_a c_{pa} V} - \frac{UA}{\rho_a c_{pa} V}(T - T_0) - \frac{1}{V}q(T - T_0). \quad (10.1)$$

where T is the only state variable. The term q in Equation (10.1) is the volumetric caused by the combination of wind and buoyancy forces, which is also a function of T as

$$q = \overline{C_d A} \cdot \sqrt{\left| 2gH \cdot \beta(T - T_0) - 2 \frac{P_w}{\rho_a} \right|}. \quad (10.2)$$

One naive way of finding the steady states of the system is to set Equation (10.1)

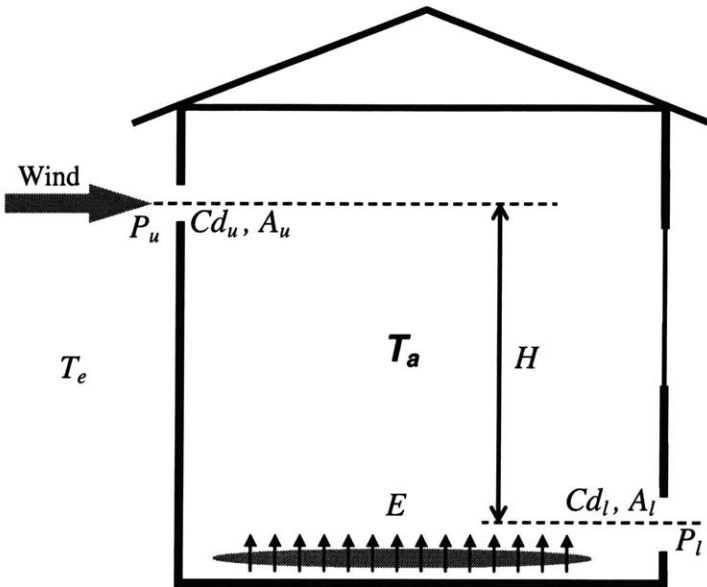


Figure 10-1: A single-zone natural ventilation system with opposing wind and buoyancy forces

to zero. A cubic (nonlinear) algebra equation will be obtained after a few transformations. One would expect to find three solutions of T from the obtained algebra equation if some conditions are satisfied (see [70, 74]).

However, purely solving the steady state equation will lose information about the stability of the three steady states. To check their stabilities, we can plot Equation (10.1) against T in Figure 10-2.

Figure 10-2 shows not only the values of the three steady states (denoted as 1, 2, and 3), but also the information about the stability of the three steady states. The three steady state solutions divided the x-axis into four sections. In each section, a horizontal arrow denotes the sign of dT/dt (y-axis) in that section. A right-pointing arrow denotes positive dT/dt and a left-pointing one denotes negative dT/dt . The arrows adequately denote the direction the system temperature T moves starting from an initial temperature. The stability of the three steady states thus can be obtained: Steady States 1 and 3 (SS1 and SS3) are stable because the arrows in the adjacent regions move towards them; Steady State 2 (SS2) is unstable because the arrows in the adjacent regions move away from it.

A dynamic simulation can be constructed by solving the differential Equation (10.1) from different initial temperatures, which is also known as the Initial Value Problem [56] (IVP). As is shown in Figure 10-3, starting from any initial temperature that is lower than SS2, the system will finally reach Steady State 1; and starting from any initial value higher than SS2, the system will finally reach SS3 (see [70, 74]). Indeed, the unstable SS2 is the critical point of the initial temperatures in determining the system's final steady state ([70, 74]).

The dynamical system characteristics shown in Figure 10-3 will help us to develop a general method to search for the multiple steady states of the single-zone system using the following procedures:

1. Define a reasonable range for the zone temperature, e.g. $[5, 40]^\circ\text{C}$;

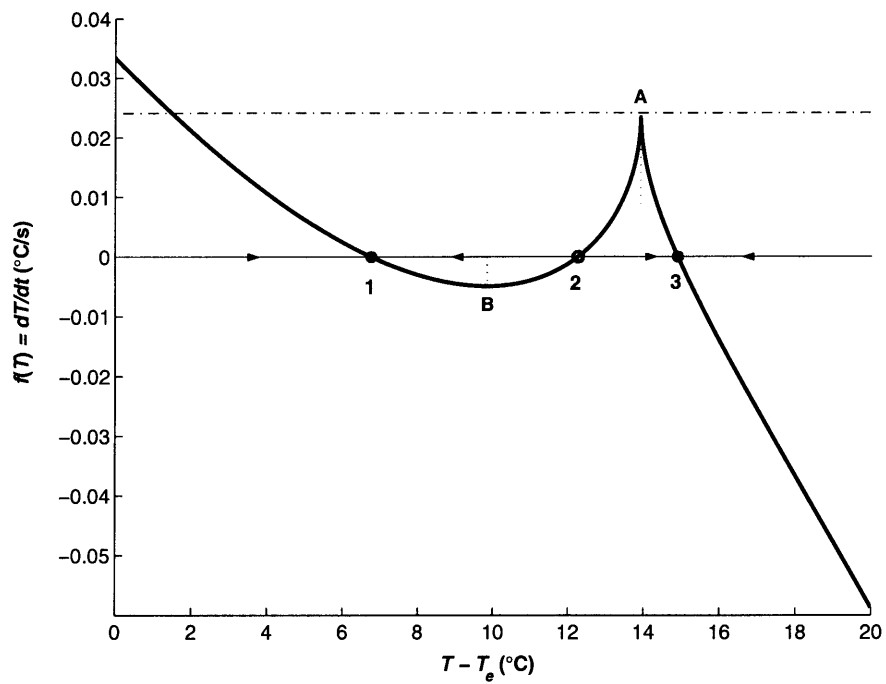


Figure 10-2: Transient characteristics of the system

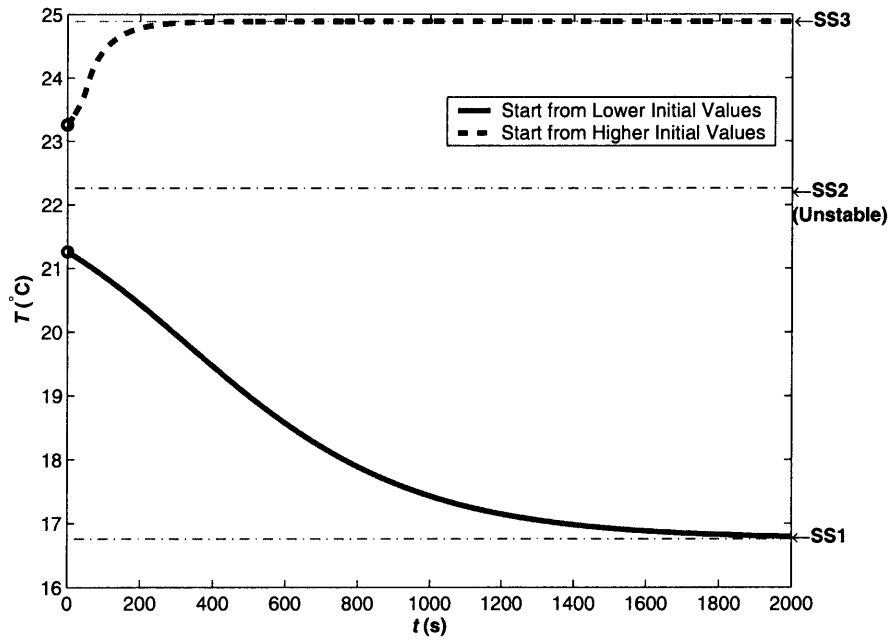


Figure 10-3: Two different (stable) steady states the system can reach, starting from two different initial temperatures

2. Solve the state equation (10.1) to obtain steady states, starting from different initial temperatures, e.g. a grid of different values shown in Figure 10-4;
3. Observe and record the different steady states obtained.

One exhaustive search method (grid search) is graphically shown in Figure 10-4. Starting from the different initial temperature points, the system will either reach SS1 and SS3. Therefore the two stable steady states can be easily identified. The unstable steady state SS2 cannot be identified using this dynamic simulation method because in reality, it will not occur in a real physical system. SS2, however, is important to the state transition behaviors of the system, which was investigated in detail in Chapter 7.

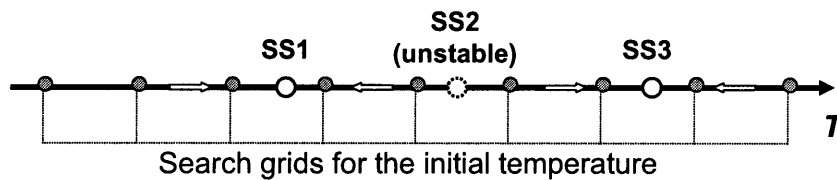


Figure 10-4: Grid search for single-variable systems

10.3 Dealing with thermal mass

An important consideration in the dynamical simulation is the thermal mass, a popular temperature-modulating design in many buildings. Figure 10-5 shows a similar single-zone building as Figure 10-1, except the addition of a (say, concrete) thermal mass. The question is thus: will the multiple steady states behavior change with the presence of the thermal mass?

As was discussed in Chapter 5, if no internal heat source is assumed for the thermal mass, the “static” behavior of system will not be affected by the thermal mass. For example, the boundary conditions for the system to exhibit multiple steady states, the number of steady states the system, and the values of the steady states, will not be affected by the presence of the thermal mass. In other words, a system with thermal mass will have the same steady states as a similar system without thermal mass. An intuitive explanation to this is that at the steady states, the thermal mass will not exhibit its thermal storage effect since it reaches a thermal equilibrium.

Since in this study we will focus only on finding these multiple steady states, we can neglect the thermal mass in the system because the system with and without thermal mass will have the same steady states. However, as was discussed in Chapters 5 and 8, some dynamical characteristics of a system, such as how the system reaches different steady states, and the transitions between the multiple steady states, will indeed be affected by the presence of thermal mass.

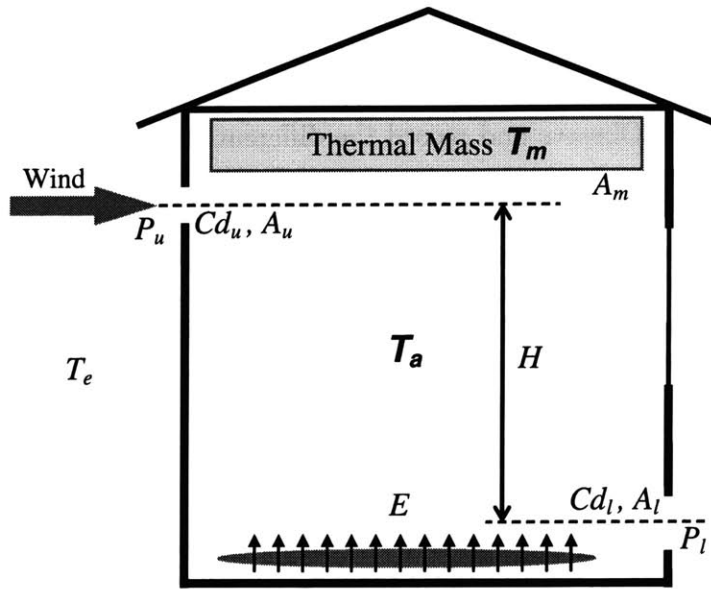


Figure 10-5: A single-zone natural ventilation system with thermal mass

10.4 Generalization to multiple-zone cases

The close-form dynamical system model can be obtained in simple geometries such as single-zone or two-zone buildings. For example, a single-zone example was shown in a previous section and a two-zone building example was studied in detail in Chapter 9. In either case, the flow rates in the system can be explicitly expressed by a close-form function (e.g. Equation (10.2) for the single-zone case) of the system temperatures, making the state equation (10.1) explicit.

When the building geometries become more complex, for example, when a building has multiple (>2) zones, the state equations usually cannot be explicitly found. In this situation, the equations need to be generalized using an implicit formulation, which can be solved numerically using a coupled equation solver.

In order to generalize the model, we assume that the building can be represented by N zones in a multi-zone model frame work. By assuming that each zone has a uniform temperature T_i , the system's state equations can be written as

$$\rho_i c_{pa} V_i \frac{dT_i}{dt} = c_{pa} \sum_{j:q_{ji}>0} \rho_j q_{ji} T_j - \rho_i c_{pa} \sum_{j:q_{ij}>0} q_{ij} T_i + S_i, \text{ for } \forall i = 1 \dots N. \quad (10.3)$$

where q_{ij} is the volumetric flow rate from zone i to zone j . The flow rate q_{ij} is usually a function of the zone temperatures and other known parameters. In general, if we denote the state vector $[T_1, T_2, \dots, T_n]'$ as \mathbf{T} , the equation above can be generally written as

$$\frac{d\mathbf{T}}{dt} = f(\mathbf{T}, \mathbf{q}). \quad (10.4)$$

\mathbf{q} is the flow rate vector that is formed by all the flow rates q_{ij} , which are, naturally, functions of the zone temperatures \mathbf{T} and other known boundary parameters. However, at each particular time, the flow rate \mathbf{q} can be solved by a multi-zone airflow

network model (see the theoretical background in [64]) for a fixed \mathbf{T} . Therefore, we will obtain the values of \mathbf{q} after solving the network model, assuming \mathbf{T} is known:

$$\mathbf{q} = g(\mathbf{T}). \quad (10.5)$$

Equations (10.4) and (10.5) are the coupled airflow and thermal formulation of the system. Unlike Equation (10.2) for the single-zone systems, Equation (10.5) usually cannot be expressed in a closed form, which makes Equation (10.4) implicit as well. However, the decoupled Equations (10.4) and (10.5) are not difficult to be solved numerically, using an ODE solver and a multi-zone airflow solver, respectively. Therefore, Equations (10.4) and (10.5) can be “simultaneously” solved using an iterative coupling scheme (e.g. see [36]).

With this formulation, the problem described by Equations (10.4) and (10.5) (with arbitrary number of zones) can be solved as an IVP. Starting from an initial condition, the system temperatures will start to change and finally reach a specific stable steady state.

The coupled simulation in this study is conducted by a coupled transient multi-zone airflow and thermal simulation program named “CoolVent” [71]. Although CoolVent has the capability to couple the thermal mass solution as well, in this study, we will not activate the thermal mass solution, because in the previous section we have concluded that the presence of thermal mass will not affect the values of the steady states.

10.5 Exhaustive search methods

Similar to the single-zone case, the next step after building up the dynamical system equations is to start the simulation with different initial values of the zone temperatures to find all (or many of) the possible stable steady states of the system. With multiple-zones (N zones), we will have an N -dimensional state space to search. The task is not easy, since there could be many possible combinations of different zone temperatures. In this section, we will discuss three potential search methods to explore the N -dimensional state space.

The first method is the general grid search. We will discretize each dimension into m ($m \geq 2$) (usually equally spaced) points. Therefore, for an N -dimensional problem (a building with N zones), we will have a total of m^N grid points to search. The complexity is thus m^N runs of ODE solving. Obviously, this number increases very fast as N increases, since it is an exponential function. Figure 10-6 shows a general grid search method applied to a two-zone ($N = 2$) case (see Chapter 9 for geometry and dynamics details). There are two zonal temperatures (T_1 and T_2) to search, whose combinations can be shown on the phase plane. The search grids are formed by the dotted points. With $m = 6$ in this case, the total number of points to search is 36 ($=6^2$) and we thus need 36 runs of coupled dynamical system simulation. Additionally, the trajectories how the system converge to the two stable steady states (marked by the two small circles) from different initial values are plotted on the phase

plane.

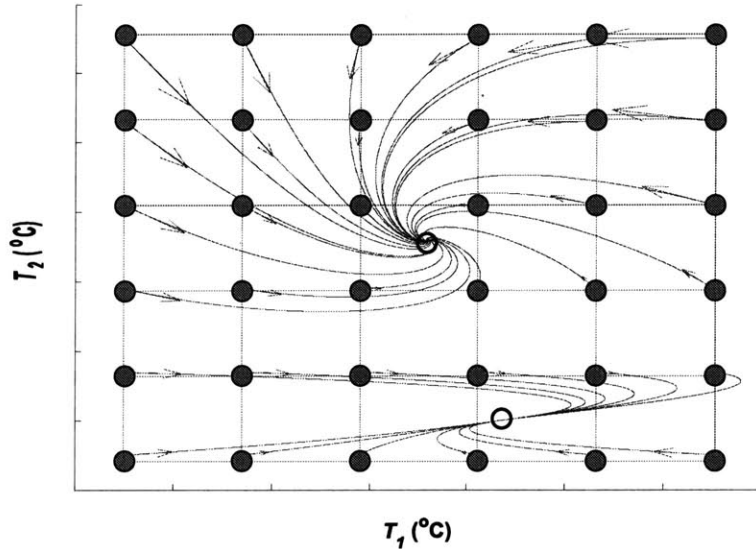


Figure 10-6: A general grid search for a 2-D system

An alternative grid search method is to set $m = 2$ in the general method, which means the coarsest grid. In this case, we search only a low temperature (e.g. 15°C) and a high temperature (e.g. 35°C) on each dimension of the state space. The complexity is still exponential but is much less than the m^N when m is large for the general grid search method. However, the drawback is also obvious: with coarser grids, the space may not be well represented. Therefore there can be more possibilities to miss some possible steady states. An example of a coarsest grid method applied to the same two-zone system (first shown in Figure 10-6) is demonstrated in Figure 10-7. In this case, we need only 4 runs (2^2) to find the two steady states.

Another search method is to use random initialization search. This initialization will not formally form a set of well-aligned grids of the possible initial values. It will just randomly draw values from a uniform distribution on each dimension and use them as the initial values. In this method the entire space is considered in a conceptually continuous fashion. However, a sufficient large sample size k is needed to make the selected points to be statistically representative. For complex problems with large N s, we can manually set the sample size k to some reasonable large number (but $\ll m^N$ or 2^N). An example of this method applied to the two-zone system (first shown in Figure 10-6) is shown in Figure 10-8, with a sample size $k = 10$.

10.6 An example multiple-zone building (Case 1)

We will apply the dynamical simulation and the exhaustive search methods to a sample multiple-zone building to test the models and methods. A hypothetical but

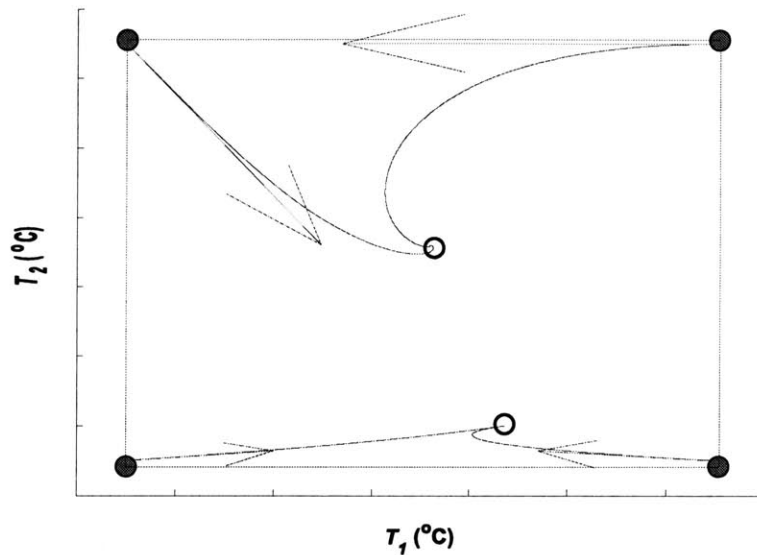


Figure 10-7: A coarsest grids ($m = 2$) grid search applied to a 2-D system

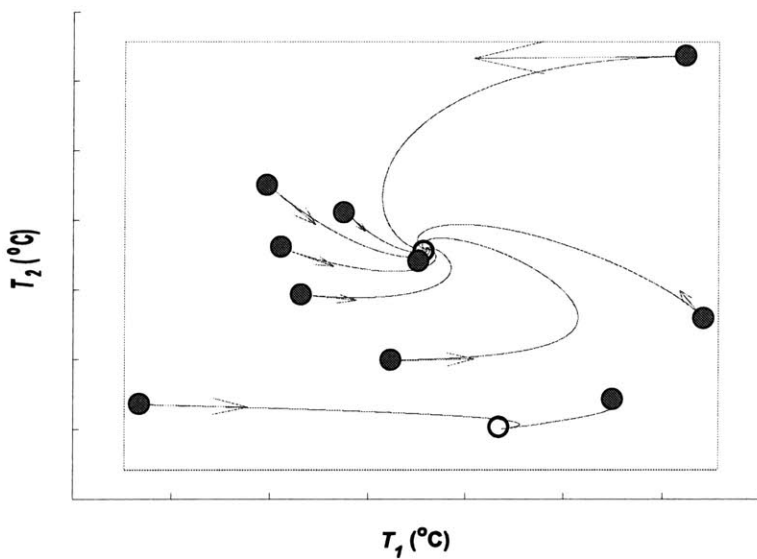


Figure 10-8: Random initialization for a 2-D system

reasonably configured building (Figure 10-9) with 7 zones (consecutively labeled as 1 to 7) is constructed for this purpose.

The hypothetical building has three stories, with a chimney type natural ventilation design. Each story has an occupied office space, whose width is 10m and length is 20m (perpendicular to the paper). The floor height is 3m and the roof height is also 3m. The heat generation in each occupied office is assumed to be 6000W (30W/m^2).

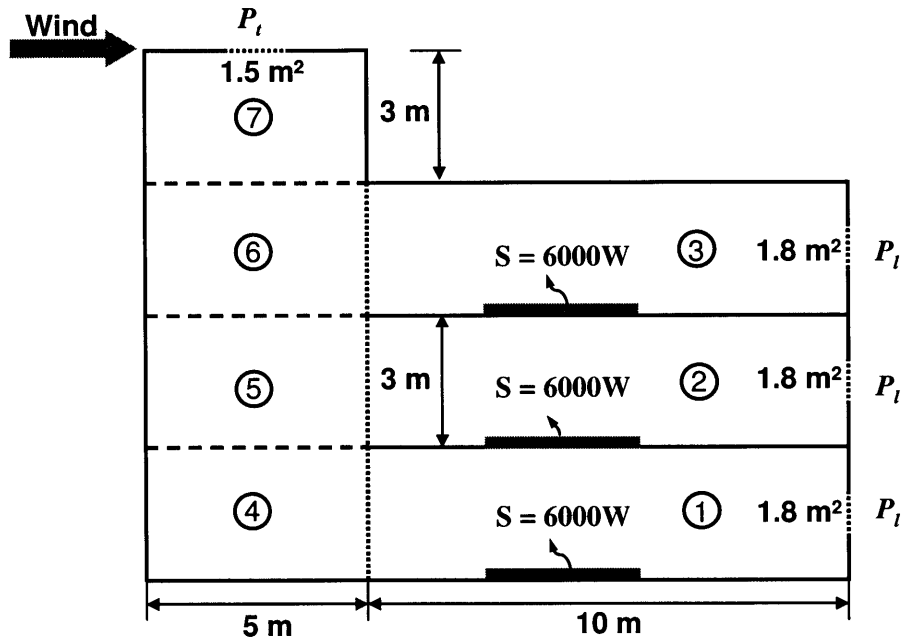


Figure 10-9: The geometries of the simulated building

The building has a top window on the roof and three exterior windows on the office side, one on each floor. The area of the top window on the roof is 1.5m^2 . The exterior window on each floor has an area of 1.8m^2 . In reality there might be multiple exterior windows on each floor, for example several windows in a row. For simplicity, on each floor we add up the areas of all these window openings to form one (1.8m^2) opening. We also assumed that the center height of the exterior window(s) on each floor is at the center height of the exterior wall on that floor (i.e. the window center's relative elevation is 1.5m).

Further, we assumed that only one-way flow occurs at all the exterior and internal openings in this study. The internal openings include the vertical connections between the office and the chimney areas and horizontal openings between the adjacent zones 4, 5, 6, and 7 on Figure 10-9.

The building will subject to a combined wind and buoyancy force. The buoyancy force is introduced by the temperature difference between the interior and the outdoor air. The outdoor air temperature is set to 20°C . The wind force is caused by the wind pressure difference between the top (roof) window and the leeward office windows. In this case, we specified the wind pressure coefficient at the roof (for P_t) as -0.3 (a lift force) and the wind pressure coefficients at the office windows (P_l) as -0.5 . The

wind velocity v_{ref} is set to 2.8m/s, and not adjusted for the height differences of the openings on different floors. Therefore, the net wind pressure is

$$P_w = P_t - P_l = (-0.3 + 0.5) \cdot \frac{1}{2} \rho_a v_{ref}^2 = 0.1 \rho_a v_{ref}^2. \quad (10.6)$$

10.7 Results

The building is simulated by a revised version of “CoolVent”[71], which can handle the different search algorithms discussed in a previous section. For this 7-zone ($N = 7$) building, we used the random search method and set the number of search $k = 128$ —equal to that for the coarsest grid method ($= 2^7$)—to explore in a reasonable region of initial values ($\sim 15^\circ\text{C} < T < \sim 35^\circ\text{C}$).

After an exhaustive search of 128 runs starting from different random initial values, three stable steady states were obtained as are shown in Figure 10-10. The temperature of each zone is displayed both by a number (in $^\circ\text{C}$) and by a color scale whose value is mapped in a horizontal color bar. The airflow directions between zones are indicated by the arrows and flow rates between interior and exterior zones are labeled in a boxed near the flow direction arrows. The unit for airflow rate is *cfm* (cubic feet per minute).

The three stable steady states represent three different flow patterns. The first flow pattern shown Figure 10-10(a) is completely wind-dominated. The fresh air first travels top-down and then outwards through the windows on all three floors.

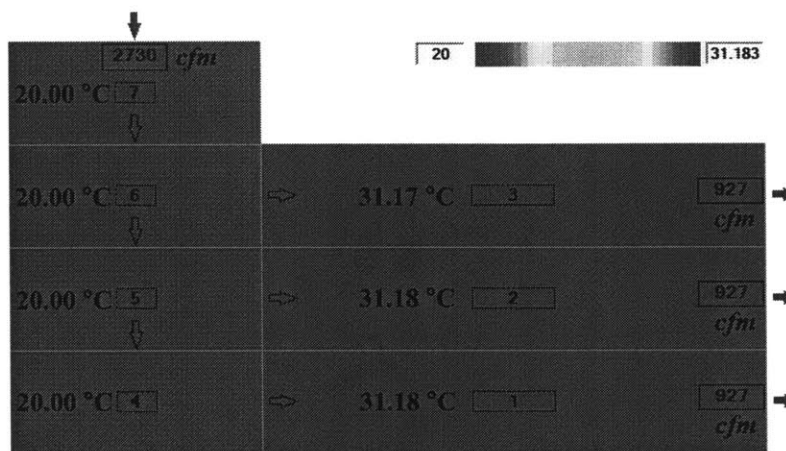
The second flow pattern is shown in Figure 10-10(b). Partial buoyancy flow is formed in the lower floors and meets with the top-down wind driven flows. Therefore the building has inflows at the window on the first floor; but outward airflows at the windows on the second and the third floors.

The third flow pattern is the buoyancy-dominated flow shown in Figure 10-10(c). The chimney is filled with warmer air rising from occupied offices on the first and the second floors. The overall flow direction is buoyancy-dominated upward, except the outward flows through the windows on the third floor.

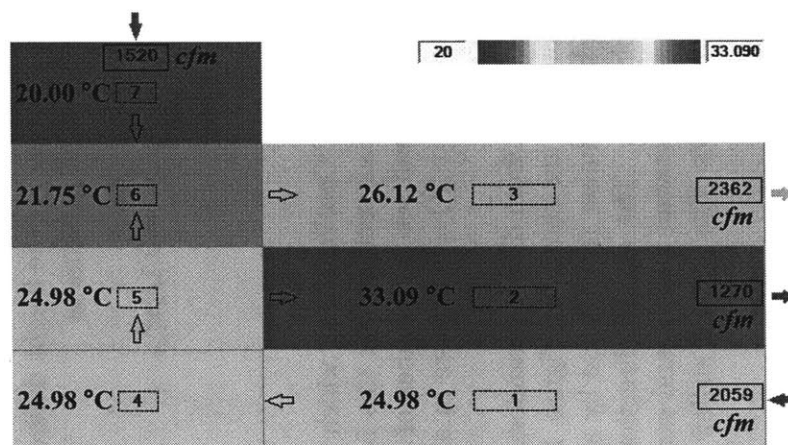
The differences between the three steady state flow patterns can be explained by the strength of the stack effect developed in the chimney. A general trend observed from Figure 10-10(a) to Figure 10-10(c) is the gradual development of a thermal stack in the chimney. In the first flow pattern (Figure 10-10(a)), no stack is developed in the chimney; in second flow pattern (Figure 10-10(b)), partial stack effect was developed, but not strong enough to overcome the wind force; in the third flow pattern (Figure 10-10(c)), even stronger stack effect (buoyancy forces) is established and overcomes the wind force, which allows an all-through upward flow to be developed in the chimney.

Another observation from the third flow pattern (in Figure 10-10(c)) is that there is insufficient buoyancy force in the chimney to draw buoyancy air to the chimney from the third floor office. This indicates that the (rough) neutral plane position in the chimney is lower than the (central) height of the window on the third floor.

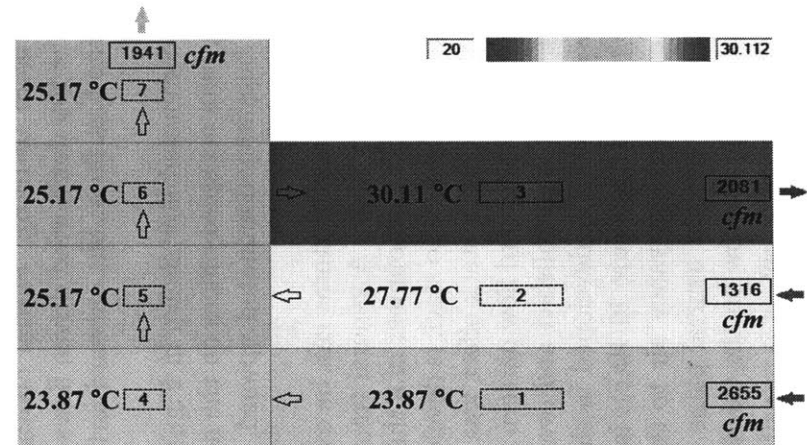
Therefore, an important question should be brought up: is it possible to have another even stronger buoyancy-dominated flow pattern in which the neutral plane



(a) Fully wind-dominated, SS1



(b) Top-down wind and bottom induction, SS2



(c) Buoyancy-dominated, SS3

Figure 10-10: Three possible stable steady states obtained in a sample multi-zone building model

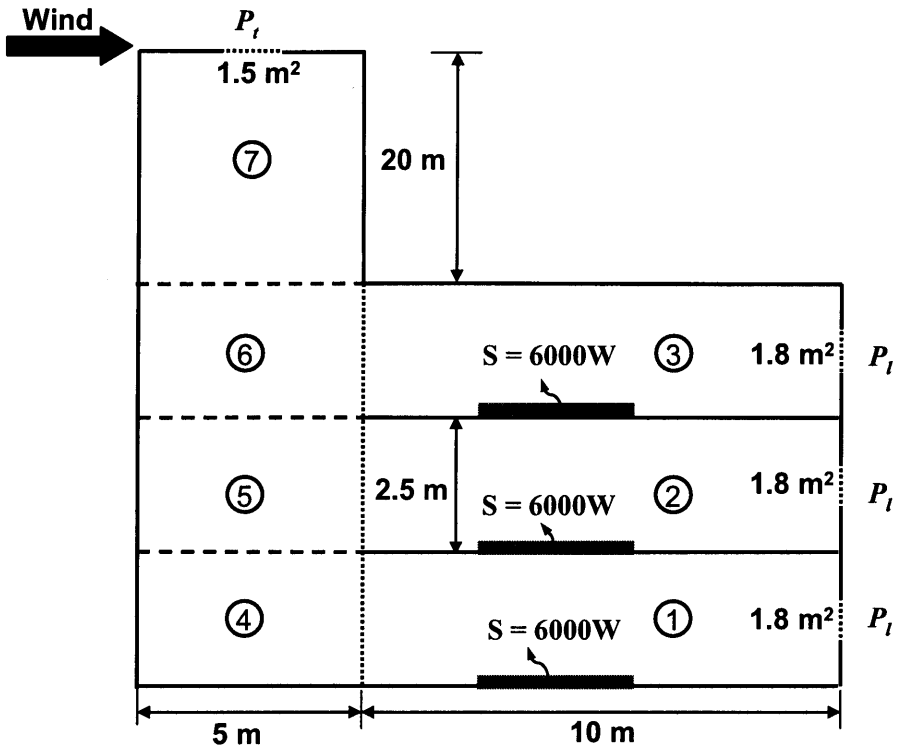


Figure 10-11: The modified building geometries

is high enough so that all the three windows in the occupied areas have incoming airflows? This may suggest another possible flow pattern may be possible in some other geometry. We will examine this possibility in the next section.

10.8 Another case with four steady states (Case 2)

To verify the conjecture about another possible steady state discussed at the end of the previous section, in this section we will investigate another example building with potentially strengthened buoyancy forces. In this new case, we increased the height of the roof (chimney) from 3m in the previous case to 20m to enhance the buoyancy force. Physically, this is similar to adding a chimney to roof. Further, we will slightly reduce the height of each floor from 3m in the previous case to 2.5m to make the relative strength of the chimney buoyancy effect even stronger. The geometries of the new building are shown in Figure 10-11.

Running similar dynamical search simulations as the previous case, we obtain the four different steady states shown in Figure 10-12. Slightly different from the previous case, one more steady state flow pattern (shown in Figure 10-12(d)) occurs in this case. In this flow pattern, all the three windows on the three floors have inward flows. The buoyancy force in the chimney is so dominant that there is no outgoing airflow from any of the windows in the occupied spaces.

In the fourth flow pattern (Figure 10-12(d)), the air temperature in Zone 3 is

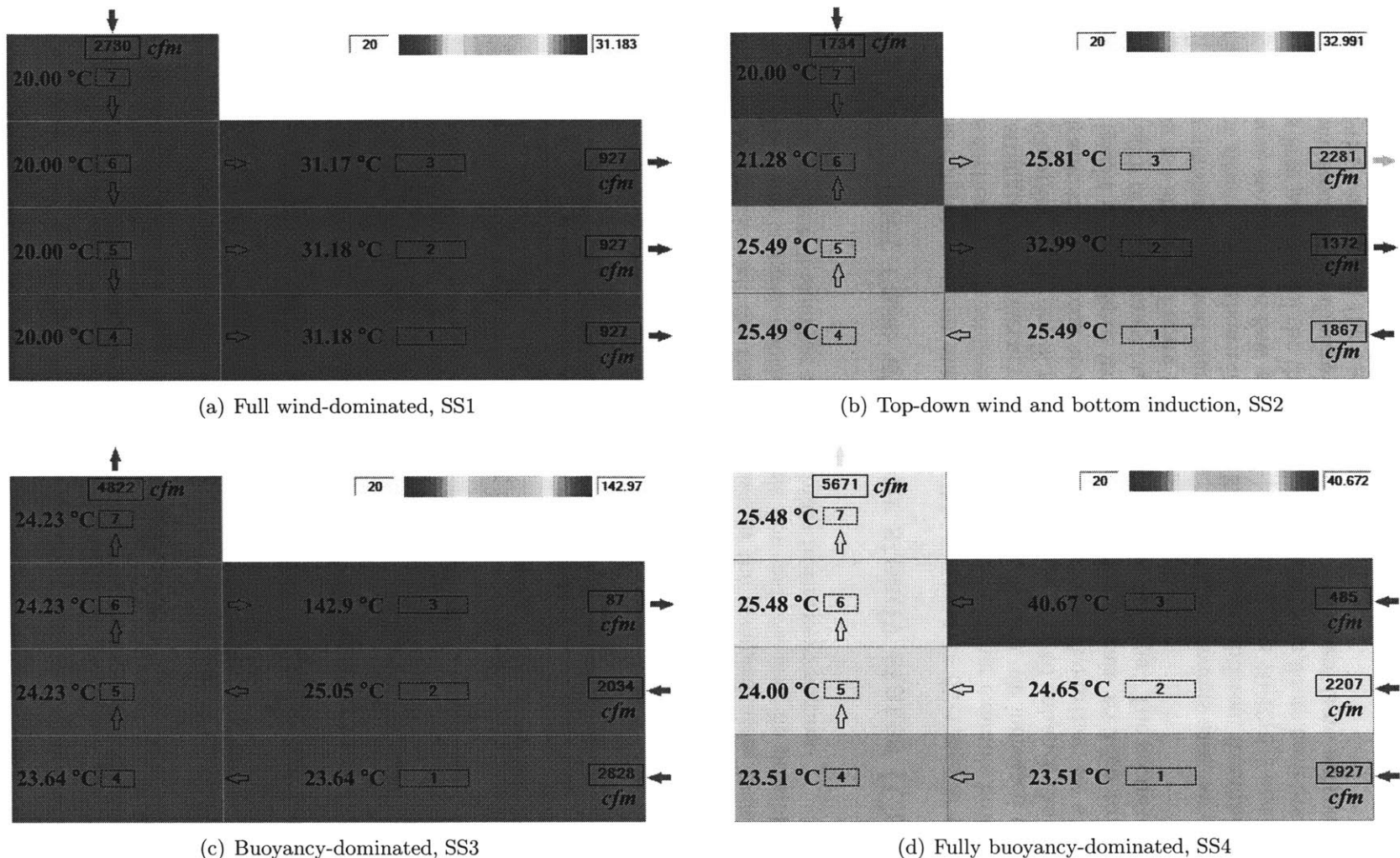


Figure 10-12: The four possible steady states in a new sample building with a higher roof chimney

slightly higher than a normally assumed reasonable temperature (if we assume $< 35^{\circ}\text{C}$ as a reasonable temperature when the outdoor temperature is 20°C). This is partially due to our one-way flow assumption. In reality, with such a high temperature difference between Zone 3 and the adjacent Zone 6, two-way flows may be formed between them; that will make Zone 3 cooler and Zones 6 and 7 hotter. In this scenario, the buoyancy force is further enhanced and a new equilibrium (with the same flow directions) will be developed (if two-way flows are allowed). Therefore, this is a reasonable steady state if the differences between the assumed one-way flows and the actual two-way flows are considered.

In this case, the third steady state (shown in Figure 10-12(c)) becomes unreasonable although it is mathematically (locally) stable. The flow rate to Zone 3 is so low that an extraordinary high temperature ($\sim 143^{\circ}\text{C}$) is built. This indicates that the chimney neutral plane position is very close to (but slightly below) the window height on the third floor. We can have a few arguments to get rid of this unreasonable steady state. First of all, with such a high zonal temperature ($\sim 143^{\circ}\text{C}$), some assumptions of the model will not be valid any more. For example, strong two-way flows can be induced between Zone 3 and Zone 6 given their huge temperature differences. This process will increase the buoyancy force in the chimney and possibly change the flow pattern to an even stronger buoyancy flow similar to the fourth flow pattern (Figure 10-12(d)). Secondly, at such a high zonal temperature, the conductive heat transfer between the indoor air and the exterior through the building enclosure systems becomes more important and may not be neglected any more. Therefore, this steady state may not be reasonable in reality given the actual physics processes that may occur.

10.9 Test the stabilities of the obtained steady states

In the previous section we have qualitatively discussed the reasonability of the different steady states obtained in the simulation. However, a quantitative method is still preferred to test the actual stabilities of these steady states. In this section, we will introduce a general method to test the stabilities and apply it to the two examples demonstrated in the previous sections.

10.9.1 Theoretical background

As we mentioned before, the steady states obtained by the dynamical simulation method are *locally stable*, which means they can resist small (usually infinitesimal) perturbations in the boundary parameters, such as the wind velocity or the heat sources. However, in Chapter 7 (or [77]), we have demonstrated that the system can transit from a steady state to another if sufficient perturbation is applied to the system. We derived two indicative terms—the *minimum perturbation magnitude* and the *minimum perturbation time*—to measure the requirements on the perturbation for such a transition. In particular, if the minimum perturbation time under a small perturbation—usually comparable to those stochastic components that naturally exist

in the environment—is very small, the locally stable steady state may not be able to stably exist any more. This is the theoretical basis for the test method we are going to develop.

10.9.2 A practical test method

However, to directly compute the minimum perturbation time is not a convenient task (although it can be empirically obtained) for a building with complex geometries. To deal with the stabilities of the obtained steady states the complex buildings, we will develop a more convenient method that can reflect the principles of the minimum perturbation.

To do that, we will use a convenient test method by introducing *stochastic components* in the boundary parameters. The test procedures are as follows:

1. Set the initial values to the steady state to be tested and start the simulation;
2. At some point, introduce stochastic components (noise) to the boundary conditions (environment parameters) to simulate the disturbances in actual systems;
3. Observe whether state transitions occur during the interference of the stochastic input.

If a steady state is very unstable and sensitive to the variations of the environment conditions, a state transition is most likely to occur during the stochastic interference period. Otherwise, if the steady state is stable enough, the solution will just vibrate locally around the original steady state—but no state transition will occur.

10.10 Test on the two cases

To demonstrate how the proposed method works, we will apply it to the case with four steady states we have simulated in the previous section.

10.10.1 Test results

Here we first assume that we will introduce a stochastic component to the wind velocity. In the simulation, we have assumed that the wind velocity is invariant (at $v_{ref} = 2.8 \text{ m/s}$). In reality, however, it is never constant. Here we assume that the wind velocity is varying within a range of $\pm 5\%$ of its nominal value. Statistically, we have assumed that the wind velocity is a random variable with a uniform distribution between $95\%v_{ref}$ and $105\%v_{ref}$. The mean of the wind velocity over time is still v_{ref} . However, at any particular time step (of 20–30s), the wind velocity can be any random value in the range of $[0.95v_{ref}, 1.05v_{ref}]$ without a systematic pattern.

For each of the four steady states, the initial values are set exactly at the steady state temperature values. Theoretically, if the wind velocity is invariant (at the nominal v_{ref}), the output of the zone temperatures will be constant horizontal lines since the starting point is already a locally stable steady state. After the stochastic

component is introduced, the output temperatures (of the seven zones in this case) will start to vary. In order to more clearly demonstrate the variations, we will only plot the temperature output of two zones—Zone 3 and Zone 7—to represent the zone temperatures in the building.

Figure 10-13 shows the test results. Each result in Figures 10-13(a) to 10-13(d) corresponds to a steady state shown in Figures 10-12(a) to 10-12(d) in order. For SS1 (Figure 10-13(a)), SS2 (Figure 10-13(b)), and SS4 (Figure 10-13(d)), the system responds to the disturbances by some degree of vibrations near the nominal steady states. However, for SS3 (Figure 10-13(c)), a state transition occurs under the stochastic wind velocity perturbations. Under such perturbations, the system was transformed to another steady state—SS4. Theoretically, the occurrence of the state transition implies that the minimum perturbation time to transit the system to another steady state is very small. The results quantitatively show why the solution SS4 is not robust enough, which agrees with the qualitative analysis we provided in the previous section.

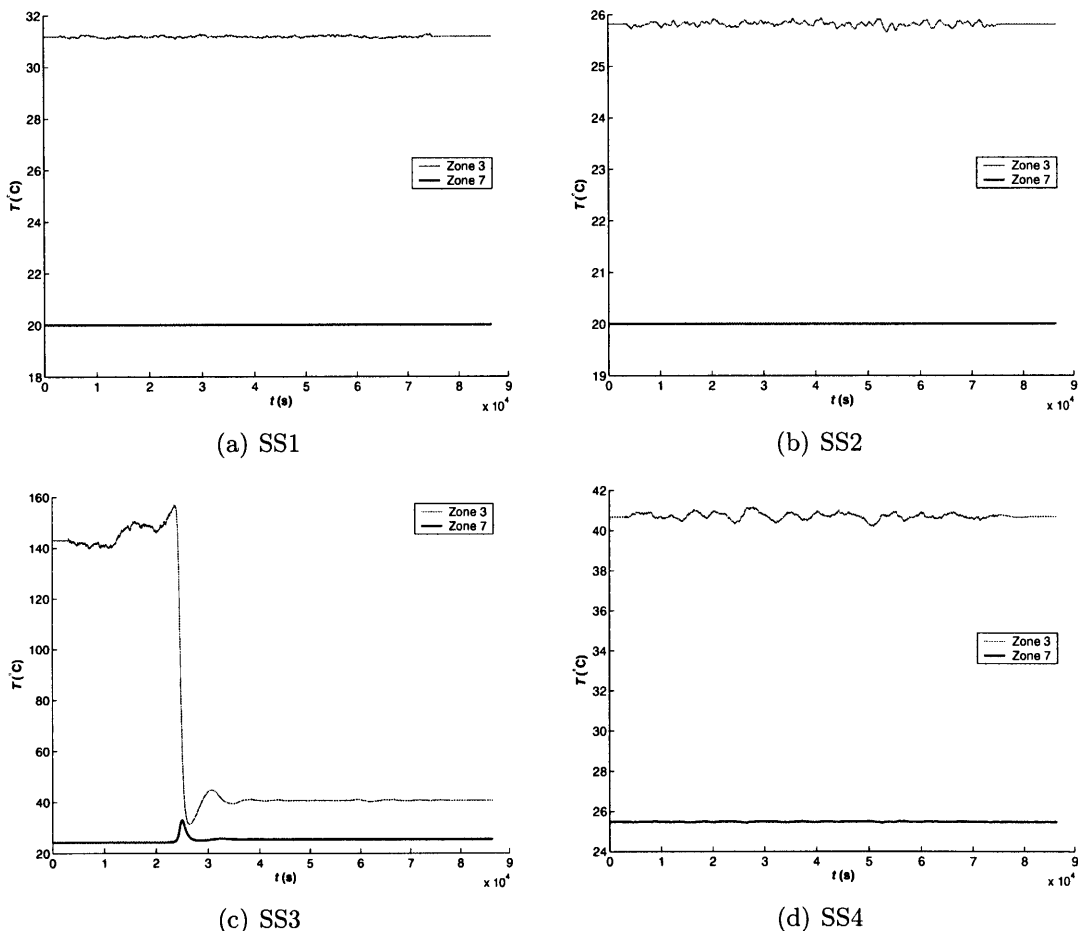


Figure 10-13: Stability tests under wind velocity disturbances within $\pm 5\%$ (for Case 2)

The selection of the perturbation magnitude is relative conservative compared to the actual conditions. In an actual natural ventilation system, a fluctuation higher than 5% in wind velocity is likely to occur. This test thus provided another reason why the extremely high solution SS3 is not likely to occur in reality, besides its unreasonably high temperature values.

The same test can be applied to the three steady states in Case 1. Figure 10-14 shows the state temperature output of the system under stochastic perturbations. For all the three steady states, no state transition occurs under the stochastic perturbations. Therefore, all the three steady states are shown to be sufficiently stable under wind velocity perturbations within the range of $\pm 5\%$.

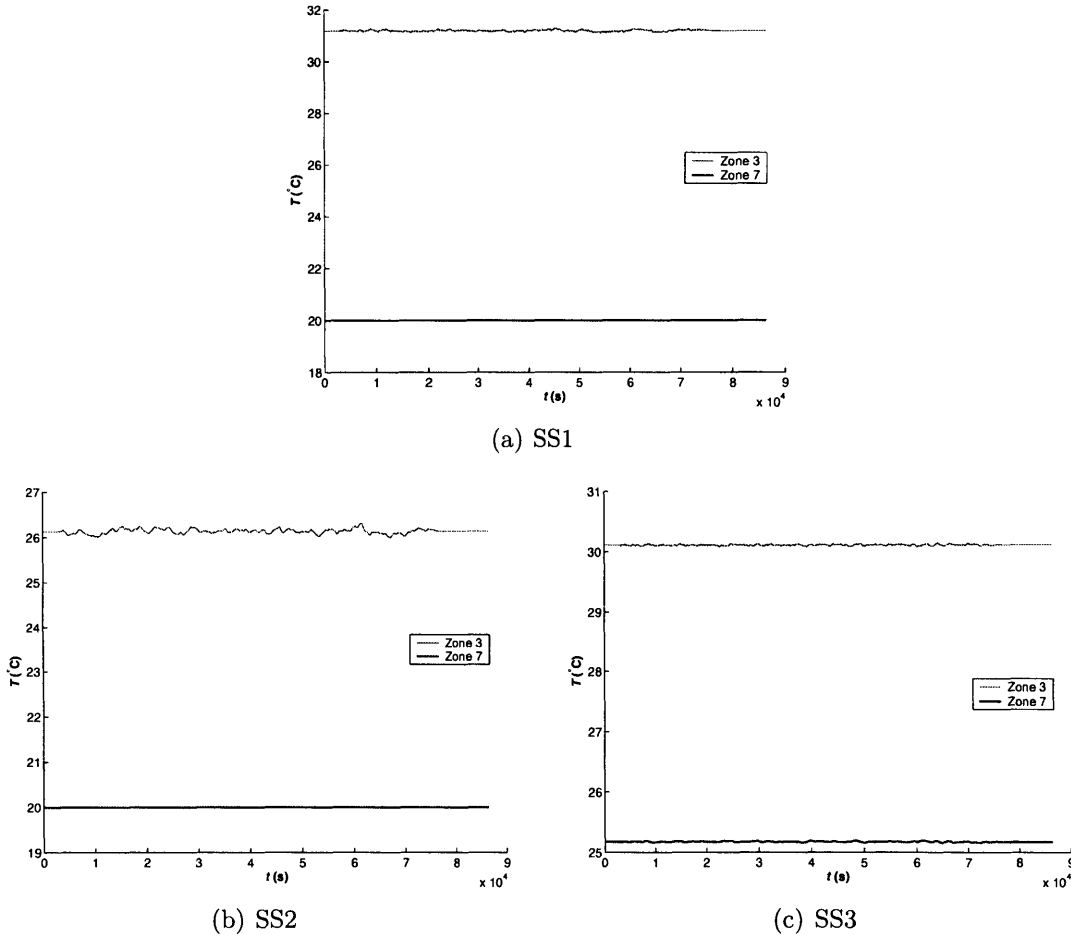


Figure 10-14: Stability tests under wind velocity disturbances within $\pm 5\%$ (for Case 1)

10.10.2 Stability of SS3 (in Case 2)

In previous sections, we have argued that SS3 is locally stable, although it is not robust enough to sustain a “strong” (finite) perturbation. In order to show that SS3

is locally stable, we conducted a few more tests to demonstrate its stability properties. To do this, we use velocity perturbations of different levels to perturb the system at SS3.

Figure 10-15 shows the system temperature output under four different levels of stochastic inferences— $\pm 1\%$, $\pm 2\%$, $\pm 5\%$, and $\pm 10\%$ of velocity perturbations. According to the plots, SS3 is stable under small perturbations. When the magnitude of the stochastic component is small (e.g., $\pm 1\%$, $\pm 2\%$), the state transitions do not occur. Only when the stochastic component (noise) is large enough (e.g., $\pm 5\%$, $\pm 10\%$) can the system transit from SS3 to another steady state SS4.

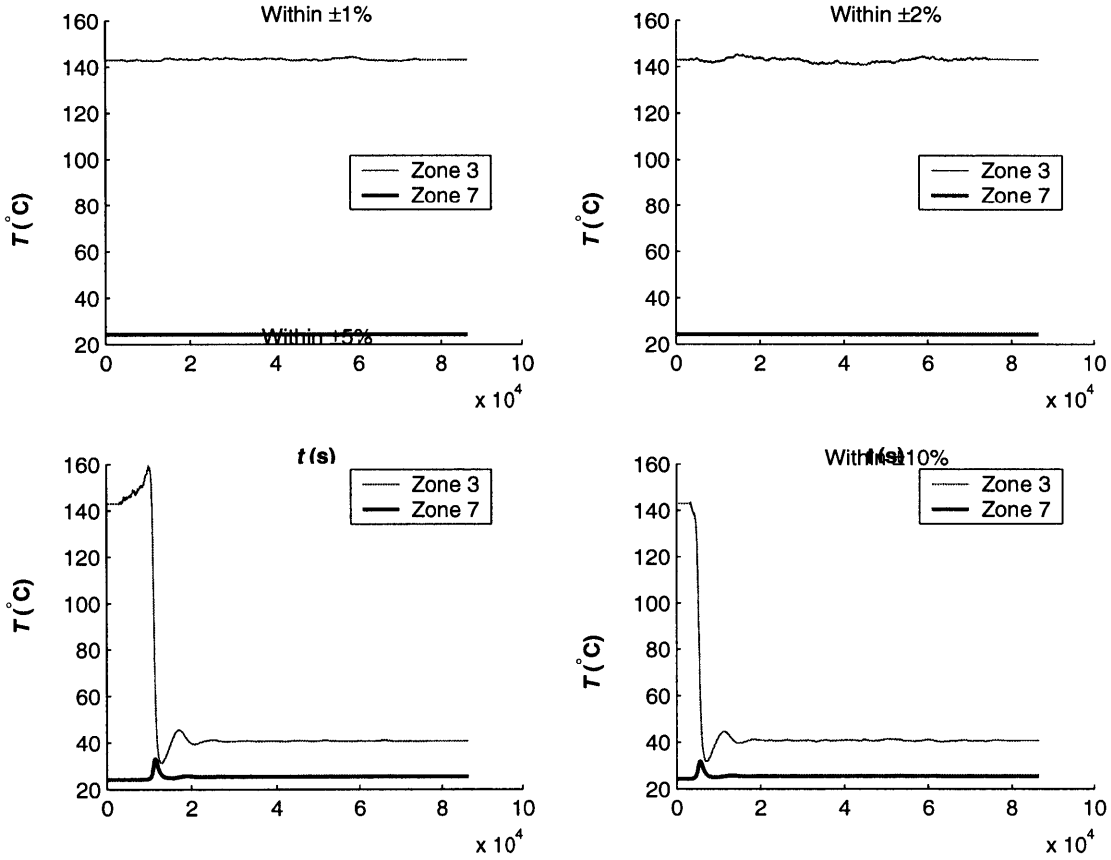


Figure 10-15: System temperatures output under different levels of stochastic wind velocity perturbations (for SS3 in Case 2)

This behavior of SS3 is different from that of a locally unstable steady state. First of all, a locally unstable steady state usually cannot be (finally) reached in a dynamic simulation. However, we did finally reach this steady state by a random initialization discussed before; and the system can stay permanently at SS3 without significant perturbations. Secondly, a locally unstable steady state is sensitive to infinitesimal perturbations. However, SS3 can survive some small finite perturbations (e.g., $\pm 1\%$ or $\pm 2\%$, which we defined as “strong perturbations”. Therefore, SS3 is locally stable

in theory; but it is insufficiently robust in the real environment when stochastic disturbances exist.

10.10.3 Further tests

The test method can be further used to test the stabilities of the rest of the steady states obtained other than SS3. By increasing the magnitude of the pressure perturbations, we can run the test again on the four steady states obtained in Case 2 (the higher-chimney example building). Through this further test, we hope to see whether other state transitions are possible in this system.

By applying stochastic wind velocity perturbations that vary in the range of $\pm 30\%$, we obtained the results in Figure 10-16. Other than at SS3, at SS2 (Figure 10-16(b)) a state transition also occurs under such strong pressure fluctuations—SS2 transformed to SS4. The result shows that SS2 seems to be the next sensitive to the stochastic pressure perturbations.

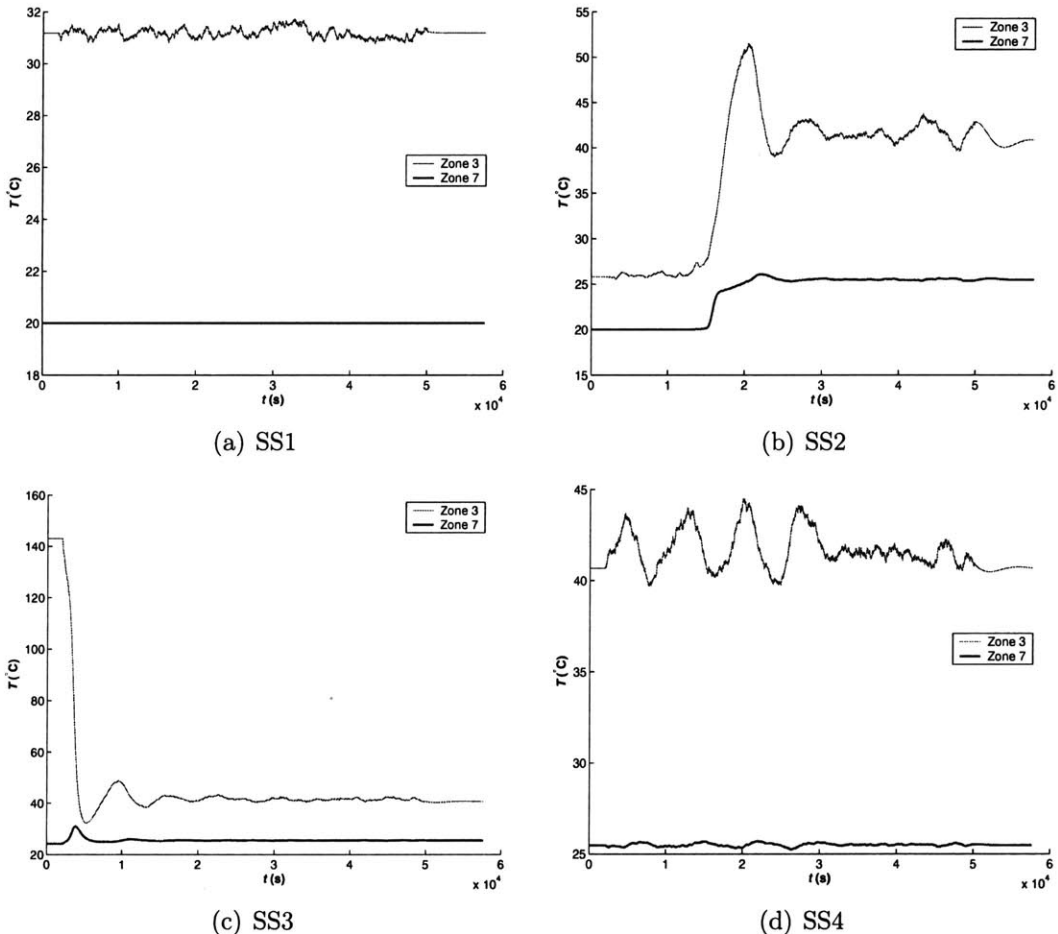


Figure 10-16: Stability tests under wind velocity disturbances within $\pm 30\%$ (for Case 2)

A similar test is applied to the three steady states obtained in Case 1 (the lower-chimney example building) using perturbations that fluctuates within $\pm 30\%$. The results are shown in Figure 10-17. Again, at SS2 a state transition occurs under perturbations—the system transforms from SS2 to SS3.

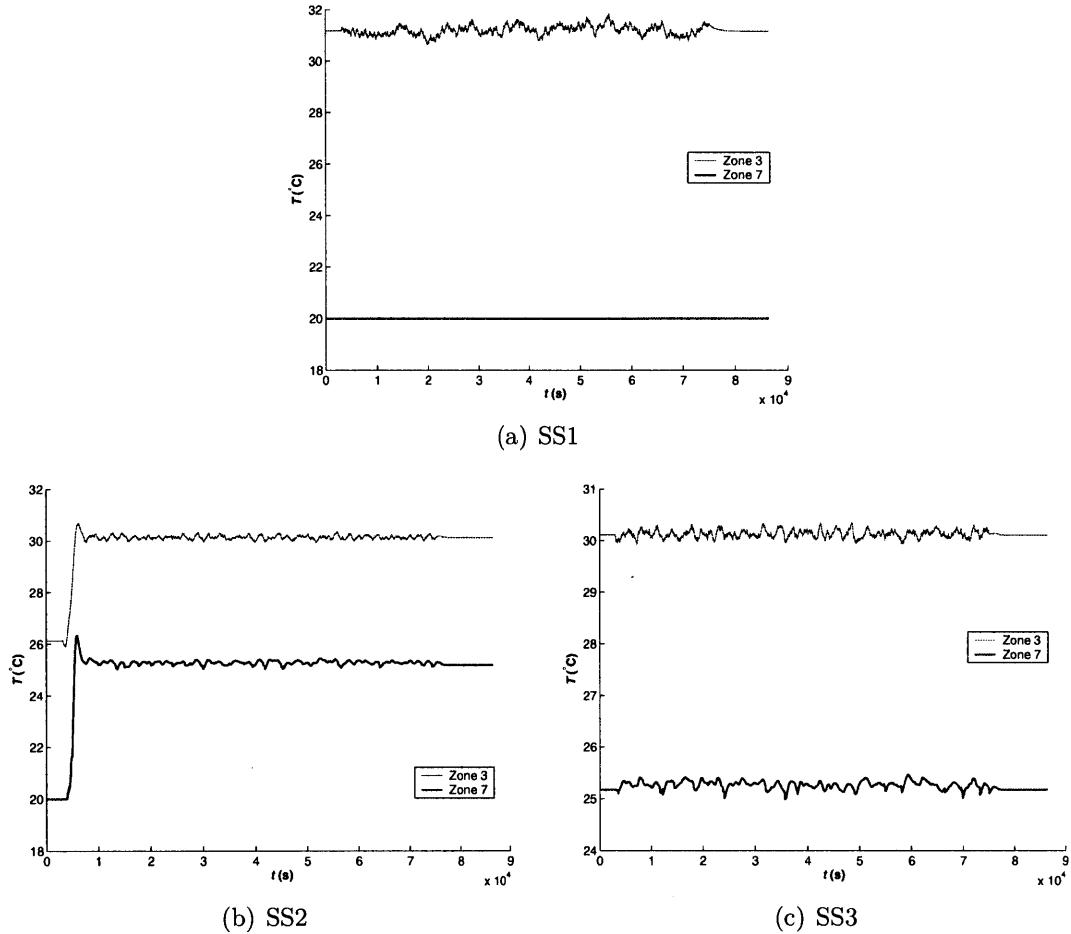


Figure 10-17: Stability tests under wind velocity disturbances within $\pm 30\%$ (for Case 1)

10.11 Discussions

The simulation, search, and test methods developed in this study provided a practical method in identifying and testing the stabilities of the steady states in a complex building. However, there are several issues that deserve discussions.

First, the simulation was based on multi-zone full-mixing assumption. Under this assumption, the airflows we considered are just the bulk flow between the physical zones. The microscopic flow details such as internal stratifications, turbulences, and eddies were not considered in the present study. When such details are considered

(e.g., using a CFD simulation), the results can be different, especially for those steady states sensitive to finite perturbations. Nevertheless, we do expect that the present study will provide a general guideline on the possible results that may show up in other numerical simulations, model experiments, or even in actual buildings.

Secondly, in the test of the stabilities, we only considered the pressure disturbances. This is based on the fact that the pressure perturbation can affect the system much quicker than a perturbation based on the thermal transport, for example, a heat source perturbation. However, another possible type of perturbation (or disturbances) in the system is the two-way flows between the internal zones, by either temperature differences or human activities. This type of perturbation will expect to have an important impact on the stabilities of a steady state. However, how to quantify this effect still seems to be a challenge.

Thirdly, in this study, we did not take special consideration of the spectrum profiles of the noise, i.e., its power-frequency distribution. We used a simple (and relative conservative) assumption on the distribution of the random perturbation components. A rough estimation is that the major frequencies of the noise are in the range of 0.1 to 0.01 Hz, according to the time steps used for the simulation. In general, natural wind can have a wider spectrum. This means it has both components that fluctuate slowly and components that fluctuate very quickly. However, we assume that those extremely high and extremely low frequencies will have a much weaker impact on the system than those in the range of 0.1 to 0.01 Hz. This is partly due to the resonance with the building flow systems. The building may not respond to those extremely high or extremely low frequencies that are too far away from its natural frequency.

Finally, in the examination stability test developed in this study, we did not consider the effect of the thermal mass. We argued in the algorithm development section (§10.3) that the thermal mass does not affect the existence and values of the multiple steady states. However, it does affect the state transition dynamics between the multiple steady states in a natural ventilation system. In the stability test presented in the later part of this study, we have therefore implicitly implies that the building is a building with little (or very light) thermal mass. Nevertheless, the stability test can be done with the existence of the thermal mass using a similar method, when the amount of thermal mass in the building is properly assumed in the model.

10.12 Conclusions

In this chapter, we developed a dynamical simulation model to identify the steady states in an arbitrary building with complex geometries. The method involves a coupled airflow and thermal simulation and an exhaustive search based on the coupled simulations.

The theoretical background the coupled airflow and thermal simulation was demonstrated by a single-zone case. The simulation method was then generalized to multiple-zone buildings with complex geometries. For the completeness of the study, the way to deal with thermal mass was also discussed.

Further, we investigated three potential search methods—general grid search, coarsest grid search, and random initialization search—for identifying the multiple steady states in complex geometries using the dynamical simulation. The computational complexities and the advantages and disadvantages of each method were discussed.

The developed identification method was applied to an example building with seven zones. Three locally stable steady states are identified. The flow characteristics physical meaning these steady states were discussed in detail. Another model with modified parameters was investigated to explore the possibility of a fourth flow pattern. Four steady states were identified in this case, with an obviously unreasonable one. The validity of two suspected states found was discussed with considerations of the differences between the mathematical assumptions and the real physical processes.

Finally, we developed a convenient method to test the actual stabilities of the steady states obtained in the simulation. Based on the theory developed in Chapter 7, we introduced stochastic disturbances to the boundary conditions to observe whether a state transition will occur in the system, starting from a steady state. The method was found to be effective and the results showed quantitatively how one of the steady states can be unstable in a real environment with stochastic disturbances.

In general, the study showed that multiple steady states, usually more than two, can occur in buildings with complex geometries. Although, strictly speaking, the developed method does not guarantee that all the possible steady states will be captured, it was demonstrated to be effective in identifying multiple steady states in a practical range.

Chapter 11

An innovative natural ventilation control strategy based on state transitions between multiple steady states

In this chapter a positive application of the multiple steady-state behaviors of natural ventilation system is investigated. A state switch strategy is proposed in natural ventilation system to switch the flow pattern from an unfavorable state to a favorable state when certain conditions are met. In this strategy, the decision on state switch is made by a dynamical system model of the system to obtain maximum ventilation rate. The transition dynamics between the two steady states are driven by a temporary perturbation in heat source, wind pressure, or other parameters. After a short period of time, the system can automatically move toward the target state without further existence of the perturbation. Therefore, this strategy is effective in achieving higher ventilation rate with less energy consumption compared with a conventional turn-on-fan ventilation control strategy. The implementation methods of the state switch strategy are further discussed.

11.1 Introduction

Multiple steady-state behavior occurs in various natural ventilation systems (Linden [44], Li and Delsante [41], and Yuan and Glicksman [74]). Due to the complexity of these multiple steady-state behaviors, they have been more or less viewed as a negative side of natural ventilation system, in either numerical simulations or design practice. For example, an issue about multiple steady states is the difficulties to distinguish a real steady state (locally stable) from those phantom ones (unstable) in the coupled airflow and thermal simulations (Li and Delsante [41], Axley [10]). Although further studies (e.g., [70, 74]) showed that the locally stable steady states can be clearly distinguished from unstable ones when the dynamical system characteristics of the system are investigated, the nonlinear nature of the multiple steady-state behavior

still causes problems to a coupled airflow and thermal simulation programs such as the CONTAMR97 (Axley [11]).

The existence of multiple steady states also poses challenges to ventilation control strategies. Before that, in experimental studies, the final steady states of the system were found to be dependent on the flow history. The uncertainty and the path-dependence made it difficult to determine the correct control strategy. Due to the complexity caused by the multiple possible steady states of the system, in previous studies it was generally assumed that multiple steady states should be avoided as much as possible in ventilation designs (e.g., Woods [66]; Livermore and Woods [45]). For example, Woods [66] proposed a method to eliminate the multiple steady states and achieve solution uniqueness by changing the building opening geometries. Livermore and Woods [66] also mentioned that the designed region should be

However, in Chapter 4 we stated that there could be a positive aspect to utilize the multiple steady-state phenomenon other than an “avoiding” statement. The system can switch between the two stable steady states (e.g., a warmer state to a cooler one) under perturbations as an innovative control strategy. Indeed, a further study in Chapter 7 on the state transition requirements between the stable steady states provided knowledge on such state transitions. In the original study, the state transition dynamics were used to investigate another important issue—the actual stabilities (or robustness) of the locally stable steady states.

As another application of the state transition dynamics, the present study will focus on the development and implementations of the state switch ventilation control strategies. The strategy will allow the system to switch from an undesired steady state (e.g., low flow rate and warmer interior temperature) to a desired steady state (e.g., high flow rate and cooler). The criteria for state transition, the minimum perturbation magnitude requirement, and the minimum perturbation time calculation investigated in the previous study [77] can be largely applied to the control strategies developed in the present study.

11.2 Theories

A transient dynamical system model was developed in Chapter 4 for the system shown in Figure 11-1. In the single zone system, the natural ventilation flow is driven by the combined effect of the exterior wind and the interior buoyancy forces.

The governing differential equation of the system is as follows:

$$Mc_p \frac{dT}{dt} = q \cdot \rho_a c_{pa} \cdot (T_e - T) + UA \cdot (T_e - T) + E, \quad (11.1)$$

where the term q is represented the flow rate of the system as a function of the temperature (time dependent state variables) and other parameters (mostly time independent boundary parameters).

$$q = \overline{C_d A} \cdot \sqrt{\left| 2gh\beta \cdot (T - T_e) - 2 \frac{P_w}{\rho_a} \right|}. \quad (11.2)$$

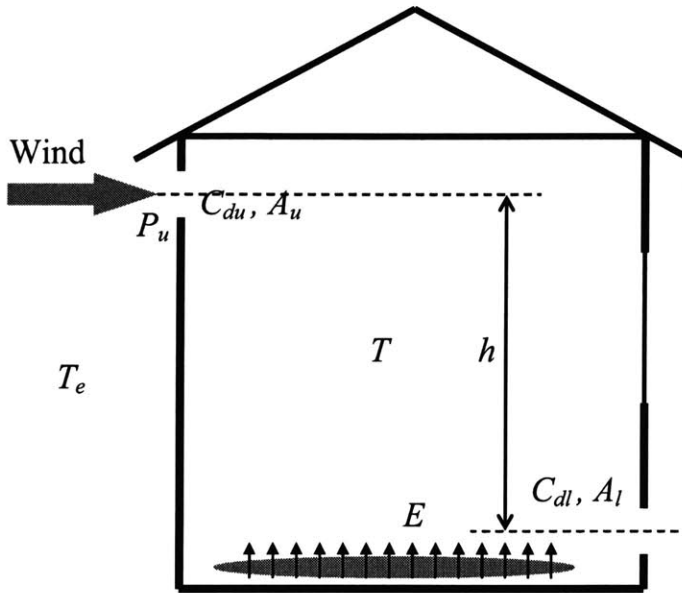


Figure 11-1: A natural ventilation system with flows driven by combined buoyancy and wind forces

The system is a single value variable of the system temperature T . Combining Equations (11.1) and (11.2) yields the following equation that describes the air temperature dynamics:

$$\frac{dT}{dt} = f(T - T_e) = \frac{E}{Mc_p} - \frac{T - T_e}{Mc_p} \cdot \left(\overline{C_d A} \cdot \rho_a c_{pa} \sqrt{\left| 2gh\beta \cdot (T - T_e) - 2\frac{P_w}{\rho_a} \right|} + UA \right). \quad (11.3)$$

Figure 11-2 plots the function of the system vs. T . It clearly shows that the system can have three mathematical steady states (denoted as 1-3) if the steady-state equation is solved. However, on the horizontal axis of Figure 11-2, the direction of the vectors is also plotted. In the region of $[-\infty, T_1]$, the direction of vector $f(T)$ is to the right, which means the corresponding $f(T)$ value (vertical axis) is positive. In between T_1 and T_2 , the direction is to the left, which corresponds to a negative $f(T)$ value. Beyond T_2 , the value is positive again. This clearly explains that the two stable steady states are 1 and 3. The state 2 is unstable but it is a critical point for the initial values: if the system starts from below T_2 , the final steady state will be 1; if it starts from above T_2 , the final steady state will be 3. This conclusions are also explained in Chapter 4.

Therefore the system can stay at two different stable steady states theoretically. Both steady states are theoretically possible and have been indeed observed in experimental studies (e.g., [44]). The flow rate characteristics of the three steady states are plotted on Figure 11-3. We assigned a sign for the airflow: the flow is defined as positive if it is upward (buoyancy-dominated); the flow is defined as negative if it is downward (wind-dominated).

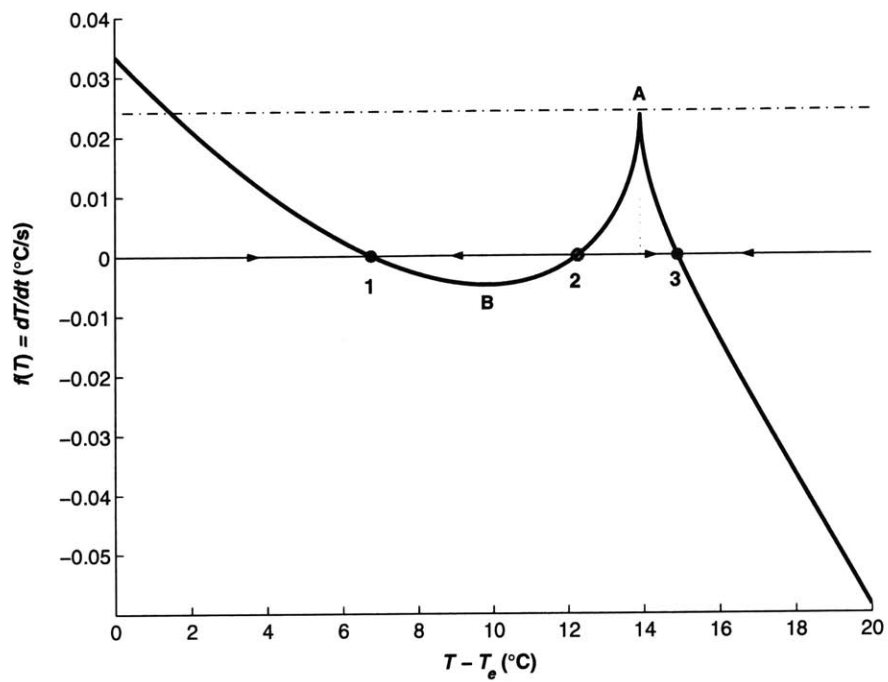


Figure 11-2: The transient temperature characteristics of the system

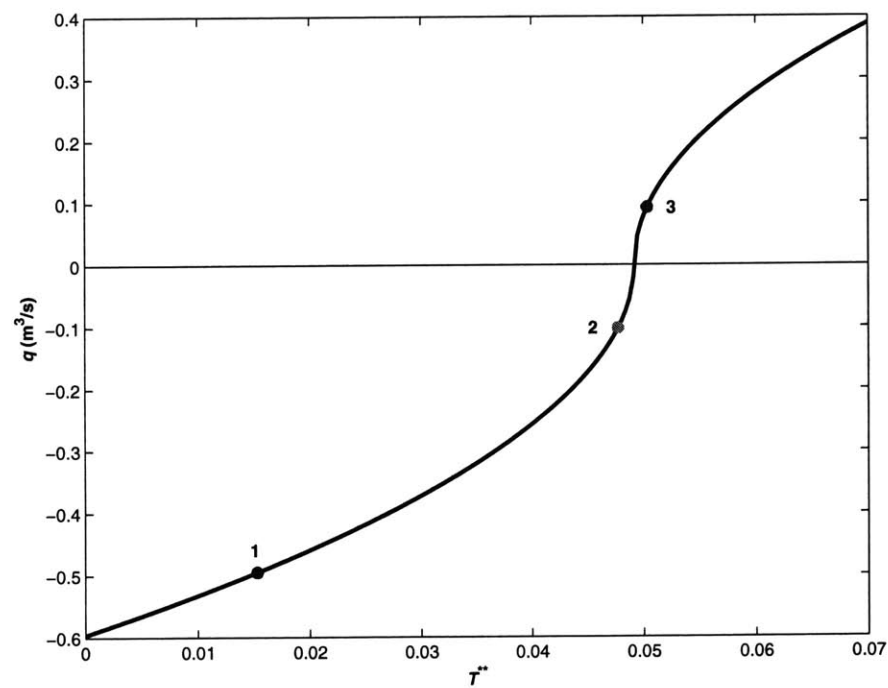


Figure 11-3: The volume flow rate of the system as a function of the system temperature

11.3 Characteristics of the two stable steady states

Figure 11-2 shows a phenomenon when multiple steady states exist in the system: the system temperature at steady state 1 is lower than the temperature of steady state 3. This is also explainable by Figure 11-3: the system have higher flow rate (absolute value) at steady state 1; since airflows must remove the equal amount of heat from the system in steady state, it follows that the zone temperature will be lower in state 1 with larger flow rate.

This flow rate and temperature differences are the basis for our strategy. Figure 11-4 shows the two ventilation patterns in a building. The values are calculated based on the settings for Figure 11-2. The two states correspond to the steady states 1 and 3 on Figure 11-2 respectively. Assume that we are doing natural ventilation during the summer. The lower zonal temperature is definitely preferred. This comes to the strategy: when both of the two steady states are possible, we will try to actively choose the steady state with lower zonal temperature (larger ventilation rate).

$$\rightarrow v_{ref} = 1.7 \text{ m/s}, T_e = 10^\circ\text{C}, E = 3000 \text{ W.}$$

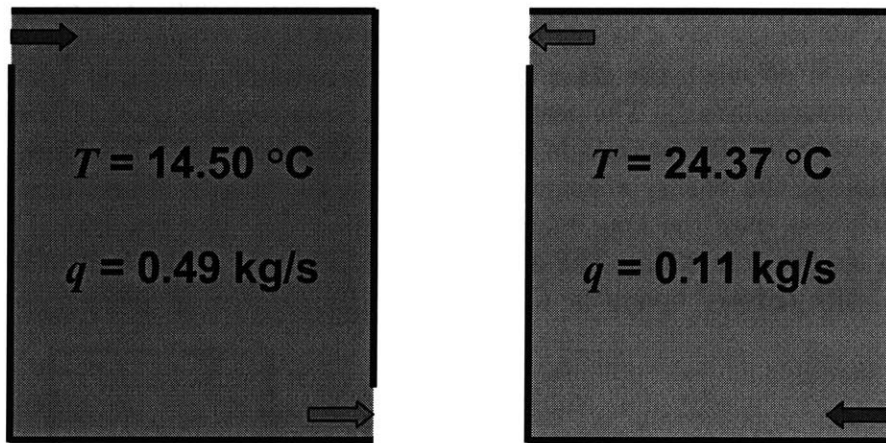


Figure 11-4: The two theoretically stable ventilation patterns

An immediate question is that it is possible to choose the steady states? The answer is YES. In Chapter 7 we quantitatively investigated the mechanism for the system to switch from one steady state to another under sufficient “strong” perturbations. Whenever the system is in the warmer state (similar to Steady State 3 (SS3) in Figure 11-2), a sufficiently strong perturbation can perturb the system to the cooler state (similar to Steady State 1 (SS1)) with finite time. The opposite transition (from SS1 to SS3) is also possible under perturbations. The magnitude and time requirements of the perturbations were also investigated in Chapter 7.

A *desirable state* needs to be defined here. In this application, we assume that the strategy will be used in summer natural ventilation, which means the major task is to provide natural cooling to remove the internal heat. Therefore, a state with larger flow rate should be a desirable state, which is the downward wind-dominated

ventilation pattern. On the other hand, the definition of a favorable state can vary depending on the specific applications. For example, for a natural ventilation system in winter (if used), a warmer upward steady state can be the desirable state. A little complication about winter conditions is that the temperature and the flow rate needs to be considered simultaneously. Even in the same winter case, it is not necessary to say a warmer state is more favorable because the minimum fresh air requirement (by ASHRAE standard 62 [7]) is also an important consideration, especially for commercial buildings. In most part of our study, we will focus on the summer operation conditions, where the desirable state is defined as the cooler state SS1 and the unfavorable state is defined as the hotter state SS3.

11.4 State switch strategy using perturbations

The novelty of the state switch strategy is that it is the way it implements the “state transition” through perturbations. As was described in Chapter 7, a perturbation is a temporary boundary condition (or input variable) change that serves to trigger a state transition. The most important feature about the “strong perturbation” defined in the study is that it will be removed after that time period. For example, if at sometime, we turned on a heater or a fan for a while to trigger a state transition, we will turn it off when the state transition is successfully triggered (although not necessarily accomplished). The perturbation can be shown in Figure 11-5 as a square function with time. Its magnitude is ΔW and its duration is t_s . Therefore, the time of operation of the energy consuming equipment to “trigger” transitions could be significantly less than the long equipment operation time in a traditional boundary condition change transition. The energy saving potential of the control strategy is apparent, with reduced operation time.

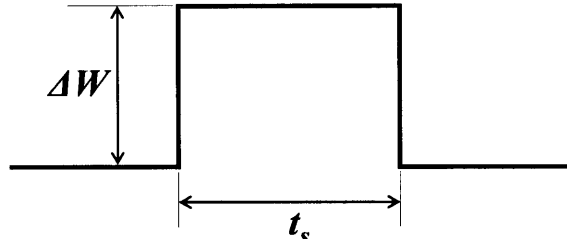


Figure 11-5: A strong perturbation acts on the system

Therefore, the “transitions” between the multiple steady states described in Chapter 7 are different from those in other studies (e.g., Linden [44]; Heiselberg et al. [35]) where the transition is just a solution conventional change caused by a permanent change in boundary conditions. Essentially, the transition defined in that conventional way does not consider the “triggering” effect of a perturbation that was discussed in details in the study [77]. The transition under perturbations was applied in quantitatively describing the actual stabilities of stable steady states.

In this chapter, we will again use the “triggering” effect in the state transitions under perturbation. The newly developed control strategy can be more predictable and optimized by the way the perturbation requirements are defined.

11.5 Triggering criteria

An important issue is when this state switch strategy should be triggered. From Figure 11-2, the only conditions in which the strategy should be triggered are: a.) the system can have multiple steady states under current boundary conditions; b.) the system is in an undesirable state (e.g., an upward flow state 3 in Figure 11-2). These two conditions have to be satisfied simultaneously so that the state transition is necessary and applicable.

For the first criterion, the conditions for the multiple steady states to exist in the system were studies in Chapter 4. Briefly, it requires that the two points on the curve shown in Figure 11-2 to satisfy the following relationship:

$$f(T_A^{**}) \geq 0 \text{ and } f(T_B^{**}) \leq 0. \quad (11.4)$$

which is equivalent to the following expression:

$$P^{**} \cdot UA \leq \beta E \leq T_B^{**} \cdot \left(\overline{C_d A} \cdot \rho_a c_{pa} \cdot \sqrt{2gh} \cdot \sqrt{P^{**} - T_B^{**}} + UA \right), \quad (11.5)$$

The terms with ** are dimensionless and are defined by the following form respectively:

$$P^{**} = \frac{P_w}{\rho_a g h}, \quad (11.6)$$

and

$$T^{**} = \beta(T - T_e). \quad (11.7)$$

T_B^{**} in Equation (11.4) is then the dimensionless form of the T_B , the local minimum temperature value in Figure 11-2. The analytical form of T_B^{**} is given in Chapter 4. It can also be computed numerically by simple computer algorithms.

The second criterion can be easily checked by measuring the steady state flow direction. Theoretically, the system is in an upward flow steady state pattern when it is in undesirable warmer mode (given that multiple steady states do exist). Therefore, a simple detection on the steady state flow direction can be used to check whether the system is in an undesired warmer steady state or not.

When the two criterions are both satisfied, a state transition is applicable, and most of the time, necessary, for energy savings. In practice, the judgment of the first criterion is more difficult to deal with due to the lack of information or accuracy in determining some variables, for example, the window opening areas and the heat source levels. However, by using data modeling and identification techniques, the parameters can be estimated and the satisfaction of the criterion can be estimated with probabilities. The data modeling and identification models will be discussed in later sections.

11.6 Stop criteria

In the system shown in Figures 11-1 and 11-2, the unstable steady state 2 is the critical temperature point for the initial values to achieve different steady states. If the system starts from a higher temperature than this temperature, it will reach the buoyancy-dominated steady state 3. Otherwise, it will finally reach the wind-dominated steady state 1.

Therefore, in the state switch control strategy, in order to achieve a cooler ventilation pattern, the system has to be perturbed below the unstable steady state temperature to assure the switch. This is the minimum requirement for the perturbation. For a control strategy, this can be easily implemented by one (or more) temperature sensor(s) that reads the zonal temperature. If the zonal temperature drops below the unstable steady state temperature, the perturbation can be removed and the system will automatically move toward the cooler state.

11.7 Switch time

We implement the state switch by applying a wind (pressure) or heat source perturbation. Generally, a pressure perturbation is easier to implement, for example, by a fan. Using heat source perturbation can also achieve the goal, although a cooling source (negative heat source perturbation) is required. This sometimes requires additional cooling equipment. In the model we developed, we can estimate the minimum time that the fan or the cooling source should be applied, although we will use a fan to implement this strategy most of the time.

The time was defined as the *minimum perturbation time* in Chapter 7. It calculates the minimum time the perturbation should persist to enable the system to reach the unstable steady state 2 from the original steady state (either 1 or 3). Mathematically, the minimum perturbation time under a certain pressure (increase) perturbation can be calculated by the following formula:

$$t_{\text{min}} = \int_{T_{ss2}}^{T_{ss3}} \frac{1}{\hat{f}(T)} dT, \quad (11.8)$$

where $\hat{f}(T)$ is the temperature derivatives over time (see Equation (11.3)) for the system under perturbation.

The state perturbation has to satisfy the following minimum magnitude. Since the two steady states are both locally stable, an infinitesimal perturbation will not be able to perturb the system to another steady state. In Chapter 7, we defined the *minimum perturbation magnitude* that describes the perturbation magnitude requirements given that the perturbation can last for an infinite long time (and then removed). Since we will mostly use a fan to provide a pressure perturbation that can be “strong” enough in most cases, the details about the minimum perturbation magnitude are left out of this chapter.

11.8 Optimal perturbation magnitude for minimum energy cost

We assume that a fan is used to implement the control strategy. When the system is in an unfavorable steady state SS3, we find that the system can have a cooler downward ventilation pattern at SS1. We will then trigger the state switch by operating the fan to assist the wind. This is unconventional in that it requires the fan to be able to blow flows (and thus add pressure) downward. But in this study we will just propose the principle and in reality, leaving the fan installation or switching device invention details to future studies. We now simplify the fan as a constant pressure fan that can provide a constant pressure head ΔP (in Pa).

As we discussed in the previous two sections, as far as the minimum perturbation magnitude is satisfied, the fan can trigger the system's state switch in a finite time. However, as the fan is an energy consuming equipment, there is an energy cost that is associated with it. Further, the magnitude and the required time of the perturbation are clearly two confliction sides: the larger the perturbation magnitude, the smaller the perturbation time; the energy consumption of the fan is defined as the integral of the product of the fan pressure head ΔP (in Pa) and the flow rate (in m^3/s). Therefore, it is possible that an optimal perturbation magnitude exists so that the total energy cost for the transition is minimized.

If we denote the energy consumption by W (in J), then it is defined by the following formula:

$$W = -\Delta P \int_0^{t_{\min}} \hat{q}(T) dT = -\Delta P \int_{T_{ss3}}^{T_{ss2}} \frac{\hat{q}(T)}{\hat{f}(T)} dT = \Delta P \int_{T_{ss2}}^{T_{ss3}} \frac{\hat{q}(T)}{\hat{f}(T)} dT, \quad (11.9)$$

where $\hat{q}(T)$ is the flow rate (see Equation (11.3)) for the system under perturbation.

Since the analytical form of the energy consumption includes an integral evaluation, an explicit formula to optimize the problem is not possible. However, we can use a parametric analysis shown in Figure 11-6 to demonstrate the energy consumption of a state switch through the fan vs. the pressure perturbation it provides.

It is clear that there is an optimal perturbation magnitude that makes the energy consumption for this state switch minimum ($\Delta P/P \approx 0.27$ in this sample case). With a perturbation magnitude smaller than this optimal value, the perturbation time required to trigger the switch is so long that the energy consumption increases. On the other hand, with a perturbation magnitude larger than this value, the flow provided by the fan is so large during the transition that the aggregated energy consumption is also higher.

11.9 Compare with conventional ventilation strategy

In order to evaluate the effectiveness of the state switch strategies we developed, a conventional fan-on model is compared with the state switch model in terms of the energy performance.

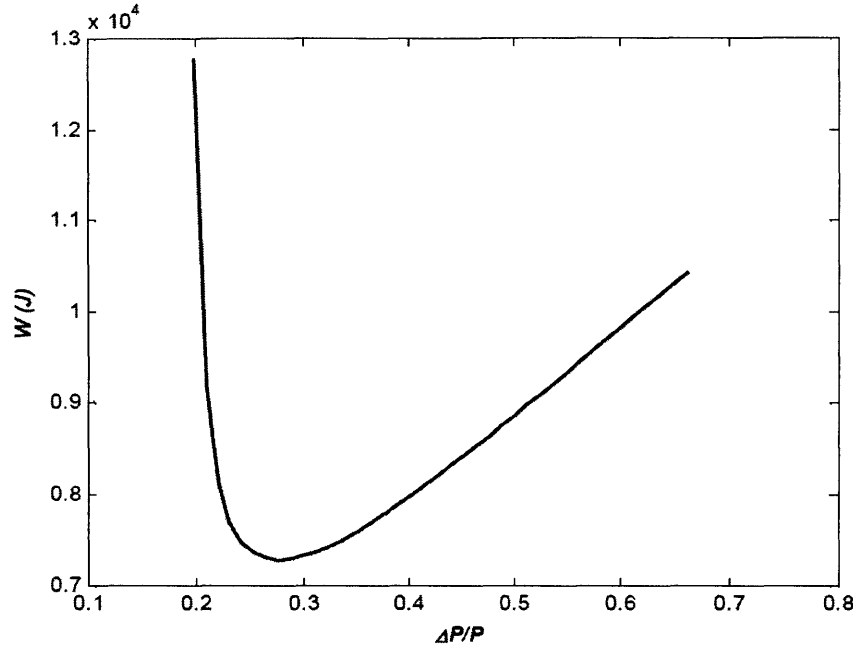


Figure 11-6: The Energy consumption for a state switch vs. the perturbation magnitudes

A conventional fan-on control model works this way: it only boosts buoyancy flows when the sensor identifies a situation of insufficient airflow (or high air temperature). Therefore, the system will turn on the fan to boost the airflow. To make it a fair comparison with the state switch strategy, we set the boosted airflow in the conventional fan-on strategy to the same level as the final switched airflow rate in the state switch strategy. With this setup, the two strategies will yield the same final zone temperature. The only difference between the two strategies is that in the conventional fan-on strategy, the final airflow direction will be upward. Further, by assuming no previous knowledge about the transition dynamics, it is clearly that to sustain the airflow in this condition the fan has to be on all the time during its operation (say 6 hours in a night operation mode). Now we need to compare the energy consumption performance of these two models.

In this conventional mode, we can neglect the energy consumptions of the system before it reaches steady states. Therefore, everything can be calculated in a steady state fashion and then multiplied by the time of the operation. The energy consumption for the conventional operation is thus:

$$W = P_{fan} q_{ss1} \Delta t. \quad (11.10)$$

The energy consumption does not rely on the perturbation pressure (essentially it does not have the concept of perturbation in this case). Therefore, we calculate the value and plot it again on Figure 11-7. For the same comparison basis, the energy consumption of the convention method is plotted as a horizontal dashed line:

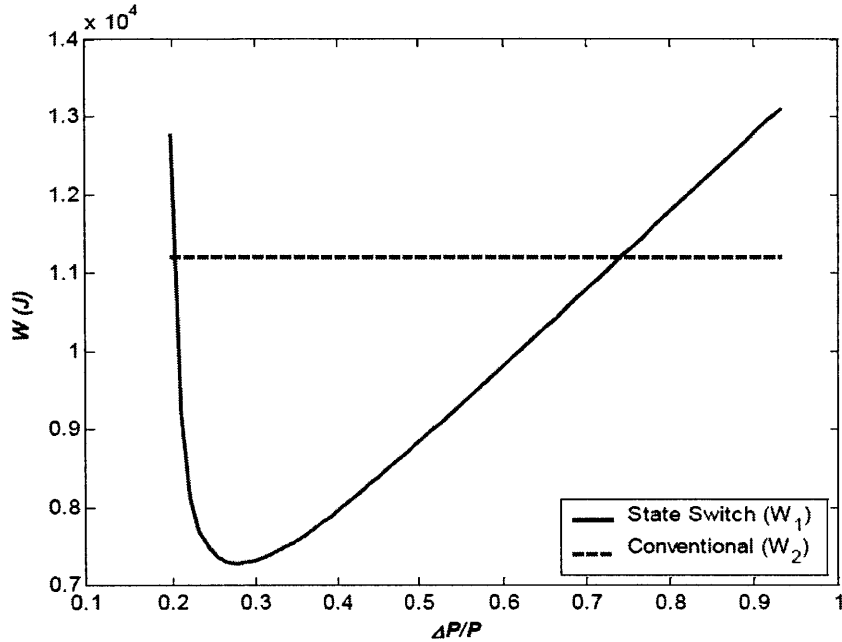


Figure 11-7: The comparison between energy consumption of a State Switch strategy and a conventional fan-on flow boosting strategy

From the retrofit aspect of using the state switch strategy, we can define a time called *Equivalent Fan-on Time*. The time is calculated not by assuming a constant 6 hours; rather, it equates W_1 and W_2 artificially and then computes what is the time need to turn-on the fan in the conventional fan-on strategy, so that the final outcomes of the two strategies are “equal”. Therefore the time is a linear scaled version of the curve shown in Figure 11-6 but in an easy-to-interpret manner. Figure 11-8 shows the calculated Equivalent Fan-on Time (in hours) vs. the pressure perturbation magnitude.

The Equivalent Fan-on Time assumes a constant operation condition. If the actual operation time in this mode is longer than this time, the state switch operation will be more energy efficient. However, if it is shorter than this time, a conventional strategy will be more efficient.

11.10 Model identifications and parameters estimations

This section discusses the model for the actual system to identify the multiple steady states. As was discussed in the previous sections, the system will have to satisfy two conditions to make the state switch meaningful. The most difficult one is to identify the multiple steady states through actual measurements in real building operations.

The mathematical model described in Equation (11.4) and (11.5) are easily feasible only if every boundary parameters involved are known. This is not too much a

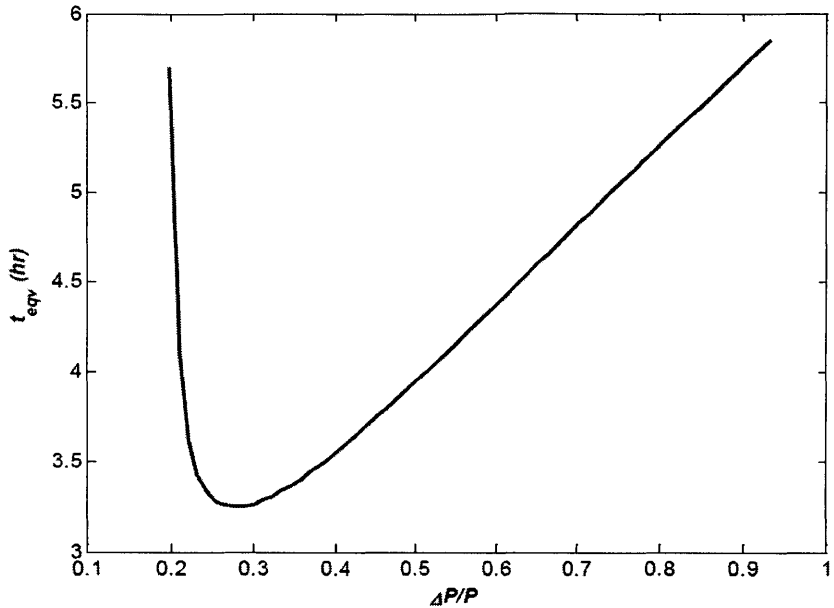


Figure 11-8: The Equivalent Fan-on Time vs. $\Delta P/P$ for a sample case

problem in design practice, where every parameter is assumed to be known. However, in actual building operation (not in design), not all the parameters can be obtained easily through sensors. For example, the effective opening area of the window (which will affect $\overline{C_d A}$) cannot be easily measured. The heat source strength E is also a variable that cannot be measured easily. The UA value is difficult to measure as well and needs to be estimated. Another parameter, the height difference h between the two openings, may also introduce some uncertainties if the building has multiple floors and the windows on different floors are open. The controller needs to know or estimate these parameters to make decision, usually by an inverse estimation algorithm.

In the following sections we first propose a way to estimate the different parameters by regression. Assume that we can obtain the following information at real time: the zonal temperature T , the outdoor air temperature T_e , the time derivative dT/dt of the zone temperature T , the wind velocity v_{ref} (namely the wind pressure ΔP), and the airflow rate q through the openings. Although it is arguable here that whether the flow rate q can be easily measured and monitored in an actual building, we currently assume that it is possible to obtain a rough airflow rate in a building with simple geometry, for example, by measuring the face velocity at the opening and correlating it to the flow rate. Other geometrical information such as the building size (volume V), and the height difference h between the upper and the lower openings, is almost fixed and does not change with time. We can set up the model by Equations (11.1) and (11.2), then regress on the unknown variables such as E , UA , and $\overline{C_d A}$. The values of E and UA can be obtained through Equation (11.1) and the value of $\overline{C_d A}$ can be obtained through Equation (11.2). Both of these two regressions will be linear, and easy to be carried out. To gain confidence in the estimated values, we can sample more data points to reduce the uncertainties.

With the estimated parameters, the identification model of the multiple steady states can be thus estimated by the two triggering criteria described in the previous sections.

11.11 Sensitivity studies

In this section we will revisit the sensitivity problems about the triggering criteria. When the sensor sampled a set of parameters, it estimates the parameters based on two regression models. Then it checks the two triggering criteria stated in previous section. Since the triggering criteria is dependent on the estimated parameters such as E , UA , and h , we will investigate how it dependent on these parameters.

First we will introduce a graph representation that will be used in the following sections. Figure 11-9 plots the relationship between the flow rate q (in m^3/s) and the temperature $T - T_e$. The points on the graph represent the buoyancy-dominated solutions (circles), the unstable solutions (stars), and the wind-dominated solutions (triangles) for a specific UA , h , and A value. The plot includes heat sources changing from 1000 W to 9000 W, and the wind velocities changing from 0 m/s to 5 m/s. This graph can be reviewed as the aggregations of Figure 11-3 for different E and v_{ref} values.

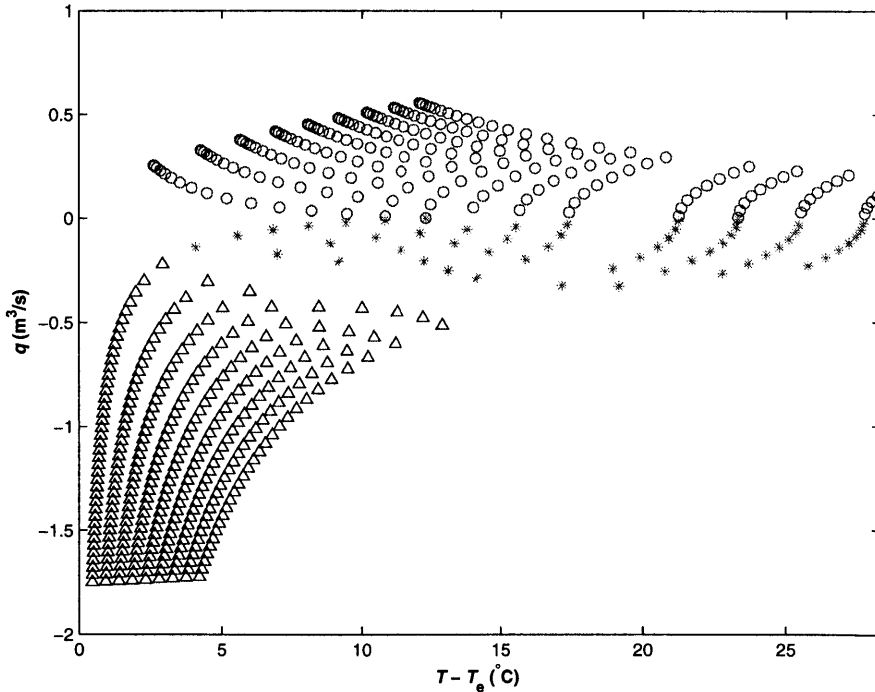


Figure 11-9: The steady state points for different heat source strength and wind velocity combinations ($UA = 80 \text{ W}/\text{°C}$, $h = 3 \text{ m}$, $A = 0.566 \text{ m}^2$)

We are interested in the steady states that are denoted by circles in Figure 11-9 in this study, since they represents the buoyancy-dominated upward ventilation patterns.

If we identified the final system state is within this region, we can exercise the state switch strategies. However, not every circle in the graph can find a corresponding triangles in the lower part. Figure 11-10 plots only the part that $q > 0$. The states that have a corresponding lower part solution are denoted by circles. The states that do not have the corresponding solutions are denoted by '*'s.

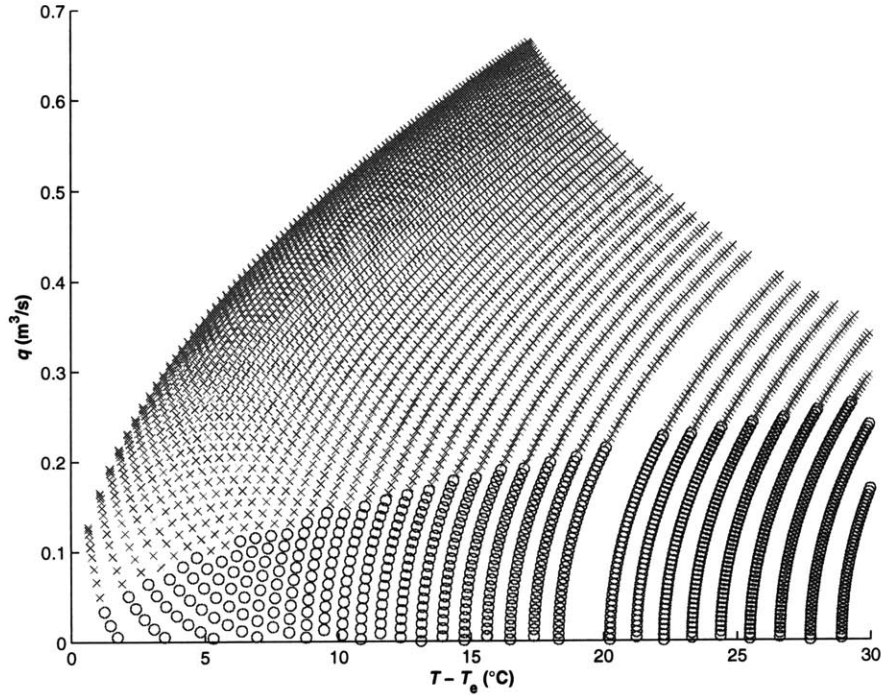


Figure 11-10: The steady states that have a corresponding lower temperature solution and the steady states that do not have one ($UA = 80 \text{ W/}^\circ\text{C}$, $h = 3 \text{ m}$, $A = 0.566 \text{ m}^2$)

Figure 11-10 is just one case for fixed opening area. In reality, the change in the opening areas can frequently occur, for example, when the occupants open the window manually. Therefore, how sensitive the identification results shown in Figure 11-10 to the opening area is of importance. Such sensitivity is presented in Figure 11-11, where the identification results for four different opening areas are reported. The figure shows that the opening areas are important to the model identification results. For example, compare the smallest opening area ($A = 0.283 \text{ m}^2$) and the largest opening area ($A = 1.13 \text{ m}^2$), it is obvious that the larger opening areas represent more occurrences for the states that have a corresponding lower ventilation pattern. The physical explanation is that when the openings are larger, the wind forces are easier to dominate. Therefore the chances to apply the state switch strategies increase when a warmer state is identified.

Further studies are conducted on the sensitivities of the identification results on the UA value, which needs an estimation based on regressions as was discussed in the previous section. The four different sets of plots in Figure 11-12 show the change of the identification results for four different UA values (0, 60, 120, and 180 $\text{W}/^\circ\text{C}$).

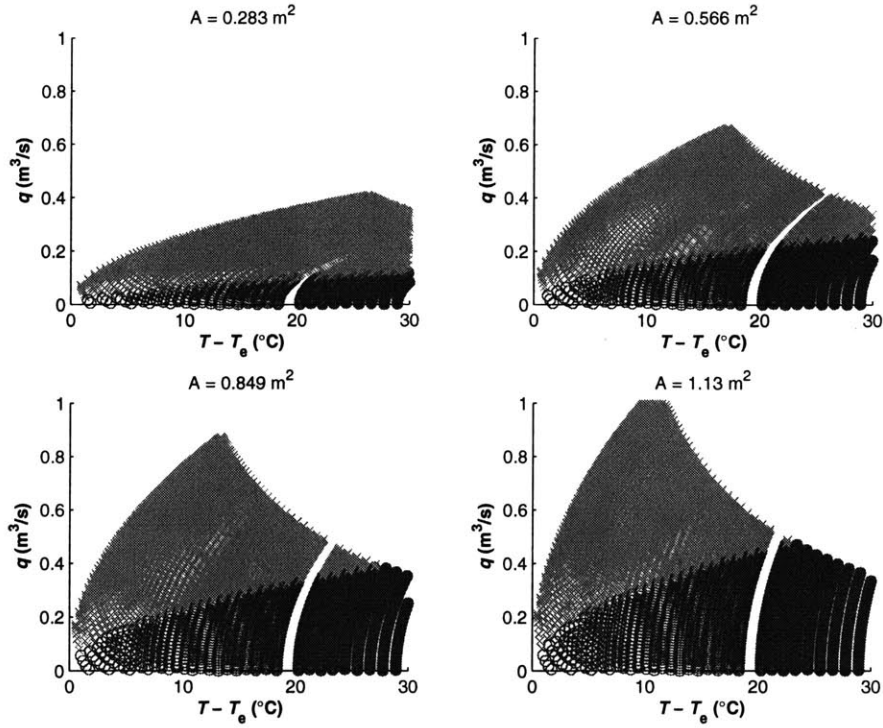


Figure 11-11: Identification results for four different opening areas ($UA = 80 \text{ W}/\text{°C}$, $h = 3 \text{ m}$)

For different UA values, the identification results do change, but not too much. The major difference in the identification results for smaller UA values (e.g., $UA = 0$ in Figure 11-12(a)) and for larger UA values (e.g., $UA = 180 \text{ W}/\text{°C}$ in Figure 11-12(d)) is mainly in the area of low temperatures (i.e. $T - T_e \rightarrow 0$). The identification result does not change too much for moderate and high temperatures (which the state switch strategies are more needed). Therefore, the UA value is not a sensitive factor in our model identification. We can tolerate a slightly larger error in the regression models we developed in the previous section.

The last parameter we care about is the height difference h between the two openings. In real operations, the occupants can open or close the windows at different levels of a building. An even simpler example is a window on the same floor but has a lower part and an upper part. Opening of the upper part or opening the lower part will have different impact which can be fuzzily reflected in the h value. More complicated physics can happen if the upper and lower parts are both open. A detailed model (e.g., [66]) needs to be developed to investigate that kind of impact if this kind of window operations are of major concerns.

Here we will just illustrate the impact of the h values and see its impact on the identification results. Figures 11-13(a) to 11-13(d) shows the results for h varies from 1.5m to 6m. Since the UA value is not an important factor in the results, we just selected a value of $UA = 80 \text{ W}/\text{°C}$ for this study.

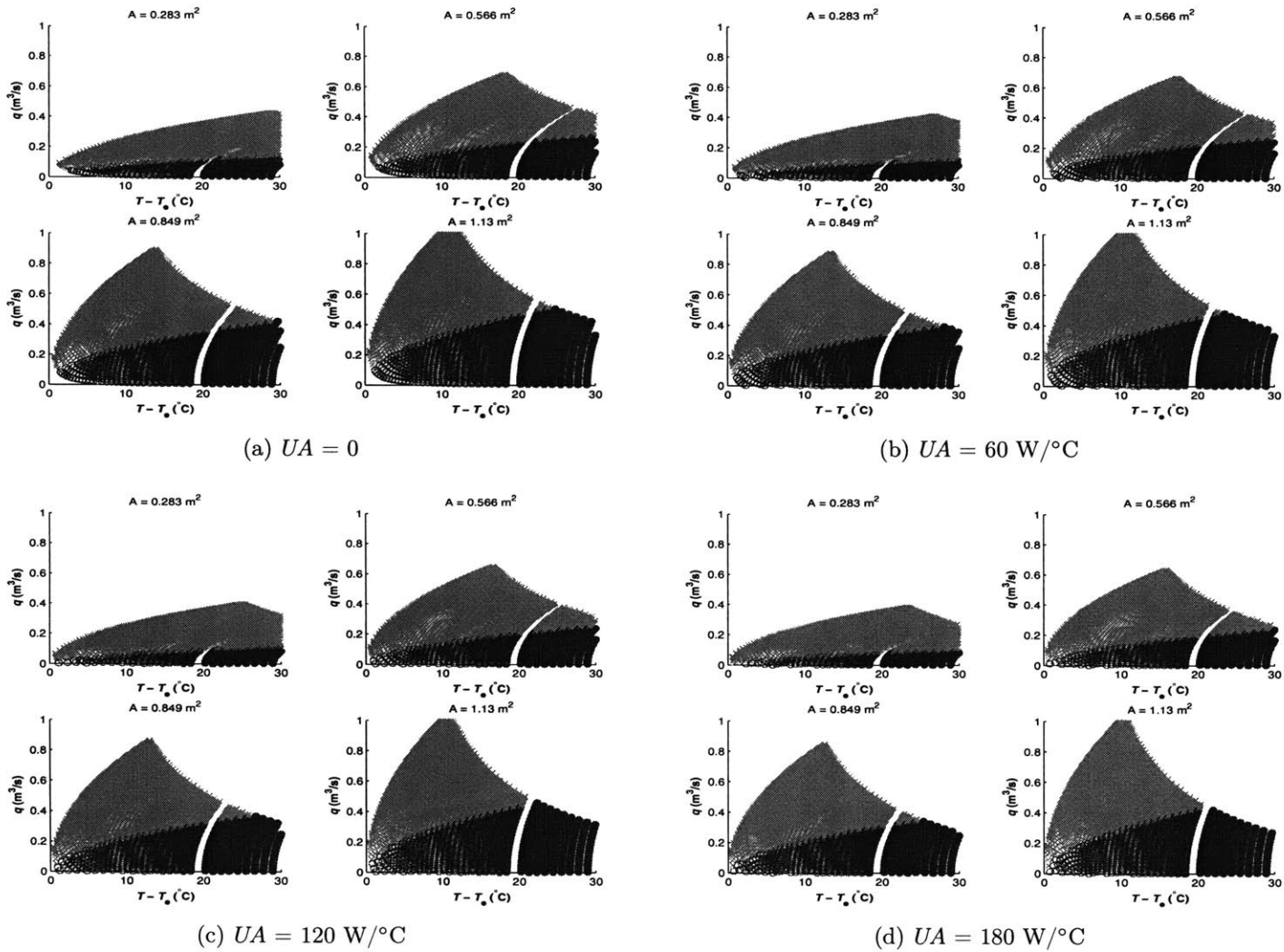


Figure 11-12: Identification results for four different UA values ($h = 3 \text{ m}$)

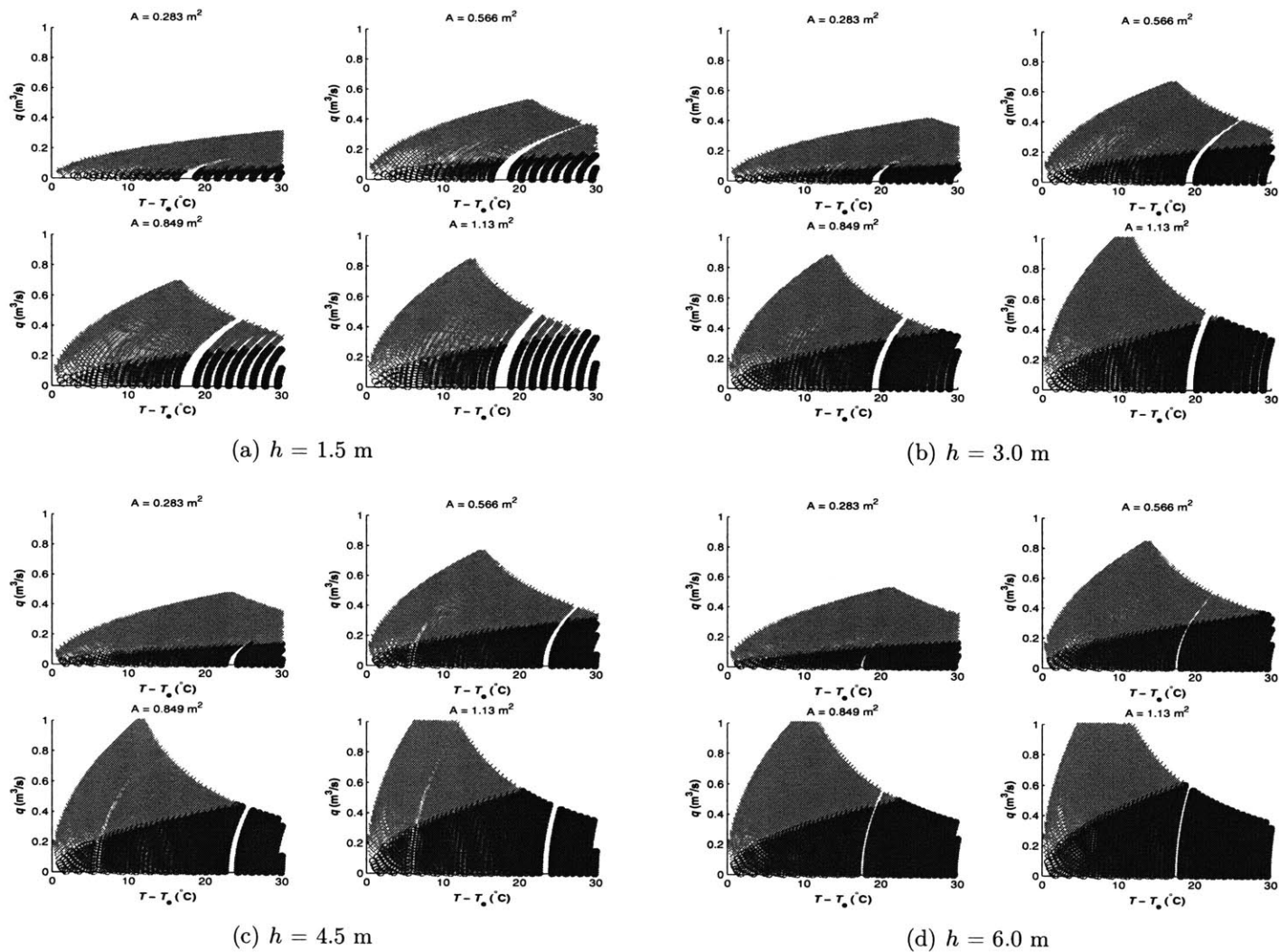


Figure 11-13: The model identification results for four different h values ($UA = 80 \text{ W}/\text{°C}$)

The identification results show significant differences for different h values, which means h is an important factor that can affect the model identifications. Physically it is explained by the direct relation between h and the major driven force - the buoyancy force. In real time building operation, if h value changes for some reason, the identification model should be able to recognize it and adjust the identification criterion accordingly.

11.12 Model implementation

The theoretical studies in the previous sections enable us to implement a state transition strategy in a building with similar geometry. Using the principles we developed in the previous sections, in this section we will embed a control strategy in the real operation of a building and simulate the response of the building flows and temperatures. Further, in real implementation, there are some practical issues needs to be considered. For example, one of the difficulties is the problem in the parameter estimation. The regression analysis using Equations (11.1) and (11.2) to find the related parameters is difficult to obtain accurate (even reasonable) results in actual buildings. Alternative ways are needed to overcome such difficulties.

We select a two-zone building shown in Figure 11-14 as the hypothetical objective of the implementation study. The building can also be viewed as a single-zone building that is divided into an upper part and a lower part, each part has a size of $10\text{m} \times 10\text{m} \times 3\text{m}$ ($L \times W \times H$). We assume that each zone has an equal amount of heat source at the level of 20 W/m^2 . Natural ventilated flow can go either upward or downward depending on the strength of buoyancy and wind forces and the flow and temperature histories (initial values) in the building. Other parameters such as outdoor air temperatures, the wind directions and speeds, are obtained from an hourly weather file for ~ 6.5 days¹. For simplicity, we normalized the wind speed to normal direction of the upper window according to the angle between the wind and the normal direction of window; and we did not assume any thermal mass in this building.

We measure several parameters in real-time for the controller: the exterior wind velocity, the flow direction within the building, and the temperature of the two zones. The controller follows a control logic like this: if the airflow is downward wind-dominated, the controller will idle; if the airflow is upward, the controller will judge based on a criterion whether there are possibility for state transitions. The judgment of the controller is based on the measured parameters. If the controller decided that the criterion is satisfied to make the transition, the fan will be turned on for a short period of time to cool down the building.

¹The weather file is obtained from National Renewable Energy Lab (NREL) website.

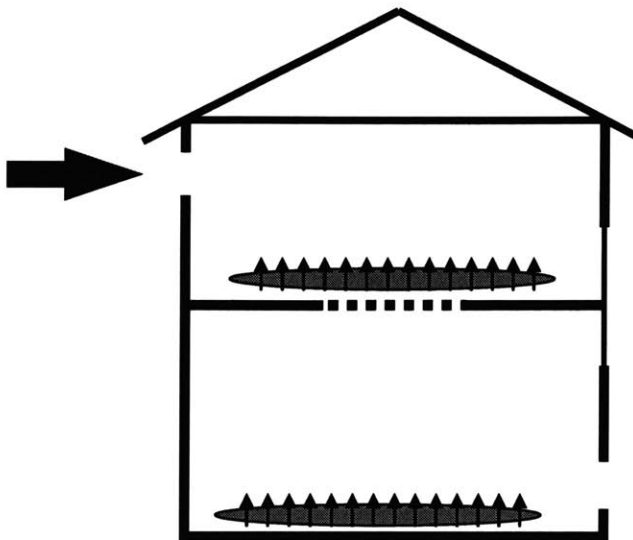


Figure 11-14: A two-zone building for implementing and testing the control strategy

11.13 Preliminary results

A successful transition will switch the airflow pattern and bring down the internal air temperature, after the transition is completed. However, an unsuccessful transition will temporarily switch the airflow pattern, but switch the airflow pattern back to the original state again after a while. This process is shown in Figure 11-15. The thin solid line indicates the average zone temperature in the building with the state transition controller actions. The thicker dashed line is for comparison, which indicates the averaged zone temperature in the building without any control actions. The thin dash-dotted line indicates the outdoor air temperatures.

The transition actions can be identified by the sudden temperature drops in the zone temperature plot in Figure 11-15. There are successful transitions and unsuccessful ones: for example, in Figure 11-15, two typical successful transitions are marked by “Success”, while two typical failed transitions are marked by “Failure”. For a successful transition, the flow pattern switch can be maintained for a relative long period of time (e.g., 1–3 hours). However, for a failed transition, the flow pattern switch will usually last less than half an hour. After that, the flow pattern will reverse back to the buoyancy-dominated pattern again and the controller will trigger new transitions again and again if the model parameters are not updated from the feedback.

11.14 Learning and self-tuning

The judge criterion can be updated upon the historical outcomes of the controller action. The model updates can be done during the training (commissioning) period or on-the-fly during operation. In either way, the controller will start with an initial set of model parameters assumed and using the outcomes of the existing result as feedback. An optimization process will be process by choosing the optimal parameters from the historical results for the model. Here we consider the optimization process as a

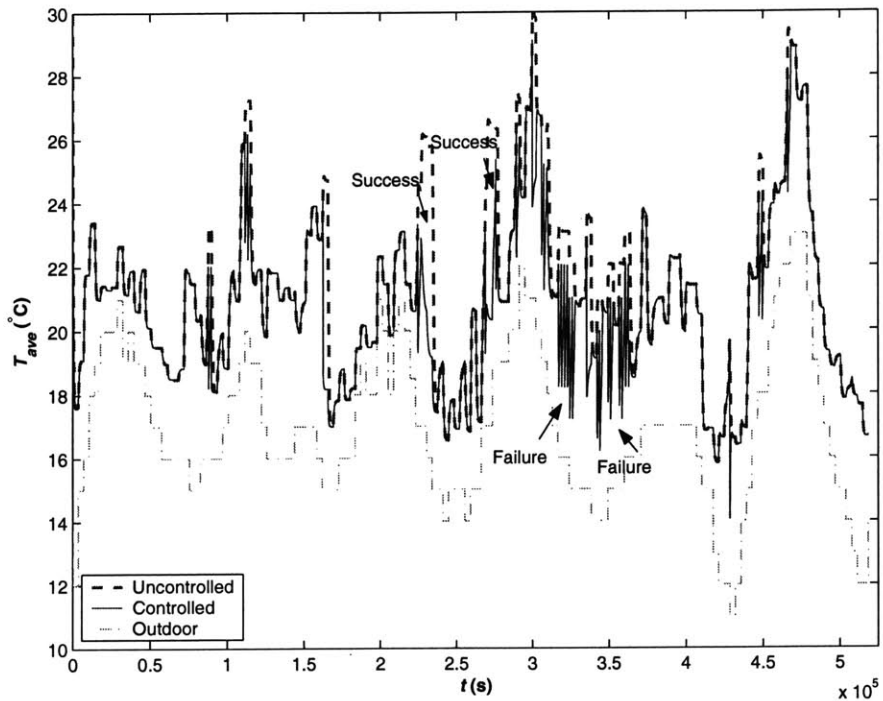


Figure 11-15: Test results on a two-zone building

classification problem which classifies the switchable conditions and the unswitchable conditions.

In the two-zone example demonstrate in Figure 11-14, we can provide a simple rule to judge whether the wind is strong enough to enable the transition from a buoyancy-dominated steady state to the wind-dominated steady state. The rule is learned from the historical transitions in Figure 11-15. Figure 11-16 shows the outcome of classification result in an updated model. The successful transitions can be distinguished from the unsuccessful ones with the updated model². It is expected that after some learning process, the model can be well-tuned and the new judgment rules will yield more accurate classification results on switchable and unswitchable conditions on the incoming judgments.

11.15 Conclusions

In this paper a novel control strategy based on the state transition dynamics between the multiple steady states were discussed. The strategy can be used in natural or hybrid ventilation systems to reach a desirable state with minimal energy cost.

The theoretical fundamentals for the control strategy were provided. The triggering criterion, the stop criterion, and the potential energy benefit are discussed in

²In this study, the updated model is not tested on a new data set for its accuracy due the time constraint. The test of accuracy of the model will be provided in a future study.

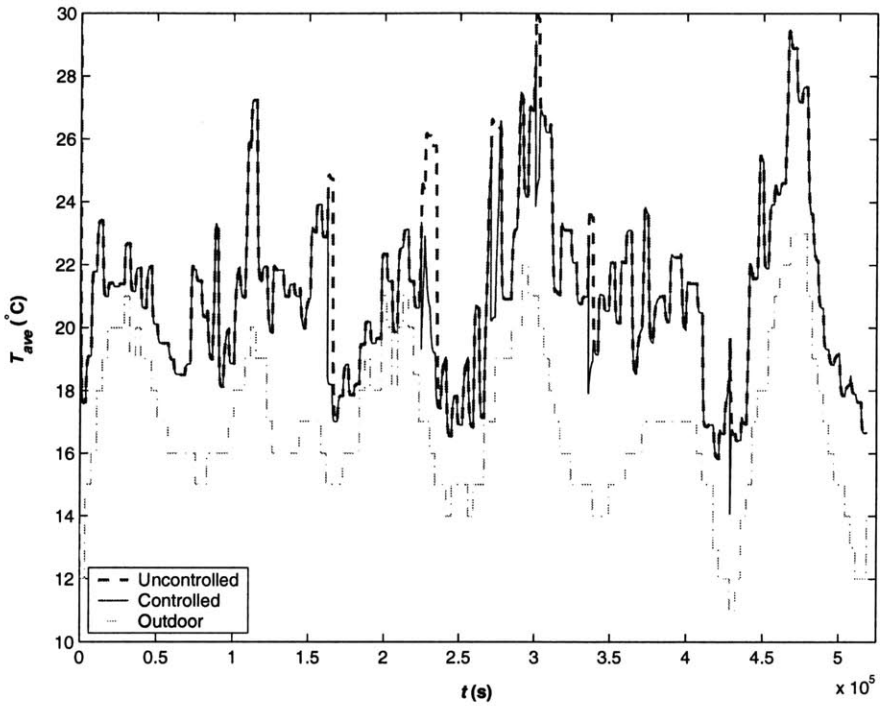


Figure 11-16: Updated model and training results

detail. The state transition dynamics plays a key role in these related issues. The model identifications will be discussed in details in future studies.

In the implementation of the state transition, there is an optimal perturbation magnitude that can minimize the energy cost of the transition. The optimal cost can also be obtained with a mathematical model and a grid-search method.

The sensitivities of the identification models were tested for different parameters such as the opening areas, the UA values, and opening height differences. The opening areas and the opening height difference were found to have significant impact on the identification results. However, the identification results were not so sensitive to the UA values.

The state transition controller was implemented in a two-zone building that enables both buoyancy-dominated and wind-dominated flows. The results showed that a correct transition from the buoyancy-dominated flow to the wind-dominated flow is possible during real-time operations. The model learning and updating procedures were also discussed and a simple example result was demonstrated. The result showed that through proper learning and tuning processes, the parameters of the controller can be trained to enhance the successful rate of the identification.

Nomenclature

A = Effective opening area of the opening m^2	in Pa
c_{pa} = (constant pressure) specific heat of the air in $\text{J/kg}\cdot\text{K}$	P_w = wind pressure difference between the inlet and outlet in Pa
$\overline{C_d A}$ = effective product of the discharge coefficient and the opening area in m^2	P^{**} = non-dimensional wind pressure dif- ference between the inlet and the outlet
C_{pl} = Wind Pressure Coefficient (WPC) for the lower openings	q = volumetric air flow rate in m^3/s
C_{pu} = Wind Pressure Coefficient (WPC) for the upper openings	t = time in s
E = heat gain of the space in W	T_e = outdoor temperature in $^\circ\text{C}$
g = gravitational acceleration in m/s^2	UA = total conductance of the building enclosure system in W/K
H = height difference between the upper and the lower openings in m	V = volume of the space (air) in m^3
M = mass of the space air in kg, which equals to $\rho_a V$	v_{ref} = reference wind velocity in m/s for Wind Pressure Coefficients
P_l = wind pressure at the upper opening in Pa	β = thermal expansion coefficient of the air in K^{-1}
P_u = wind pressure at the upper opening	ρ_a = density of air in kg/m^3

Greek

	β = thermal expansion coefficient of the air in K^{-1}
	ρ_a = density of air in kg/m^3

Chapter 12

Conclusions and recommendations

The issues addressed in this thesis can be logically divided into four parts: coupled airflow simulation, dynamical system analysis of multiple-steady-state behaviors, transition dynamics between multiple steady states, and applications of multiple steady states. In this chapter, we will summarize the major points in all these parts and chapters; and make recommendations for possible future work.

12.1 Conclusions

In this section, the major conclusions in the thesis chapters will be presented.

12.1.1 Coupled airflow simulation

In Chapter 2 we presented a newly developed transient simulation program that couples transient airflow, temperature, and thermal mass solutions in entire buildings. The mathematical fundamentals, framework of coupling, numerical improvement strategies were discussed in detail. Major contributions include: the development of transient dynamics solution procedures; airflow, temperatures, and thermal mass integrations; newly implemented simple windows control strategies options; and major enhancement in numerical performance. The program can be conveniently used to simulate building airflows and temperatures, especially in natural ventilated buildings, with reliable numerical performance. The program introduced in the section is referred as the *CoolVent core* thereafter.

In order to facilitate the use of the program, a graphical user interface was also developed along with the CoolVent core program. As was introduced in Appendix A, the interface program allows a less technically sophisticated user to quickly simulate different types of natural ventilated buildings, and to conveniently compare different conceptual designs.

In Chapter 3, we validated the program in-depth by three different data sources: CONTAMW for steady state airflows, CFD for steady state airflow and temperatures, and field monitoring data for transient air-thermal-mass solutions. Although discrepancies exist between the CoolVent results and the validation source, the overall

results predicted CoolVent was reasonable close to all the three validation sources. The coupled program results have general good agreement with the validation sources in airflow and temperature predictions. A major discrepancy existed in a zone that has the strongest internal stratifications. However, we tend to believe that this discrepancy is not a specific pitfall of CoolVent program implementation. Rather, it is a general drawback of nearly all multi-zone type models, which usually assume well-mixed zones and uniform zone temperatures.

In the transient validations, we have developed a sub-module to account for the internal radiation simulation. The successful integration of the sub-module demonstrates that the flexibility in the program implementation allows future development and modification.

12.1.2 Dynamical system analysis of multiple steady state phenomena

In Chapter 4, we discussed the important issue of dynamical system analysis of the multiple steady state phenomena in a single-zone building. In a simple system that has three steady states—two stable and the other unstable, the unstable steady state is important to determine the final steady state of the system. It serves as a critical point for the initial values in determining the final state of the system: if the system starts from an initial temperature higher than this critical point, it will finally reach a buoyancy-dominated steady state; otherwise, if the system starts from an initial temperature lower than this critical point, it will finally reach a wind-dominated steady state.

In Chapters 5 and 6, we investigated the dynamical system behaviors of a single-zone natural ventilation system with thermal mass. In Chapter 5, we focused mainly on the fundamentals of the general dynamical system characteristics of the air-mass system. The existence of thermal mass does not affect several aspects of the air-mass system, compared with a similar system without thermal mass. For example, the steady state temperature values do not change; the conditions for multiple steady states to exist do not change; and the bifurcation process does not change as well. A further mathematical analysis linked the system with thermal mass and a system without thermal mass. The analysis proved that the qualitative stability characteristics—the signs of the eigenvalues—do not change with existence of thermal mass.

However, the time-dependent system features (i.e., the transient behaviors of the system) can indeed be affected by the thermal mass parameters. Chapter 6 focused on the transient behaviors of the air-mass system, and how the thermal mass parameters influence these transient behaviors. A linear approximation of the system around the steady states explained the different responses of the air and the thermal mass upon a step change. In a linear approximation, the two eigenvectors of the air-mass system represent two evolving directions of the system along time; and the temperature trajectories are governed by the summation of the change on the two eigendirections. In a typical air-mass system where the heat capacity of the thermal

mass is much higher than that of the air, the eigendirection that corresponds to the larger eigenvalue (in absolute magnitude) governs the initial change of the system. Conventionally, this eigendirection is called *fast eigendirection* and usually represents a fast air temperature change towards the steady states in the initial stage. The eigendirection that corresponds to a smaller eigenvalue (in absolute magnitude as well) governs the mutual change of air and thermal mass temperatures, which usually takes a longer time to accomplish than the initial stage. This eigendirection is thus called the *slow eigendirection* of the air-mass system. One important application of the eigendirections is in accurately computing the shape of the separatrices of the air-mass system on the phase plane when multiple steady states exist. By initializing the system at the unstable steady state along an eigenvector direction in a reversed time domain, the shape of the separatrices can be accurately captured on the phase plot.

The linear approximations can be affected by the nonlinearity of the system, especially the multiple steady states. Even in cases where the system can have only one steady state, the transient behaviors (and the linear approximates) can be affected by a “remnant” effect of a saddle-node bifurcation process. One example is the “bottleneck” effect caused by the remnant effect of the destroyed fixed points (or a “ghost” steady state) during a saddle-node bifurcation. Some of the trajectories of the system will be significantly affected by the nonlinearity of the system (which has just moved out of the multiple-steady-state region). In the time domain, the “bottleneck” effect may cause significant time delay in a system to reach a steady state, when the trajectories have to reach close to the “ghost” steady state to pass the “bottleneck”.

The thermal mass parameters were found to have significant impacts on the transient dynamics features of the system. We investigated the impact of the air-mass interaction strength (which is represented by hA_m) and the impact of the mass weight (which is represented by M_mc_m). In linear approximations, both the eigenvalues and the eigenvectors will change when the thermal mass parameters change. With a very strong air-mass interaction strength (i.e., large hA_m value), the air and the mass show a pattern of fast reaching a common temperature and then evolves together. With a weak air-mass interaction, the air temperature will change in a quicker pace than the mass temperature. Different thermal mass weight will also cause the dynamics feature change. A heavier thermal mass will tend to cause the thermal mass temperature response time to become much longer.

A direct impact of the time-characteristics change with thermal mass parameters is the change of shapes of the separatrices on the phase plane when multiple steady states exist. With larger hA_m values, separatrices become flatter. For the extreme case of $hA_m \rightarrow \infty$, the separatrices will approach towards a straight line whose slope is determined by the ratio of air-mass thermal capacities. With larger M_mc_m values, the separatrices will also become flatter, mainly on the two wings.

12.1.3 Transition dynamics between the multiple steady states

In Chapter 7, we presented an important issue—the transition dynamics between the multiple steady states in ventilation systems. From Chapter 4, we have known

that a single-zone natural ventilation system with opposing wind and buoyancy forces may have two locally stable steady states, which are capable of surviving small (or infinitesimal) perturbations. However, the system can still transit from one steady state to another—under sufficient “strong” perturbation. We defined “strong” perturbations as boundary condition disturbances that have significant magnitude and durations.

Under a strong perturbation, the system curve may change, which will lead to different outcomes depending on whether the perturbation can perturb the system to another steady state or not. The transition dynamics provided new information to explain several previous studies. One of them is the experiment conducted by Linden [44], where the airflow pattern of an opposing wind-buoyancy system were found to be dependent on how the wind force had been applied.

Further, the transition dynamics were found to be a stability indicator to identify the stability (and existence) of the mathematically (local) stability of a stable steady state in an actual system. The result was applied to explain another experiment results observed by Heiselberg et al. [35], where some theoretically stable solutions were found unstable and unobservable in both CFD and scaled experiments.

In Chapter 8, we investigated the impact of thermal mass on the state transition dynamics between the multiple steady states. Compared to the state transitions in a single-zone system without thermal mass in Chapter 7, in a system with thermal mass, the state transition behavior is more complicated. The thermal mass was found to have significant impact on the minimum transition time for the system to transit from one (stable) steady state to another. It is very possible that, if the perturbation does not last long enough, the system will turn to its original state when the perturbation is removed. This means the thermal mass will serve as an impedance of the state transition between two stable steady states by requiring much longer perturbation time, compare to a system without thermal mass. The stability of a steady state, therefore, will be improved, against possible disturbances in the boundary conditions.

12.1.4 Applications of multiple steady states

In Chapter 9, we investigated the multiple steady state phenomena of a building with two zones. The major purpose of this study is to investigate how possibly the multiple steady state behaviors can be used in natural ventilation designs. First, we investigated the underlying dynamics features of the system and presented a new eigen characteristic of the system that is different from the air-mass system investigated in Chapter 5. The eigenvalues of the system are not real numbers. Rather, they are complex numbers with imaginary parts. This eigen characteristic usually represents an oscillating pattern (usually with a decreasing magnitude if a steady state is stable) in the state variable in converging to a steady states. There is a critical point of initial temperatures that is independent of the heat source strength. The results were found to be useful in guiding the chimney and wind scoop designs by achieving a desirable steady state.

In Chapter 10, we investigated the multiple steady state behaviors in complex geometries with multiple zones, by the aid of a coupled airflow and thermal program. A

general numerical framework is proposed to solve such a problem. In this framework, the thermal mass does not need to be considered for identifying the steady states. Further, three different computational search methods—grid search, coarsest grid search, and random search—were discussed. Two example buildings were provided to demonstrate the existence of multiple steady states in a complex building with seven zones. In one building, three stable steady states were found; and in another building, four possible steady states were found. Mathematically, all these solutions are stable. However, there are practical limitations on whether such a system can be stable or not. An analysis on the model assumptions was provided to discern the practicability of the steady states obtained.

The most important finding in this chapter is that we developed a convenient test method to quantitatively test the stabilities of the obtained steady states. In Chapter 7 we have shown how a locally stable steady state that is not robust enough may transform to another steady state under sufficient “strong” perturbation. Based on these state transition dynamics, we developed the convenient stability check method by introducing stochastic perturbation components to the boundary conditions. If a steady state is not robust enough, the system may undergo a state transition from this steady state to another.

In Chapter 11, we investigated an application of the state transition dynamics in ventilation controls. Among the multiple steady states a system can have, one steady state may be more desirable than the other. A control strategy can be developed in a real-time controller to actively transit the system from an undesirable state to a desirable one, or in other words, maintain a desirable state in real time. Optimal operation strategies were developed based on a model-based learning process to maximize ventilation effectiveness and energy efficiency. The state transition strategy was found to be potentially more energy efficient than a conventional ventilation strategy. As a preliminary study, we also provided the general framework of such a control strategy and several sensitivity studies on the system.

12.2 Recommendations

In this section, we will make recommendations for future research.

12.2.1 Coupled program

For the coupled program, we currently have not included a precise load estimation module, especially for the solar gain. Future studies can be carried out to implement part of load estimation features, especially for solar loads.

A higher level of load estimation is to couple CoolVent with an energy simulation program, where load estimation, airflow solution, temperature solution, and thermal mass solution are coupled together. A possible coupling is to couple the CoolVent program and the MIT design advisor [33] together.

As we stated in the validation study of Chapter 3, the internal stratification is one of the major factors that could affect the buoyancy forces and the predicted flow rates.

However, in the current version of CoolVent program, we did not provide a mathematical internal stratification model. Rather, to model the internal stratification, the current program can only use the general practice of artificially dividing a physical zone (e.g., a room) into different sub-zones in the multi-zone model, which is not that convenient for quick building configurations and simulations. It is recommended to incorporate a mathematical model that can describe the internal stratifications, for example, a model for a plume.

In the current study, although an internal radiation model was implemented for the specific building in the research version for the validation purpose (see Chapter 3), we did not incorporate the internal radiation models in the general CoolVent version. The internal radiation model is recommended to be incorporated into the CoolVent program.

For the CoolVent interface program, it is recommended to incorporate more building prototypes. In the current version, four different prototypes are included. With incorporation of more prototypes, the designer will have more flexibility to match the prototype with their actual designs in natural ventilation simulations. Ideally, an interface that can handle arbitrary building geometries is preferred.

12.2.2 Multiple steady state phenomena

For the multiple steady state phenomena, there are several directions the research can go. One direction is on the fluid mechanics side. The actual airflow dynamics are more complex than the representation of usual multi-zone model. Even turbulence models for CFD do not explain the full underlying nature of the micro-scale fluid motion patterns. The solution multiplicity is believed to be closely related to the micro-scale fluid motions. This direction is more theoretically oriented on the micro-scale fluid dynamics modeling.

In this thesis, we did not assume the buoyancy stratification in a single zone in multi-zone model. Instead, we considered the non-uniformity of the internal space by dividing a physical space into several zones in multi-zone models (e.g., the atrium in Chapter 10). However, a detailed internal plume model was not incorporated. We did not consider a theoretical plume models because most of the internal plume models are based on point sources, which could represent some of the true conditions but not necessarily the general situations. An incorporation of such a model or other models is recommended as a future study of the current thesis.

Another possible direction for future research is discovering of more nonlinear dynamic behaviors in building ventilation systems, which may be in both macroscopic (entire building) level and microscopic (single-zone) level. For example, it is still unclear whether chaos¹ could occur in the building airflow. As a typical characteristic of a chaotic system, the output (including the final steady state) of the system can be extremely sensitive to the initial conditions. Whether such extreme dependencies on the initial values exist in building airflows is still unknown to researchers.

¹I thank Dr. Yuguo Li at Hongkong University and Dr. James Axley at Yale University for a short email discussion on this topic.

Finally, the application of state transition can be further investigated with thermal mass consideration. In this study, we have provided a state space thermal mass model for the air-mass system, and the transition dynamics between the multiple steady states in such a system. Further applications of state transitions in a system with thermal mass are recommended as future research.

Bibliography

- [1] Allard, F. (1998). *Natural ventilation in buildings: a design handbook*. James & James (Science Publishers), London, UK.
- [2] Arens, A., Glicksman, L. R., and Chen, Q. (2000). Evaluation of displacement ventilation for high-ceiling areas. In *Proceedings of Roomvent*.
- [3] Aris, R. (1965). *Introduction to the Analysis of Chemical Reactors*. Prentice-Hall, Inc., Englewood Cliffs, NJ.
- [4] Armstrong, P. R., Leeb, S. B., and Norford, L. K. (2006a). Control with building mass—Part I: Thermal response model. *ASHRAE Transactions*, 112(1):449–461.
- [5] Armstrong, P. R., Leeb, S. B., and Norford, L. K. (2006b). Control with building mass—Part II: Simulation. *ASHRAE Transactions*, 112(1):462–473.
- [6] ASHRAE (2001). *ASHRAE Handbook—Fundamentals*. American Society of Heating, Refrigeration, and Air-conditioning Engineers, Atlanta, Georgia.
- [7] ASHRAE (2004). *ASHRAE Standard 62.1-2004—Ventilation for Acceptable Indoor Air Quality*. the American Society of Heating, Refrigerating and Air-Conditioning Engineers, Atlanta, Georgia.
- [8] Axley, J. W. (2000). Zonal models using loop equations and surface drag cell-to-cell flow relations. In *Proceedings of Roomvent*, pages 235–240.
- [9] Axley, J. W. (2001). Application of natural ventilation for u.s. commercial buildings: Climate suitability design strategies and methods modeling studies. Technical Report GCR 01-820, National Institute of Standard and Technology.
- [10] Axley, J. W. (2006). *Building Ventilation: the state of the art*, chapter 2: Analytical Methods and Computing Tools for Ventilation. Earthscan, UK and USA.
- [11] Axley, J. W., Emmerich, S., Dols, S., and Walton, G. N. (2002). An approach to the design of natural and hybrid ventilation system for cooling buildings. In *Proceedings of Indoor Air*.
- [12] Beausoleil-Morrison, I. (2000). *The Adaptive Coupling of Heat and Air Flow Modeling Within Dynamic Whole-Building Simulation*. PhD thesis, University of Strathclyde, Glasgow, UK.

- [13] Braun, J. E. (1990). Reducing energy costs and peak electric demand through optimal control of building thermal storage. *ASHRAE Transactions*, 96(2).
- [14] Braun, J. E. and Lee, K. H. (2006). Assessment of demand-limiting using building thermal mass in small commercial buildings. *ASHRAE Transactions*, 112(1).
- [15] Braun, J. E., Montgomery, K. W., and Chaturvedi, N. (2001). Evaluating the performance of building thermal mass control strategies. *HVAC&R Research*, 7(4):403–428.
- [16] Ceylan, H. T. and Myers, G. E. (1980). Long-time solutions to heat conduction transients with time-dependent inputs. *ASME Journal of Heat Transfer*, 102(1):115–120.
- [17] CHAM (2001). *Phoenics-VR3.4 Reference Guide*. Concentration Heat And Momentum (CHAM) Limited, London, UK.
- [18] CHAM (2002). *Documentation for PHOENICS (Version 3.5.1)*. Concentration Heat And Momentum (CHAM) Limited, London, UK.
- [19] Chen, Q. (1995). Comparison of different k- ϵ models for indoor air flow computations. *Numerical Heat Transfer, Part B*, 28:353–369.
- [20] Chen, Q. and Chao, N.-T. (1997). Comparing turbulence models for buoyant plume and displacement ventilation simulation. *Indoor and Built Environment*, 6(3):140–149.
- [21] Chen, Q. and Jiang, Z. (1992). Significant questions in predicting room air motion. *ASHRAE Transactions*, 98(1):929–939.
- [22] Chenvidyakarn, T. and Woods, A. W. (2004). Multiple steady states in stack ventilation. *Building and Environment*, 40(3):399–410.
- [23] Dols, S. W. and Walton, G. N. (2002). *CONTAMW2.0 User Manual*. National Institute of Standard and Technology. NISTIR 6921.
- [24] Dols, S. W., Walton, G. N., and Denton, K. R. (2000). *CONTAMW 1.0 User Manual*. National Institute of Standard and Technology. NISTIR 6476.
- [25] Duffie, J. A. and Beckman, W. A. (1991). *Solar engineering of thermal processes*. John Wiley & Sons Inc., New York, NY.
- [26] EnergyPlus™(2002). *EnergyPlus Engineering Reference: The Reference to EnergyPlus Calculations*. Department of Energy, USA.
- [27] ESRU (2002). The ESP-r system for building energy simulation—User Guide Version 10 Series. Technical report, University of Strathclyde, Energy Systems Research Unit(ESRU).

- [28] Etheridge, D. and Sandberg, M. (1996). *Building ventilation: Theory and measurement*. John Wiley & Sons Inc., New York.
- [29] Feustel, H. E. (1998). COMIS – An international multizone air-flow and contaminant transport model. Technical Report 42182, LBNL.
- [30] Feustel, H. E. and Dieris, J. (1992). A survey of air flow models for multizone structures. *Energy and Buildings*, 18:79–100.
- [31] Fisk, W. (2000). Health and productivity gains from better indoor environments and their relationship with building energy efficiency. *Annual Review of Energy Environment*, 25:537–566.
- [32] Gladstone, C. and Woods, A. W. (2001). On buoyancy-driven natural ventilation of a room with a heated floor. *Journal of Fluid Mechanics*, 441:293–314.
- [33] Glicksman, L. R., Jim, G., and Matthew, L. (2005). MIT design advisor website. <http://designadvisor.mit.edu>.
- [34] Grosso, M. (1992). Wind pressure distribution around buildings: a parametrical model. *Energy and Buildings*, 18(2):101–131.
- [35] Heiselberg, P., Li, Y., Andersen, A., Bjerre, M., and Chen, Z. (2004). Experimental and CFD evidence of multiple solutions in a naturally ventilated building. *Indoor Air*, 14:43–54.
- [36] Hensen, J. L. (1999). A comparison of coupled and de-coupled solutions for temperature and air flow in a building. *ASHRAE Transactions*, 105(2):962–969.
- [37] Hunt, G. R. and Linden, P. F. (2004). Displacement and mixing ventilation driven by opposing wind and buoyancy. *Journal of Fluid Mechanics*, 527:27–55.
- [38] Inard, C., Bouia, H., and Dalieieux, P. (1996). Prediction of air temperature distribution in buildings with a zonal model. *Energy and Buildings*, 24:125–132.
- [39] Incropera, F. P. and DeWitt, D. P. (2002). *Introduction to heat transfer*. John Wiley & Sons, Inc., New York, NY, fourth edition.
- [40] Kaplan, D. and Glass, L. (1995). *Understanding nonlinear dynamics*. Springer-Verlag, New York.
- [41] Li, Y. and Delsante, A. (2001). Natural ventilation induced by combined wind and thermal forces. *Building and Environment*, 36:59–71.
- [42] Li, Y., Delsante, A., Chen, Z., Sandberg, M., Andersen, A., Bjerre, M., and Heiselberg, P. (2001). Some examples of solution multiplicity in natural ventilation. *Building and Environment*, 36:851–858.
- [43] Lienhard, J. H. I. and Lienhard, J. H. V. (2006). *A heat transfer textbook*. Phlogiston Press, Lexington MA, third edition.

- [44] Linden, P. F. (1999). The fluid mechanics of natural ventilation. *Annual Review of Fluid Mechanics*, 31:201–238.
- [45] Livermore, S. and Woods, A. W. (2004). Multiple steady states in buoyancy driven natural ventilation. In *Proceedings of Roomvent*, Portugal.
- [46] MathWorks (2002). *Matlab user's guide*. The MathWorks, Natick, MA.
- [47] McDowell, T. P., Emmerich, S., Thornton, J. W., and Walton, G. (2003). Integration of airflow and energy simulation using CONTAM and TRNSYS. *ASHRAE Transactions*, 109(1).
- [48] Mehta, M. (2005). Natural ventilation analyses of an office building with open atrium. In *Ninth International IBPSA Conference*.
- [49] Negrao, C. (1995). *Conflation of Computational Fluid Dynamics and Building Thermal Simulation*. PhD thesis, University of Strathclyde, Glasgow, UK.
- [50] Nitta, K. (1996). Study on the variety of theoretical solutions of ventilation network. *Journal of Architecture, Planning, and Environmental Engineering*, 480:31–38.
- [51] Press, W. H., Teukolsky, S. A., Vetterling, W. T., and Flannery, B. P. (1992). *Numerical Recipes in C: The Art of Scientific Computing*. Cambridge University Press, Cambridge, UK, second edition.
- [52] Rabl, A. and Norford, L. K. (1991). Peak load reduction by preconditioning buildings at night. *International Journal of Energy Research*, 15:781–798.
- [53] Schaelin, A., Dorer, V., van der Maas, J., and Moser, A. (1993). Improvement of multizone model prediction by detailed flow path values from CFD calculations. *ASHRAE Transactions*, 7(4):709–720.
- [54] Seem, J. E. (1987). *Modeling of Heat Transfer in Buildings*. PhD thesis, University of Wisconsin, Madison, WI.
- [55] Srebric, J. (2000). *Simplified Methodology for Indoor Environment Designs*. PhD thesis, the Massachusetts Institute of Technology, Cambridge, MA, USA.
- [56] Strang, G. (1986). *Introduction to Applied Mathematics*, chapter 6: Initial Value Problems. Wellesley-Cambridge Press, Wellesley, Massachusetts.
- [57] Strogatz, S. H. (1994). *Nonlinear dynamics and chaos: with applications to physics, biology, chemistry, and engineering*. Addison-Wesley Publishing Company, Reading, Massachusetts.
- [58] Tan, G. (2005). *Study of Natural Ventilation Design by Integrating the Multizone Model with CFD Simulation*. PhD thesis, the Massachusetts Institute of Technology, Cambridge, MA, USA.

- [59] Urban, B. and Glicksman, L. R. (2006). The MIT design advisor – a fast, simple tool for energy efficient building design. In *Proceedings of Simbuild*, Cambridge, MA.
- [60] van der Maas, J. and Roulet, C.-A. (1991). Nighttime ventilation by stack effect. *ASHRAE Transitions*, 5(3):516–524.
- [61] Walker, C. E. (2005). *Methodology for the Evaluation of Natural Ventilation in Buildings Using a Reduced-scale Air Model*. PhD thesis, the Massachusetts Institute of Technology, Cambridge, MA, USA.
- [62] Walker, C. E., Manchanda, S., Spindler, H. C., and Norford, L. K. (2004). Building performance: Analysis of naturally ventilated UK office building. In *Proceeding of Roomvent*, Coimbra, Portugal.
- [63] Walton, G. N. (1998). A multi-zone thermal analysis program. Slide.
- [64] Walton, G. N. and Dols, S. W. (2005). *CONTAM 2.4 User Guide and Program Documentation*. National Institute of Standard and Technology. NISTIR 7251.
- [65] Wang, Y. and Gao, F. (2001). Main factors having affect on wind pressure coefficient used for infiltration calculation. *Journal of Harbin University of C. E. & Architecture*, 34(4):87–90.
- [66] Woods, A. W. (2004). Wind-buoyancy interaction in natural ventilation: How to avoid multiple steady states. In *Proceeding of Roomvent*, Coimbra, Portugal.
- [67] Yang, L., Xu, P., and Li, Y. (2006). Nonlinear dynamics analysis of natural ventilation in a two-zone building: Part A—Theoretical analysis. *HVAC&R Research*, 12(2):231–255.
- [68] Yang, L. N., Li, Y. G., Zhang, G. Q., and Chen, Y. M. (2005). Dependence of CFD predictions on initial conditions for turbulent indoor airflows and pollutant spread. In *Proceedings of Indoor Air*, pages 2690–2695, Beijing, China.
- [69] Yuan, J. (2003). Effective prediction of air distribution and contaminant transport in entire buildings by coupling multi-zone, CFD and energy models. Master's thesis, the Pennsylvania State University, University Park, PA.
- [70] Yuan, J. and Glickman, L. R. (2005). Multiple steady states in a combined buoyancy and wind driven natural ventilation system: necessary conditions and initial values. In *Proceedings of Indoor Air*, pages 1207–1212, Beijing, China.
- [71] Yuan, J. and Glicksman, L. R. (2006). Validation of a multi-zone model with integrated energy equation and impact of thermal mass modeling methodology. In *SimBuild*.
- [72] Yuan, J. and Glicksman, L. R. (2007a). Identification of multiple steady states in buildings with complex geometries by a computer model. In *Proceedings of Roomvent*, Helsinki, Finland.

- [73] Yuan, J. and Glicksman, L. R. (2007b). Multiple steady state behaviors of a natural ventilation system with thermal mass. In *Proceedings of Roomvent*, Helsinki, Finland.
- [74] Yuan, J. and Glicksman, L. R. (2007c). Multiple steady states in combined buoyancy and wind driven natural ventilation: The conditions for multiple solutions and the critical point for initial conditions. *Building and Environment*, in press. doi:10.1016/j.buildenv.2006.11.035.
- [75] Yuan, J. and Glicksman, L. R. (2007d). Nonlinear dynamics behaviors in a natural ventilation system with thermal mass—Part I: Dynamical system characteristics generalization. Submitted to *Building and Environment*.
- [76] Yuan, J. and Glicksman, L. R. (2007e). Nonlinear dynamics behaviors in a natural ventilation system with thermal mass—Part II: Transient characteristics and impact of the mass. Submitted to *Building and Environment*.
- [77] Yuan, J. and Glicksman, L. R. (2007f). Transitions between the multiple steady states in a natural ventilation system with combined buoyancy and wind driven flows. *Building and Environment*, 42:3500–3516.
- [78] Yuan, J. and Srebric, J. (2002). Improved prediction of indoor contaminant distribution for the entire buildings. In *Proceedings of ASME Winter Meeting*, volume 258, pages 111–118, New Orleans, Louisiana.

Appendix A

Interface of the CoolVent program

The CoolVent program interface is a windows-based interface that enables the users to quickly configure the settings of a coupled thermal and airflow simulation. The interface is straightforward with a few prototypes of buildings that are commonly used in natural ventilation design. It serves to bridge the actual buildings and the mathematical representation of the buildings that are essential to the underlying airflow and thermal modeling process.

Different from the core program used in Chapter 3 for validation, the CoolVent interface program has simplified certain input settings in order to achieve the effectiveness in configuring the prototype buildings. In this appendix, these parameters settings will be introduced as well as the settings for the prototype buildings.

A.1 Major model assumptions

The program is based on a coupled airflow and thermal multi-zone model. Major assumptions are:

Full mixing zones The zones are assumed to be well-mixed so that each room is represented by an uniform temperature.

Multi-zone airflow model Multi-zone airflow model is used in calculating the pressurization of the zones and the airflows between zones. More about multi-zone airflow model is described in Chapter 2.

Power-law relation for airflow openings The flow-path resistances are assumed to follow a Power-law relation [1].

One dimensional heat transfer through the thermal mass In modeling the thermal mass, only one dimensional heat transfer along the thickness direction of the thermal mass (usually a slab) is considered.

A.2 Major parameters used in the program

The program allows the user to configure values through the interface. These parameters will be presented in the next sections. Here, we provided the parameters that the program has assumed and not open to the users. They can be categorized as the airflow resistances, load schedules, and the wind pressure coefficients.

A.2.1 Airflow resistance

The openings in the program are modeled as open orifices which one-dimensional flows pass through. The orifices are assumed to satisfy the Power-law flow resistance relation. In CoolVent, we used discharge coefficient form of this Power-law relationship, which states

$$q = C_d A \left(\frac{2\Delta P}{\rho} \right)^n, \quad (\text{A.1})$$

where q is the flow rate through an opening; ΔP is the pressure differences across the orifice; A is the area of the opening; and ρ is the density of the fluids. Further, C_d is the discharge coefficient of the orifice and n is the flow exponent.

To form the equations for multi-zone airflow models, we used the actual opening (e.g. a window opening or door opening) size of an opening for A . The density of the fluids is assumed to be the upward air density. In the normal ranges of building air temperatures, its value is around 1.18 kg/m³.

The discharge coefficient C_d is selected based on whether the opening is an exterior opening or interior opening. For exterior (small) openings, the CoolVent interface program assigns 0.65 for C_d ; and for internal (large) openings, the CoolVent interface program assigns 0.99 for C_d . The flow exponent is assumed to be 0.5 for all the openings in the program.

A.2.2 Load values and schedules

The CoolVent program assumes a heat load inside the occupied spaces for air temperature calculation. The option is implicitly implemented in selecting the functionality of the building. The CoolVent program allows for three different functionalities - office, residential, and educational. For office buildings, the heat load is set based on a value of 30 W per square meter of floor area (i.e. 30 W/m²). For residential buildings, the heat load is set based on a value of 20 W/m². For educational buildings, the heat load is set based on a value of 40 W/m².

The CoolVent program also assumes a heat load schedule for a typical day. During the day (7am to 7pm), the load schedule is set to the values set above depending on different building functionalities. During the night (7pm to 7am), the load schedule is set to 20% of the above per floor values. Therefore, the night loads for the three types of buildings are 6 W/m², 4 W/m², and 8 W/m² respectively. This variation pattern of load during day and night is assumed in the current version of CoolVent to roughly account for the variation of solar loads in a day. In the current version, the quantitative calculation of the solar loads with time, however, is not quantitatively

computed within CoolVent. If needed, the detailed solar gain can be estimated by an external procedure (see Chapter 3) or program.

A.2.3 Wind pressure coefficients

The CoolVent program currently uses a formula from a regression study [65]. The formula takes related parameters such as relative building height, terrain roughness, surround building height, front and side aspect ratio, and the wind incident angle to calculate the Wind Pressure Coefficients (WPC or C_p) of the openings.

The regression study gives the following relationship between WPC and the input parameters:

$$C_p = 1.198 + 0.1721zh - 1.6104\alpha - 0.0080rbh - 0.2636far + 0.1777sar - 0.0094anw, \quad (\text{A.2})$$

where zh is the relative height of the opening to the height of the building; α is the terrain roughness of the site; rbh is the ratio of the height of the building to the height of the surrounding buildings; far is the front aspect ratio; sar is the side aspect ratio; and anw is the incidence angle of the wind.

An alternative model for the Wind Pressure Coefficient is the model presented by Grosso [34]. In the Grosso model, the C_p values are calculated through a regression formula for the airflow. The wind pressure coefficient at any point on a building surface was modeled by

$$C_p = C_{p\text{ref}}(zh) \times CF, \quad (\text{A.3})$$

where $C_{p\text{ref}}$ is the reference wind pressure coefficient at the height of zh , the non-dimensional height of the point; CF is a correction factor defined by

$$CF = Cf_{zh}(\alpha) \times Cf_{zh}(pad) \times Cf_{zh,pad}(rbh) \times Cf_{zh,pad}(far) \times Cf_{zh,pad}(sar) \times Cf_{zh,anw}(xl), \quad (\text{A.4})$$

where α , rbh , far , sar , and anw have the same meanings as are in Equation (A.2); while *pad* is *plan area density* that represents the density of buildings in the surrounding areas. The six multiplier terms - $Cf_{zh}(\alpha)$, $Cf_{zh}(pad)$, $Cf_{zh,pad}(rbh)$, $Cf_{zh,pad}(far)$, $Cf_{zh,pad}(sar)$, and $Cf_{zh,anw}(xl)$ - are six regression functions obtained from a data source gather from a broad spectrum of historical experiments and analysis.

Currently, the Grosso [34] model has been implemented in Java code by the author (of CoolVent) but has not been actually used in CoolVent program yet. Rather, the implemented code was used in another energy calculation program developed at MIT – the MIT design advisor [33, 59].

A.3 Program interface

The CoolVent program interface consists of three major stages. In the first stage, the program will prompt the user to select the general simulation information such as building type, simulation type, and geographical information. In the second stage, the program will allow the user to configure the geometries, thermal mass, and control

strategies in detail. At the end of the second stage, the user can start the simulation. In the third stage, the program post-processes the computational results and displays the results by different methods. In the next few sections, we will introduce the detailed specifications in these three major stages.

A.4 Stage 1—General information

In Stage 1 of the program, the user can select among the four prototypes of buildings to simulate. The procedures such as building selection, geographical information, weather information, and functionalities can be specified in this section. Figure A-1 demonstrates the program interface for this stage.

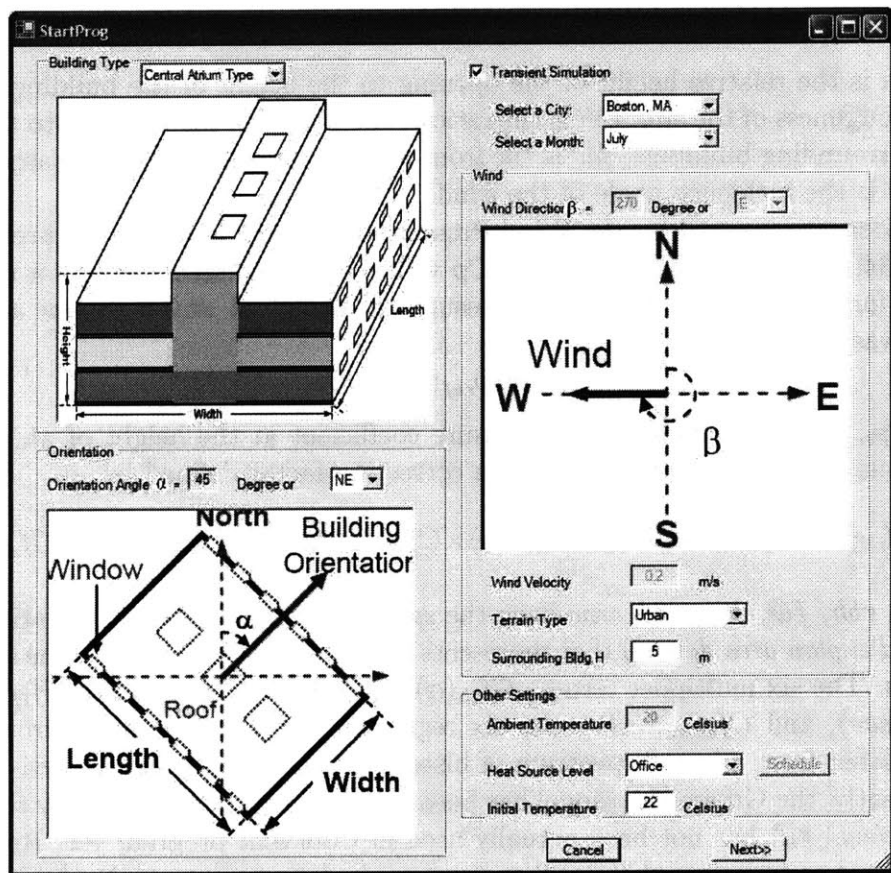


Figure A-1: Stage 1 of CoolVent program

A.4.1 Weather/Environment parameters

A.4.1.1 For steady state simulations

To choose steady state simulation, the checkbox of “Transient simulation” should be unchecked. This check box is checked by default for transient simulation. By

unchecked the transient simulation option, several grayed out options such as the wind direction and wind velocity, outdoor air temperature will become active. The active parameters are demonstrated in Table A.1.

Item	Types	Unit	Default Value
Wind direction	Dropdown List	-	E
Wind velocity	Input value	m/s	0.2
Ambient temperature	Input value	°C	20

Table A.1: Input parameters for steady state simulations

A.4.1.2 For transient simulations

The program starts by assuming a transient simulation. After the "transient simulation" checkbox is checked, the program will allow the user to pick a month and a city to run the simulation. The major parameter settings for the transient simulation are listed in Table A.2.

Item	Types	Unit	Default Value
Transient simulation	Check/Uncheck	-	Checked
City Name	Dropdown List	-	Boston
Month	Dropdown List	-	July

Table A.2: Input parameters for transient simulations

The program allows the user to select in a wide range of cities to conduct a transient simulation. In the program, TMY2 weather files are used. The wind velocity, wind direction, and outdoor dry bulb temperatures are read by the program to perform the transient simulation. Currently, we have included a list of weather files for a selection of cities that can geographically cover the climate characteristics from coast to coast. Table A.3 list the name of the cities/regions whose weather files have been included in the release package of CoolVent.

A.4.2 Terrain information

The program also needs terrain information such as the orientation, the terrain roughness, and the height of the surround building to calculate the Wind Pressure Coefficient (WPC) described in Section §A.2.3.

The configurable parameters are listed in Table A.4. The user can select among the eight directions (W, E, N, S, NE, NW, SE, SW) for the building orientation. When a direction is selected, the program will automatically rotate the building in the building orientation display window to align with the selected direction. In an early version continues degree number can also be allowed. This feature (to input continuous degree numbers), although is disabled in the current version, will likely to be recovered in later versions.

City	State	Country
Atlanta	GA	United States
Boston	MA	United States
Charlotte	NC	United States
Chicago	IL	United States
Houston	TX	United States
Los Angeles	CA	United States
Miami	FL	United States
Puerto Rico	PR	Puerto Rico
San Francisco	CA	United States
Seattle	WA	United States

Table A.3: TM2 weather files included in current CoolVent release

Item	Types	Unit	Default Value
Building Orientation	Dropdown List	-	NE
Terrain Roughness	Dropdown List	-	Urban
Surrounding building Height	Input value	m	5

Table A.4: Terrain information

The terrain roughness (namely, the α in Equations (A.2) and (A.4))^{*} and the surrounding building height are used to compute the Wind Pressure Coefficients in Equations (A.2) and (A.3). For the terrain roughness α , we used empirical values for different terrain types. In a city, α is set to 0.24; in a rural area, α is set to 0.18; and in a terrain similar to a airport, α is set to 0.14.

A.4.3 Parameters for temperature solution

Since the CoolVent program can solve the air and thermal mass temperatures, the heat source loads needs to be specified. In this interface, the heat source is assumed to be the specified inputted value during the daytime (7:00am to 7:00pm) and is assumed to be 20% of the specified value during the night (7:00pm to 7:00am).

Item	Types	Unit	Default Value
Heat Source	Dropdown List	-	Office
Initial Temperature	Input value	°C	22

Table A.5: Temperature solution parameters

The two related parameters are listed in Table A.5. The values used for heat source was explained in Section §A.2.2. For the initial temperature, it is an option offered to the user to quickly check the possible multiple steady states of the system behaviors. For the dependency of the steady state on the initial values, refer to previous chapters (4, 5, 9, and 10) or the listed reference [74].

*The α used here is NOT the same as the building orientation angle shown in Figure A-1.

A.4.4 Buttons

Next Proceed to Stage 2, with the parameters inputted in the current stage saved.

Cancel Quit the program. A dialogue box will pop up to ask the user to confirm the quit or cancel the quit. If the quit is confirmed, the program will quit without saving any data.

A.5 Stage 2—Detailed descriptions

In Stage 2, the users are prompted to specify the detailed geometry information of the building such as the dimensions, the number of floors, and the window opening areas (and more). After the geometry specification, the thermal mass in the building can be configured to be included or not in the simulation. Further, we can specify the windows control strategies during cold seasons. Finally, after all the parameters are specified, the user can click to start the simulation.

Figure A-2 shows the interface of this stage. In this stage, the interface appearance may vary depending on the building type specified in the first stage. For example, if the central atrium type was selected in Stage 1, the interface will reach an interface with a major graph of a three-story central atrium building, as is shown in Figure A-2. On the top of the graph, the building type is indicated by an active radio button. The corresponding radio buttons for the other three unselected building types are automatically disabled.

A.5.1 Central atrium type

The central atrium design is a typical natural ventilation design that intends to foster buoyancy driven natural ventilation flows. A typical building geometry is shown in Figure A-2, with occupied spaces on the two sides and a central atrium in between.

The parameters that can be configured in the central atrium type building are listed in Table A.6. Most of these parameters are used to specify the dimensions of the occupied spaces and the atrium space. The number of floors, which is set to "3" by default, can also be user-defined. Although in the current stage the change of this floor number will not immediately show a building with corresponding number of floors (e.g. change it to "4" will not change the look of the three-story building graph shown in this stage), in the next stage, after the computation, the program will indeed visualize the temperatures and airflow rates on a building with the specified number of floors.

A.5.2 Chimney type

If the user selected the Chimney case in the first stage, the program will proceed to the interface shown in Figure A-3. This building geometry is similar to the central atrium case, except that only half of the occupied space is presented. It looks like an

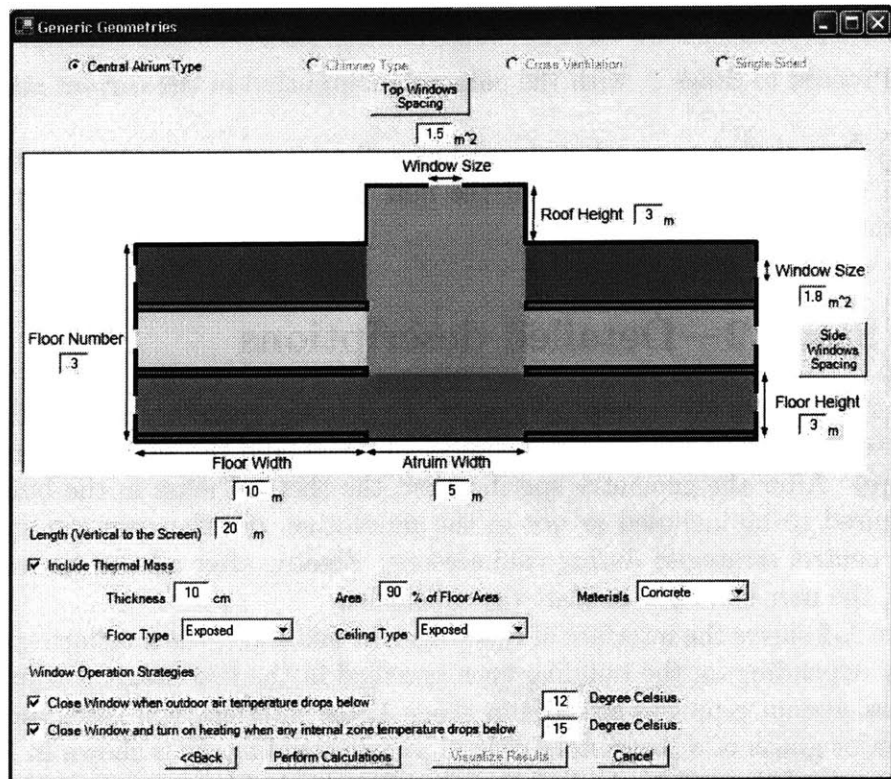


Figure A-2: Central Atrium prototype

office area connecting a chimney atrium. This case is very similar to a typical solar chimney or wind scoop type of design.

The input parameters are similar to those in the central atrium type. The detailed parameter list is demonstrated in Table A.7.

A.5.3 Cross ventilation type

The third type of geometry is shown in Figure A-4. This type of building consists of a series of continuous spaces that are internally connected. In a typical design, the cross ventilation airflow will run through these rooms in series to ventilate and cool down the building.

The detailed parameters for the cross-ventilation type of building are given in Table A.8. In this graph, the view is taken from the top. Several important parameters that can determine the building characteristics can be specified by the users. For example, the number of sections the building has is not confined to the default "3", but can be change to other values. The size of the building can also be configured by inputting the three dimensions of a single zone. The exterior window size and the interior door sizes can also be specified by user rather than using the default values.

Item	Types	Unit	Default Value
Floor Width	Input value	m	10
Atrium Width	Input value	m	5
Length	Input value	m	20
Floor Height	Input value	m	3
Floor Number	Input value	-	3
Roof Height	Input value	m	3
Side Window Size	Input value	m^2	1.8
Top Window Size	Input value	m^2	1.5

Table A.6: Central atrium type specifications

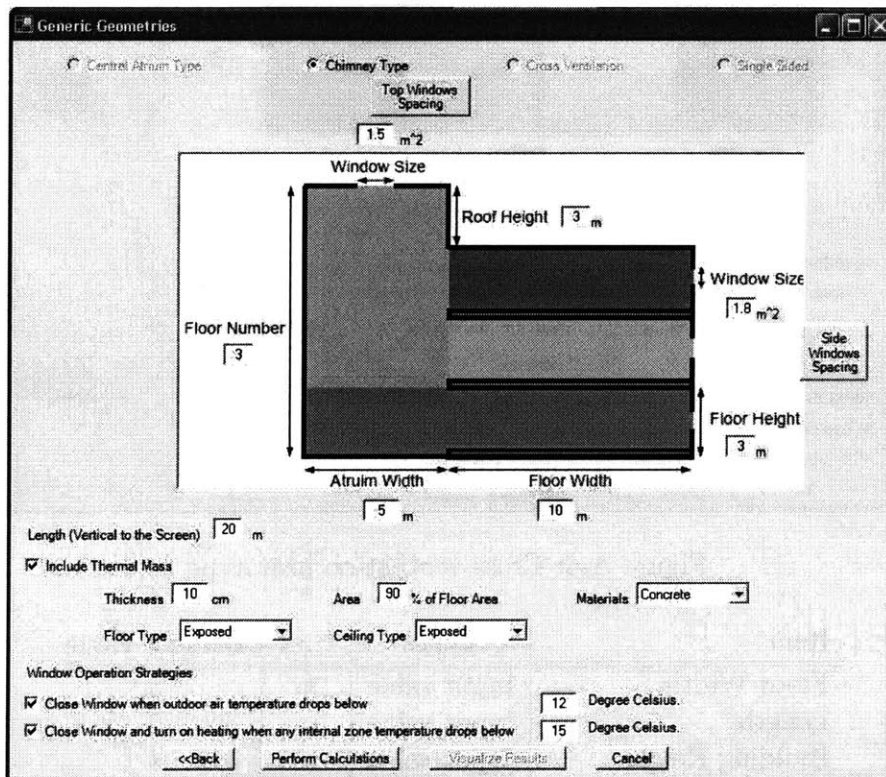


Figure A-3: Chimney type prototype

Item	Types	Unit	Default Value
Floor Width	Input value	m	10
Atrium Width	Input value	m	5
Building Length	Input value	m	20
Floor Height	Input value	m	3
Floor Number	Input value	-	3
Roof Height	Input value	m	3
Side Window size	Input value	m^2	1.8
Top Window size	Input value	m^2	1.5

Table A.7: Chimney type building specifications

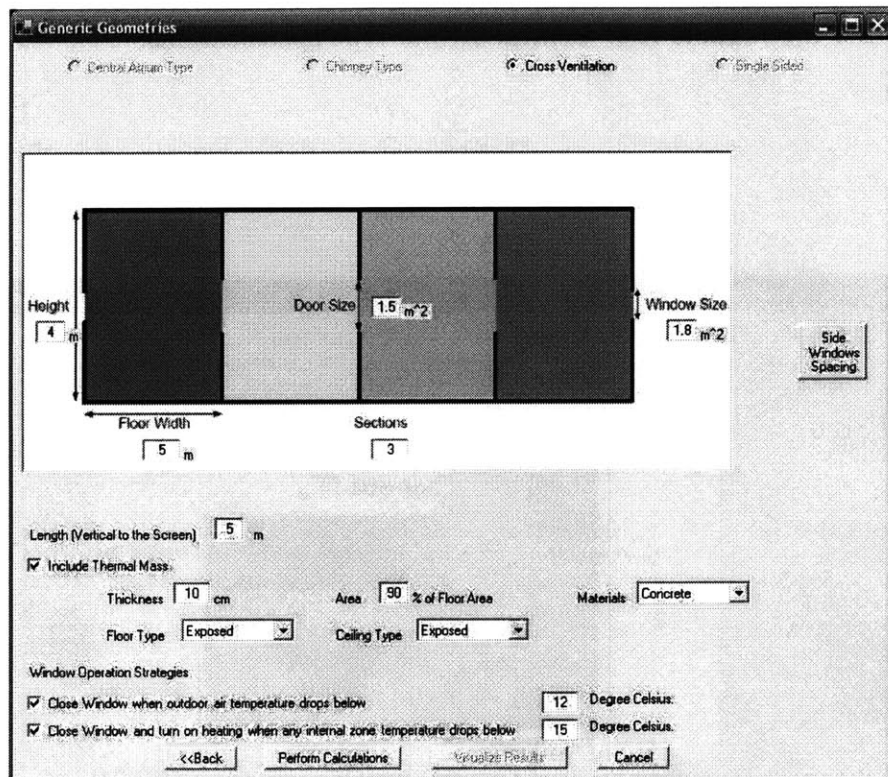


Figure A-4: Cross ventilation prototype

Item	Types	Unit	Default Value
Floor Width	Input value	m	5
Length	Input value	m	5
Building Height	Input value	m	4
Section Number	Input value	-	3
Exterior Window size	Input value	m^2	1.8
Internal Door size	Input value	m^2	1.5

Table A.8: Cross ventilation type specifications

A.5.4 Single-sided ventilation type

The single-sided ventilation is designed in many natural ventilation systems, for example, a single room with an upper window and a lower window. In the CoolVent program, such a prototype can also be modeled, as is shown in Figure A-5.

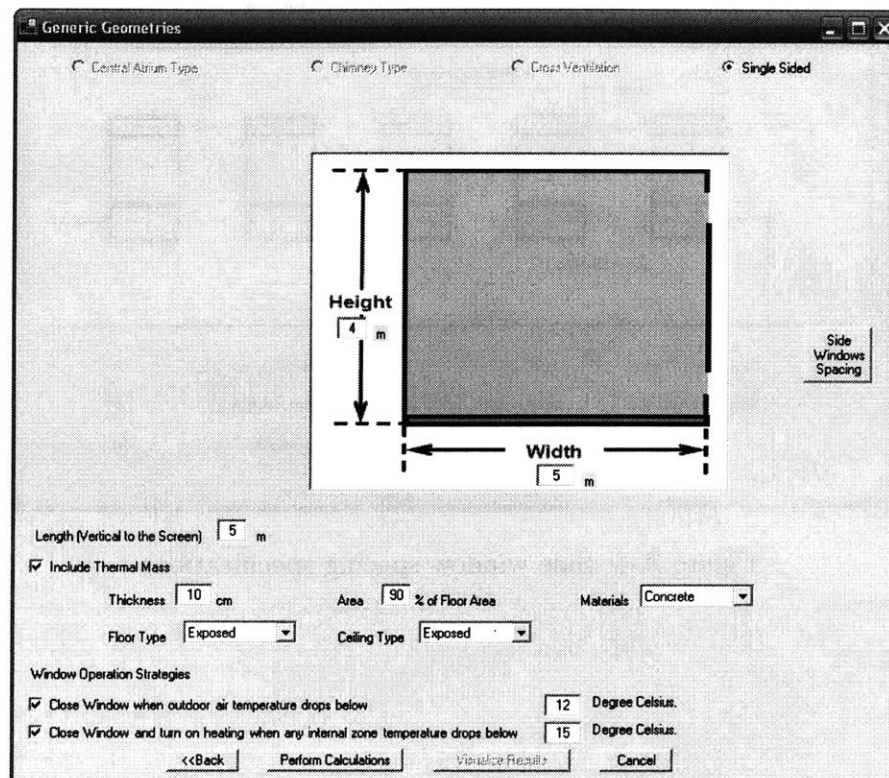


Figure A-5: Single-sided Ventilation prototype

The parameters to be specified in the single-sided ventilation type are shown in Table A.9. The input parameters include the basic building dimensions. In addition, to configure the geometry of the side windows need to be specified through the **Side Window Space** button. When the **Side Window Space** button is clicked, a dialogue box shown in Figure A-6 will pop up. In this dialogue box, the parameters for window geometries—such as the number, sizes, and positions of the windows—can be specified in detail. The default values for these parameters are listed in Table A.10.

Item	Types	Unit	Default Value
Width	Input value	m	5
Height	Input value	m	4
Length	Input value	m	5
Side Window Spacing	Click to specify	-	-

Table A.9: Single-sided ventilation parameters

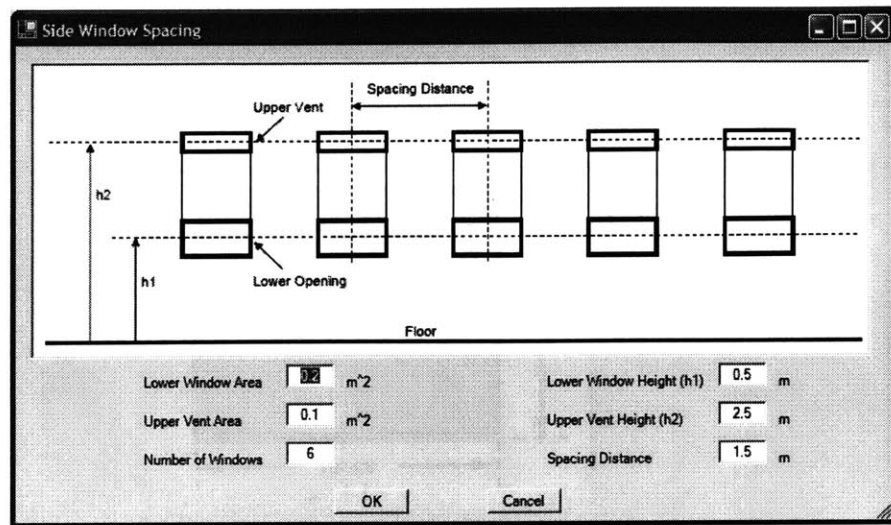


Figure A-6: Side window spacing specifications

Item	Types	Unit	Default Value
Lower Window Area	Input value	m^2	0.2
Upper Vent Area	Input value	m^2	0.1
Number of Windows	Input value	-	6
Lower Window Height (h1)	Input value	m	0.5
Upper Vent Height (h2)	Input value	m	2.5
Spacing Distance	Input value	m	1.5

Table A.10: Specifications for side window spacing

A.5.5 Thermal mass description

The user can specify the thermal mass options in the simulation as well. This is implemented through checking the “Include thermal mass” checkbox in Stage 2 (see Figure A-2). In transient simulations, this checkbox is automatically checked when the program proceeds to Stage 2. In steady state simulations, this option is automatically unchecked.

The thermal mass is assumed to be a ceiling slab or a floor slab (or both). In general, we naturally assume the floor slab in one room is the ceiling slab of the room beneath it (i.e. the lower floor). Only one dimensional heat transfer through the thickness of the slab is assumed as was stated in the model assumptions in Section §A.1.

When the thermal mass is selected to be included in the simulation, the program will allow the user to specify the thicknesses, areas, and materials of the thermal mass. The area is specified by inputting a percentage of floor area in the occupied space. The detailed parameter settings are listed in Table A.11.

Further, some details about the way the thermal mass contacts with the air can be specified as is shown in Table A.11. For example, the ceiling may be exposed or suspended, which will affect the way the zonal air interacts with the thermal mass. The floor can be exposed (default), carpeted or of a raised floor type, which stands for different contact type between the air and the thermal mass.

Item	Types	Unit	Default Value
Thickness	Input value	cm	10
Area	Input value	% floor area	90
Materials	Dropdown List	-	Concrete
Floor type	Dropdown List	-	Exposed
Ceiling type	Dropdown List	-	Exposed

Table A.11: Thermal mass parameters

A.5.6 Windows control strategies

Provide two simple control strategies to control the window openings. Further, we also provided a way to control the heating in the space. They are:

Based on outdoor temperature If checked, the exterior windows will be closed if the outdoor air temperature drops below a certain set point temperature;

Based on indoor temperatures If checked, the exterior windows will be closed if the minimum air temperature in the building drops below a certain point (configurable, see Table A.12); at the same time heating will be turned on based on the temperature difference between the zone air temperature and a set-point temperature. Currently, we implicitly set the set-point temperature to 20 °C.

The major input parameters for the two control strategies above are listed in Table A.12. In the CoolVent program, the outdoor air temperature based strategy is on (checked) by default, with a default set point of 12 °C. The indoor air temperature based strategy is off (unchecked) by default. When this option is checked on by the user, the default temperature value is 15 °C.

Item	Types	Unit	Default Value
Control based on outdoor air	Checkbox	-	Checked
Minimum outdoor temperature	Input value	°C	12
Control based on indoor air	Checkbox	-	Unchecked
Minimum indoor temperature	Input value	°C	15

Table A.12: Window control strategies options

A.5.7 Buttons

Back Go to Stage 1

Perform Calculations Save input data, generate files, and start computation

Visualize Results Visualize the calculation results

Cancel Quit the program

A.6 Stage 3—Visualization and output

This stage we provided three types of output methods to visualize the zone air temperatures and the flow path airflows.

A.6.1 Animated visualization

The zone temperatures can be visualized using a color scale that stands for different temperatures. This is especially effective for transient simulation. The temperatures of the building at different time will be animated in an adjustable time interval. Figure A-7 demonstrates an example of this visualization.

In this visualization method, the temperatures are represented by different colors representing hot or cold temperatures. We choose a scale which uses “blue” as the coldest and “red” as the hottest. The temperature scale is shown as a color bar in Figure A-7, with the minimum temperature and the maximum temperatures printed on the two ends. These two extreme temperatures can be also manually adjustable, which will be introduced shortly.

The airflow information is also displayed in this method. The directions of the airflows are displayed by the arrows at each of the openings. Especially, for the flow paths that connect the outdoors, the arrow is filled with the color of the upwind flow.

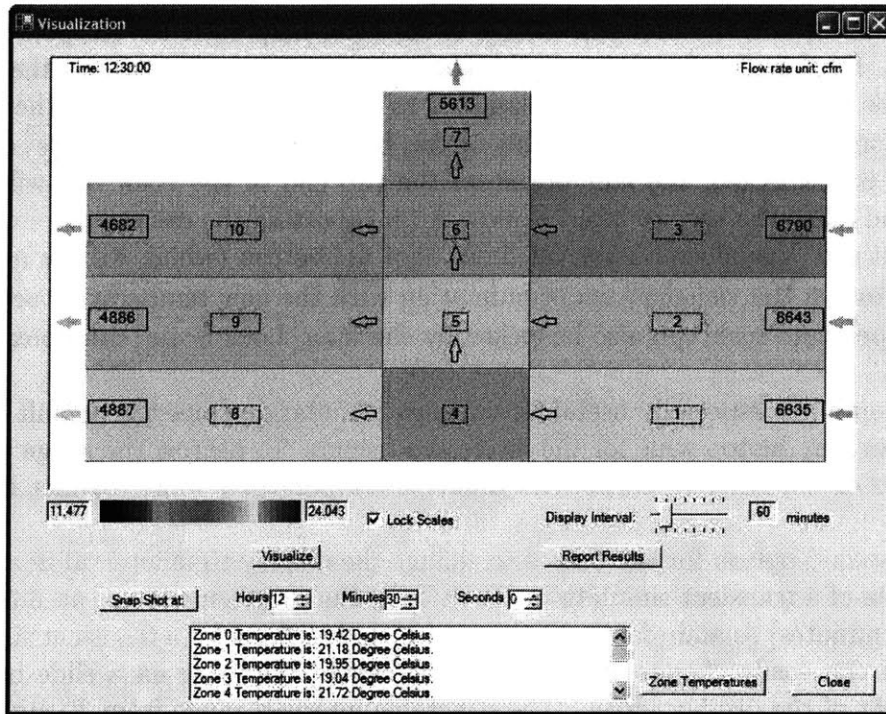


Figure A-7: Animation output

This is to say, if the airflow rate is going outward at an exterior opening (e.g. a window), the flow arrow is filled with a color that corresponds to the interior zone temperature; the airflow is going inward from an exterior opening, the flow arrow is filled with a color that corresponds to the outdoor air temperature. For an internal airflow path (i.e., a flow path that connects the zones on both sides), the airflow arrows only stands for the direction of the airflow.

The airflow rates are also presented in the visualization graph. They are printed in a small rectangular box near the exterior airflow arrows. The unit for the airflow rates is given in *cfm* (cubic feet per minute).

In the middle of each zone (rooms) in the visualization plot, a zone number is displayed in a dashed-line box. These zone numbers are the number the program used to number the zones for calculation and visualization. In a later sections A.6.1.1 to A.6.3, we will introduce the multiple ways to examine the detailed temperatures of each zone and the airflow rates between zones at any particular time.

For transient simulation, during an animation, the time of the corresponding frame is also displayed in text in the upper-left corner of the displayed figure area as a digital clock. For steady state simulation, such information will not be displayed.

A.6.1.1 Customize the visualization

There are several customizable options for the user to better visualize the results. This is done by the several options we provided in the visualization.

The first option the user can change is the color map scale for temperature visualization. By default, the coldest and highest temperatures obtained by the program in all time steps are automatically assigned to the “coldest” (blue) and the “hottest” (red) colors. The user can change this option by uncheck the [Lock Scale] checkbox. When it is unchecked, the edit boxed on the two end of the color bar will become active and allow the user to input values. After inputting the desired values, the user can select the [Visualize] button or [Snap Shot at] button (which will be introduced shortly) to run the visualization or animation with the new temperature scales. The new temperature scale can also be locked by checking [Lock Scale] checkbox after the new run.

This option is especially useful for transient simulation since the default temperature scales may be too wide for the interested frames. To narrow the range will make the colors of the different zones with different temperatures more distinct from each other.

The second option for the user is to change the display time interval in animating the results of a transient simulation. By default, the program will use an interval of 1 hour (60 minutes) to animate the temperatures and airflows for a transient simulation. The user can easily change this option by changing the value on a slide bar to the lower-right of the display screen. The selectable intervals range from 30 minutes to 4 hours. The speed of the animation is thus can be adjusted by changing the interval values. For larger intervals, the program automatically select a slightly larger pause time between each frames to keep visualization easier to capture. Similarly, for smaller intervals, the pause time between each frame will be slightly reduced automatically to allow a faster view through the many frames.

The third method to facilitate the visualization is through the [Snap Shot at] button. This button allows the user to examine the temperature distributions in the building in detail at a time in a day. The user only needs to specify the hour, the minutes, and even the seconds in a day in the three text boxes marked as [hour], [minute], and [second] (see Table A.13). After clicking the [Snap Shot at] button, the airflow and the temperature will be visualized in the displaying area. The corresponding air temperature values in each zone will be displayed a list box in the lower part of the program window, as is shown in Figure A-7.

Item	Types	Unit	Default Value
Hour	+/- or Input value	hr	0
Minutes	+/- or Input value	min	30
Seconds	+/- or Input value	sec	0

Table A.13: Snapshot input settings

A.6.1.2 Buttons and controls

[Visualize] Visualize/animate the zone temperature and airflow values using color images. This option will be disabled if there is an active animation going on.

Snap Shot at Visualize the temperature and airflow values at a particular time. The temperature values will be listed as text in a list box as well.

Lock Scale Change temperature color map scale. When unchecked, the program allows the user to specify the minimum and the maximum temperatures for the “coldest” (blue) and the “hottest” (red) color.

Display Interval Change the interval for the airflow and temperature result animation. The option is disabled in steady state simulations.

A.6.2 Graphical report by charts

An alternative method to display the simulation results is to use a temperature history chart. In this scenario, we can select a zone and plot the temperature changes in this zone for an entire day. The temperature is plotted against the outdoor air temperature to show their differences. This method is shown in Figure A-8, which is an effective way to examine the performance of the ventilation and the thermal mass designs.

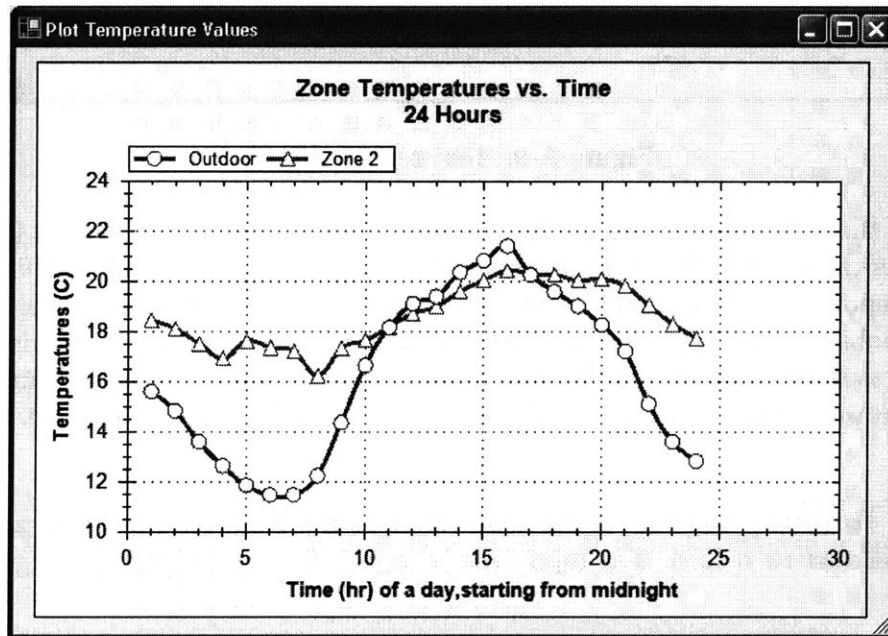


Figure A-8: Temperature history output

The only button associated with the temperature history plot is as follows:

Zone Temperatures Plot the zone temperature history. A shortcut to do this is to double click an item on the zone temperature list.

A.6.3 Text report by text files

Another alternative method to report the simulation result is to write the result into a text file. Figure A-9 shows the text report information. The text file will begin with

a short description of the major simulation parameters, followed by a description of the unit used for the reporting variables.

This simulation is transient.
The simulated city is: Boston, MA.
The simulated month is: July.
The building orientation is: 45 Degree.
Temperatures are reported in Degree Celsius.
Airflows are reported in kg/s.

Hour	Zone#	Temperature	AirflowFromAmbient	AirflowtoAmbient
1	0	15.61	-	-
1	1	16.99	1.744	-
1	2	17.54	1.562	-
1	3	17.84	1.303	-
1	4	17.00	-	-
1	5	17.29	-	-
1	6	17.51	-	-
1	7	17.51	-	2.134
1	8	18.54	-	0.391
1	9	18.46	-	0.865
1	10	18.53	-	1.217
2	0	14.85	-	-
2	1	16.68	1.419	-
2	2	17.48	1.032	-
2	3	18.53	0.217	-
2	4	16.94	-	-
2	5	17.11	-	-
2	6	17.20	-	-
2	7	17.20	-	2.364
2	8	17.32	0.947	-
2	9	18.71	-	0.224
2	10	18.49	-	1.027

Figure A-9: Text report output

After the unit description, the file contains the zone temperatures and (external) airflows of the building for each time hour. For steady simulation, only the final result will be reported. In the zonal temperature and airflow information, Zone 0 stands for the ambient. There are four columns in the reported data, which stands for zone number, zone temperature, airflow rate coming in from the ambient, and airflow rate exiting to the ambient. There is only one button associated with this text report as follows:

Report Results Generate a file that contains the zone temperatures and inter-zonal airflow record. The report file is opened for review after being generated.

Appendix B

Supplemental validation studies on the CoolVent program

In this chapter, several simple test cases are presented to validate CoolVent program as the supplemental and preliminary tests for the study presented in Chapter 3. The purpose was to test whether the temperature dynamics modules of program are implemented correctly during the development by comparing with simple (mostly analytical) models. For example, the airflow thermal dynamics will be tested using exponential decay models of the temperature. The thermal mass dynamics will be tested using a transient plate heat transfer case and a transient semi-infinite body transfer case. Finally, a slightly more complex test with varying temperature boundary conditions was conducted on an air-mass system. The result was compared with the simulation results predicted by the fourth order ODE solver in Matlab [46] with a similar model.

B.1 Compare with analytical models

In this section, four analytical cases will be conducted to validate the correctness of the program modules implementations. In Section §B.1.1, the transient air temperature dynamics will be examined by two exponential decay cases. In Section §B.1.2, the transient thermal mass dynamics will be examined by two transient conductive heat transfer cases. All these cases are analytical studies and the analytical solutions are available in multiple resources (e.g. [39]).

B.1.1 Transient air temperature dynamics by exponential decay tests

The exponential decay model is one of the most common models that can be used to test the program as a first move. We will test two decay models: one without heat source and the other with heat source.

The exponential decay model without heat source is set up as follows: a well-mixed space without thermal mass is originally stagnant (i.e., no airflow) and maintained at

a temperature of T_1 . The outdoor air temperature is constant at time T_0 . Suddenly at time 0, a constant flow rate of q (m^3/s) is applied (say due to a wind that blows in and causes the air movement). The space is assumed to be fully mixed all the time during the process. Thus, the air temperature T of the space is analytically described by

$$T = T_0 + (T_1 - T_0) \cdot e^{-\frac{q}{V}t}, \quad (\text{B.1})$$

where t is the time (in s) and V is the volume of the space.

Figure B-1 shows the comparison between the CoolVent predictions and the analytical results.* The difference between the two is minimal. This test, although simple, shows that the program works well with the basic transient air temperature dynamics solution.

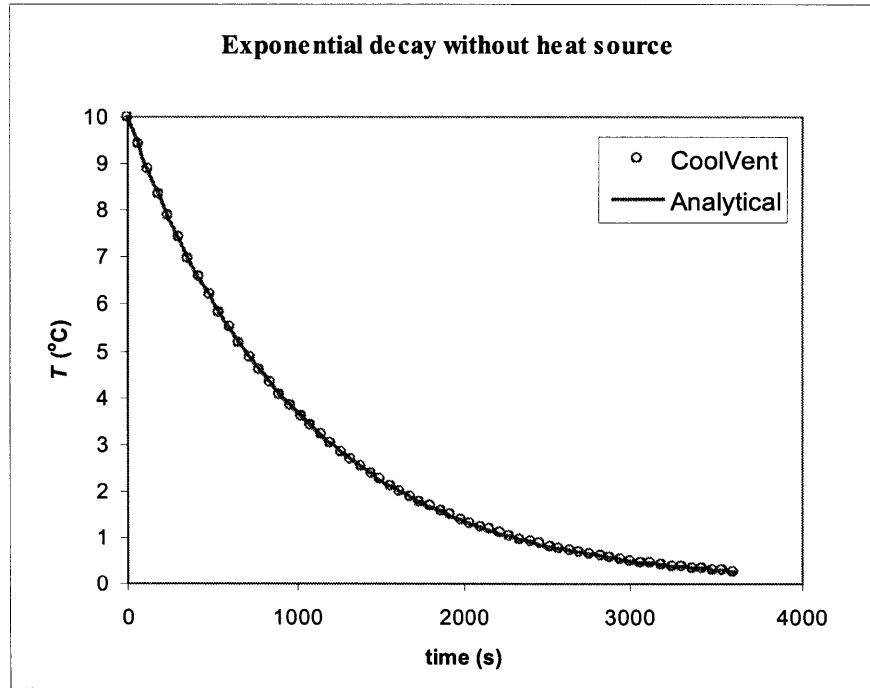


Figure B-1: Exponential decay case without heat source

The next test is similar to the test above except the addition of a heat source into the space. In this scenario, the space is assumed to have a constant heat source S (in W). The analytical solution to this model becomes

$$T = \left(T_0 + \frac{S}{\rho_a q} \right) + \left[T_1 - \left(T_0 + \frac{S}{\rho_a q} \right) \right] \cdot e^{-\frac{q}{V}t}, \quad (\text{B.2})$$

where ρ_a is the density of the air (in kg/m^3 , assumed constant).

The simulation results are shown in Figure B-2. The results, again, show a good

*We set $T_0 = 0^\circ\text{C}$ for convenience. The same setting is used for the case with heat sources.

agreement with the analytical solutions. This test indicated in depth that the air temperature dynamics are correctly implemented with given airflows and heat sources.

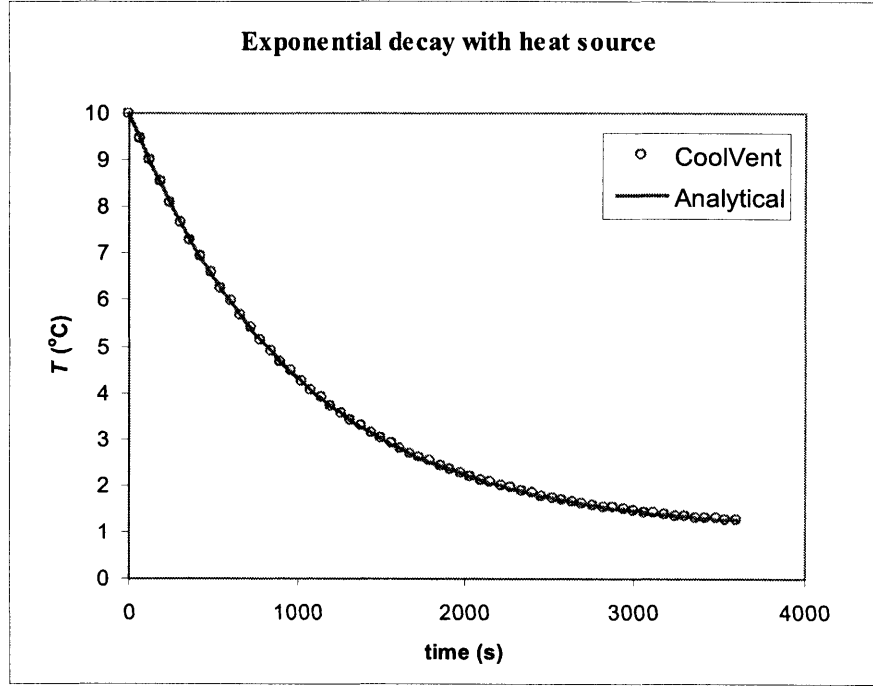


Figure B-2: Exponential decay case with heat source

B.1.2 Transient heat transfer with thermal mass

In CoolVent, thermal mass is modeled by dividing it into thin layers so that for each layer has a small enough (< 0.1) *Biot number*, which is defined by:

$$Bi = \frac{hl}{k}, \quad (B.3)$$

where h is the convective heat transfer coefficient between the air and the thermal mass (in $\text{W}/\text{m}^2\text{-K}$), l is the thickness of the layer (in m), and k is the conductivity of the thermal mass material (in $\text{W}/\text{m}\text{-K}$). In this case, we assume h is constant so that it does not change with the fluid velocities.

In this subsection, we will use a slab of a finite thickness $2L$ (in m) (but an infinite area) to test the validity of the thermal mass temperature prediction. We assume it is a concrete slab ($k = 1.3 \text{ W}/\text{m}\text{-K}$, and $\alpha^\dagger = 5.91 \times 10^{-7} \text{ m}^2/\text{s}$) of 15 cm thick in total (half thickness $L = 7.5 \text{ cm}$); and we assume the heat transfer coefficient between the air and the slab to be $10 \text{ W}/\text{m}^2\text{-K}$. The slab is initially maintained at a uniform high temperature T_0 and at time 0 it was immersed into a liquid (air) with a lower

[†] α is the thermal diffusion coefficient of the mass, which is defined by $\alpha = \frac{k}{\rho c_p}$.

but constant temperature T_{air} . Besides the change of the thermal mass temperature with time, there are also spatial differences inside the thermal mass. For example, the temperature of the interior part of the thermal mass will decrease with time in a slower pace.

The analytical solution to this problem is given by (see [43])

$$\frac{T - T_{air}}{T_0 - T_{air}} = \sum_{n=1}^{\infty} C_n e^{-\zeta_n^2 F_o} \cos(\zeta_n \cdot \frac{x}{L}), \quad (\text{B.4})$$

where x is the distance from the center of the slab and F_o is the Fourier number defined by

$$F_o = \frac{\alpha t}{L^2}, \quad (\text{B.5})$$

ζ_n is the positive solution to the equation

$$\zeta_n \tan \zeta_n = Bi, \quad (\text{B.6})$$

and C_n is defined as:

$$C_n = \frac{4 \sin \zeta_n}{2\zeta_n + \sin(2\zeta_n)}. \quad (\text{B.7})$$

Equation (B.4) can also be simplified in various forms. For example, when F_o is greater than 0.2, the temperature T can be well approximated by the first term of the infinite series in Equation (B.4).

In CoolVent, we simulated this simple transient heat transfer problem using a time step of 30s. Figure B-3 shows the result comparison between the analytical and the CoolVent predicted thermal mass temperatures for different time frames. In this setting, the exterior air temperature is set at 20 °C and the initial temperature of the thermal mass is uniformly set at 25 °C. The analytical solutions and the CoolVent predictions are very close to each other, within an error of ~0.05 °C in general. Figure B-4 shows the analytical and CoolVent results for one time period (5560s). The difference between the analytical results and the thermal mass is less than 0.05 °C in this case.

Figure B-3 and Figure B-4 also show that the temperature inside the thermal mass has significant gradients even after over an hour (e.g. for 4100s and 5560s). Therefore, a lumped sum method is not suitable for modeling the thermal mass temperatures and their impacts on the air temperatures. Therefore, a finite element type method is used in CoolVent to model the transient behaviors of the thermal mass.

B.1.3 Transient heat transfer through semi-infinite body

Another important transient conductive heat transfer model is the semi-infinite body. For example, the ground can sometimes be simplified as a one-dimensional semi-infinite body. The analytical solutions for the transient semi-infinite body heat trans-

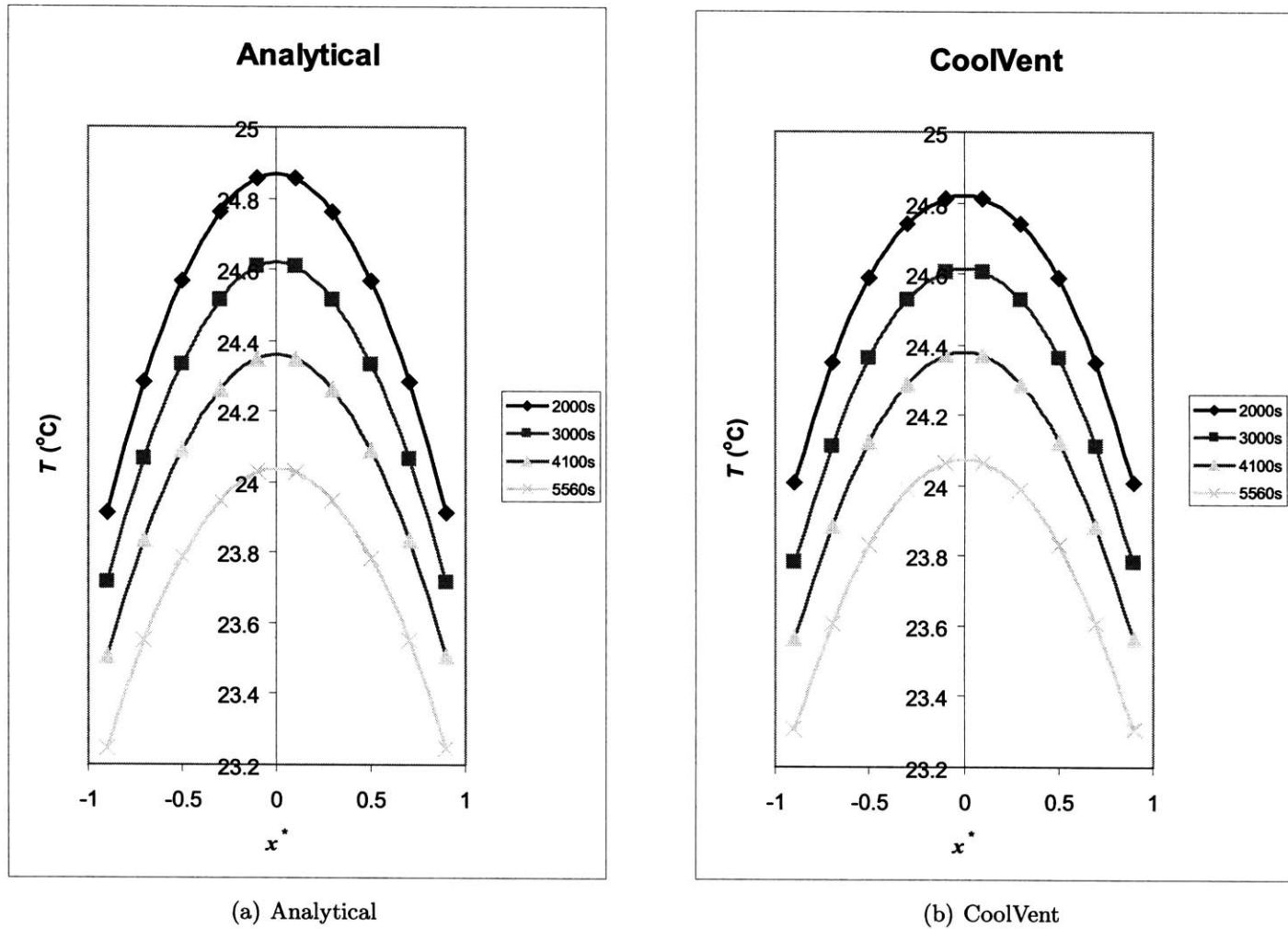


Figure B-3: Analytical vs. CoolVent predicted thermal mass temperatures^a

^a x^* is defined by x/L .

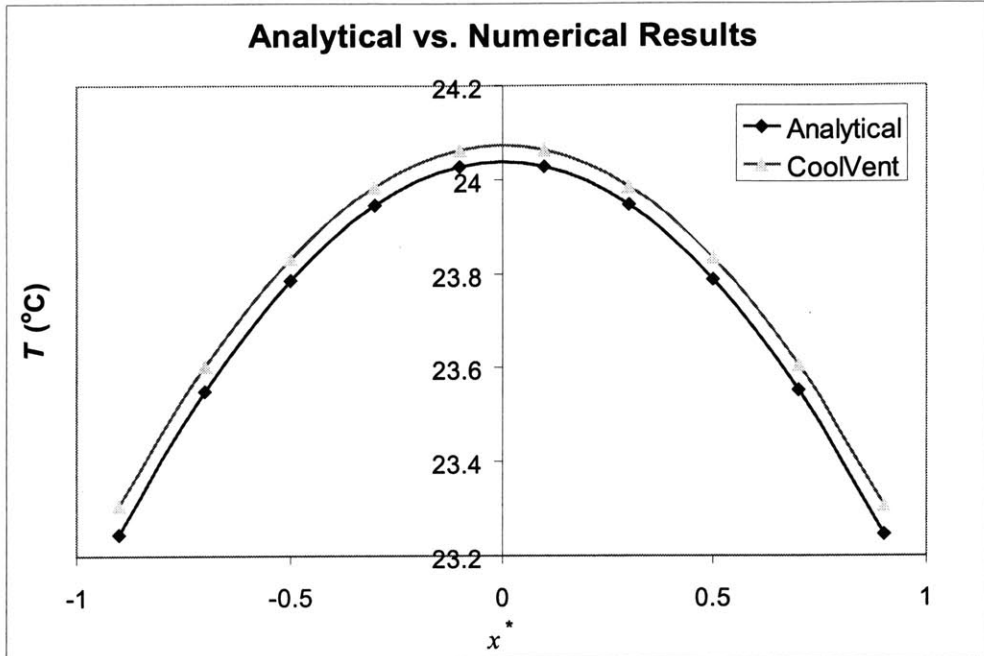


Figure B-4: Analytical vs. CoolVent: thermal mass temperatures at $t = 5560\text{s}$

fer under constant temperature boundary conditions can be expressed as ([43])

$$\frac{T - T_b}{T_0 - T_b} = \operatorname{erf}(\zeta/2), \quad (\text{B.8})$$

where T_b is the boundary temperature and $\operatorname{erf}()$ is the error function with the parameter $\zeta/2$ defined by

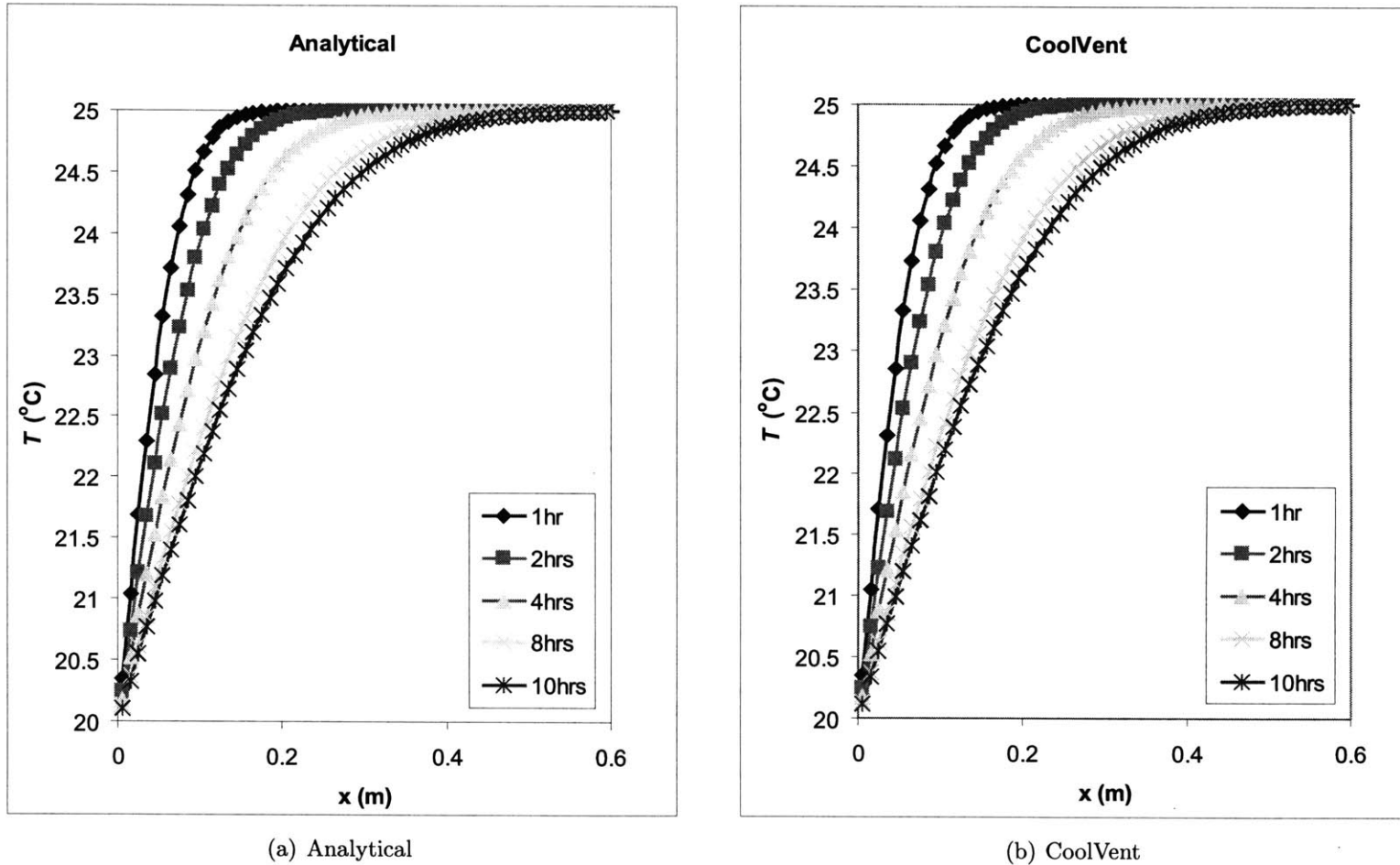
$$\zeta/2 = \frac{x}{2\sqrt{\alpha t}}, \quad (\text{B.9})$$

where x is the distance into the semi-infinite body from the boundary.

For the semi-infinite body materials, we used the same material properties as was used in Section §B.1.2. The comparison between the analytical solutions and the CoolVent simulation results is shown in Figure B-5. The CoolVent predicted results are almost identical to the analytical solutions, with a difference of only ~ 0.01 to 0.02 °C.

B.2 Comparing with Matlab ODE solver

In the comparison with Matlab, we used a cyclic sine outdoor temperature as an input to test the responses of the thermal mass. The thermal mass is subjected to a sine temperature boundary condition. The thermal mass is modeled using a finite element type of method in both CoolVent and Matlab. The air temperature is change between a maximum value T_{max} and a minimum value T_{min} in a sine pattern with



(a) Analytical

(b) CoolVent

Figure B-5: Analytical vs. CoolVent predicted semi-infinite body temperatures

a period of 24 hrs. The thermal mass temperatures are also supposed to follow the air temperature in a cyclic pattern (but with a time lag). Figure B-6 shows the comparison of the thermal mass temperatures obtained from the two programs. The temperature difference between the results provided by CoolVent and Matlab is small (~ 0.2 °C). The x-axis starts from a higher number (around 450 hrs or 19 days) to eliminate the “thermal mass” memory effect. With cyclic training, the responds is no longer sensitive to the initial value. This thermal mass training effect is also discussed in Chapter 3 when real field monitoring data is used to validate the program.

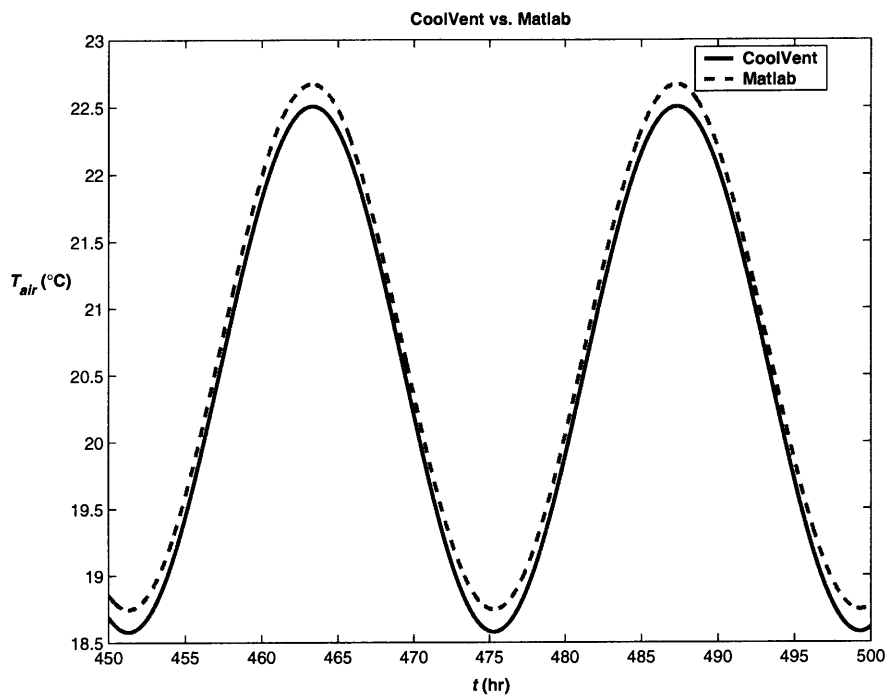


Figure B-6: Matlab vs. CoolVent under cyclic sine temperature input

B.3 Summary

In this document, the CoolVent program was validated by a few analytical models (and a well-established differential equation solver) to test the correctness of the implementation. The results show that the major parts of the program are correctly implemented and functions well to provide reliable results. For further validation studies on CoolVent, refer to Chapter 3.